



# NOVEL APPROACHES TO PERVASIVE AND REMOTE SENSING IN CARDIOVASCULAR DISEASE ASSESSMENT

**DANIEL FAUSTINO DE NORONHA OSÓRIO**

Master in Biomedical Engineering

DOCTORATE IN BIOMEDICAL ENGINEERING

NOVA University Lisbon  
September, 2022

# NOVEL APPROACHES TO PERVASIVE AND REMOTE SENSING IN CARDIOVASCULAR DISEASE ASSESSMENT

**DANIEL FAUSTINO DE NORONHA OSÓRIO**

Master in Biomedical Engineering

**Adviser:** Hugo Filipe Silveira Gamboa

*Associate Professor, Faculdade de Ciências e Tecnologia, Universidade Nova de Lisboa*

**Co-adviser:** Hugo Humberto Plácido da Silva

*Senior Researcher, Instituto Superior Técnico, Universidade de Lisboa*

## Examination Committee

**Chair:** José Paulo Moreira dos Santos

*Full Professor, Faculdade de Ciências e Tecnologia, Universidade Nova de Lisboa*

**Rapporteurs:** Hui Liu

*Researcher, University of Bremen*

Ricardo João Ferreira Simões

*Coordinator Professor with Habilitation, Instituto Politécnico do Cávado e Ave*

**Adviser:** Hugo Humberto Plácido da Silva

*Senior Researcher, Instituto Superior Técnico, Universidade de Lisboa*

**Members:** Paulo Fernando Pereira Carvalho

*Full Professor, Faculdade de Ciências e Tecnologia, Universidade de Coimbra*

José Paulo Moreira dos Santos

*Full Professor, Faculdade de Ciências e Tecnologia, Universidade Nova de Lisboa*

## **Novel Approaches to Pervasive and Remote Sensing in Cardiovascular Disease Assessment**

Copyright © Daniel Faustino de Noronha Osório, NOVA School of Science and Technology, NOVA University Lisbon.

The NOVA School of Science and Technology and the NOVA University Lisbon have the right, perpetual and without geographical boundaries, to file and publish this dissertation through printed copies reproduced on paper or on digital form, or by any other means known or that may be invented, and to disseminate through scientific repositories and admit its copying and distribution for non-commercial, educational or research purposes, as long as credit is given to the author and editor.

## ACKNOWLEDGEMENTS

What a journey it has been. First, I would like to thank my supervisor, Professor Hugo Gamboa, for his continuous support and guidance, and for being a role model for a modern scientist, taking on new and challenging endeavors in both academia and industry. The same can be said of my co-supervisor, Professor Hugo Silva, especially his eye for detail and pushing me to explore different avenues and topics, making this body of work much more complete.

I extend my acknowledgments to the University Nova of Lisbon for having me, especially LIBPHys at the Faculty of Sciences and Technology and my funding institution Fundação para a Ciência e Tecnologia and PLUX. Furthermore, I would like to thank and Instituto de Telecomunicações (IT) for their help, and all the different companies involved in the Senior Inclusive project (funded under Portugal 2020 grant, reference NORTE-01-0247-FEDER-017967).

Next, I would like to thank two equally important work groups, LIBPhys Biosignals and PLUX. From LIBPhys, I want to thank Cátia, David, João, Andreia, Jorge, and Paulo, for the fun moments that we had during our shared stay in FCT. From PLUX, I want to thank Carla, Diogo, Guilherme, Gonçalo, Nuno, and Paulo, for their friendship and for making my stay at PLUX always welcomed.

Another important group in this period of my life was my friends, especially those that were in Lisbon with me and helped me switch off and enjoy my stay in this beautiful city. Many thanks to Diogo M., Diogo P., and Teresa.

Finally, my family. My life companion, Liliana, for putting up with me when my nervous side kicked in, calming me, and helping me get through those troubled times. My parents, Aida e Paulo, from whom I had all the support that I needed. They are my cornerstones; my sister, Filipa, and our friendly competitions; and the rest of my family, for always supporting me and helping me in times of need. Without their help and support, this journey would have been much more difficult and less fulfilling.



*“Ups and downs in life are very important to keep  
us going, because a straight line even in an ECG  
means we are not alive” (Ratan Tata)*

## ABSTRACT

Cardiovascular diseases (CVDs) are the leading cause of death worldwide, responsible for 45% of all deaths. Nevertheless, their mortality is decreasing in the last decade due to better prevention, diagnosis, and treatment resources. An important medical instrument for the latter processes is the Electrocardiogram (ECG).

The ECG is a versatile technique used worldwide for its ease of use, low cost, and accessibility, having evolved from devices that filled up a room, to small patches or wrist-worn devices. Such evolution allowed for more pervasive and near-continuous recordings.

The analysis of an ECG allows for studying the functioning of other physiological systems of the body. One such is the Autonomic Nervous System (ANS), responsible for controlling key bodily functions. The ANS can be studied by analyzing the characteristic inter-beat variations, known as Heart Rate Variability (HRV). Leveraging this relation, a pilot study was developed, where HRV was used to quantify the contribution of the ANS in modulating cardioprotection offered by an experimental medical procedure called Remote Ischemic Conditioning (RIC), offering a more objective perspective.

To record an ECG, electrodes are responsible for converting the ion-propagated action potential to electrons, needed to record it. They are produced from different materials, including metal, carbon-based, or polymers. Also, they can be divided into wet (if an electrolyte gel is used) or dry (if no added electrolyte is used). Electrodes can be positioned either inside the body (in-the-person), attached to the skin (on-the-body), or embedded in daily life objects (off-the-person), with the latter allowing for more pervasive recordings. To this effect, a novel mobile acquisition device for recording ECG rhythm strips was developed, where polymer-based embedded electrodes are used to record ECG signals similar to a medical-grade device.

One drawback of off-the-person solutions is the increased noise, mainly caused by the intermittent contact with the recording surfaces. A new signal quality metric was developed based on delayed phase mapping, a technique that maps time series to a two-dimensional space, which is then used to classify a segment into good or noisy. Two different approaches were developed, one using a popular image descriptor, the Hu image moments; and the other using a Convolutional Neural Network, both with promising

results for their usage as signal quality index classifiers.

**Keywords:** Electrocardiogram, Off-the-person, Signal Processing, Signal Quality, RIC, ANS, Pervasive

## RESUMO

As doenças cardiovasculares (DCVs) são a principal causa de morte no mundo, responsáveis por 45% de todas estas. No entanto, a sua mortalidade tem vindo a diminuir na última década, devido a melhores recursos na prevenção, diagnóstico e tratamento. Um instrumento médico importante para estes recursos é o Eletrocardiograma (ECG).

O ECG é uma técnica versátil utilizada em todo o mundo pela sua facilidade de uso, baixo custo e acessibilidade, tendo evoluído de dispositivos que ocupavam uma sala inteira para pequenos adesivos ou dispositivos de pulso. Tal evolução permitiu aquisições mais pervasivas e quase contínuas.

A análise de um ECG permite estudar o funcionamento de outros sistemas fisiológicos do corpo. Um deles é o Sistema Nervoso Autônomo (SNA), responsável por controlar as principais funções corporais. O SNA pode ser estudado analisando as variações interbatidas, conhecidas como Variabilidade da Frequência Cardíaca (VFC). Aproveitando essa relação, foi desenvolvido um estudo piloto, onde a VFC foi utilizada para quantificar a contribuição do SNA na modulação da cardioproteção oferecida por um procedimento médico experimental, denominado Condicionamento Isquêmico Remoto (CIR), oferecendo uma perspectiva mais objetiva.

Na aquisição de um ECG, os elétrodos são os responsáveis por converter o potencial de ação propagado por iões em eletrões, necessários para a sua recolha. Estes podem ser produzidos a partir de diferentes materiais, incluindo metal, à base de carbono ou polímeros. Além disso, os elétrodos podem ser classificados em húmidos (se for usado um gel eletrolítico) ou secos (se não for usado um eletrólito adicional). Os elétrodos podem ser posicionados dentro do corpo (dentro-da-pessoa), colocados em contacto com a pele (na-pessoa) ou embutidos em objetos da vida quotidiana (fora-da-pessoa), sendo que este último permite gravações mais pervasivas. Para este efeito, foi desenvolvido um novo dispositivo de aquisição móvel para gravar sinal de ECG, onde elétrodos embutidos à base de polímeros são usados para recolher sinais de ECG semelhantes a um dispositivo de grau médico.

Uma desvantagem das soluções onde os elétrodos estão embutidos é o aumento do ruído, causado principalmente pelo contato intermitente com as superfícies de aquisição.

Uma nova métrica de qualidade de sinal foi desenvolvida com base no mapeamento de fase atrasada, uma técnica que mapeia séries temporais para um espaço bidimensional, que é então usado para classificar um segmento em bom ou ruidoso. Duas abordagens diferentes foram desenvolvidas, uma usando um popular descritor de imagem, e outra utilizando uma Rede Neural Convolucional, com resultados promissores para o seu uso como classificadores de qualidade de sinal.

**Palavras-chave:** ECG, Fora-da-pessoa, Qualidade de sinal, SNA, VFC, Pervasivo

# CONTENTS

<b>List of Figures</b>	<b>xii</b>
<b>List of Tables</b>	<b>xv</b>
<b>List of Algorithms</b>	<b>xvii</b>
<b>Acronyms</b>	<b>xviii</b>
<b>1 Introduction</b>	<b>1</b>
1.1 Overview . . . . .	1
1.2 Motivation . . . . .	4
1.3 Objectives . . . . .	7
1.4 Structure . . . . .	7
<b>2 Electrocardiography (ECG) Past and Present</b>	<b>9</b>
2.1 The Different Ways to Sense the Heart . . . . .	9
2.1.1 In the Beginning . . . . .	9
2.1.2 Physiology of the Heart . . . . .	12
2.2 A Deeper Journey Into the Past . . . . .	16
2.2.1 Electrode Count . . . . .	16
2.2.2 Device Evolution . . . . .	22
2.3 The ECG as a Cardiovascular Diagnostic Tool . . . . .	25
2.4 Unlocking the Secrets of the Heart Through Heart Rate Variability (HRV)	27
2.5 HRV Features as Keys to the Cardiac Activity . . . . .	32
2.5.1 Time Domain . . . . .	33
2.5.2 Frequency Domain . . . . .	34
2.5.3 Non-Linear Domain . . . . .	36
2.6 Summary . . . . .	38
<b>3 Remote Ischemic Conditioning (RIC)</b>	<b>39</b>
3.1 What is RIC . . . . .	39

3.1.1	Overview . . . . .	39
3.1.2	RIC Protection Pathways . . . . .	42
3.2	Methodology for Studying RIC Using HRV . . . . .	44
3.3	Results and Discussion . . . . .	49
3.4	Summary . . . . .	51
<b>4</b>	<b>A Mobile ECG Acquisition System</b>	<b>52</b>
4.1	What is an Electrode? . . . . .	52
4.1.1	Electrical Modeling . . . . .	52
4.1.2	Wet or Dry? . . . . .	54
4.1.3	Classification According to Placement . . . . .	56
4.2	Novel Mobile ECG Acquisition System . . . . .	56
4.2.1	Motivation . . . . .	57
4.2.2	Polymers Short List . . . . .	59
4.2.3	Preliminary Tests . . . . .	61
4.2.4	SiosLIFE Monitoring Device . . . . .	62
4.3	SiosLIFE Experimental Evaluation . . . . .	64
4.3.1	Data Acquisition Protocol . . . . .	64
4.3.2	Data Synchronization and Analysis Methodology . . . . .	66
4.3.3	Results and Discussion . . . . .	70
4.4	Summary . . . . .	74
<b>5</b>	<b>Outlier Detection</b>	<b>76</b>
5.1	What are Outliers in an ECG? . . . . .	76
5.2	How to Handle an ECG Outlier . . . . .	82
5.2.1	Time-domain Techniques . . . . .	83
5.2.2	Frequency-domain Techniques . . . . .	85
5.2.3	Trend-based Approaches . . . . .	86
5.2.4	Decision Rules . . . . .	86
5.2.5	Discussion . . . . .	88
5.3	Proposed Approach . . . . .	88
5.3.1	Area . . . . .	90
5.3.2	Image Descriptors . . . . .	92
5.3.3	Images as Input to an Artificial Neural Network . . . . .	93
5.4	Results of each technique . . . . .	96
5.4.1	Database . . . . .	96
5.4.2	Area . . . . .	98
5.4.3	Hu Image Moments . . . . .	101
5.4.4	Image as Input to an Artificial Neural Network . . . . .	105
5.5	Discussion . . . . .	106
5.6	Summary . . . . .	109

<b>6 Conclusion</b>	<b>111</b>
6.1 Overview . . . . .	111
6.2 Contributions . . . . .	113
6.3 Future work . . . . .	115
6.4 Other Contributions . . . . .	116
6.5 Published Scientific Contributions . . . . .	118
<b>Bibliography</b>	<b>119</b>
<b>Appendices</b>	
<b>A Typical HRV Features</b>	<b>136</b>
<b>B Remote Ischemic Conditioning</b>	<b>138</b>
<b>C Proposed Mobile ECG Acquisition System</b>	<b>145</b>
<b>D Hu Image Moments</b>	<b>148</b>
<b>E Signal Quality Index Table Appendix</b>	<b>150</b>
E.1 Hu Image Moments . . . . .	150
E.1.1 k-Nearest Neighbors (k-NN) . . . . .	150
E.1.2 Random Forest . . . . .	154
E.1.3 Support Vector Machine (SVM) . . . . .	159
E.1.4 K-Means . . . . .	164
E.1.5 Comparison . . . . .	166
E.2 Image as Input to an Artificial Neural Network . . . . .	167
<b>Annexes</b>	
<b>I Fitbit ECG Report Example</b>	<b>168</b>



## LIST OF FIGURES

1.1	Age-standardized CVD mortality rate. . . . .	2
1.2	Number of PUBMED Entries. . . . .	3
1.3	Two popular ECG-enabled smartwatches. . . . .	4
1.4	Recording an ECG using a Fitbit Sense. . . . .	5
2.1	The first human electrocardiogram. . . . .	11
2.2	Einthoven ECG correction. . . . .	12
2.3	Types of cardiac muscles. . . . .	13
2.4	Heart muscles action potential. . . . .	14
2.5	Rhythmic depolarization. . . . .	15
2.6	The cardiac cycle. . . . .	16
2.7	Early commercial ECG machine. . . . .	17
2.8	Einthoven triangle. . . . .	18
2.9	Anatomical planes. . . . .	19
2.10	Wilson Central Terminal leads. . . . .	19
2.11	Complete 12-lead placement. . . . .	20
2.12	Examples of early ECG recorders. . . . .	22
2.13	ECG waveform before, during, and after a STEMI. . . . .	26
2.14	Schematic overview of sympathetic and parasympathetic innervation. . . . .	28
2.15	Effect of parasympathetic control on HR in dogs. . . . .	30
2.16	Normal and drug blocked inter-beat interval power spectrum of a dog. . . . .	31
3.1	Effects of pre-conditioning on infarct size. . . . .	40
3.2	Comparison between two RIC trials. . . . .	41
3.3	Neural and humoral mechanisms of RIC. . . . .	42
3.4	Occlusion and non-occlusion protocol timeline. . . . .	45
3.5	Illustration of the sensors and cuff positioning. . . . .	46
3.6	Example of an acquisition made during RIC. . . . .	47
4.1	Electrode electrical equivalent. . . . .	53

4.2	Electrode and skin electrical equivalent. . . . .	54
4.3	Device intrusiveness vs potential outreach. . . . .	57
4.4	Examples of commercial available off-the-person ECG devices. . . . .	59
4.5	Dry electrodes samples used to test their signal quality. . . . .	60
4.6	Preliminary test setup using alligator clips. . . . .	61
4.7	Experimental setup and signal example obtained during preliminary testing. . . . .	63
4.8	Example of a full cardiac cycle in the preliminary test. . . . .	63
4.9	Prototype of the data acquisition unit to be embedded in the tablet. . . . .	64
4.10	Experimental setup used for the signal similarity evaluation test. . . . .	65
4.11	Distances used to asses their influence in signal quality. . . . .	66
4.12	Illustration of the synchronization process. . . . .	69
4.13	Boxplots of the aggregate results. . . . .	72
4.14	Result when using CF at 1 and 2cm. . . . .	73
4.15	Pre-production unit of the final design for the tablet. . . . .	75
5.1	Normalized ECG power spectrum. . . . .	78
5.2	Example of the most common ECG noise sources. . . . .	79
5.3	Respiratory modulation on ECG. . . . .	80
5.4	Example of how an EMI artifact can be perceived as life-threatening. . . . .	81
5.5	Lead off event on an ECG. . . . .	82
5.6	Lag-coordinate mapping output. . . . .	89
5.7	Convex hull representation. . . . .	91
5.8	Example of the Jordan Curve Theorem. . . . .	91
5.9	Example of Hu image moments used for different shapes and transformations. . . . .	92
5.10	Comparison between a neuron and a perceptron. . . . .	93
5.11	Example of a CNN for character recognition. . . . .	94
5.12	CNN model. . . . .	95
5.13	Histogram of segments' duration. . . . .	96
5.14	Example of different signals from the database. . . . .	97
5.15	Example of a phase portrait using a 20 milliseconds delay. . . . .	98
5.16	Convex hull template using a 20 milliseconds delay. . . . .	99
5.17	Example of a noisy segment using the convex hull template. . . . .	99
5.18	Result of edge detection and Monte-Carlo simulation. . . . .	100
5.19	Example of correct and incorrectly classified rhythm strips (k-NN, 30ms). . . . .	108
5.20	Example of correct and incorrectly classified phase portraits (k-NN, 30ms). . . . .	109
A.1	Sample density distribution of the NN intervals. . . . .	136
A.2	Example of a Poincaré plot. . . . .	136
C.1	Raw signals overlap from a preliminary test. . . . .	145
C.2	Boxplot with the cosine similarity per material and per distance. . . . .	146
C.3	Boxplot with the NRMSE per material and per distance. . . . .	146

C.4	Boxplot with the Spearman correlation per material and per distance. . . .	147
-----	--	-----

## LIST OF TABLES

3.1	HRV metrics used and their relation with the ANS. . . . .	48
3.2	Location for each of the mean values of the HRV metrics used. . . . .	49
3.3	Significant differences found in the HRV analyses. . . . .	50
4.1	Dry electrodes samples characteristics. . . . .	61
4.2	Average and standard deviation for the similarity tests. . . . .	71
4.3	Pressure influence tests using SS and PO electrodes. CS referrers to cosine similarity. . . . .	73
5.1	Grid-search optimization example. . . . .	102
5.2	Hu image moment's estimators results. . . . .	103
5.3	F1-Scores for the Noise Class using K-NN and Random Forests. . . . .	104
5.4	CNN estimators results for different delays. . . . .	105
5.5	F1-Scores for the Noise Class using Convolutional Neural Network (CNN) model. . . . .	106
5.6	Example of models using the same database. . . . .	107
A.1	Principal metrics used in HRV. . . . .	137
B.1	Overview of pre pilot subjects condition. . . . .	138
B.2	Global population analysis. . . . .	139
B.3	Senior population analysis. . . . .	141
B.4	Young population analysis. . . . .	143
E.1	k-NN classifier results for a 20ms delay, using accuracy. . . . .	150
E.2	k-NN classifier results for a 20ms delay, using F1-Score. . . . .	151
E.3	k-NN classifier results for a 20ms delay, using F1 Macro Average. . . . .	151
E.4	k-NN classifier results for a 30ms delay, using accuracy. . . . .	152
E.5	k-NN classifier results for a 30ms delay, using F1-Score. . . . .	152
E.6	k-NN classifier results for a 30ms delay, using F1 Macro Average. . . . .	153
E.7	k-NN classifier results for a 40ms delay, using accuracy. . . . .	153

E.8 k-NN classifier results for a 40ms delay, using F1-Score. . . . .	154
E.9 k-NN classifier results for a 40ms delay, using F1 Macro Average). . . . .	154
E.10 Random forest classifier results for a 20ms delay, using accuracy. . . . .	155
E.11 Random forest classifier results for a 20ms delay, using F1-Score. . . . .	155
E.12 Random forest classifier results for a 20ms delay, using F1 Macro Average. . . . .	156
E.13 Random forest classifier results for a 30ms delay, using accuracy. . . . .	156
E.14 Random forest classifier results for a 30ms delay, using F1-Score. . . . .	157
E.15 Random forest classifier results for a 30ms delay, using F1 Macro Average. . . . .	157
E.16 Random forest classifier results for a 40ms delay, using accuracy. . . . .	158
E.17 Random forest classifier results for a 40ms delay, using F1-Score. . . . .	158
E.18 Random forest classifier results for a 40ms delay, using F1 Macro Average. . . . .	159
E.19 SVM classifier results for a 20ms delay, using accuracy. . . . .	159
E.20 SVM classifier results for a 20ms delay, using F1-Score. . . . .	160
E.21 SVM classifier results for a 20ms delay, using F1 Macro Average. . . . .	160
E.22 SVM classifier classifier results for a 30ms delay, using accuracy. . . . .	161
E.23 SVM classifier classifier results for a 30ms delay, using F1-Score. . . . .	161
E.24 SVM classifier results for a 30ms delay, using F1 Macro Average. . . . .	162
E.25 SVM classifier results for a 40ms delay, using accuracy. . . . .	162
E.26 SVM classifier results for a 40ms delay, using F1-Score. . . . .	163
E.27 SVM classifier results for a 40ms delay, using F1 Macro Average. . . . .	163
E.28 K-Means clustering results for a 20ms delay. . . . .	164
E.29 K-Means clustering results for a 30ms delay. . . . .	164
E.30 K-Means clustering results for a 40ms delay. . . . .	165
E.31 Hu image moment's estimators results for all delays. . . . .	166
E.32 CNN model results for a 20ms delay. . . . .	167
E.33 CNN model results for a 30ms delay. . . . .	167
E.34 CNN model results for a 40ms delay. . . . .	167

## LIST OF ALGORITHMS

1	ECGs sources signal synchronization. . . . .	68
2	Delayed phase portrait building. . . . .	101

## ACRONYMS

<b>ANN</b>	Artificial Neural Network ( <i>pp. 87, 89, 93–95, 116</i> )
<b>ANS</b>	Autonomic Nervous System ( <i>pp. 4, 7–9, 27, 29–32, 34, 38, 39, 44, 45, 48–51, 111–113, 117</i> )
<b>ApEn</b>	Aproximate Entropy ( <i>p. 37</i> )
<b>BPM</b>	Beats Per Minute ( <i>p. 84</i> )
<b>BVP</b>	Blood Volume Pulse ( <i>pp. 45–47</i> )
<b>CD</b>	Correlation Dimension ( <i>p. 37</i> )
<b>CF</b>	SAATI's CC202 ET445 ( <i>pp. 60, 70, 71, 73</i> )
<b>CHD</b>	Coronary Heart Disease ( <i>pp. 25, 26</i> )
<b>CNN</b>	Convolutional Neural Network ( <i>pp. xv, 94, 95, 105–107, 109, 110, 115, 116, 167</i> )
<b>CRT</b>	Cathode-Ray Tube ( <i>pp. 22, 23</i> )
<b>CVD</b>	Cardiovascular Disease ( <i>pp. 1–3, 6, 8, 25, 50, 57, 74, 111, 115, 116</i> )
<b>DFA</b>	Detrended Fluctuation Analysis ( <i>p. 37</i> )
<b>DNN</b>	Deep Neural Network ( <i>pp. 87, 93, 94</i> )
<b>ECG</b>	Electrocardiogram ( <i>pp. 3–12, 15–18, 20–29, 31, 32, 38, 44–48, 51, 52, 54–56, 58–65, 67–71, 73–90, 94, 96–98, 100, 107–117</i> )
<b>eHealth</b>	Electronic Health ( <i>pp. 2, 57</i> )
<b>EMA</b>	European Medicine Agency ( <i>p. 26</i> )
<b>EMG</b>	Electromyography ( <i>p. 117</i> )
<b>EMI</b>	Electromagnetic Interference ( <i>pp. 77, 81, 115</i> )
<b>FDA</b>	US Food and Drug Administration ( <i>pp. 26, 83</i> )
<b>FFT</b>	Fast Fourier Transformation ( <i>p. 34</i> )
<b>HB</b>	Heartbeat ( <i>pp. 27, 28, 79, 83, 85, 117</i> )

<b>HR</b>	Heart Rate ( <i>pp.</i> 23–25, 27–31, 33, 35, 48, 76, 78–80, 83, 84, 112)
<b>HRV</b>	Heart Rate Variability ( <i>pp.</i> 4, 7, 8, 27–34, 36–39, 44–46, 48–51, 76, 85, 107, 112, 113, 115, 117, 137)
<b>ICU</b>	Intensive Care Unit ( <i>pp.</i> 22, 23)
<b>IMU</b>	Inertial Measurement Unit ( <i>p.</i> 24)
<b>k-NN</b>	k-Nearest Neighbors ( <i>pp.</i> xi, 93, 101–104, 106, 108, 150–154, 166)
<b>LDS</b>	Vectra’s 840i LCP ( <i>pp.</i> 60–62, 70, 71)
<b>LV</b>	LUVOCOM’s 1850-8023 PTB ( <i>pp.</i> 60, 70, 71)
<b>mHealth</b>	Mobile Health ( <i>pp.</i> 2, 5, 57, 58)
<b>MI</b>	Myocardial Infarction ( <i>pp.</i> 18, 25, 26, 39, 40, 43, 51, 112)
<b>MSE</b>	Multiscale Entropy ( <i>p.</i> 37)
<b>NRMSE</b>	Normalized Root Mean Square Error ( <i>pp.</i> 70–74)
<b>P2020</b>	Portugal 2020 ( <i>p.</i> 56)
<b>PO</b>	PolyOne’s OnForce LFT LF6600-5023 ( <i>pp.</i> 60–63, 66, 69–71, 73, 74, 114)
<b>poly</b>	Polynomial ( <i>p.</i> 159)
<b>PPG</b>	Photoplethysmography ( <i>pp.</i> 23, 24)
<b>PSD</b>	Power Spectral Density ( <i>pp.</i> 34, 48, 78, 85, 139–144)
<b>RBF</b>	Radial Basis Function ( <i>pp.</i> 159–163)
<b>RIC</b>	Remote Ischemic Conditioning ( <i>pp.</i> 4, 7, 39–51, 112, 113, 115)
<b>RMS</b>	Root Mean Square ( <i>p.</i> 84)
<b>RMSE</b>	Root Mean Square Error ( <i>pp.</i> 69, 70, 73, 74)
<b>RMSSD</b>	Root Mean Square of Successive Difference ( <i>pp.</i> 32, 44, 48, 50)
<b>ROC</b>	Receiver Operating Characteristics ( <i>p.</i> 87)
<b>RSA</b>	Respiratory Sinus Arrhythmia ( <i>pp.</i> 77, 79)
<b>RTPE</b>	RTP’s 199 X 137556 E ( <i>pp.</i> 60, 70, 71)
<b>SampEn</b>	Sample Entropy ( <i>p.</i> 37)
<b>SDNN</b>	Standard Deviation of Normal QRS Distances ( <i>p.</i> 30)
<b>SpO<sub>2</sub></b>	Oxygen saturation ( <i>p.</i> 24)
<b>SS</b>	Stainless Steel ( <i>pp.</i> 59–61, 70, 71, 73)
<b>STEMI</b>	ST-Segment Elevation Myocardial Infarction ( <i>pp.</i> 25, 26, 40, 41)
<b>SVM</b>	Support Vector Machine ( <i>pp.</i> xi, 87, 92, 93, 102–104, 107, 159–163, 166)



**VT**      Ventricular Tachycardia (*p. [81](#)*)

# INTRODUCTION

Heart-related diseases are one of the leading causes of death in the world. Tools and techniques have been and continue to be developed and perfected to prevent, manage, or cure them. One such technique is remote sensing, where near-continuous measurement allows for the assessment of the cardiovascular system. Throughout this chapter, this and other topics are explored to explain and detail the motivation for this thesis.

## 1.1 Overview

The prevalence of [Cardiovascular Disease \(CVD\)](#) and other pathologies related to the heart are increasing throughout the world. In Europe<sup>1</sup> alone, [CVDs](#) account for 3.9 million deaths every year [2]. Putting this number in perspective, [CVDs](#) are approximately 45% of all the deaths, making them by far the leading cause of death in Europe [2]. At the same time, the number of new cases is also increasing, with 85 million people in Europe suffering from [CVDs](#). Between 1990 and 2015, there was a 34% increase in new male cases and a 29% in females [2]. These high numbers have a significant economic impact, with a 210,000€ million Euros cost for the European Union, ranging from healthcare costs, loss in productivity, and informal care [2].

Nonetheless, in the last decade, the number of deaths due to these pathologies has been decreasing, as summarized in [Figure 1.1](#). This is partially due to a better understanding of the underlying causes or habits that can trigger the appearance of these types of diseases. These risk factors are, for example, high blood pressure, alcohol consumption, smoking, obesity, physical activity, and diet. Another important element for the decreasing number of deaths is the appearance of new diagnostic technologies and the improvement of existing ones. The combination of all this knowledge contributes to the big three causes for lower morbidity: prevention, diagnosis, and treatment [3]. To diagnose [CVDs](#) and related pathologies, clinicians nowadays have a plethora of tools, devices, and techniques to help them in making their decisions faster and more accurately, with some of these same tools used for prevention.

---

<sup>1</sup>The continent.

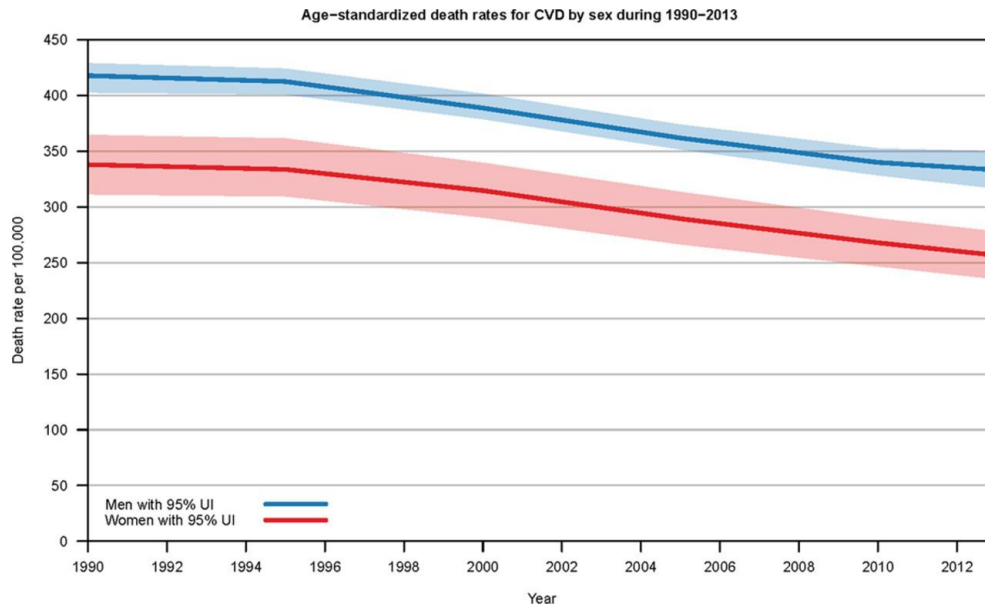
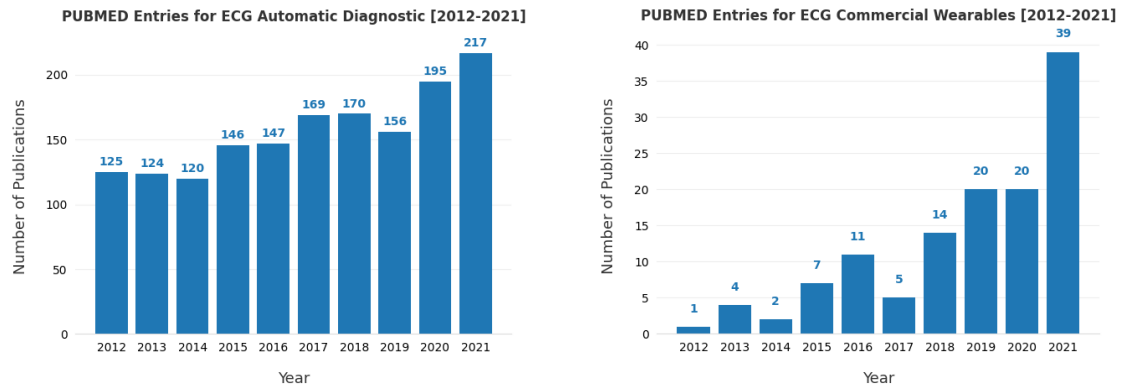


Figure 1.1: Age-standardized [CVD](#) mortality rate globally. It is possible to observe a steady decline in the mortality rate due to these diseases throughout the last decades; UI is the uncertainty interval. Extracted from [4].

In conjunction with new technologies clinicians can use at point-of-care facilities, such as hospitals or clinics, a new trend in the consumer market is also emerging, through the self-monitoring and gamification of health monitoring in day-to-day life. More and more products appear in this segment, in which a user can take their measurements and either generate reports for self-assessment, or send these measurements to their clinicians. It can even go a step forward and generate automated alerts for both parties. This enables an almost continuous monitoring, predicting and anticipating future complications before the need for urgent care. For example, if a user has an unusually high heart rate in a period where no relevant physical activity (e.g. running or hiking) was performed, it may be a sign of a cardiac complication and an alert may be generated. This inference can be made by using an accelerometer, a heart rate monitor, and fusing both data sources [5, 6].

More mobile and patient/consumer-focused devices are starting to shape how patients and doctors approach healthcare, with the sprawl of exciting fields such as [Electronic Health \(eHealth\)](#) or [Mobile Health \(mHealth\)](#). These two concepts are relatively new, with the introduction of more smartphone and wearable-based solutions for either the transmission or the gathering of physiological data [6, 7]. [eHealth](#) is the umbrella term for information and communication technologies used in health services, while [mHealth](#) is the term applied when smart portable devices are used to deliver health services [8]. The usage of such systems gives an improvement in operational efficiency, higher quality of care, and a positive return on investments [9]. In [CVD](#) monitoring and management, these technologies ([eHealth](#) and [mHealth](#)) are starting to be adopted on a larger scale and considered the new normal [10].



(a) Number of PUBMED entries for ECG automatic diagnostic.

(b) Number of PUBMED entries for ECG commercial wearables.

Figure 1.2: Number of PUBMED entries for ECG automatic diagnostic (a) and commercial wearables (b) between 2012 and 2021. The number of new entries for both terms increased for this period, especially the number of publications referencing a commercial wearable. The latter include devices used in clinical practice and research, such as smartwatches.

An important assessment method used in CVDs and that suffered a revolution in the last decade is the **Electrocardiogram (ECG)**, a medical exam based on the recording of the electrical activity of the heart, allowing the clinicians to assess the resulting waveform and quickly gauge parameters indicative of the status of the heart [5]. The heart is one of the few muscles in the body with periodic activity produced by self-excitatory cells, resulting in waveforms and patterns that allow clinicians to distinguish between normal and pathological conditions. In the past decade, the number of commercial solutions for recording and/or analyzing an ECG has increased, as well as the number of researchers applying more and more complex techniques to make diagnosis [11–13]. Figure 1.2 include the number of entries in PUBMED for two different search terms, ECG automatic diagnostic<sup>2</sup> (Sub-Figure 1.2a) and ECG commercial wearables<sup>3</sup> (Sub-Figure 1.2b), between 2012 and 2021. The latter search term was selected since it illustrates a niche segment of commercial ECG devices, being actively explored by some of the largest producers of consumer goods products, wanting to include this type of capabilities (i.e. health monitoring) in their products, leading to a rapid increase in the yearly number of publications.

There are many different techniques to record an ECG (detailed in Chapter 2). The simplest is measuring the difference between the right and left limb electrical potentials, caused by the difference in dipole created by the heart’s activity throughout the cardiac cycle. This simplicity allows companies to develop or even integrate ECG recording capabilities in their devices. One of the most widespread examples is the Apple Watch<sup>4</sup>, which allows the user to record a 30-second (s) ECG segment by placing their finger on the watch’s digital crown. Other similar smartwatches include the Fitbit Sense, Galaxy

<sup>2</sup><https://pubmed.ncbi.nlm.nih.gov/?term=ecg+automatic+diagnosis&filter=years.2012-2021>

<sup>3</sup><https://pubmed.ncbi.nlm.nih.gov/?term=ecg+commercial+wearables&filter=years.2012-2021>

<sup>4</sup>Starting from the fourth generation and only available in certain countries due to regulations.



Figure 1.3: Two popular ECG-enabled smartwatches, namely the Apple Watch (left) and the Fitbit Sense (right), capable of recording and processing 30 seconds rhythm strips.

Watch 3, or even specialized devices like AliveCor Kardia Mobile [11]. Figure 1.3 illustrates two of these devices, while Annex I presents an example of a report that can be shared with a clinician of an ECG rhythm strip recorded using a Fitbit Sense.

Developing ECG-enabled pervasive mobile devices is an area of interest, in rapid expansion in the last decade in both a clinical setting and in the consumer/end-user space [11, 12]. These new solutions, capable of recording near-continuous, good-quality signals, can improve quality of life and reduce mortality in heart-related diseases while promoting a more conscious lifestyle.

## 1.2 Motivation

With an ECG rhythm strip, clinicians have the ability to assess the condition of the heart by studying the morphology of the ECG wave. Building upon the study of the ECG, another methodology to study the heart is through the inter-beat variability, known as Heart Rate Variability (HRV), a concept explored in Chapter 2. Although the cardiac cycle is periodic, it does not have a perfect rhythm. Therefore, studying the changes in inter-beat intervals became a growing field of study, not only to assess the condition of the heart, but also the pathways that control its activity. One of such pathways is the Autonomic Nervous System (ANS), which can either increase or decrease the frequency of the cardiac cycles. Hence, an ECG can be used to not only study the heart, but also to study the systems that regulate it [14–16].

This was the basis for one of the motivations of this thesis, leveraging the inter-beat variability and its connection to the ANS to study the cardioprotection offered in response to an experimental medical procedure, known as Remote Ischemic Conditioning (RIC). The main unknown surrounding this technique is how this protection is mediated, albeit likely it is through humoral factors or the ANS. This motivation is the focus of Chapter 3, where this technique is described in detail and the results of a small pilot test are presented.

To record an [ECG](#), the conventional approach is to glue the electrodes directly on the skin and use, in a [mHealth](#) context, small devices to either save or transmit the rhythm strips. Although this approach allows for near-continuous remote [ECG](#) sensing, the placement of these devices' electrodes on the skin has to be done by an expert, challenging their dissemination as simple-to-use devices by non-medical experts. To address their dissemination and ease of use by non-medical experts, electrodes are starting to be embedded in everyday use devices, such as smartwatches. By having them embedded in the device itself, acquiring an [ECG](#) is greatly simplified [12].

Despite the benefits of having an [ECG](#) in a watch form factor to record the rhythm strip, the user has to actively and consciously perform a specific action (Figure 1.4 is an example of how to take an [ECG](#) using a Fitbit Sense). The problem with asking the user to perform a voluntary action (closing the circuit) lies in human psychology, which after the initial thrill of these new technologies eventually stops using them when the novelty fades, not recognizing the added benefit of regularly taking those measurements. Another problem is the need for regular charging since many of these devices are small and have other functionalities than just recording [ECG](#), sometimes leading to high abandonment rates [6, 17].

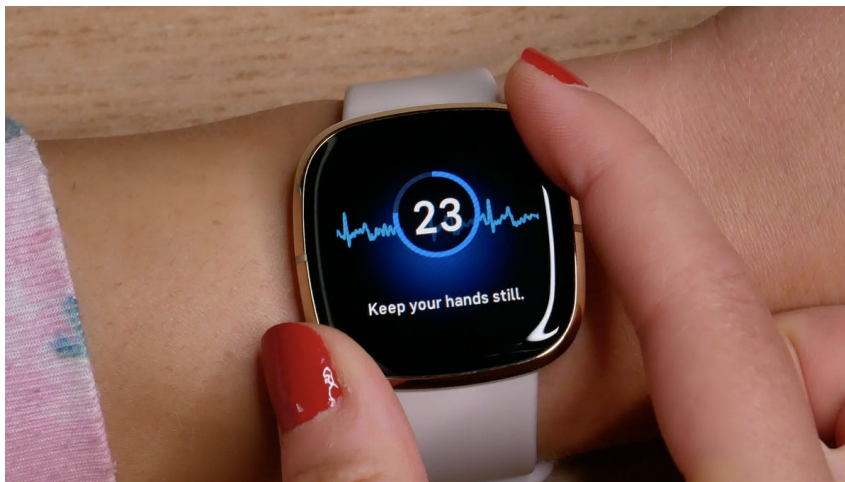


Figure 1.4: Recording an [ECG](#) using a Fitbit Sense, by holding two opposite corners of the watch for 30 seconds.

Due to the aforementioned, the [ECG](#) functionality of these devices is either used by subjects hyper vigilant with their health, or as a method to provide further detail into triggers made by other sensors/algorithms of the devices. If an [ECG](#) is performed only when the user feels the need (e.g. has chest pain, a widely known symptom of a heart attack, thus recording a rhythm strip) or when a smartwatch generates an alert (e.g. high heart rate but low activity, an irregular circumstance), it can lead to cardiac events being undetected [18].

Another approach is to embed the electrodes in other devices or surfaces, where the natural interaction with them would allow a more regular and effortless recording. Handles of gym equipment, a steering wheel, or a keyboard (or its wrist rest) [19, 20], examples of said devices, can be used to achieve coverage through the day without breaking routines or relying on alerts, reaching near-continuous monitoring. Using such approaches, users can be monitored as an extension of their interaction with the device.

For CVDs monitoring (diagnosed or undiagnosed), it is important to record the full ECG rhythm strip, since many of the indicators used in their assessment rely on the morphology and timing between the different waves in a cardiac cycle [21]. Patients suffering from CVDs are also from more senior demography, which requires an easy-to-use device, equipped with an unintrusive method to record an ECG, whether it is the material from which the electrodes is constructed from, their positioning in the device, and the subject's interaction with them. This is the motivation behind Chapter 4, the development of a novel mobile ECG acquisition system, with a more naturalistic approach to the recording of these signals and focusing on a more senior population.

There is, although, a significant drawback when using these kinds of methods to record an ECG rhythm strip, namely pertaining to the quality of the signal recorded. While the quality when there is suitable contact with the electrodes is typically good, getting this good contact can sometimes be difficult. This difficulty in maintaining a good and constant contact with the electrodes can generate noisy signals, which are not of interest to be either saved, processed, transmitted, and/or analyzed. As will be described in more detail in this thesis, the task of detecting what is and what is not a good signal can be difficult, since some noise sources can mimic parts of the ECG morphology. Nevertheless, there are many different methods to detect these outliers, either by using the statistical properties of the signal, its morphology, frequency domain features, and/or a combination of all, which can then be used to classify the waveform or parts of it as good or bad. With the advances in machine learning, there has been a shift to using more and more complex techniques, while leveraging on simpler rules as a type of pre-processing stage, to quickly and efficiently classify blatantly obvious outliers, leaving the more challenging tasks to those more advanced and complex methods [22].

Since all the different contents of a cardiac cycle are required for an effective diagnosis or monitoring of CVDs, it is important to report good quality strips to clinicians. Furthermore, having a pervasive and mobile device adds a new set of constraints, such as storage, battery life, or transmission of the ECG strips. Only those with good quality should be stored and posteriorly sent for further analysis, thus saving said resources. Chapter 5 tackle this problem, proposing a new approach to detecting and classifying outlier segments.

The following sections of this chapter, the objectives (Section 1.3) and the structure (Section 1.4), characterize in more detail said steps and how the work was segmented.



## 1.3 Objectives

The main objectives for this thesis were:

- Review of the state of the art regarding the ECG physiology, acquisition methods, and signal processing;
- Study of ECG signals to better understand the needs for the system (i.e. familiarization with ECG rhythm strips);
- Study the relation of the ECG and HRV with the ANS;
- Use the relation between the HRV and ANS to improve the state of art on an experimental medical procedure, known as RIC;
- Develop a novel device for recording off-the-person ECG signals pervasively;
- Development and benchmarking of a new signal quality metric applicable to off-the-person ECG;
- Publication of intermediate and final results in peer-reviewed international journals and/or conferences;

Overall, this thesis aims to demonstrate the importance of the ECG as a vital tool in the diagnosis, treatment, and management of various medical conditions. By understanding its generation, how to record it, and how to assess if the signal has the sufficient quality for its different applications, we can continue to advance the field of medical research and improve patient outcomes.

## 1.4 Structure

This thesis is divided into the different aspects for achieving the above-mentioned objectives and fulfilling the motivation set forth for this work. These include a journey through the heart, its intricacies and functioning, and how can it be more pervasively monitored, providing a good quality signal that can be used to study it and other systems in the human body.

**Chapter 1** A brief introduction to the problem at hand is presented as well as the motivation for the development of this thesis. Afterward, the objectives set out for this work are described.

**Chapter 2** This chapter starts with a historical perspective of the ECG, both as a technique and concerning the measurement methods. At the end of this chapter, there is an overview of how ECG is used as a diagnosis tool, either by using its morphology or by exploring the HRV.



**Chapter 3** Overviews a pilot study developed in the context of this thesis, using [ECG](#) and [HRV](#) to assess the [ANS](#) effect on the outcome of an experimental procedure, that can offer a better protection to patients that suffered cardiac ischemia.

**Chapter 4** Explores the concept of electrodes and their positioning in relation to the body. Afterward, there is an overview of the development of a novel mobile device enabling more pervasive and naturalistic [ECG](#) recordings, using embedded polymeric electrodes in a custom back cover for a tablet.

**Chapter 5** While acquiring data, many different interferences can occur that will lower its quality. Therefore, some pre-processing and signal acceptance criteria need to be ensured so that the signals can be used by either a clinician or an algorithm, and has the best quality possible. In this chapter, the different sources of noise are presented and a solution used to mitigate them is presented.

**Chapter 6** Presents a brief overview of the different topics that were addressed during the course of this work, followed by the contributions section, future work, contributions that were made to other fields, and all the academic outputs.

The topics covered in this thesis, while diverse, are inherently interconnected, being the [ECG](#) a common thread that ties everything together. It covers the evolution of [ECG](#), both as a technique and a technology, and its usefulness in modern medical practice. Subsequent chapters will delve into how to acquire and process [ECG](#) signals, including strategies for promoting more pervasive and continuous monitoring. Whether there is an interest in [CVD](#) or using it as a proxy to study [ANS](#), the quality of the [ECG](#) signal is of utmost importance, and this thesis will provide insight into how to assess signal quality.

Furthermore, and taking into consideration that some of the work was developed within a company, the research and solutions proposed were specifically designed to meet real-world needs, with a focus on practicality and applicability in industry settings.

# ELECTROCARDIOGRAPHY (ECG) PAST AND PRESENT

In this chapter, the rich history of the [Electrocardiogram \(ECG\)](#) is presented, from ancient Greece to the modern day. Furthermore, there is an overview of both the evolution of measurement methods and the technique itself.

At the end of the chapter, there is an introduction to a technique that uses the [ECG](#) and the inter-beat intervals to study not only the heart but other systems in the body, such as the [Autonomic Nervous System \(ANS\)](#).

## 2.1 The Different Ways to Sense the Heart

### 2.1.1 In the Beginning

The heart is one of the most important organs in our body, responsible for moving blood to every crevice. It has been a subject of study throughout history, and from ancient Greece to the modern world, its pulsating nature fascinates everybody. The Ebers papyrus contained the first known essay on cardiology of humanity, written in 3000 B.C., in old Mesopotamia (which nowadays comprises the territories of Syria and Iraq), where the heart is described as being at the center of the body, both physically and spiritually. It was regarded as having such an important role that it was the only organ that the ancient Egyptians handled with special care when embalming corpses, while the Aztecs offered it to their gods in sacrificial rituals [23, 24].

There are three major moments in the history of heart knowledge, corresponding to three changes in the understanding about its purpose within the body. Starting with the Greek philosopher Aristotle, which in the 4th century B.C. stated that the heart is the most important organ, responsible for almost every function, from intelligence to sensation [25].

Then, in the 2nd century A.D, the Greek physician Galen reaffirmed Aristotle's convictions that the heart has a strong correlation with the soul, but offered a different idea on its importance. Instead of the heart being the most important organ, this role belonged to

the liver, since it was the producer of the humors, while the heart helped by circulating these spirits. This was the term for the different bodily juices responsible for regulating the human behavior, which included the blood, created from food and drinks. Another belief held by Galen was the purpose of the septum, believed to be porous, which allowed some of the venous blood to be mixed with the arterial one, with each stream serving a distinct and essential role [25].

This view, called Galeanism, remained as state-of-the-art until the 16th century (about 1400 years), when these views started to be questioned in favor of the modern circulatory model. This includes the role of the septum, now a solid wall, dividing the systemic and the pulmonary circulatory loops (which were first discovered by Ibn al-Nafis in the 13th century), and cementing the role of the heart in the transmission and propulsion of the blood. These new theories that spawn in the middle of the 16th century were published by physician William Harvey in its book *On the Circulation of the Blood*, considered one of the cornerstones of modern physiology, with theology starting to take a secondary role to experimentation and empirical knowledge. This new model took nearly half a century to replace the Galen model, culminating in its acceptance by the University of Paris [25].

The final major leap in understanding the functioning of the heart was the discovery of bioelectricity and the role it played in the body. In the late 18th century, the first steps in electrophysiology were taken. Two main sparks lighten this new field, with the first spark coming literally from an electric eel in 1773, which was noticed by John Walsh in his work with electric fish. Although his work helped advance the knowledge in both physiology and the physics of the electric phenomena, he failed to publish his results, and thus is largely dismissed [26].

For the other spark, we travel to 1786 Bologna, Italy, where Luigi Galvani, an anatomist, noticed something that changed physiology forever. While working on the leg of a dissected frog, the leg twitched when a metal scalpel touched the inner nerve. Galvani called this discovery animal electricity, the force needed to activate the muscles, which he published in a manuscript in 1791, *De Viribus Electricitatis in Motu Musculari*. This new field of study was initially called Galvanism and is today known as electrophysiology. His name also designates the instrument used to measure and record electricity, the galvanometer, with the name coined by André-Marie Ampère in the early 1820s. Furthermore, in 1842, Carlo Matteucci makes an astonishing discovery, that each heartbeat of a frog had a companion electric current. This was called an action potential by German physiologist Emil DuBois-Reymond, the founder of electrophysiology, in the following year, and thus the journey of the ECG begins [27, 28].

As with John Walsh and the first reports of electricity in animals, the history of the first recorded human ECG is controversial. It is believed that the first recording was done by Alexander Muirhead in 1870, but was never published.

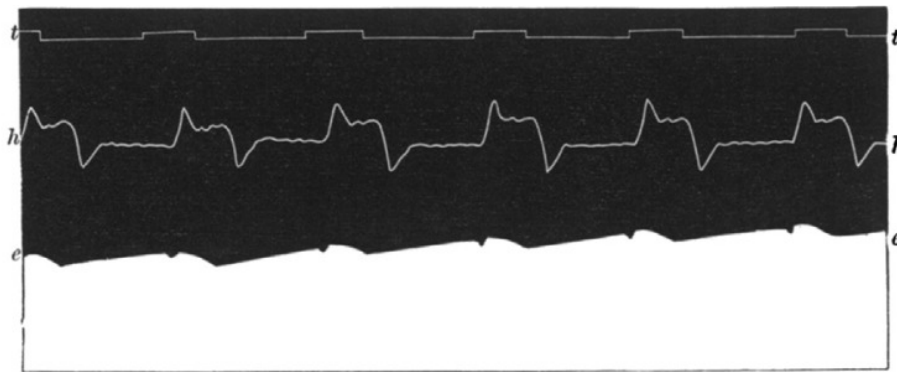


**FIG. 1. Man. Heart led off to electrometer from front and back of chest (front to Hg; back to  $\text{H}_2\text{SO}_4$ ).**  
*e.e.* electrometer. *h.h.* cardiograph. *t.t.* time in seconds.

Figure 2.1: The first human ECG, recorded by Augustus Waller of St. Mary's Medical School, with simultaneous electrometer and cardiograph tracings, showing an electrical activity preceding every heartbeat. Extracted from [29].

Therefore, the first electrocardiogram is attributed to British physiologist Augustus Waller, using a capillary electrometer<sup>1</sup>, a device invented in 1873 by Gabriel Lippmann, with an electrode strapped to the front of the chest and another in the back (Figure 2.1). Waller also discovered that the heart acts as a dipole, by moving the electrodes throughout the thorax and recording the isopotential lines. Waller brought his discovery to the First International Congress of Physiology, in Basel 1889, where in addition to showing his recording, he brought an amusing experiment using his pet dog Jimmy with its feet inside a glass jar of saline and recording the dog's electrocardiogram [27–29].

In attendance at that conference was a Dutch physician and physiologist named Willem Einthoven. Inspired by what he saw, he sets to improve the experimental apparatus in order to create an easy-to-use machine for recording ECGs. It is Einthoven himself who coins the term Electrocardiogram (more precisely Electrocardiogrammem), in 1893, during a meeting of the Dutch Medical Association. Einthoven is considered the father of the ECG, since he was the first to take into account the physical phenomena that occur inside the electrometer capillaries. The capillary electrometer is filled with a mixture of liquid mercury and sulfuric acid, that moves when a voltage is applied. Since the liquid is trapped inside the capillary, it is subject to fluid mechanics such as inertia and friction. Armed with this knowledge, in 1895 Einthoven developed a mathematical correction for the signals recorded with these devices, characterizing the familiar PQRST wave<sup>2</sup> (Figure 2.2) [27, 30–32].

<sup>1</sup>John Burden Sanderson and Frederick Page were the first to use this instrument to study the action potential of the heart and also the first to note two distinct phases.

<sup>2</sup>Since these waves were a derivation from the recorded signal, Einthoven followed the mathematical convention at the time by using the second half of the alphabet to name the structures. The first available character was the letter P.

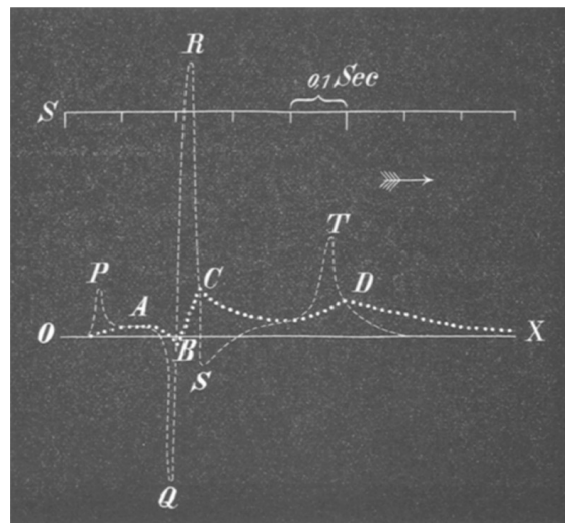


Figure 2.2: Two superimposed ECGs are shown. An uncorrected curve is labeled ABCD, from a tracing made with the refined Lippmann capillary electrometer. The other curve was a mathematically corrected version by Einthoven, to allow for inertia and friction in the capillary tube. Extracted from [32].

This marks the start of the ECG as a field of study, both as a new and exciting research opportunity but also with clinical applications. It took only twenty years from the first recorded ECG by Waller until it would be used in a clinical setting, when Mt. Sinai hospital in the United States of America used it to study arrhythmias in 1909 [31]. But before diving more into the rich history of the ECG, a brief overview is provided on how these signals are generated in the first place.

### 2.1.2 Physiology of the Heart

The heart is a muscle, a type of fibrous tissue that has the ability to contract. There are three different types of muscles, skeletal, smooth, and cardiac (Figure 2.3). In a succinct explanation, the skeletal muscles are long, multi-nuclear cells, typically bundled and linked in series forming strides that allow these bundles to slide over each other, causing them to contract. On the other hand, smooth muscles are single nucleolus cells that are non-striated, with their contractile mechanism being different from the latter. To contract, inside each cell there are fibers connecting different anchor points in the cell membrane, which are pulled towards the middle when there is a signal to contract. Another big difference is in how they are recruited. Smooth muscles are completely controlled unconsciously by the autonomic nervous system. On the other hand, skeletal muscles are controlled by the peripheral central nervous system, which can be recruited consciously. The heart muscle is a special type of fiber, borrowing characteristics from the other two types. Its cells only have one nucleolus, much like smooth fibers, but they are striated (similarly to skeletal muscles) to increase the muscle's strength. Its operation is also involuntary [33].

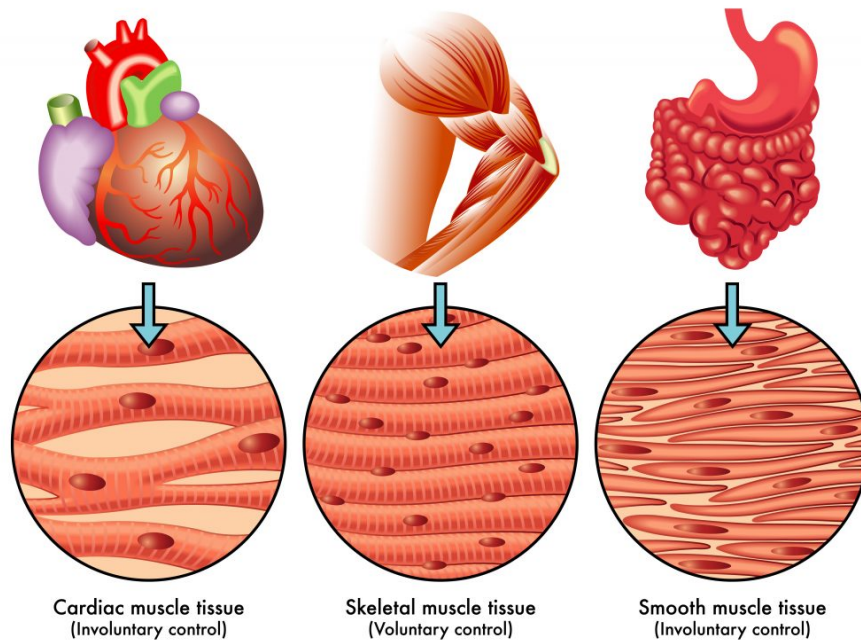
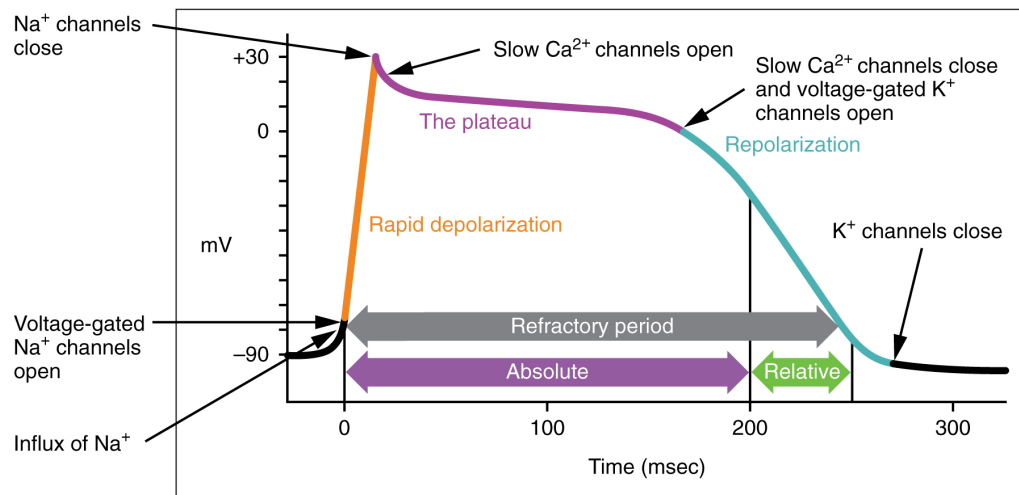


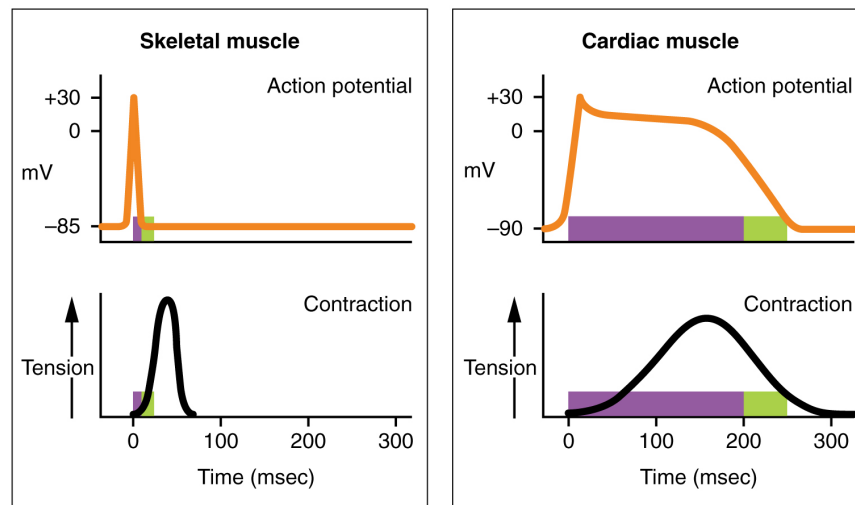
Figure 2.3: The three different types of muscles, skeletal, smooth, and cardiac. Adapted from [34].

The cells of a fiber typically have a negative potential, called the resting potential, due to the concentration of different ions inside and outside the cell, such as Potassium ( $K^+$ ), Sodium ( $Na^+$ ), and Chloride ( $Cl^-$ ). This potential is typically stable until the depolarization signal, which forces Sodium channels in the membrane to open and allows those ions to flow inside. This exchange starts slowly, but it is sped up when a threshold is crossed, causing a sudden increase in the number of channels open and the start of the contraction. Finally, there is a *plateau* where the cellular potential is near 0V, followed by the re-polarization, where there is again an ion exchange, causing the muscle to relax (Figure 2.4.a). In skeletal muscles, the *plateau* is almost non-existent, leading to a short duration contraction and with the cell being able to be recruited almost immediately (Figure 2.4.b) [33].

Building upon this summary of how a muscle cell contracts, the heart muscles can be further subdivided into conductive or contractile. Conductive fibers, as the name hints, specialize in propagating the stimuli. This cell type is unique in that its resting potential is not constant. There are channels within the membrane that are constantly open, allowing for a slow re-polarization of the cell until the discharge threshold is crossed and a faster depolarization occurs, creating a rhythmical event (Figure 2.5). On the other hand, the contractile cells have a stable resting potential but a very low action potential threshold, causing a very fast depolarization, but they are able to hold the *plateau* for a long time, increasing the contraction time of the cell (Figure 2.4.b) [33].



(a)



(b)

Figure 2.4: a) Action potential phases of a cardiac muscle cell, with an emphasis on the long *plateau* due to the opening of Calcium channels within the cell membrane, absent in other muscle cells. A long refractory period allows all the blood within the heart to be pumped effectively, leading to a cardiac cycle between 250 and 300ms; b) Difference between a skeletal and a cardiac muscle action potential and contraction periods. A skeletal muscle has a very short refractory period, leading to a fast contraction. On the contrary, the cardiac muscle contraction is spread throughout a larger period, pumping all the blood before a new contraction begins. Adapted from [35].



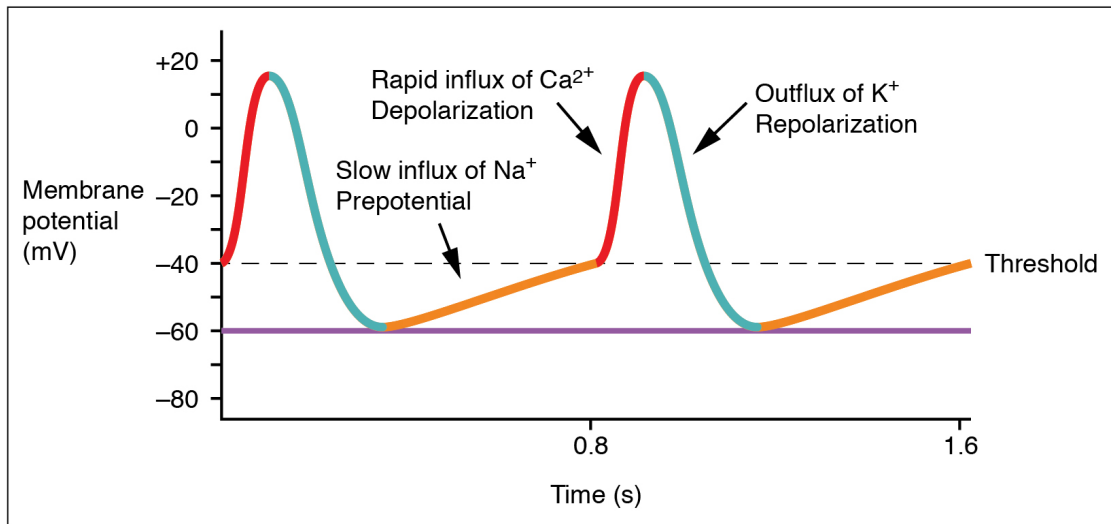


Figure 2.5: Conductive heart muscle fibers, which have a constant rhythmic depolarization. Adapted from [35].

The cardiac cycle (Figure 2.6) has four major phases, generation, delay, the start of the contraction, and its spread. The action potential responsible for the heartbeat is originated in the sinoatrial node, a group of conductive fibers located at the top of the right atrium. When these cells suffer their self-re-polarization, an action potential is generated, and the cardiac cycle starts. The next phase is when this potential arrives at the atrioventricular node, where there is a slight delay in the conduction of the signal by slowing down the progression of this wave, allowing the contraction of the atria (the atrial systole) to be completed and the valves connecting it to the ventricles to close. The wave is then routed through the His bundle, which are conductive fibers present in the heart septum, reaching the Purkinje fibers, which spread the wave through the bottom part of the ventricles. The walls of the ventricles are lined with contractile fibers, for which the re-polarization wave leads to their contraction (ventricular systole), expelling the blood from the heart [33].

To end this brief interlude and start a deeper journey into the history of the ECG, the cardiac cycle can be correlated with the ECG wave. The small P wave, the first landmark in a typical Lead I ECG, is correlated with the atrial depolarization, the auto-generation of the depolarization wave. Afterward, there is the P-Q segment, the conduction of the wave from the sinoatrial node to the atrioventricular node. In parallel, the atria are also contracting, filling their corresponding ventricles. The QRS complex is the conduction of the wave through the septum, ending in the S landmark that corresponds to the time in which the signal is propagated through the ventricles, from the bottom to the top. With the spread of the wave throughout the ventricles, they start to contract, corresponding to the S-T segment, ending in the ventricular re-polarization, represented by the T wave [33].



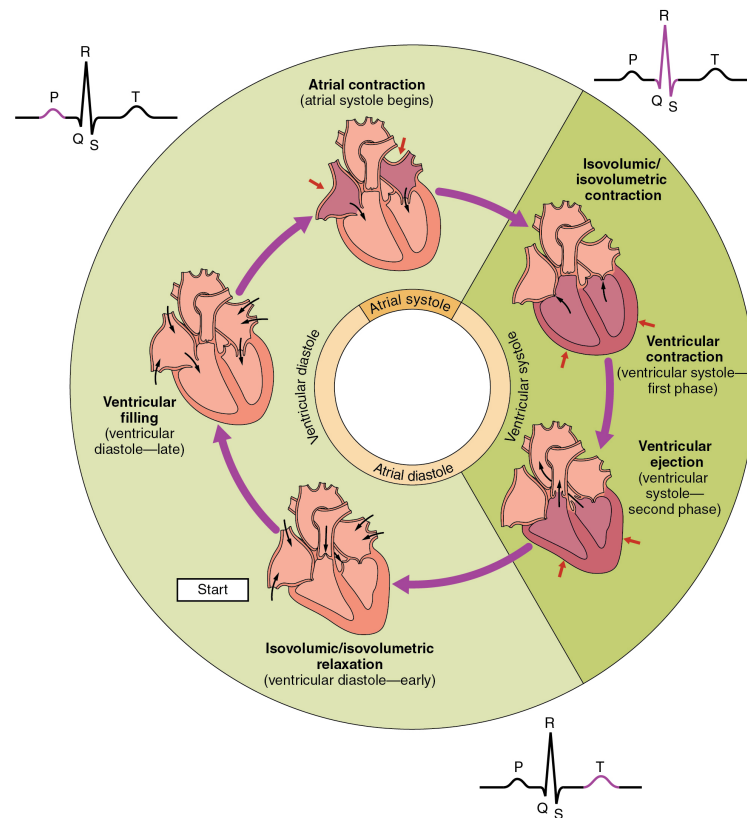


Figure 2.6: The cardiac cycle begins with the atrial systole and progresses to the ventricular systole, atrial diastole, and ventricular diastole. The corresponding ECG correlation is highlighted. Adapted from [36].

## 2.2 A Deeper Journey Into the Past

### 2.2.1 Electrode Count

Einthoven not only developed a mathematical correction for a capillary electrometer, but also a new device to record the ECG signal. Although he first tried to improve the capillary electrometer, this device had a slow response time, thus limiting its frequency response [30].

In 1901, and after spending 7 years working with a capillary electrometer, Einthoven invented a more sensitive string galvanometer. This device has a string in the middle of two strong electromagnets, which moves due to electrical currents recorded with electrodes connected to the subject. The galvanometer was a very inconvenient device, weighing 275Kg and occupying two rooms. Like Walsh and his dog experiment, the first galvanometer used buckets filled with electrolyte solution as electrodes (Figure 2.7) [27].

Through this machine, the usage of ECG as a diagnosis tool started to flourish, with the first ECG recorded using this device occurring in the following year and the first trace of atrial fibrillation being published in 1907.

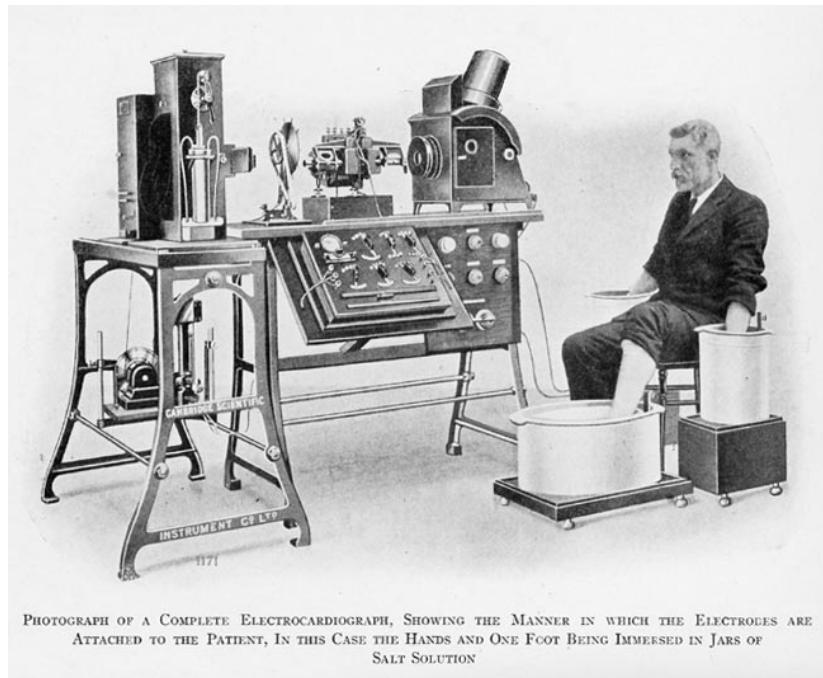


Figure 2.7: Early commercial ECG machine, built in 1911 by the Cambridge Scientific Instrument Company. Adapted from [31].

The clinical use of Einthoven's stationary equipment required trans-telephonic transmission of the ECG from the physiology laboratory to the clinic at the Academic Hospital, about a mile away, as documented in the 1906 paper on the "*le télécardiogramme*". For his work on the ECG, Einthoven earned the Nobel Prize in Physiology in 1924 [27, 30].

In order for this technique to be adopted and recognized as a diagnostics tool, there was a need to standardize the placement of the electrodes. This was yet another major contribution made by Einthoven to the newly established field. Up until 1912, Einthoven tried multiple combinations for limbs immersion and ended up with three established leads, I, II, and III, forming a triangle with the heart at its center and both arms and one of the legs<sup>3</sup> as a vertices (the unused leg served as a ground electrode). [30, 31, 37]. Figure 2.8 is the illustration provided by Einthoven for the electrode placement.

Lead I is obtained by subtracting the positive electrode connected to the left limb from the negative electrode connected to the right one. Lead II is obtained by subtracting the positive electrode connected to one of the legs from the one connected to the right limb, a 60-degree angle from the previous lead. Finally, lead III is obtained by subtracting the positive electrode connected to one of the legs from the negative electrode on the left limb, a 120-degree angle from lead I, closing the triangle. These leads (and their augmentations) constitute the limb leads [31].

With the standardization of electrode placement came the first clinical applications of this brand new technique. It was initially used to study and assess cardiac arrhythmia, an abnormal heart rhythm such as atrial fibrillation (when heartbeats are irregular and

<sup>3</sup>Although both legs can be used, typically the left leg provides a stronger signal.

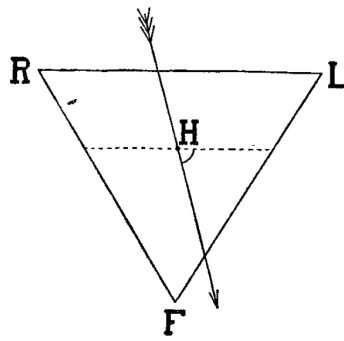


Figure 2.8: Einthoven triangle for electrode placement, where R is the right hand, L the left hand, and F both feet. The H is the heart and the arrow is the direction of the potential difference in the heart. Adapted from [37].

faster than normal), or bradycardia (when the heart beats more slowly). In fact, by the 1930s, with the parallel advances in other engineering fields, the machines became more portable, which in turn made possible the dissemination of this promising technique around the world. By then, a three lead [ECG](#) was useful to distinguish between cardiac and non-cardiac events in patients with chest pain, a frequent symptom of heart-related complications. To this day, the [ECG](#) is a key test performed in an emergency room (or by first responders) when a patient reports chest pain, as a mean of triage [27, 31, 38].

In the 1910s, there was an explosion in the number of articles, publications, and books using the [ECG](#), with one of the forefathers being Sir Thomas Lewis, an English physician. He used the [ECG](#) to study and summarize knowledge about arrhythmia, and also introduced the basic principles and terms of a heartbeat, such as the "sinoauricular node" or "pacemaker", crediting the usage of [ECGs](#) as the main reason for detection and study of cardiac events, hence bringing credibility to this new technique as a clinical tool and not just a lab instrument [28, 30].

This new interest in recording [ECG](#) traces lead to the development of smaller and more portable machines. At the start of the 20th century, the first [ECG](#) machines occupied an entire room and were usually located in special labs. Only ten years later, the first table electrocardiograph started to be sold; by 1920, the first machines that could be used by the bedside started to appear, and by the end of the 1920s these machines could be carried instead of rolled in a cart [27, 28].

Although the three-lead [ECG](#) aids in detecting arrhythmia and other heart-related pathologies, it was still hard to recognize a [Myocardial Infarction \(MI\)](#) using only the Einthoven leads. A [MI](#), or as it is more commonly known a heart attack, occurs when regions of the heart muscle (myocardium) stop receiving blood, and thus start to die (infarction) due to the lack of oxygen. There are some regions of the heart that are invisible, or "silent areas" as they became known, to a three-lead [ECG](#); and if a [MI](#) occurred in any of those regions it would be missed. These silent areas appear since the limb leads trace a vector in the frontal plane of the body, from the head (superior) to the foot (inferior).

To catch an infraction in the "silent areas", there is a need to trace a vector in the horizontal plane, from the front (anterior) to the back (posterior) (Figure 2.9) [28, 31].

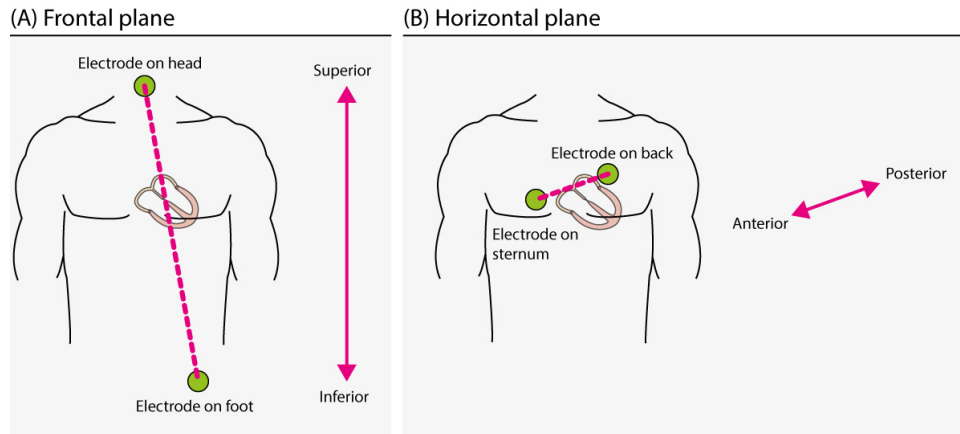


Figure 2.9: Anatomical planes. Adapted from [39].

This was the conclusion Dr. Frank Wilson arrived at in 1934. To explore the horizontal plane, he combined the three limb electrodes, creating a negative lead within the heart. This lead is known as Wilson Central Terminal and can be used to compare the potential difference using a single exploratory electrode since the central terminal under ideal circumstances should be zero. With an electrode inside the chest (the Wilson Central Terminal), the horizontal plane can now be explored by placing one of these uni-polar leads anteriorly on the chest wall. As with the Einthoven triangle, there was a need for standardization of their placement, in order for them to be useful in a medical diagnosis. The next standardized leads arrived in 1938 when the American Heart Association and the Cardiac Society of Great Britain published the placement of the precordial leads across the precordium, an anatomical region on the anterior chest wall over the heart, comprised of six unipolar electrodes named V1 through V6 (Figure 2.10) [28, 31].

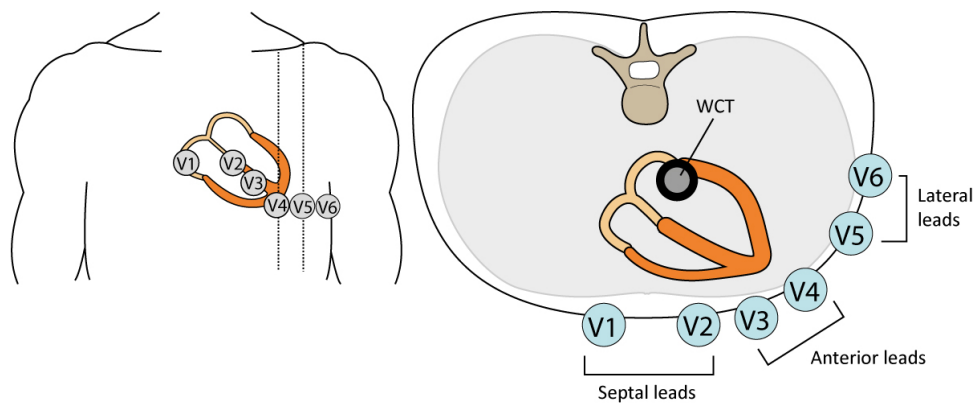


Figure 2.10: Wilson's pre-cordial leads V1 through V6; WCT is the Wilson Central Terminal. Adapted from [39].

By the end of the 1930s, a typical ECG had nine leads, comprised of the Einthoven's limb and the precordial leads. With the introduction of unipolar leads (and the ability for the recorders to perform more intricate electrical operations), Dr. Emanuel Goldberger used them to further explore the frontal plane, augmenting the Einthoven leads. The initial three leads were augmented by dividing the frontal plane in 30-degree increments instead of 60, providing more information from 0 (right to the left side, lead I) to 120-degrees (lead III). These new leads were constructed by using the electrodes placed on one of the limbs as exploratory, while the other two are averaged and used as the reference, creating three new ECG traces called augmented unipolar leads. Their name adopts the following convention, a for augmented, V for voltage, and a letter for their location, thus, aVR, aVL, and aVF, for the augmented voltage right arm, left arm, and foot leads (Figure 2.11.a) [31].

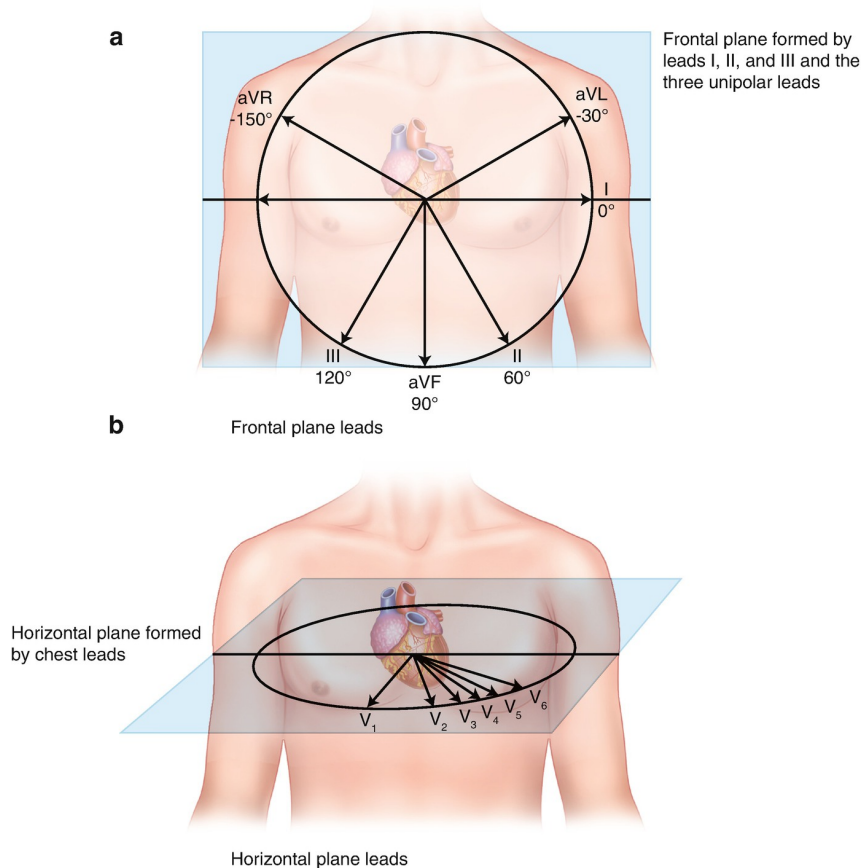


Figure 2.11: Complete 12-lead placement, divided by their recording planes. Adapted from [40].

$$\text{Lead I} = LA - RA$$

$$\text{Lead II} = LL - RA$$

$$\text{Lead III} = LL - LA$$

$$aVR = RA - (LA + LL)/2$$

$$aVL = LA - (LL + RA)/2$$

$$aVF = LL - (LA + RA)/2$$

(2.1)

$$V1 = V1p - (LA + LL + RA)/3$$

$$V2 = V2p - (LA + LL + RA)/3$$

$$V3 = V3p - (LA + LL + RA)/3$$

$$V4 = V4p - (LA + LL + RA)/3$$

$$V5 = V5p - (LA + LL + RA)/3$$

$$V6 = V6p - (LA + LL + RA)/3$$

With these three new leads, the modern electrode placement came to fruition, i.e. the 12-lead electrocardiogram, standardized in 1954 by the American Heart Association, with 9 lead electrodes and a ground that are combined as shown by Equation 2.1 to form the 12-lead, where RA, LA, and LL are the right arm, left arm, and left leg electrodes, and V1p to V6p the unipolar leads on the chest [31, 41].

In summary, the first machines capable of recording an ECG appeared at the end of the 19th century, using buckets of salt water as electrodes and a device that captured the shadow of a mercury column that moved due to the electrical potentials, i.e. the capillary electrometer. The next breakthrough was the development of a new method for recording these electrical potentials at the beginning of the 20th century, the string galvanometer, which allowed for better recordings and started the field of electrocardiography, earning Einthoven (its inventor) the Nobel prize. However, the first iterations of this machine were bulky and occupied an entire room due to the large electromagnets needed, which in turn required the machine to be water cooled and have a staff of up to five people to operate. In parallel, there was an effort for the standardization of the electrode placement, a requirement if this technique was to be used in the clinical field. The number of leads started small, with Einthoven three leads, but soon grew to the current number of 12, with the initial three enhanced by the Wilson (precordial) and the Goldberg (augmented) leads.



### 2.2.2 Device Evolution

The original room filing machines were quickly improved, occupying a tabletop by 1911. A practical version of the string galvanometer was able to be commercially bought instead of being just a lab instrument [28]. The "first portable" ECG machine was developed in 1928, when a tabletop galvanometer was converted to a wooden case, weighing 20Kg and using a car battery for power (Figure 2.12). Next came the introduction of vacuum tubes, which improved the signal amplification and further reduced the size. These improvements led to the appearance of multi-channel portable devices. Another change that aided in the miniaturization was the use of a mirror instead of a string galvanometer, which traded sensitivity with ruggedness, in the middle 1930s [28].



(a) Cambridge Electrocardiograph from 1920. Extracted from [42].



(b) Sanborn Viso 100 portable ECG machine from 1935-1955. Extracted from [43].

Figure 2.12: Example of early ECG machines spun from the original Einthoven string galvanometer.

Up to this point in history, all machines used film to record the trace, which needed to be processed, decreasing the appeal of ECG recordings in small clinics or general practitioner's offices. This is where the next breakthrough really contributed to the proliferation of the electrocardiograph as a diagnosis tool. In 1932, a Swiss company introduced the first system with direct writing, using a pen to trace the ECG. Although this was a major improvement, this technology was not broadly adopted until the 1950s, mainly due to their fidelity in tracing the wave. Direct writing became ubiquitous with the development of ink-jet printers [44].

At the same time, the introduction of Cathode-Ray Tube (CRT)s enabled real-time monitoring of patients, especially during surgeries and in Intensive Care Unit (ICU)s. Commercial machines equipped with CRTs started to appear in the early 1950s, with some models referred to as oscilloscopes, since the only feature they provided was a signal

output. CRT equipped machines had typically a worse frequency response than electrocardiographs (where the wave was traced on a rhythm strip), so their use proliferated first in surgery rooms and afterward in ICUs, where real-time data is more important than detailed information. Coupled with heart rate indicators, alarms for low or high heart rates, and output connections for printouts, these machines became a presence in every operating room or ICU ever since [45].

Advancements in semiconductor technology and later on solid-state electronics led to the increase in processing power of the machines, enabling them to perform tasks with increased complexity. From the 1970s, a range of new features started to become standard in electrocardiographs. Examples include internal memory banks for storing data for analysis, interfaces to connect external devices for processing ECG traces such as arrhythmia detection done by specialized computers, numerical display for Heart Rate (HR), and some devices started to offer isolated inputs for patient protection. The next logical step was to bring arrhythmia analysis from a central processing location to the bedside, which was a big improvement in the 1980s. Another big advance was modularity, or the ability to increase a machine feature set by attaching modules to it. In addition, the machines gained new and better screens. From the end of the 1980s and throughout the 1990s there was a race for mobility and connectivity, trying to make the machines smaller and more flexible, combining both ECG and other physiological signals, especially when monitoring critical patients or during surgery [45].

With improvements in battery and integrated circuits, smaller and more portable devices started to appear in the twenty-first century. In the 2010s, with the prevalence of smartphones throughout the population, new solutions for acquiring, transmitting, and processing the ECG started to appear. The recorders started to leverage wireless communication technologies, such as Bluetooth or Wi-Fi, to transmit data from the recorder to the physician. The quest for portability and remote transmission can be traced to 1947 when Norman "Jeff" Holter was able to transmit an electroencephalographic signal from a moving test subject. After this experiment, he moved the electrodes to the chest and the first "portable" wireless ECG machine was invented (although in the beginning it had to be carried in a backpack and weighed 38Kg) [45, 46].

Due to the invention of the transistor, the need to transmit the traces became obsolete (for the time), since all the components could now be placed in a small unit for local recording and storage. From there onward, the number of leads recorded started to increase, from 1 in the 1960s to 12 channels in the 1990s, and the recording medium went from tape to solid state (RAM chips, to disk mediums such as CDs, to Flash Memory), and the telemetry capabilities went from standard radio to cellular communications, enabling external storage and transmission of data instead of just locally [45, 46].

Finally, in the last ten years, a new trend started to appear, involving self-monitoring using wearable devices. By 2014, the incorporation of a Photoplethysmography (PPG)



sensor became common in these devices, allowing users to track their HR throughout the day and also to monitor their sleep patterns and quality. The next step was to evolve the PPG sensor to a Oxygen saturation ( $\text{SpO}_2$ ) tracker, enabling not only HR measurements but also blood oxygenation. The latest sensor to be included in commercial consumer wearables was the ECG sensor, typically recording Lead I traces [5, 47].

A brief timeline of these consumer-grade portable devices can be drawn, starting in 2006 with the introduction of the Nike+ iPod kit, where a small pebble with an embedded accelerometer could be inserted within the shoe insole and connected to an iPod, allowing the user to track their pace and step count during a workout. Since this was a product more focused on fitness, Fitbit introduced the Fitbit classic, the first commercially successful pedometer, a small clip-on device worn at the waist and allowed its users to track the number of steps taken during the day. The next big step was the introduction of the Nike+ FuelBand in 2012, a wrist-worn activity band that displayed the amount of physical activity done by the user during the day. It displayed this metric using simple color code, while also introducing a gamification<sup>4</sup> element to day-to-day activities by creating online communities and challenges users could participate.

From 2014 onward there has been a growth in both the number of wearable health trackers and the number of parameters these track. The first physiological focus sensor that was added to these devices in addition to the accelerometer/*Inertial Measurement Unit (IMU)* was the PPG sensor, from which the extraction of heart rate was now possible using commercial wrist-worn devices. This sensor extracts the heart rate by measuring the amount of light that is absorbed by hemoglobin in the blood, which changes as a function of the blood volume increase/decrease caused by the cardiac cycles [48]. Next, the PPG sensor was upgraded to include an infrared sensor, allowing it to measure  $\text{SpO}_2$ . There are two main varieties of hemoglobin, oxygenated and deoxygenated, with different absorptivity depending on the light source wavelength. Oxygenated hemoglobin absorbs more infrared light. Deoxygenated hemoglobin allows more infrared light to pass through and absorbs more red light. By using these two different wavelengths, a ratio between oxygenated and deoxygenated hemoglobin can be calculated, and the oxygen saturation measured [49]. With the growing adoption of commercial self-measuring devices by the general population, more and more processing power and sensors were added, and in 2019 the world best selling smartwatch, the Apple Watch, introduced an ECG sensor. ECG measurements are taken by placing an electrode on the bottom of the watch case and the other on the device's digital crown (a small rotary button on the side of the device), allowing their users to extract a 30-second Lead I ECG trace<sup>5</sup>. Soon all the big brands in this field, e.g. Samsung and Fitbit, introduced products that include this feature. An example report generated using a Fitbit Sense can be found in Annex I.

---

<sup>4</sup>Gamification is adding game mechanics into non-game environments.

<sup>5</sup>This smartwatch and its iterations have been clinically validated in two different multi-centre clinical studies. An overview of these studies can be found in the following link [https://www.apple.com/ca/healthcare/docs/site/Apple\\_Watch\\_Arrhythmia\\_Detection.pdf](https://www.apple.com/ca/healthcare/docs/site/Apple_Watch_Arrhythmia_Detection.pdf).

Although the consumer market for small and portable ECG recorders only started to appear in the last couple of years, as a medical device there are many specialized devices with the sole purpose of recording and processing ECG signals. In [5], the authors tested at least 15 different devices, from handheld recorders to patches attached to the chest, and using 1 to 3 lead recorders. All of these iterative improvements bring us to the present, where we have devices on our wrists/chest that can detect changes in our normal day-to-day HR, prompt us to perform a local ECG for further analysis, and evaluate if these changes are potentially indicative of Cardiovascular Disease (CVD)s, recommending a clinician appointment or even sending the traces to a clinician for real-time analysis, which has been shown to help in lowering the number of fatalities due to cardiac events [5].

## 2.3 The ECG as a Cardiovascular Diagnostic Tool

As previously described in this chapter, the miniaturization of ECG recorders and the standardization of electrode placement enabled clinicians to use the ECG as a tool for analysis of CVDs, becoming one of the most used diagnostic tools for heart disease. An ECG can provide information about the electrical conduction system of the heart, including the timing of depolarization and repolarization. This information is important for diagnosing and monitoring certain conditions, such as conduction disorders and prolonged QT syndrome, which can have serious clinical implications.

The usage of ECG in diagnosis is especially important for "silent" diseases. This type of disorder produces mild symptoms, such as fatigue or mild chest pain, as opposed to the classical tell signs of a major cardiac event, such as intense chest pain or numbness in the arm. Nevertheless, these types of events ("silent") account for 45% of all heart attacks, and one powerful and quick detection method is the ECG [18].

As a long-term monitoring tool, the ECG is also a very powerful exam. In [50], the authors found that for CVD and Coronary Heart Disease (CHD), major changes to the baseline ECG are only second to age in predicting mortality due to those disorders, performing better than the traditional risk factors including hypertension, obesity, or sex. Therefore, for example, long-term monitoring of patients using the ECG is very useful for both disease management and prevention of sudden cardiac death.

Long-term studies [21, 51] revealed that even for people without a history of CVDs, changes in the baseline ECG are associated with an increase of CHD later in life, therefore being a good candidate exam for risk stratification of asymptomatic participants given its low cost, wide availability, and safety [21].

As an example of what an ECG waveform looks before, during and after a CHD event, Figure 2.13 presents an illustration of a ST-Segment Elevation Myocardial Infarction (STEMI) (a class of MI), the most acute manifestation of coronary artery disease, and associated with great morbidity and mortality [52].

Figure 2.13 also illustrates that it is possible to observe changes in the ECG even weeks after the event, which is important in "silent" diseases or if symptoms are unnoticed/ignored by the patient, leading to a quicker diagnosis.

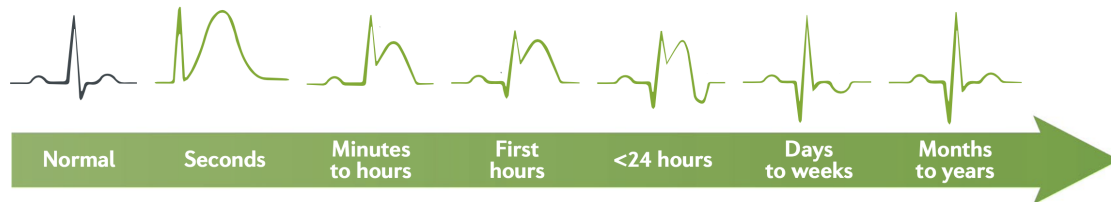


Figure 2.13: ECG waveform before, during, and after a MI illustrating a STEMI. It gets its name due to the elevated ST-segment right after the event (the second leftmost waveform). It is also possible to see the evolution of the waveform, which remains altered even weeks after the event, displaying a characteristic inverted T-wave. Adapted from [52].

As a result, the ECG is a powerful tool for analyzing the different stages of the cardiac cycle, such as re-polarization, depolarization, and valve movements. By studying the shape of the signal and the timings between fiducial points, such as the duration of the QRS complex or the amplitude of the R-peak, specific information about the heart's functionality can be obtained and used to diagnose diseases such as MI, hypertensive heart diseases, arrhythmia, or CHD [53]. Other examples include:

- Duration of QRS complex, QT interval, and TP down-sloping segment (Spodick's sign) in an ECG signal with ST-segment elevation can be used to detect acute pericarditis [54].
- Q, R, and S amplitudes and the Q-S duration in V2–V4 can be used to diagnose anterior infarct [54].
- Sokolow-Lyon score [55], Romhilt-Estes score [56], or Cornell voltage [55], which use amplitude and timing between different fiducial points, can be used to diagnose left ventricular hypertrophy.

Physicians are thus trained to look and identify changes in ECG waveforms similar to what has been illustrated in Figure 2.13. At the same time, an increasingly number of algorithms and consumer-grade hardware are starting to appear and be cleared for medical use by the US Food and Drug Administration (FDA)<sup>6</sup> and its European counterpart, the European Medicine Agency (EMA)<sup>7</sup>. These technologies aid the clinicians and patients either by detecting potential life-threatening events and raising an alert, improving the time taken in segmenting long ECG segments for further decision making, or making ECGs easily available in day-to-day situations [57, 58].

<sup>6</sup>Responsible for regulating medical devices in the United States of America.

<sup>7</sup>Responsible for regulating medical devices in the European Union.

Nevertheless, the [ECG](#) contains information beyond what can be derived from its morphology, in particular, arising from the [ANS](#) influence, which is reflected by the inter-beat intervals. Therefore, another tool that can be used to study the heart is the [Heart Rate Variability \(HRV\)](#), or the dynamics of the inter-beat intervals over time, especially since a lower variability is usually associated with a bad outcome/prognosis for many diseases [59].

*A healthy heart is not a metronome [60].*

## 2.4 Unlocking the Secrets of the Heart Through Heart Rate Variability (HRV)

As previously mentioned, [HRV](#) is the temporal variation of consecutive [Heartbeat \(HB\)](#)s, which are believed to be caused by the balance of the two antagonistically branches of the [ANS](#), the sympathetic and parasympathetic, and their influence on the cardiovascular dynamics [61].

The [ANS](#) term was coined based on its functioning, operating without any voluntary or conscious control, being also known as the involuntary nervous system. Another name by which it is known is the visceral nervous system, since many of the inputs come from the thoracic and abdominal viscera, via the vagus nerve. The [ANS](#) is responsible for many important physiological processes, including [HR](#) and blood pressure control [62].

For example, blood pressure is controlled by the brain based on the measurement of the number of impulses coming from baroreceptors, present in major systemic arteries and responsible for monitoring said pressure. If there is a decrease in pressure, then there are fewer impulses, and thus the [ANS](#) modulates the activity of the heart and blood vessels in order to increase both the [HR](#) and vascular resistance, increasing the pressure as a result [62].

The two branches, the sympathetic and parasympathetic, are anatomically and functionally distinct divisions that maintain a continuous nervous input at all times (tonically active), and increase or decrease their activity according to bodily needs. The sympathetic system generates the response known as the "fight-or-flight", preparing the body for physical activity, while on the other hand, the parasympathetic predominates in quiet and resting conditions, conserving and storing energy (also known as "rest-and-digest") [62]. Figure 2.14 offers an overview of sympathetic and parasympathetic innervation.

Looking at the [HRV](#) history, this starts with a familiar individual, the Greek physician Galen (131 - 200 A.D.), whose studies on pulse became the standard for sixteen centuries. Galen attributes the discovery of the pulsating nature of arteries to Greek physician Herophilos (335 - 280 B.C.), while the first writings that correlate this pulse to the beating of the heart come from another Greek physician, Rufus (2nd century). Galen used all this previous work, built upon it, and published many books and treatises on this

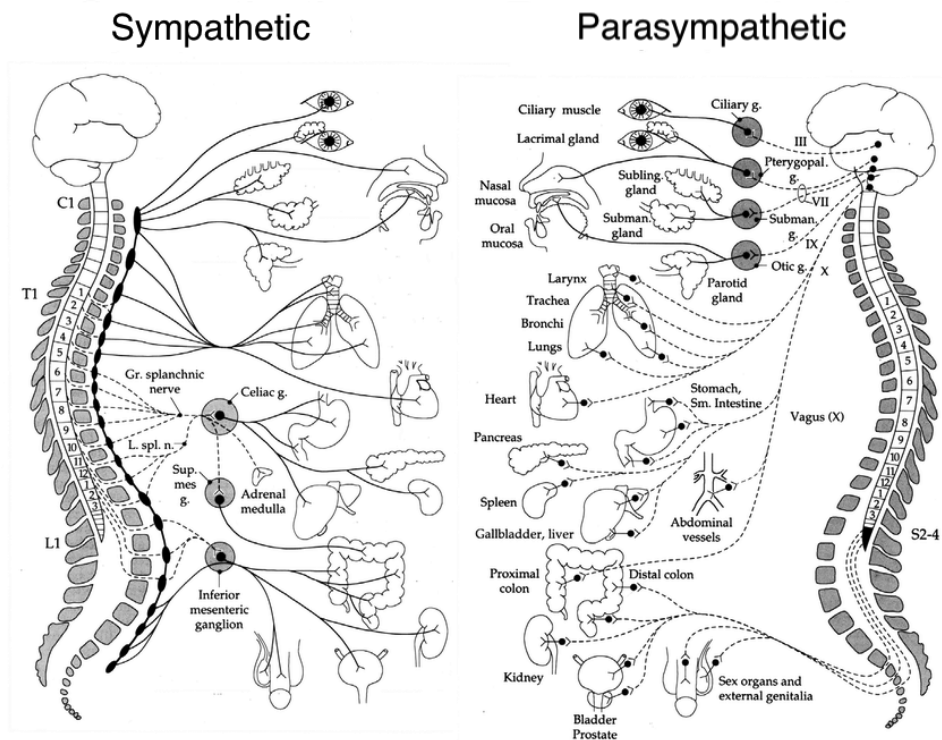


Figure 2.14: Schematic overview of sympathetic and parasympathetic innervation. Adapted from [63].

subject, some of which describing how to use the pulse in the diagnosis and prognosis of diseases [59]. On other hand, Chinese and other Asian cultures also used the pulse as a diagnosis tool, with Bian Que (500 B.C.) describing four diagnosis methods using tongue and artery pulses [64].

Physicians had to wait until the 18th century to be able to start doing more advanced studies around the HR. What allowed them this possibility was the ability to measure time much more accurately, with English physician John Floyer inventing a portable clock with a special stopwatch mechanism, an extra clock hand, and a graded dial called "The Physician Pulse Watch" in 1701. Floyer was also an advocate of using the pulse to assess diseases, and it is also due to this invention that the HB is presented in beats per minute, since this watch reported the number of beats after 60 seconds [59]. This allowed the analysis to jump from qualitative to quantitative [64].

Before the big boom in the HRV field of the 1960s and 1970s, three more major events occurred. In 1733, English Rev. Stephen Hales reported that inter-beat intervals and arterial pressure varied with the respiratory cycle. This phenomenon was further developed by German physician Carl Ludwig, which showed that inspiration increases the HR, while expiration decreases it. Finally, there was the invention of the ECG in the early 1900s. All these discoveries helped the recognition of the HRV as an important technique, which became widely available with the invention of the 24-hour Holter device, modern digital signal processing, and wearable devices [59].

#### 2.4. UNLOCKING THE SECRETS OF THE HEART THROUGH HEART RATE VARIABILITY (HRV)

---

The acceptance of the modulation of the HR by the ANS has its roots in the start of the 19th century, with the work of French physiologist Claude Bernard (1813–1878) and his understanding of homeostasis, and later due to the work of American physiologist Walter Cannon (1871–1945), stating that this homeostasis was maintained through the connection of several subsystems and controlled by what is now known as the ANS. British physiologist John Langley (1852 - 1925) expanded these works by dividing the autonomic control into the divisions used today, i.e. the sympathetic and parasympathetic [64].

At the start of the 20th century, the relation between breathing rates and HR was already known, however, in 1910 German physiologist Karl Ewald Hering (1834 - 1918) was the first to describe the relationship between these changes and the ANS via the vagal tone<sup>8</sup>. Furthermore, his son Heinrich Ewald Hering (1866 - 1948) explored these concepts, publishing several papers on the baroreceptor reflex [64].

In another interesting history crossover, at the time of Heinrich's studies on the ANS, Einthoven had just finished inventing his ECG recorder. Heinrich used it in 1908<sup>9</sup> to record ECG traces. It is believed that Heinrich was one of the first to publish a trace showing atrial fibrillation, where no supraventricular action (P-wave) is detected, while many of his other studies were cited in Sir Thomas Lewis's book "The Mechanism and Graphic Registration of the Heart Beat", an early reference in ECG studies [65].

Austrian physicians Hans Eppinger (1879 - 1946) and Leo Hess (1879 - 1963) were the first to suggest that HRV could be used to study diseases via changes in the autonomic regulation (in 1915) [59], and in 1937 U.S. psychiatric Benjamin Maltzberg (1893–1975) reported the relationship between major depression (at the time called "involution melancholia") and cardiac diseases [64]. However, only in the 1960s HRV started to be used in clinical applications [59].

The first major study using HRV in a clinical setting came in 1965 from the U.S.-based physicians Edward H. Hon, MD (1917–2006)<sup>10</sup> and Stanley T. Lee, with the analysis of fetal ECGs, where the authors noticed that when the fetus was in distress, their ECG manifested a lower HRV before any changes in the HR could be seen (e.g. a major depression in HR). This was such an important discovery that this principle is still used in the present day [64].

Shifting the focus to cardiology from obstetrics, the first major study linking the activity of the ANS and the HRV came in 1978, when an Australian team of physicians managed to establish a relationship between sinus arrhythmia<sup>11</sup> and mortality after an

---

<sup>8</sup>Hering in conjunction with his colleague physician Josef Breuer, discovered in 1868 that the lungs have several baroreceptors that, when stretched, send inhibitory signals in order to prevent over-inflation. This is known as the Hering-Breuer reflex.

<sup>9</sup>Einthoven initially commissioned Edelman and Sons of Munich to manufacture said machine before going with Cambridge Scientific Instrument.

<sup>10</sup>Dr. Hon was a pioneer in the usage of fetal ECG, publishing several papers in the field of fetal cardiac monitoring and inventing the first commercially available fetal ECG monitor in the 1960's [66].

<sup>11</sup>Normal occurring arrhythmia that, when present, typically indicates good cardiovascular health.



acute myocardial infarction. This association was based on the value of the [Standard Deviation of Normal QRS Distances \(SDNN\)](#), a metric that will be described later in this chapter, in which patients that suffered an infarction but had a higher value for this metric were more likely to survive [59, 64].

These studies are just two examples from the growing field at the time. The next big step in the field was to establish methods to assess the individual contributions from each of the two branches of the [ANS](#) in the modulation of the [HR](#). One of those studies was performed in 1975, where the authors established a relation between the parasympathetic control of the heart and the breathing-induced arrhythmia in dogs, proposing using the variations of the [HR](#) as a metric to study the parasympathetic system [64, 67]. Figure 2.15 is one of the charts the authors present in their paper [67] to demonstrate the effect of the parasympathetic system in the [HR](#) in dogs, where during its suppression the inter-beat interval remains much more stable, thus lowering the variability between them.

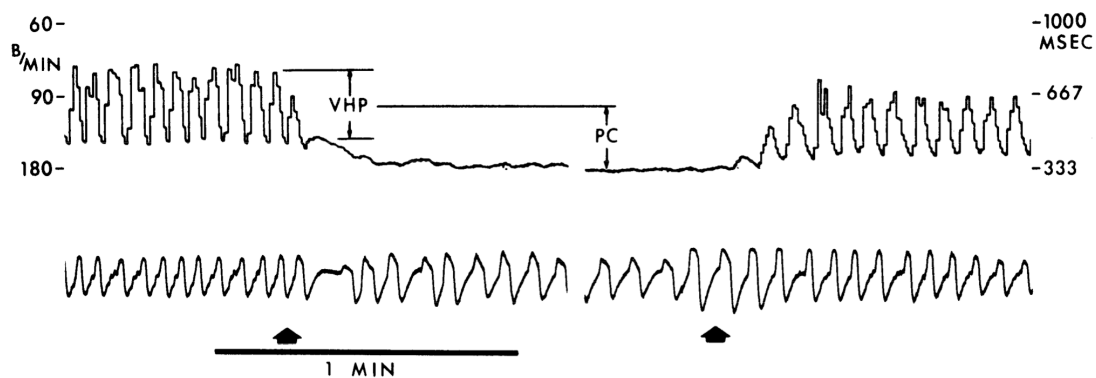


Figure 2.15: Effect of parasympathetic control on [HR](#) in dogs. The top chart is the inter-beat interval, while the bottom chart is the respiratory cycle. The two arrows represent the start and end of the cooling of the vagus nerve, which suppresses the activity of the parasympathetic control in breathing, thus removing the arrhythmia caused by it. Extracted from [67].

Another landmark study was performed by Solange Akselrod and her group in 1981, where in [68], frequency domain analysis was used to distinguish between sympathetic and parasympathetic activity. They did this by comparing the power spectrum of the inter-beat variation in a dog under normal conditions (Figure 2.16.a)) with those when sympathetic and, afterward, parasympathetic activity was blocked (Figure 2.16.b)), to assess the contribution each branch. It was then possible to infer that the lower part of the spectrum is likely the contribution of the sympathetic system while the higher frequencies are more likely due to the parasympathetic, which the authors attributed to a faster and more direct regulation mechanism by this system [64, 68].

By the end of the 1980s and early 1990s, [HRV](#) was an established technique, used for both the study of the heart, diagnosis, and/or study of the [ANS](#). However, there were many different metrics used without any guidelines. These metrics were mostly derived

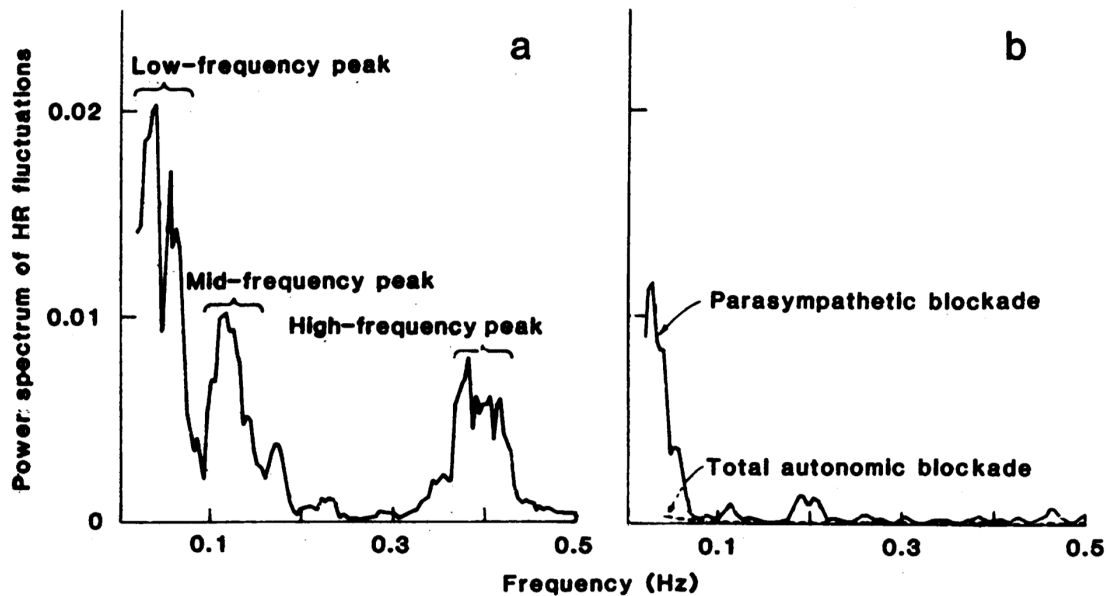


Figure 2.16: Normal and drug blocked inter-beat interval power spectrum of a dog. Sub-figure a) represents the normal power spectrum of the inter-beat interval from a 5-minute segment; Sub-figure b) is the power spectrum when drugs are given in order to suppress the activity of each branch of the [ANS](#). Extracted from [68].

from time and frequency domains, however, borrowing inspiration from chaos theory, non-linear features also started to appear, when Ary Goldberger and his group argued that [HR](#) was a conjunction of seemingly random sequences of events with an underlying structure instead of being just a periodic oscillator [69].

All of this led to the development of a taskforce in 1996 that aggregated the different metrics at the time, providing a standard that is still the base for much of the work in the field today. This taskforce also described different use cases of [HRV](#) in both clinical research and patient diagnosis, offering practical recommendations [16, 64].

As mentioned in Section 2.3, the [ECG](#) and the [HRV](#) can be used to assess sudden cardiac death prognostic. But these can also be used as dynamic indicators of disease progression/prognostic. Diabetes is a major research subject where [HRV](#) is widely used, considering that this disease can cause dysfunction of the [ANS](#). Several studies (starting from the 1970s) were able to prove that diabetic patients suffering from neuropathy due to the disease had lower [HRV](#) indices even before the clinical symptoms manifested, very useful for prevention and early diagnosis. Another disease for which effects can be monitored using [HRV](#) is chronic renal failure, which causes the inter-beat spectral power to have lower amplitudes. This could be due to the higher blood pressure affecting the baroreflex, leading to lower variability, since this is also found in patients suffering from hypertension [15].



Yet another field of study where HRV is also used is psychological research, where higher levels of inter-beat variability are associated with better adaptivity to adversities and stress [64], being an indicator of resiliency and flexibility to adapt the day-to-day changes [15]. For example, distress disorders (e.g. Post Traumatic Stress Disorder), or cognitive impairments, are typically reflected by a lower inter-beat variability (lower values for some short-term HRV indices, such as Root Mean Square of Successive Difference (RMSSD)) [69, 70]. On the other hand, individuals with higher inter-beat variability usually get better results in tasks requiring sustained attention, memory, or cognitive flexibility. In the end, for good emotional regulation, there has to be autonomic flexibility, which can be monitored via different HRV indices [69].

## 2.5 HRV Features as Keys to the Cardiac Activity

Throughout its history, the HRV features grew from simple inter-beat variance to non-linear methods. Currently, HRV features are commonly divided into their domain, either time, frequency, or non-linear [16]. This is also the division that will be used in this section, where an overview of the most used features will be given. Nevertheless, other divisions have been proposed. For example, in [14] the authors aggregated 70+ features and techniques for describing HRV and proposed a division into five groups, statistical, geometric, energetic, information, and invariant.

These metrics are typically calculated either using a 24-hour or a 5-minute recording, although shorter periods limit the usage of some of the metrics. Nevertheless, values calculated with different time segments cannot be compared [16]. Table A.1 in Appendix A summarizes all the features described below.

The previous section, Section 2.4, highlighted the increasing popularity of HRV analysis as a tool for assessing ANS function in research and clinical settings. HRV analysis has become widely recognized and utilized due to its ability to provide valuable insights into the functioning of the ANS. However, the analysis results' accuracy is heavily reliant on the quality of the ECG recording and the precise extraction of inter-beat intervals. Several HRV indices lack standardized definitions and inaccurate R-R intervals can significantly skew the overall analysis. Therefore, it is imperative to ensure high-quality ECG recordings and meticulous inter-beat intervals extraction to produce reliable and meaningful HRV results [71].

To ensure the accuracy and reliability of HRV analysis, it is crucial to eliminate all nonsinus (ectopic) beats and other ECG artifacts that may occur. This can be achieved through several methods, such as performing real-time validation and correction of the R-R series [72], or having an expert conduct the analysis [73]. By removing these erroneous beats and artifacts, the resulting HRV metrics will be of higher quality and more accurately reflect the functioning of the ANS.

### 2.5.1 Time Domain

These methods are considered the simplest to both understand and compute, being also the most reported. Time domain features can be either statistical if the features measure the variation of the intervals, or geometric (i.e. graphical) if they are extracted from either plots or histograms [16, 69]. When dealing with HRV, typically only normal beats are included in the sequence, and those that are abnormal (e.g. ventricular arrhythmia) are excluded, originating the normal to normal interval (NN) [59], which can then be used either directly or as the difference between consecutive NN intervals [16].

**SDNN** Standard deviation of normal beat intervals, typically reported in milliseconds. Represents the total variance in the segment in study [69]. It is considered one of the most used HRV parameters [64], and typically reflects the effect of both branches in the control of the HR when using 24-hour segments [16]. In this time period, it is used for cardiac risk stratification, where values for this metric below 50ms are considered unhealthy [69, 74]. This feature can also be used in shorter 5-minute segments, which can then be calculated over a period of 24 hours to form the Standard Deviation (SD) of the average NN intervals (SDANN) [16].

**RMSSD** Root mean square of successive difference, typically reported in milliseconds. This index uses the difference between successive NN intervals, which are then used for correlation with short-term variations, being a proxy for high-frequency events and thus of parasympathetic activity [16, 64, 69]. This metric is typically used in 24-hour or 5-minute windows, although 60, 30, and 10-second windows have also been used [74].

**SDSD** Standard deviation of the successive differences, typically reported in milliseconds, which also reflects short-term control [69].

**NNxx and pNNxx** Number of successive NNs pairs than are larger than a given threshold (NNxx) and its proportion to all NN intervals (pNNxx). This metric is constructed by analyzing the difference between consecutive NN intervals, and counting those that exceed a certain threshold [16]. The standard threshold is 50 milliseconds [16], although other values can be used, such as 20 milliseconds [69], which in some cases can enhance discrimination between a variety of normal and pathological conditions [75]. Since it uses the difference of successive NN intervals, it is typically correlated with the activity of the parasympathetic system [64].

**HTI** HRV triangular index. Similarly to SDNN, this index reflects global changes of the HRV, and it is typically used with 24-hour segments, using 5-minute windows. However, unlike the SDNN, it is not affected as much by irregular beats that can be present in the recording [74]. On the other hand, to build a reliable metric, enough data points should be used and therefore it is recommended that this indicator is computed for windows of

at least 20 minutes [69]. This metric can be extracted by first building a histogram of all NN intervals, with bin sizes of approximately 8 milliseconds [16]. Afterwards, the total number of NN intervals is divided by the maximum value of this distribution (Y variable in Figure A.1) [16].

**TINN** Triangular interpolation of NN histogram, typically reported in milliseconds, represents the baseline width of a histogram displaying NN intervals, for the triangle that has the maximum value of the distributions as its height. In Figure A.1, this metric is obtained by subtracting the values M and N, the other two vertices of the triangle that has Y as height [16]. Unlike the HTI, this metric can be influenced by outliers in the NN intervals [74].

### 2.5.2 Frequency Domain

Another methodology to study HRV is analyzing the frequency domain, which provides the basic information on how power (variance) distributes as a function of frequency [16]. The main advantage of using this domain is that it can provide a much more detailed view of the contribution from each of the ANS branches, dividing it into the different rhythms that comprise the inter-beat interval waveform [60]. These different rhythms are then separated into ULF<sup>12</sup>, VLF, LF, and HF, the different frequency bands used when analyzing the spectrum [74], where the area under the curve within each range can be used to quantify their contribution [59].

To get the Power Spectral Density (PSD), two methods can be used, namely non-parametric such as Fast Fourier Transformation (FFT) (assumes only deterministic components in the time series [59]), or parametric such as autoregressive models (assumes both deterministic and random components [59]) [16, 74]. The most used method is the non-parametric FFT [64], since this uses a simpler algorithm leading to a lower processing time [16].

When using non-parametric methods, an extra pre-processing step should be performed. Since the RR intervals are not evenly sampled, it is necessary to resample them using a frequency that can encompass the region of interest, which is up to 2Hz. Accordingly, following the Nyquist principle, a minimum of 4Hz should be used to capture all the oscillations [16, 64].

**ULF** Ultra-low frequencies, typically reported in milliseconds squared. This band represents frequencies that are lower than 0.003Hz, corresponding to segments that have a minimum of 5.6 minutes (333 seconds) [60], thus only being possible to determine for long-term recordings (24 hours) [64]. There is no exact physiological mechanism that can be attributed to this frequency band due to its early abandonment in research, caused

---

<sup>12</sup>Only available for recordings of at least 24 hours.

by not being included in the 1996 Task Force guidelines [60, 69]. However, some possible contributions are core body temperature regulation, metabolism, and circadian oscillations [60].

**VLF** Very-low frequencies, typically reported in milliseconds squared. This band represents frequencies that are between 0.0033 and 0.04Hz [60], and hence can be computed for short segments (5 minutes). This frequency band is said to be a method for evaluating physical activity and is mediated via sympathetic activity, however, there are uncertainties to this relation [64]. At the time of writing the guidelines, the 1996 task force was not sure of the underlying physiological mechanism and thus gave small importance to this region, leading to it being largely ignored [60]. Nevertheless, Dr. Andrew Armour and his group proposed that this band is produced by the heart, with the amplitude and frequency of these oscillations modulated by efferent sympathetic activity, being fundamental to health, since this band has a strong association with general mortality [60]. Low power in this band has also been associated with arrhythmic death, post-traumatic stress disorders, and high levels of inflammation [60].

**LF** Low frequencies, typically reported in milliseconds squared. This band represents frequencies that are between 0.04 and 0.15Hz [60]. This spectrum was initially called the baroreceptor range because in resting conditions it reflects their activity [74]. It was also believed that this spectrum range was an index of sympathetic activity, which has been challenged in the last decades, with the consensus being that is modulated by both branches plus the baroreceptors [69]. In fact, the sympathetic branch does not appear to produce rhythms above 0.1Hz, while the parasympathetic can produce them as low as 0.05Hz [74]. One possible explanation for the confusion is the usage of long and short-term recordings. When using 24-hour (long-term) recordings, the sympathetic branch will indeed have a larger influence due to its frequent activation in response to physical or mental activities, which can be confused with the short-term changes caused by the baroreflex [60].

**HF** High frequencies, typically reported in milliseconds squared. This band represents frequencies that are between 0.15 and 0.4Hz. This power band is associated with parasympathetic activity, while also being a known respiratory band due to the effect breathing has in this spectrum. It is also associated with vagal activity, since, during inspiration, the vagal nerve outflow is inhibited leading to an increase of [HR](#), while expiration leads to a restored outflow and a decrease in [HR](#). The correlation with vagal activity also comes from the total blockade of the vagal nerve, which leads to a significant reduction in HF power (almost to zero), while also decreasing the LF power [60]. Finally, this metric is highly correlated with pNN50 and RMSSD, and a decrease in this band can be caused by stress, panic, anxiety, or worry, while on the other hand at rest (e.g. during the night) there seems to be an increase in power [74].

**nuLF and nuHF** Normalized units low and high frequencies. The last two metrics, LF and HF, can be presented in their normalized form, by dividing each by the total power allowing for a better comparison between studies [69]. Normally, the total power (TP) is considered the sum between the LF and HF bands, excluding the VLF and ULF<sup>13</sup> [59].

**LF/HF ratio** Low to high-frequency ratio. This metric is controversial, since when it was first introduced it was thought that the LF was predominantly sympathetic activation while HF was parasympathetic, and thus this ratio would be a metric to compare them [74]. However, this has been contested in the last decades, since the LF is not driven solely by the sympathetic branch, with the interaction between the two branches being not linear and not mutually excluded (i.e. both can be active at the same time); furthermore, the breathing mechanism (e.g. baroreflex) can influence the power spectrum density of the bands [74]. Nevertheless, if the proper context is taken into account (for example an ambulatory condition for 24 hours would see a more pronounced activity in the sympathetic branch reflected in the LF power band), then this metric can be used to describe the relation between both systems [60].

### 2.5.3 Non-Linear Domain

Typically, **HRV** would be analyzed using the other two domains. However cardiovascular regulation research in non-linear dynamics has been growing, capturing properties that are unable to be analyzed by the other two domains [69]. Physicist Erwin Schrödinger summarized this by expressing that life is aperiodic, operating between random and periodicity [74].

Unlike, for example, the frequency domain methods that work with the assumptions of established patterns, non-linear metrics attempt to characterize the similarities in the signal throughout the time interval [64]. Some of these approaches are based on chaos theory, which states that there is order in a seemingly random sequence of events, thus being aperiodic with just a hint of a regular pattern, that, although never repeating, is bounded within a range of values. Otherwise, the system would be unstable, wandering off into infinity [59].

**Poincaré Plot Metrics** S, SD1, SD2, and SD1/SD2. These metrics are obtained from the Poincaré plot, which is drawn by plotting every NN interval against (typically) the preceding interval, and then fitting an ellipse to the generated cloud of points [74]. The area of the ellipse represents the total **HRV** and is denoted S. This metric correlates with RMSSD, and both LF and HF power [74]. SD1 is the standard deviation of the points perpendicular to the line  $y=x$ , being the ellipse width. This metric is equivalent to the RMSSD and correlates with HF power, being an index for short-term variability while also being associated with parasympathetic activation [64, 69, 74]. SD2 corresponds to the

---

<sup>13</sup>In longer recordings

length of the ellipse, being the standard deviation of the points parallel to the line  $y = x$ . This metric correlates with LF power, and SDNN, while also being an index for long-term variability [64, 69, 74]. Finally, there is the ratio between these two metrics, SD1/SD2, which reflects the unpredictability of the RR intervals, and it is used to represent the sympathovagal balance, much as the LF/HF ratio (with both metrics being correlated). In the last few years, there has been the recommendation of using a larger delay between the NN beats, using a five or six beat gap instead of one [69]. Figure A.2 is a representation of the point cloud, a fitted ellipse, and the two major axes, SD1 and SD2.

**Entropy** [Approximate Entropy \(ApEn\)](#), [Sample Entropy \(SampEn\)](#), [Multiscale Entropy \(MSE\)](#). For entropy-based methods, there are three main metrics, [ApEn](#), [SampEn](#), [MSE](#), each an evolution of the previous. The basis of all of them is the same, being a measure of complexity, or unpredictability, of a signal, quantifying the repetitions of patterns. A larger value for these metrics typically implies higher randomness, complexity, and unpredictability of the cardiac system [69]. The first of the three is [ApEn](#), an influential metric at the start of the 1990s, which returns a value between 0 and 1, with the latter indicating fewer patterns and more complexity; healthy adults tend to have a value closer to it [64]. This metric is typically calculated with shorter time sequences, with the shortest being 20 minutes [64, 69]. [SampEn](#) was developed to overcome the tendency of [ApEn](#) to overestimate the regularity of the signal, since every sequence is also matched with itself, making it a biased estimator and producing a lack of internal consistency [64, 69]. This is typically used with larger sequences (the entire time series for example) [69], although it can be used with time series with 200 to 250 points [64]. Finally, [MSE](#) addresses another concern, that not always higher irregularity is equivalent to higher complexity [69]. This problem can be overcome by using [SampEn](#) with different time scales, which can then be combined to produce a better relation between low [HRV](#) and cardiac abnormalities [69].

**Fractal Measures** [Correlation Dimension \(CD\)](#) and [Detrended Fluctuation Analysis \(DFA\)](#). Fractals are shapes that are infinitely complex and self-similar at different time scales, i.e., if the pattern was magnified, the same shape would eventually be displayed over and over again. This concept can also be applied in [HRV](#), where self-similarity across different time scales would imply a less random nature, a more predictable pattern, and a lower variability [69]. To study these fractals for [HRV](#), there are two main techniques, using [CD](#) and [DFA](#). [CD](#) is used to measure the dimension of the fractal, an estimate of the number of variables that are needed to reproduce the system dynamics, where a higher [CD](#) leads to a larger number of variables, and thus greater complexity and variability [69, 74]. [DFA](#) is another widely used method, measuring the correlation between the intervals at different timescales, outputting two different slopes which represent either short or long-term modulation [69, 74].

## 2.6 Summary

This chapter began with the history of [ECG](#), from ancient Egypt and Greece, to Galvani's frog leg experiment, Weller's first [ECG](#), and Einthoven's breakthroughs in both mathematical and hardware domains. It followed with a description of the standardization of the different leads, the first usage of an [ECG](#) as a means of diagnosis, the constant evolution of the recording device's abilities, and the increase in portability and miniaturization of these. Finally, it culminated in the variety of devices that exist nowadays, from medical grade portable monitors to small wrist based consumer devices.

Also in this chapter, an overview was provided on how the [ECG](#) can be used to study the heart, either by using its morphology, or differences between the inter-beat interval. The latter is called [HRV](#), a technique used more frequently not only to study the heart but also other systems such as the [ANS](#). Several metrics can be extracted from the inter-beat interval, divided into time, frequency, and non-linear domain, which can then be used to study the workings of the heart or the [ANS](#).



## REMOTE ISCHEMIC CONDITIONING (RIC)

This chapter will focus on a simple, safe, and inexpensive procedure for cardiovascular protection that, when performed, can have a significant positive result in an outcome and life of a patient, called [Remote Ischemic Conditioning \(RIC\)](#). The main unknown surrounding this technique is how this protection is mediated, albeit likely it is through humoral factors or the [Autonomic Nervous System \(ANS\)](#).

As seen in Chapter 2, [Heart Rate Variability \(HRV\)](#) can be used to study not only the heart but other systems as well, due to the effects they have on the inter-beat variability, with one of such systems being the [ANS](#). During the development of this work, there was the opportunity of applying this technique in a pilot project (developed in conjunction with researchers from CEDOC<sup>1</sup>, a medical research center from NOVA Medical School), where the effects of [ANS](#) during the application of the [RIC](#) procedure were studied.

The results of this chapter were published in the paper entitled "Autonomic nervous system response to remote ischemic conditioning: Heart rate variability assessment" [76].

### 3.1 What is RIC

#### 3.1.1 Overview

[RIC](#) is a procedure where one of the limbs (arm or leg) goes through repeated cycles of constriction and relaxation of blood vessels and tissue, in order to trigger protective pathways in a distant organ, be it, for example, the kidney, heart, and/or the brain [77, 78]. The pressure generated by the constriction is thought to be responsible for triggering the protection signal, which is then mediated either by humoral, neurogenic, immune system, and/or blood-borne factors [77, 78]. This technique has gained some interest in cerebrovascular disease management, due to its safety and feasibility, having, for example, multiple ongoing clinical studies in the field of strokes [77, 78]. It is also one of the most promising techniques in limiting the damage caused by reperfusion injuries after an acute [Myocardial Infarction \(MI\)](#) [79].

---

<sup>1</sup>Centro de Estudos de Doenças Crónicas.



This technique was first demonstrated in 1986, where 5-minute cycles of occlusion and releasing of an artery in the myocardium<sup>2</sup> of a dog led to a reduction in the size of an infarct (area of dead tissue due to a prolonged lack of blood), which was caused by a prolonged induced ischemic and subsequent re-perfusion in the myocardium. [77, 80]. Figure 3.1 adapted from [77] is an illustration of such reduction in infarct size. Then, in 1994, it was demonstrated that performing this conditioning in another organ's artery lead to the protection of other organs as well, and inter-organ RIC was discovered.

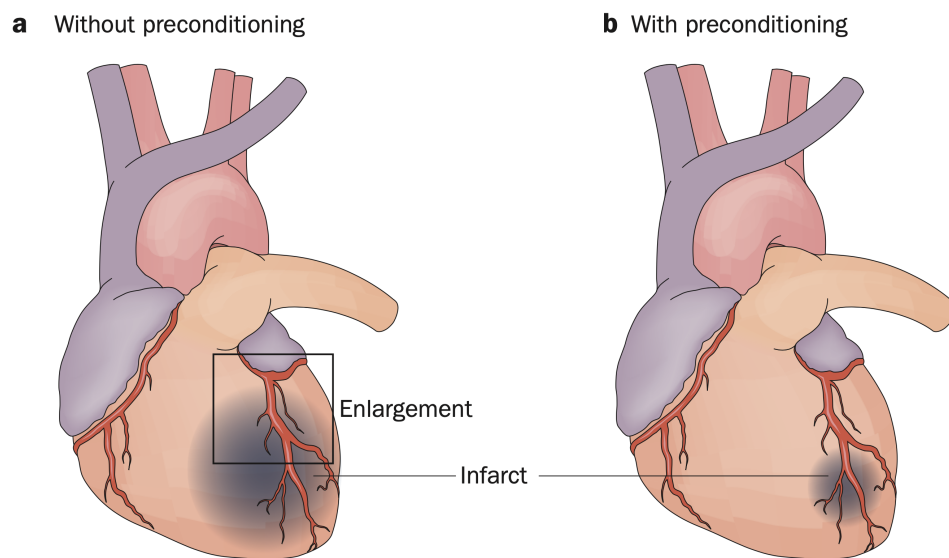


Figure 3.1: Effects of pre-conditioning on infarct size. It was shown that pre-conditioning tends to reduce infarct size, thus minimizing the effects of a cardiac occlusion that can be originated, for example, due to a MI. Extracted from [77].

This culminated with a case in 2002, where applying this protocol on a limb (in this case an arm), lead to the protection against endothelial dysfunction in humans and coronary ischemia in pigs [77]. Prior to this discovery, the techniques employed involved applying the conditioning directly to either the heart or the organ/arteries promoting the protection, requiring an invasive intervention [81]. There are other remote conditioning stimuli that can be used, such as surgical trauma, where an abdominal incision will also trigger protection mechanisms [77], while some disorders can also mimic the protection conferred by RIC, e.g. an unstable angina<sup>3</sup> tends to offer some protection when the patient has a MI [81].

The usefulness of RIC in a clinical context has been highly debated in recent years, with the conclusion of one major clinical study, the CONDI-2/ERIC-PPCI trial [82]. In this trial, the effect of the procedure was assessed in the twelve months following its application in patients that suffered a ST-Segment Elevation Myocardial Infarction (STEMI),

<sup>2</sup>Heart muscle.

<sup>3</sup>Condition characterized by the reduction in blood flow to the heart muscles, typically accompanied by chest pain.

but no improvement in the clinical outcome of the patients was observed, with no reduction in either cardiac deaths or hospitalizations [83]. This was not the expected outcome, and subsequent studies and papers offer some possible explanations and criticism of the trial. For example, the differences between animal models and the patients enrolled in the study, or the applied limb protocol, which may have not been maximized for cardiac protection and to take into account the limb in which the procedure was applied [84].

Perhaps the biggest criticism of that large study is the population enrolled, namely patients that after STEMI had the gold standard in the treatment of this condition, either by using newer drugs, access to advanced recovering centers, or coming from developed countries in Europe [79, 84]. Another study performed in Mauritius, a sub-Saharan African country with a multi-ethnic population, the ERIC-LYSIS trial, saw an improvement in infarct size in the patients recruited in the study [84]. In these countries (low-to-middle income countries), patients suffering an ischemic heart disease are typically younger (<65 years), have a higher risk of dying from such diseases since there is a lack of preventive and continuous care, and are typically treated with sub-optimal drugs and procedures, resulting in larger infarcts [79, 84]. Figure 3.2 from [79] presents a summary of these two studies.

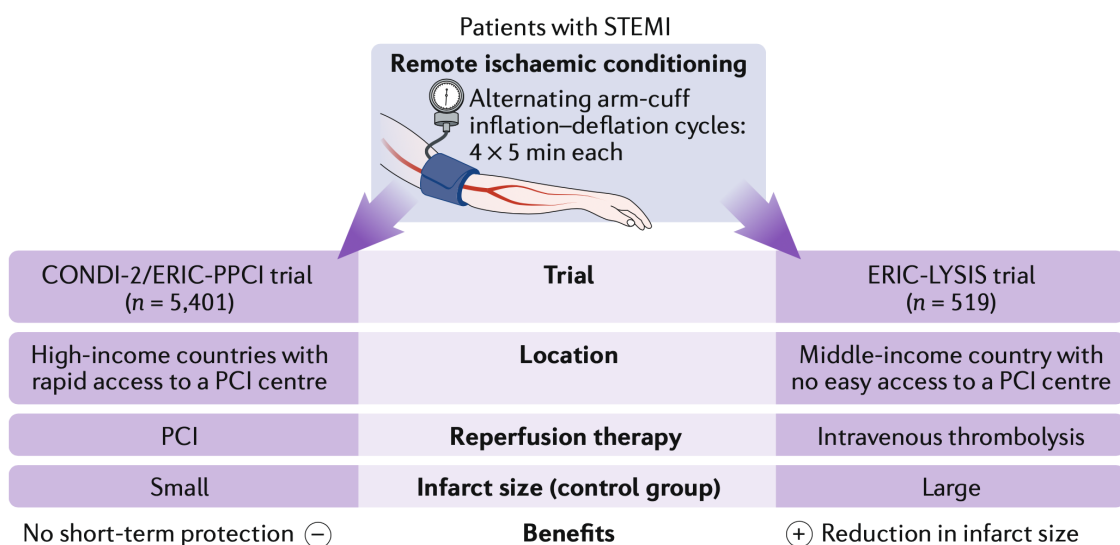


Figure 3.2: Comparison between two RIC trials. The results from these two trials are very different, where in the CONDI trial no short-term protection was found, , while in the ERIC trial a reduction in infarct size was observed. Some of the possible explanations for this difference could be due to the location and the therapy used. Extracted from [79].

A common outcome of both studies was the unanimous consensus that the procedure is safe [79, 83, 84]. With this being a very simple and low-cost procedure, it could prove to be an important technique in low to middle-income countries for improving the outcome of patients that suffer a STEMI, reducing the size of infarcts that may be formed [79].

### 3.1.2 RIC Protection Pathways

The regulation mechanisms of this process are not fully understood. These can be, neural and/or humoral mechanisms, the activation of the immune system, and/or blood-borne factors that are released into the bloodstream and transported to the different organs [77]. The sequence of events seems to be the following: the generation of the signal that will promote the protection (either on a remote organ/limb or directly on the organ); the conduction of said signal to the target organ (e.g. the heart); and the activation of the intra-organ mechanism that protects it [81]. Figure 3.3 represents the known and unknown pathways that might be involved in cardioprotection mediated by RIC, with a focus on neural and humoral pathways.

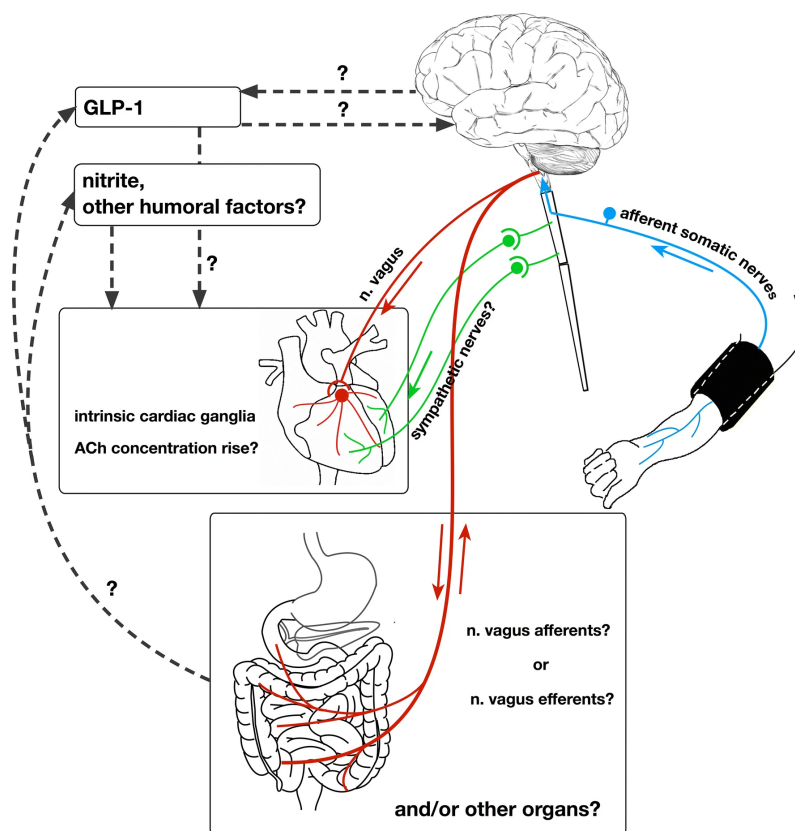


Figure 3.3: Neural and humoral mechanisms of RIC. Although there are probably other pathways that mediate the protection conferred by this procedure (e.g. the immune system response), these two mechanisms are thought to be the most important. This figure illustrates the different interconnection between these two pathways, from the generation of the RIC protection signal in the remote limb, to the conduction of the signal, and finally the triggering of intra-organ protection pathways. Extracted from [80].

The humoral pathways are supported by different experiments in which blood from one animal where the procedure was applied triggers the protection when transfused to another animal. Thus, there is a presence and possible necessity for a factor (which might be a protein) that is present in the blood when the procedure is applied [81]. Moreover, some other substances were found to exist when the procedure is applied. For example,

nitric oxide is released by the femoral artery endothelium when its subjected to stress, which then is transported to the heart, and is thought to also be responsible for the reduction of the infarct 30 minutes after a MI [80]. Another characterized substance is the Glucagon-Like Peptide 1 (GLP-1), a hormone that was shown to be involved in mediating cardioprotection by the activation of its receptor (GLP-1R), although the exact mechanism that leads to the protection is not yet established. Other molecules that are involved in the mediation and signaling of the protection could be opioids, bradykinin, and adenosine [80].

Another similar pathway that could be involved in the protection of remote organs, in particular the heart, is the immune system, the contributions of which remain even more mysterious than the other two pathways. Some of the outcomes of MI include endothelial dysfunction or cardiac failures, with one of the mechanisms that contribute to those outcomes being acute inflammation, mainly due to the presence of proteins and tissue that mark the infarction area as a danger zone. There are four different types of programmed cell death triggered by an MI in the surrounding areas of the blockage, apoptosis, necrosis, necroptosis, and pyroptosis. Apoptosis is a controlled death, without the release of cellular content to the surrounding area, unlike necroptosis and pyroptosis, which release cytokines (important proteins for cell communication). Some of these proteins enhance inflammation, while in a MI they increase the size of the infarct, due to the activation of the immune cells in the area to remove the damaged cells. RIC has been shown to reduce the level of these pro-inflammation cytokines in animal models, while in the majority of human trials it had an ambiguous effect on their release. However, if the results from the two larger trials are used, they fall in line with those from the animal model in showing that there is a reduction in cytokine levels [83], exerting some protection via an immune system pathway.

Finally, there is the neural hypothesis, that argued in favor of the involvement of the nervous system in mediating the protection. Its role has been studied by mainly observing the changes in outcome when this system is not present, either by reversible procedures such as drugs (e.g. drugs blocking its influence), irreversible procedures (e.g. cutting nerves, direct stimulation of nerves), or by natural causes (e.g. neuropathy or nephropathy) [80, 81]. One of the nervous system divisions that appears to be directly involved is the parasympathetic system, where blockage of brain areas that mediate its activity or cutting nerves used by this system resulted in larger infarcts, while direct stimulation of the vagal nerves resulted in smaller infarcts [80]. While the direct contribution of the sympathetic nervous system is not clear [80], when there is a blockage of its ganglia (which is also controlled by the parasympathetic system) there is a reduction in the protection [81]. To further establish the neural pathway as a mediator, some studies have determined that if the femoral nerve is transected, then the RIC procedure performed in that leg does not provide any protection. Other studies were able to observe an increase in afferent nerve activity in the kidney when its artery was occluded. Finally, direct stimulation of a remote organ's nerve mimicked the protection provided by the RIC procedure [81].

Nevertheless, the consensus is that a complex mixture of the nervous and humoral pathways, combined with others such as the immune system, are responsible for the activation and mediation of the protection provided by the RIC procedure. When the vagal nerves are directly stimulated, there is the release of many protective factors into the bloodstream, be it, for example, the unnamed protective factor, or the release of nitric oxide. There are still many doubts in this articulation, especially about the source of the protection factor (which can come from the visceral organs), and what system is triggered first, namely if the neural system elicits a response from the humoral pathways or the other way around [80, 81].

Another unknown, and one that is going to be only briefly addressed, is the different nomenclature for RIC procedures, or to that effect, the different ischemic conditioning, with respect to when it is applied. This procedure can be applied either prior to an intervention that will lead to a prolonged ischemic event, which is then called remote ischemic pre-conditioning. If the protocol is applied during the ischemic event, then it is called remote ischemic per-conditioning. Finally, if it is applied after the ischemic event, then it is called remote ischemic post-conditioning [85].

## 3.2 Methodology for Studying RIC Using HRV

Since the ANS is one of the mechanisms that could be involved in this protection, it is important to study its behavior before, during, and after the RIC protocol. This can be done by recording an **Electrocardiogram (ECG)** signal before, throughout, and after the procedure, and afterward, use **HRV** to peek into the ANS. In Chapter 2, Sub-Sections 2.4 and 2.5, the relation between the ANS, more specifically the contributions of each of its branches, and **HRV** was described. There are several metrics that can be used either to reveal a change in the activation of the ANS as a whole or the contribution of its branches. For example, if there are significant changes in the **RMSSD** metric (root mean square of successive difference) before and after the procedure, then it is possible that the parasympathetic branch suffered a change in its activation, since this metric can be used as a proxy of that system activation. Thus, by using **HRV**, a more thorough insight can be obtained into the neural pathways that can be part of the RIC mediated protection.

The RIC protocol chosen for this work consisted of four cycles of 5 minutes of ischemia / 5 minutes of non-occlusion. Figure 3.4 is a representation of the procedure timeline. To ensure that the limb was ischemic, a manual blood pressure cuff placed on an arm was either inflated to above 220mmHg or 20mmHg above the maximum systolic pressure of the subject. Furthermore, and to ensure that the same experimental conditions were present, the subjects were asked to do their normal life (i.e. take medication and eat breakfast), the procedure was performed between 9 and 10 AM, and done in a quiet and isolated room.

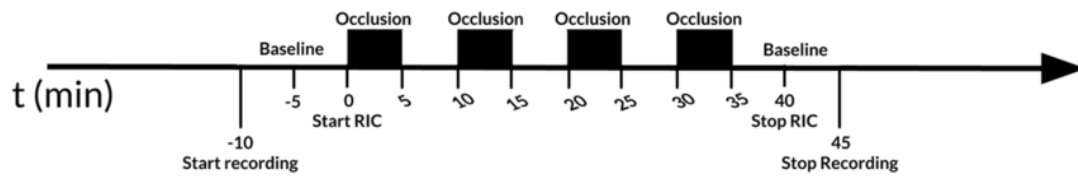


Figure 3.4: Occlusion and non-occlusion protocol timeline. Data starts to be recorded 5 minutes before the baseline 5-minute window in order for the patient to get used to the experimental conditions and settle in. After the last occlusion, there is the final non-ischemic interval of the procedure, after which the last baseline is taken to be compared with the initial one. Extracted from [76].

Data was recorded using a PLUX biosignalsplux data acquisition module, using a sampling rate of 1000Hz, with 16-bit resolution, which was streamed to a computer nearby using Bluetooth<sup>4</sup>. Connected to this device were two sensors, a 1-lead bipolar differential ECG sensor<sup>5</sup>, used to record the ECG waveform from which the R-peak locations needed for HRV are derived, and a Blood Volume Pulse (BVP) sensor<sup>6</sup>, used to ensure that the cuffed arm was indeed occluded, and thus no blood pulse wave should be detected by the sensor during the ischemic portion of the protocol. Also, the data acquisition unit ensures that both data sources are synchronized, facilitating post-processing tasks such as the segmentation of the signal. The ECG sensor used Ag/AgCl wet electrodes connected to the chest following the Einthoven Lead I and positioned by trained clinicians. Figure 3.5 is an illustration of the data acquisition setup.

In this pilot, 20 subjects were enrolled (11 Females), divided into two subgroups according to their age: senior (n=10) and young (n=10). The senior subjects were part of the São Francisco Xavier hospital volunteer group<sup>7</sup>, and the young subjects were recruited from NOVA Medical School. The following exclusion criteria were applied: any previous neurological disease or neurosurgical procedure, severe heart failure (NYHA class III or higher [86]), peripheral artery disease, skin ulcers or other severe dermatological disease. Subjects were also excluded per investigator judgment if they had any unstable/severe disease. Subjects were screened for vascular risk factors (e.g. arterial hypertension, diabetes, dyslipidemia, smoking, obesity, coronary artery disease, or atrial fibrillation) [76]. The inclusion of both senior and younger subjects was motivated by the differences in basal HRV values for these two populations, since with age the ability of the body to respond to external stimuli and adapt to new conditions deteriorates, leading to lower levels of HRV and different responses of the ANS to the RIC procedure [87].

<sup>4</sup>The biosignalsplux hub datasheet can be found at <https://support.pluxbiosignals.com/wp-content/uploads/2021/10/biosignalsplux-8-Channel-Hub-Datasheet.pdf>.

<sup>5</sup>The ECG sensor datasheet can be found at <https://support.pluxbiosignals.com/wp-content/uploads/2021/10/biosignalsplux-Electrocardiography-ECG-Datasheet.pdf>.

<sup>6</sup>The BVP sensor datasheet can be found at [https://support.pluxbiosignals.com/wp-content/uploads/2021/11/Blood\\_Volume\\_Pulse\\_BVP\\_Datasheet.pdf](https://support.pluxbiosignals.com/wp-content/uploads/2021/11/Blood_Volume_Pulse_BVP_Datasheet.pdf).

<sup>7</sup>Liga dos Amigos do Hospital São Francisco Xavier.



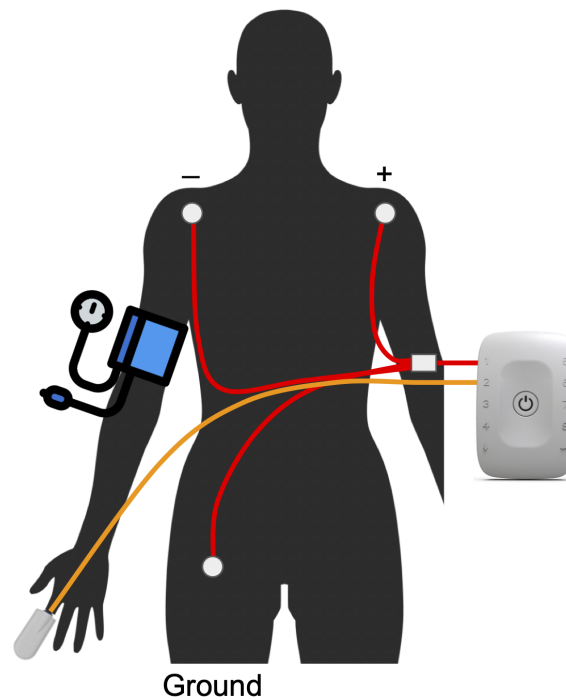
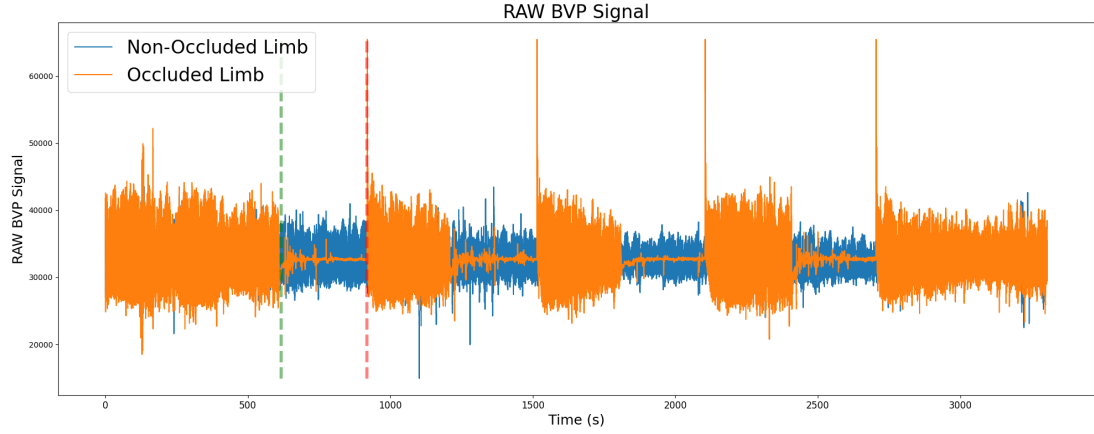


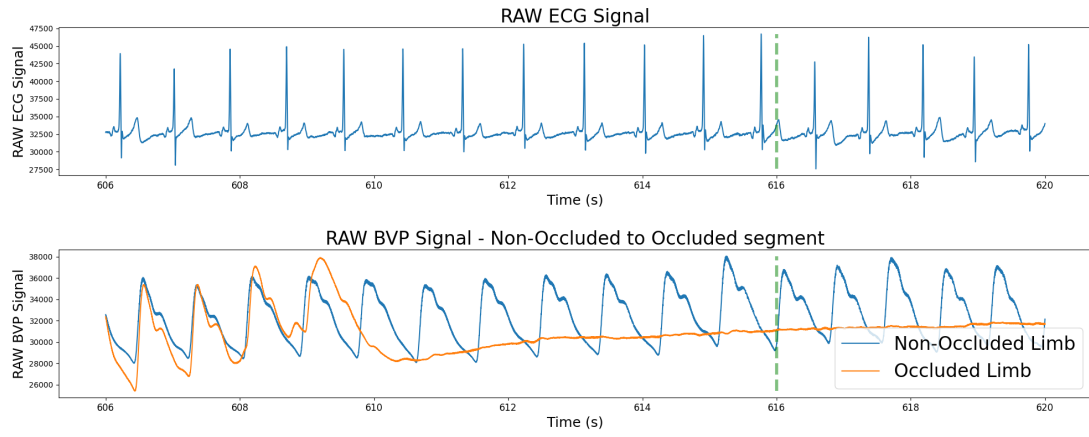
Figure 3.5: Illustration of the sensors and cuff positioning. The electrodes were positioned according to the Einthoven Lead I. The [BVP](#) sensor was placed on the index finger of both the limbs (for simplicity, only one is shown). Both the [ECG](#) and [BVP](#) sensors were connected to a PLUX biosignalsplux data acquisition unit, ensuring that both data sources were synchronized. The data was then streamed to a nearby computer (not depicted) via Bluetooth.

Each subset had initially ten participants. However, two of the senior subjects had to be excluded due to the [ECG](#) being very noisy to perform a reliable QRS complex detection. Furthermore, an extra senior subject had to be partially removed (only part of the comparison was made) due to an error in the protocol application, where the baseline before the procedure was not recorded. Table [B.1](#) contains a more detailed overview of the population, including vascular risk factors and medication at the time of the study.

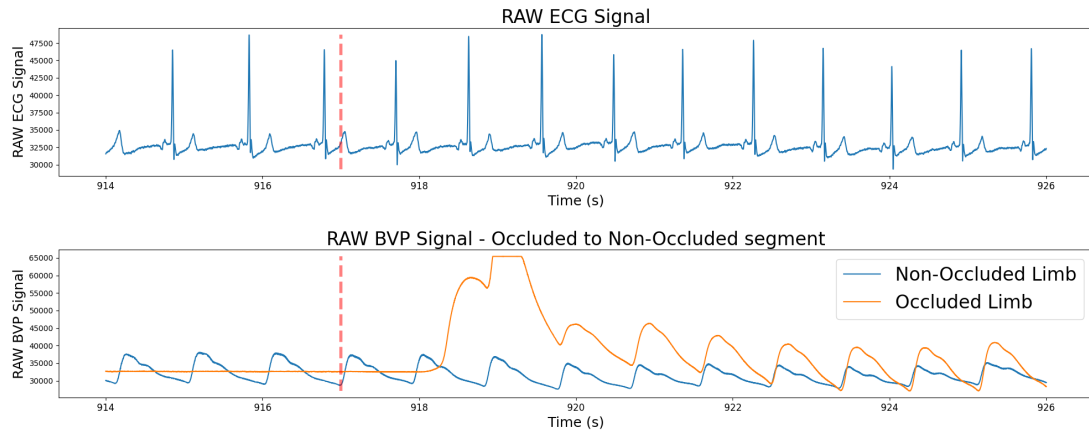
As mentioned before, [HRV](#) analysis is typically done in either 24-hour (long term) or 5-minute (short term) segments. Since the [RIC](#) protocol chosen has 5 minutes windows of occlusion / non-occlusion intervals, short term [HRV](#) metrics were chosen. The signal from the [BVP](#) sensor was used to segment the [ECG](#) signal into the different stages of the procedure, and then a QRS complex detection algorithm was used to get the R-peaks needed for the [HRV](#) analysis (Pan-Tompkins algorithm [88]). The detected peaks were afterward manually confirmed, with missed or miss-classified R-peaks corrected. This is an important step, since some of the metrics used (especially in the time domain) are sensitive to gaps in the inter-beat intervals. Figure [3.6](#) is an example of an acquisition made, in which in Sub-Figure [3.6a](#) it is possible to observe from the [BVP](#) signal each of the phases of the procedure.



(a) Raw **BVP** signal for the full protocol.



(b) Raw **ECG** and **BVP** signals in the non-occlusion to occlusion transition.



(c) Raw **ECG** and **BVP** signal in the occlusion to non-occlusion transition.

Figure 3.6: Example of an acquisition made during **RIC**. In Sub-Figure (a) the full protocol is depicted, where the green and red dashed lines de-limit an occlusion period. Sub-Figure (b) and (c) are the start and end (respectively) of said period. In Sub-Figure (b), the **BVP** of the occluded arm (orange line) flattens when the cuff is inflated, starting the ischemic period. In Sub-Figure (c) the opposite occurs, with a big rush of blood when the cuff is deflated, leading to a large amplitude wave to be recorded.



The selected metrics for this pilot were as follows: mean R-R intervals in milliseconds (ms); median R-R intervals (ms); percentage of intervals falling outside a 50ms difference, pNN50 (%); root mean square of successive differences of the R-R interval values per event, **RMSSD** (ms); normalized low-frequency power spectrum density, nuLF PSD (%); normalized high-frequency power spectrum density, nuHF PSD (%); LF and HF normalized power spectrum density ratio, LF/HF; SD1 axis of the Poincaré plot, SD1 axis (ms); SD2 axis of the Poincaré plot, SD2 axis (ms) and SD1/SD2 per event. These are the typical features used in **HRV** analysis [16], with a representation from all three domains. A detailed explanation of each of these metrics can be found in Chapter 2, Sub-Section 2.5.

One of the metrics excluded for this pilot was the SDNN, which is sometimes considered the most used **HRV** feature, since it is more suitable for analyzing long-term recordings (such as 24h-hour **ECG** traces) rather than 5-minute segments [64]. , **RMSSD**, pNN50, nuHF, and SD1 were chosen since they are referred to in the literature as proxies for parasympathetic activity. nuHF and SD2 were selected for their relation with sympathetic activation (contested, since there is also influence of the parasympathetic system in these metrics [74]). The LF/HF and SD1/SD2 represent the balance between both branches of the **ANS** (also contested due to the latter point) [64, 69, 74]. The mean and median intervals are only used for statistical representation of **Heart Rate (HR)** on the intervals in analysis. Table 3.1 depicts a summary of the metrics used in this pilot.

Table 3.1: **HRV** metrics were used in the pilot to assess the neural influence in mediating cardioprotection provided by the **RIC** procedure and their relation with the **ANS**. The statistical features were used as a statistical representation of the **HR** during the time window in analysis.

<b>Parasympathetic nervous system proxies</b>	RMSSD pNN50 nuHF SD1
<b>Sympathetic nervous system proxies</b>	nuLF SD2
<b>Ratio between branches</b>	LF/HF SD1/SD2
<b>Statistical features</b>	Mean R-R interval Median R-R interval

To obtain the frequency domain features, the non-parametric Welch method was used to compute the frequency **Power Spectral Density (PSD)** (using a 256 sample Hanning window). When using non-parametric methods, it is recommended that RR intervals be interpolated, since it is not a perfectly uniform sampled interval. Therefore, the RR interval was re-sampled to 10Hz using a cubic spline interpolation. Furthermore, the mean value was subtracted to remove the DC component of the signal.

To get the two axis of the elipsis when using the Poicaré plot, Equations 3.1 and 3.2 were used [89]. In Equation 3.1,  $\sigma^2$  represents the variance.

$$SD1^2 = \frac{1}{2}\sigma^2(RR_n - RR_{n+1}) = \frac{1}{2}SDSD^2 \quad (3.1)$$

$$SD2^2 = 2SDRR^2 - \frac{1}{2}SDSD^2 \quad (3.2)$$

To compare if any changes were detected in the [ANS](#) due to the [RIC](#) procedure, six different analyses were performed. First, the metrics from occlusion and non-occlusion segments were compared. Then, the 10 minutes before and after the procedure were also compared. Finally, both these two analyses were performed separately for the young and the senior subjects, thus resulting in six different analyses. For all these analyses, the non-parametric Wilcoxon signed-rank test was used to assess if there were any significant differences between the before and after, with the significance level set at 0.05, where p-values below that level indicate a statistical difference. This test was selected since it was designed to assess repeated measures from the same subject under different conditions [90].

### 3.3 Results and Discussion

The results for the mean value for each metric (Table 3.1) for each of the six analyses can be found using Table 3.2. The significant differences found in the [HRV](#) analyses are compiled in Table 3.3. Additional Figures can be found in the published version of this study [76]. These figures contain the boxplots for each metric in analysis (Table 3.1) before and after the procedure, per dataset (global, senior, young).

Table 3.2: Location for each of the mean values of the [HRV](#) metrics used, divided by each subset. For each subset, the occlusion vs non-occlusion and the first vs last 10 minutes comparison was made, resulting in six different analyses condensed in three tables. The global dataset incorporates all the volunteers.

	Occlusion vs Non-occlusion	First vs Last 10 minutes
Global Dataset (n=18)	Table B.2	
Senior Subset (n=8)	Table B.3	
Young Subset (n=10)	Table B.4	

Table 3.3: Significant differences found in the [HRV](#) analyses for each of the dataset divisions. In the young population, no significant differences were found. A difference was considered significant if the p-value was below 0.05.

Global population	Feature variation	p-value
SD2 axis (ms)	Last 10 minutes higher	0.044
RMSSD (ms)	Non-occlusion higher	0.044
SD1 axis (ms)	Non-occlusion higher	0.044
Senior population		
SD2 axis (ms)	Last 10 minutes higher	0.018
Young population		
No significant differences		

The first comparison analyzed was between the 10 minutes before and after the procedure was applied. Out of the 10 metrics assessed, only SD2 had a p-value lower than 0.05 in the global dataset when comparing the before and after values. This statistical difference was also found in the senior subset, while in the young subset it was higher than 0.05. This metric has a higher value after the [RIC](#) procedure is performed (being the difference larger in the senior subset), which can be an indication of a change in the [ANS](#), since both the parasympathetic (via fast vagal response) and sympathetic systems (via the baroreceptors) contribute to this metric. For the remaining metrics, all the p-value were higher than 0.05 in all subsets, thus no statistically significant changes were found.

Comparing the occlusion with non-occlusion segments, significant differences were only found in the global dataset (all volunteers), specifically the SD1 and [RMSSD](#) (although in the young subset it was close to the significant threshold). These features were higher in non-occlusion than occlusion segments. SD1 and [RMSSD](#) are typically associated with short-term [HRV](#), which might indicate a decrease in parasympathetic activity in occlusion segments.

As mentioned before, the increase of the SD2 metric seems to be higher in the senior population when comparing the before and after the procedure 10-minute window, which could mean that the [RIC](#) leads to higher activation of the [ANS](#) in this population. Age typically leads to a loss in the adaptability and responsiveness of the [ANS](#), with the basal levels of the [HRV](#) metrics being lower in older subjects [87]. This was also observed not only in the SD2 metric ( $\approx 44$ ms for younger subjects vs  $\approx 86$ ms for older), but also in other metrics such as pNN50, [RMSSD](#), and nuLF. Another byproduct of the higher value of SD2 due to the [RIC](#) procedure is a higher variability of the inter-beat interval, which is associated with a better prognostic outcome in many diseases, especially [Cardiovascular Disease \(CVD\)](#)s<sup>8</sup> [64, 91].

<sup>8</sup>Also, no difference in [HRV](#) was found whenever gender is considered (data not shown).

A more significant difference was expected in the [HRV](#) metrics between occlusion and non-occlusion segments, considering the disturbance caused by the procedure. Nevertheless, parameters associated with parasympathetic activity seemed to be elevated in non-occlusion segments when analyzing the global subset. As seen in the Sub-Section [3.1.1](#), the activation of the parasympathetic system seems to be a crucial influencing factor, considering that when there is a suppression in its activity, no protective effect tends to be seen. This activation could then come during the non-occlusion intervals of the procedure.

Some limitations will be discussed in Chapter [6](#), but even so, using [HRV](#) metrics extracted from an [ECG](#), it was possible to see some changes in features associated with the [ANS](#) during and after the [RIC](#) procedure was performed. Such evidence further consolidates the influence of neural pathways in mediating cardiac protection and therapeutic effects that are observed when the procedure is applied.

### 3.4 Summary

This chapter focused on [RIC](#), a procedure that consists of intermittent cycles of occlusion and non-occlusion of a limb, where the blood flow is stopped during the occlusion intervals. This procedure has shown promising results in promoting protection in certain vital organs in animal models and certain clinical trials, such as the reduction of infarct size after a [MI](#). This is especially true for low to medium-income countries, where medical standards are still sub-optimal and a low-cost, safe, and simple procedure like the one herein proposed can make a difference.

One of the many unknowns of [RIC](#) is how the protection is mediated, with some of the leading candidates being humoral factors, due to the protection effects observed when blood is transfused from a subject where the [RIC](#) procedure was performed to another where this procedure was not. Neural pathways are another candidate, since no cardiac protection is present when a complete and functional nervous system is not present, while protection is offered when there is direct stimulation of some of its parts.

Since one of the mechanisms mediating this protection seems to be neural, more specifically, the [ANS](#), one technique that can be used to assess this influence in a more quantitative manner is [HRV](#), which can be correlated with the general activity of this system or the activity of each branch. To that effect, a small pilot study was devised, in which the [RIC](#) procedure was to be applied while simultaneously an [ECG](#) was recorded for [HRV](#) analysis.

This pilot was applied to 18 subjects, where the four cycles of occlusion and non-occlusion were performed, while also recording the 10 minutes before and after the procedure. The main outcome of this pilot was a statistically significant increase of the non-linear parameter SD2 after the [RIC](#) protocol, suggesting that [ANS](#) involvement could be one of the mechanisms for [RIC](#) therapeutic effectiveness. This parameter is typically a proxy for both branches of the [ANS](#) (although initially it was attributed to the sympathetic branch, this has been a topic of controversy throughout the latest studies).

## A MOBILE ECG ACQUISITION SYSTEM

This chapter tackles one of the motivations for this thesis, the development of a more pervasive and naturalistic [Electrocardiogram \(ECG\)](#) monitoring device. A custom back cover for a tablet device was developed, having the electrodes embedded in it. With the electrodes on the back cover, the acquisitions can be made without a conscious action by the tablet's user, recording the [ECG](#) strip when the user holds said device.

Due to the importance of the interface with the body, the chapter starts with an introduction to what an electrode is, the different materials from which they can be constructed, and how to classify them according to their placement.

The results presented in this chapter were published as a book chapter [92]. Additionally, a open-source library for reading and parsing the GE MUSE proprietary XML file was also made publicly available.

### 4.1 What is an Electrode?

The machines by themselves and all the different lead positioning are just a piece in the workflow required for recording an [ECG](#). In reality, a key element is the electrode, an electrically conductive material that is used as interface with the body to record the activity of the heart (in this case). The electrical activity of the heart, and all the other organs, is propagated inside the body by ions present in the different body fluids and tissues [41]. These changes in ion concentration need to be tracked and converted to electric currents in order to enable a measurement [93]. This conversion occurs at the electrode-body interface, also known as the electrode-electrolyte interface, with the underlying mechanism called charge transference [41].

#### 4.1.1 Electrical Modeling

In this interface, reduction and oxidation reactions are occurring constantly. Oxidation leads to a current flow from the electrode towards the electrolyte, due to the atoms in the electrode losing an electron and causing it to be negatively charged. On the other hand, there is also reduction reaction occurring, where electrons combine with the ions

in the electrolyte and the new atoms are deposited in the electrode [93]. These reactions occur at the same rate under equilibrium, however, there is an increased concentration of electrolyte ions near the contact point of the electrode, establishing what is called the half-cell potential. These should be the same in both electrodes on a differential measurement, otherwise they can be an extra source of noise [94].

Shifting to the electric characteristics of an electrode, this can be approximated by a battery representing the half-cell potential, then a resistance and capacitor in parallel modeling the electrode-electrolyte interface, and finally a resistance in series corresponding to the effects of the electrolyte between the electrode and the skin [93, 95]. Figure 4.1 illustrates an electrode electrical equivalent. The capacitor and resistance modeling the interface are needed since this transduction can be either polarizable or non-polarizable. For polarizable electrodes, there is no current flow, thus the electrode behaves like a capacitor, while on the other hand, non-polarizable electrodes allow for direct current flow, behaving like a resistor. However, most electrodes behave in the middle of these two extremes [96].

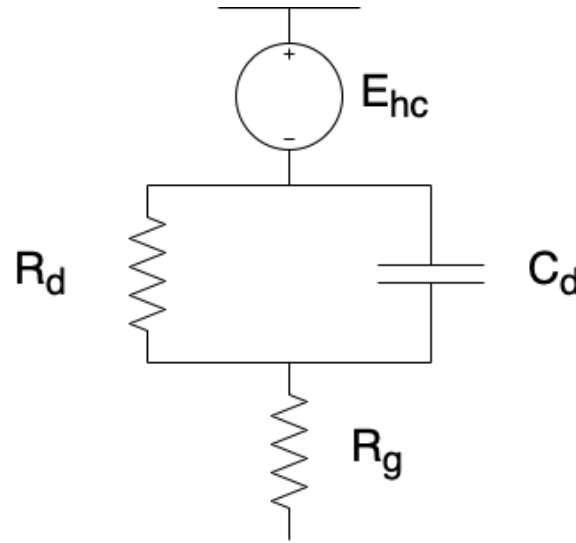


Figure 4.1: Electrode electrical equivalent.  $E_{hc}$  is the half-cell potential,  $R_d$  and  $C_d$  are the electrode-electrolyte interface modeling, and  $R_g$  the electrolyte resistance between the skin and the electrode.

The skin can also be described by its electric characteristic. As an organ, the skin has multiple layers, consisting primarily of the *epidermis*, *dermis*, and subcutaneous tissues, with the latter two containing the structures responsible for the transport of ions [96, 97]. The *epidermis* is the outermost layer out of those and can be modeled as a capacitor and a resistance in parallel. The topmost layer, the *stratum corneum*, consists of dead cells, making it electrically insulating [97], although in some areas it is semipermeable to ions (e.g. sweat); differences in the ionic concentration in this layer result in a voltage potential [96]. Figure 4.2 is the electrode equivalent including the different skin layers.

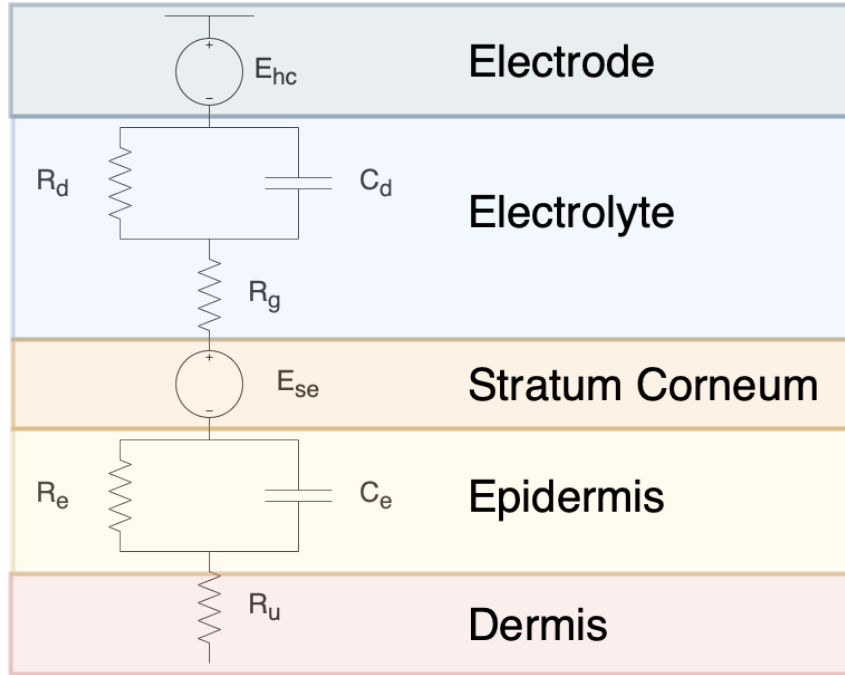


Figure 4.2: Electrode electrical equivalent including the different skin layers.  $E_{se}$  is the potential due to the ionic differential off the *stratum corneum*,  $R_e$  and  $C_e$  are the *epidermis* electrical modeling, and  $R_u$  the resistance of the lower skin layers from the *dermis* down.

#### 4.1.2 Wet or Dry?

Electrodes can be divided into two main groups, wet or dry. Wet electrodes have an electrolytic gel between the skin and the electrode surface in order to reduce the skin-electrode impedance, which is high for low-frequency signals such as an ECG [94]. The weakly polarizing Ag/AgCl gel electrode is the standard electrode used for recording signals. However, for long-term usage, there are some disadvantages associated with the use of an electrolyte solution, which can dehydrate and require reapplication of the gel, a time-consuming procedure. Also, sometimes these gels are not suitable for long-term usage and can cause skin irritation [94, 98].

The second group, dry electrodes, do not use any electrolytic gel, using instead direct contact with the skin and leveraging the subject's own moisture from natural transepidermal water loss and/or sweating as an electrolyte [97]. Despite having a higher impedance, they are more suitable for a wearable recording device since the user does not have to apply any gels prior to its use [94, 98]. There are three main types of dry electrodes: surface, penetrating, and capacitive.

For surface electrodes, there is a mixture of capacitive and resistive coupling. Due to the rough surface of the skin, there are air pockets between the skin and the electrode, acting as a dielectric layer. On the other hand, if sweat or natural humidity is present, there is a decrease in resistance between the electrode and skin as well as a half-cell potential [95, 96]. Penetrating electrodes, as the name implies, pierce into the surface of the skin, minimizing the effects of the dielectric layer and interfacing directly with the

body ions [96]. Finally, the last type of dry electrodes are capacitive, which do not require direct contact with the skin, working either through an insulating layer, air, and/or clothing [95, 96].

As mentioned before, wet electrodes require the attachment of an electrode to the human skin. Furthermore, for better results, the skin has to be prepared, normally by the abrasion of the selected location to remove any dead cells or other debris (such as hair follicles). If these electrodes do not have pre-applied gel and require its application, the amount of electrolyte used can be another obstacle, while also introducing the need for the electrode and the skin to be cleaned after a recording. Finally, with time, the electrolyte dries, deteriorating the quality of the signal with the increase of the impedance [99]. Dry electrodes are therefore a more suitable candidate to be used in personal monitoring comparatively to a wet electrodes, and out of the three categories, surface electrodes are the more practical choice to be embedded in an everyday use device.

To establish high-quality and stable signals, electrodes should meet the three conditions: low impedance in order to have a high signal-to-noise ratio, stable contact with the skin to attenuate motion artifacts, and the materials needed to take into account the impact on human health and avoid harm to the human body [100]. There are three main materials from which a contact surface electrode can be constructed, metallic-based, carbon-based, or polymer-based materials [95, 96].

Regarding metallic dry electrodes, these seem an obvious choice due to their good electric conductivity. Some of the metals considered ideal for the preparation of dry electrodes are silver and silver nanowires (Ag, AgNW), and titanium nitride (TiN). Carbon materials are also good candidates due to their conductivity, stability, mechanical strength, and low cost when mass-produced, and are often used together with metals or polymeric materials. Examples of these materials are carbon, graphene, carbon nanotubes, and carbon nanofibers [96, 100]. Finally, the other class of materials used to make dry electrodes is polymers. These materials have worse conductive properties than the last two, but they are superior in biocompatibility and stability, being typically divided into two categories: intrinsically conductive polymers (ICPs) or extrinsically conductive polymers (ECPs), depending on the need for the addition of conductive materials [96, 100].

Dry electrodes also open the door for less intrusive measurement devices. Recalling Weller and Einthoven recordings, the first electrodes used were buckets of water filled with an electrolytic solution, not the most practical solution for recording an ECG. With time, both machines and electrodes shrunk, going from an entire room and buckets to small portable machines, implanted devices, or embedded into everyday objects.



### 4.1.3 Classification According to Placement

There is an inverse relationship between a device's intrusiveness and its potential outreach, which can be divided into three levels: in-, on- and off-the-person devices. The first category, in-the-person, are devices where the electrodes are located inside the body, typically surgically implanted. These are very intrusive devices, only used in extreme scenarios, such as Implantable Loop Recorders (ILRs) or Insertable Cardiac Monitors (ICM), used when there are infrequent arrhythmias or in the cases where other ambulatory devices are indeterminate, hence these have a very limited outreach [101].

The second category, on-the-person, is where the vast majority of medical and well-being devices fall, in which the electrodes are attached to the surface of the body. The intrusiveness and outreach of these devices depend on the number of leads they require and if the placement of the electrodes is pre-defined (e.g. [cardiac patches](#)<sup>1</sup>, devices where the electrode position is pre-defined and the user just has to apply them to the chest). Another classic example is the Holter monitor, which are devices that record an [ECG](#) for periods of up to 48 hours worn by patients with suspected, frequent palpitations having slow, fast or uneven heartbeat [101].

Finally, there are off-the-person devices, in which the electrodes are embedded in the day-to-day devices, enabling a more pervasive measurement. These are the least intrusive devices, with some being able to record signals without a voluntary action by the user [101]. Such devices can be embedded for example in the rim of a steering wheel [102], or even bathtubs [103]. However, not all devices that have embedded electrodes are considered off-the-person. Some wearables that have their electrodes embedded, such as clothing [104] or smartwatches [105], are considered on-the-person [ECG](#) devices due to their intrusiveness, with the user having to take a conscious interaction with them instead of a natural one (which will be explored in Section 4.2).

Figure 4.3 is an illustration of device intrusiveness vs potential outreach.

## 4.2 Novel Mobile ECG Acquisition System

This section describes the work accomplished in developing a tablet capable of performing naturalistic [ECG](#) data acquisitions, aiming to increase senior citizens' daily life autonomy and give peace of mind to their caregivers. This project, called Senior Inclusive (shortened to SiosLIFE), was executed in collaboration with other research institutes and companies in the scope of [Portugal 2020 \(P2020\)](#) grant<sup>2</sup>, reference NORTE-01-0247-FEDER-017967, promoted by HidePixel.

---

<sup>1</sup><https://www.vivalink.com/wearable-ecg-monitor>.

<sup>2</sup>PLUX, the co-sponsor of this PhD, was the partner responsible for the development of a pervasive [ECG](#) measuring solution.

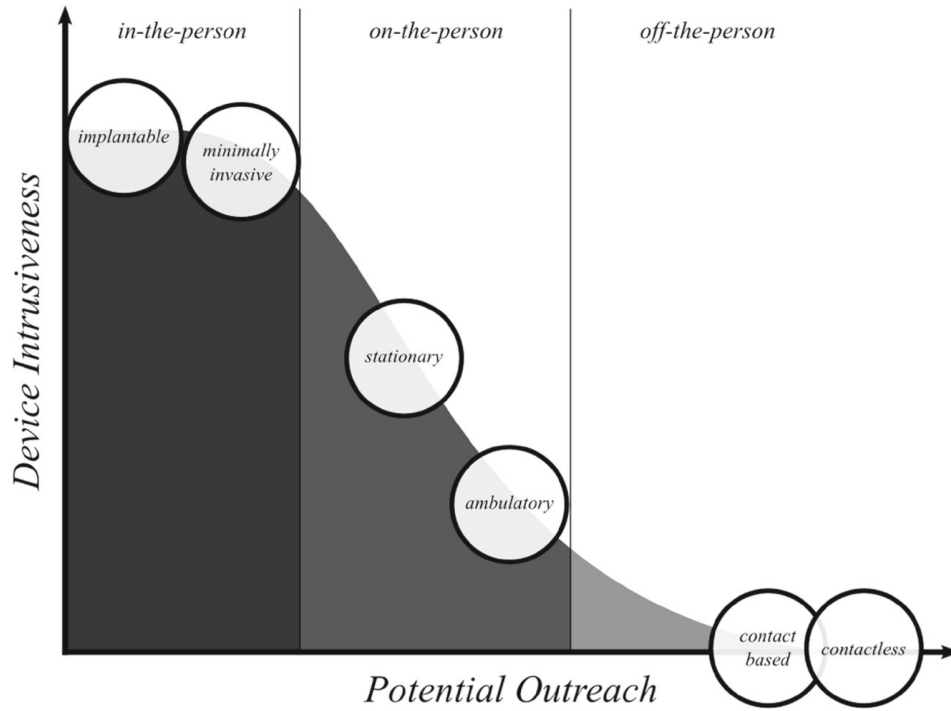


Figure 4.3: Device intrusiveness vs potential outreach, where devices with a lower intrusiveness have a larger number of people that can use them. Adapted from [101].

#### 4.2.1 Motivation

As mentioned in Chapter 1, Sub-Section 1.1, [Cardiovascular Disease \(CVD\)](#)s are the leading cause of death in the world, and the ECG is one tool that clinicians and caretakers can use in (near) continuous monitoring of some physiological parameters to assess their patients. With the advent of the Internet, the growing evolution and adoption of information and communication technologies, and the surge in mobile technologies (smartphones, tablets, watches, glasses), there is also increasing adoption of these innovations by healthcare providers and patients, paving the way for more pervasive solutions [6].

With these adoptions, two new concepts appeared in the last decade, [Electronic Health \(eHealth\)](#) and [Mobile Health \(mHealth\)](#), becoming prominent components of healthcare. Their adoption by the patients can improve the flexibility and accessibility to health care services, facilitate day-to-day health management, and promote healthy behaviors. It is especially true in elderly populations, where such a system can be used effectively to prevent or manage chronic diseases, support lifestyle modifications, enhance patients' knowledge about their illnesses, self-management capacities, and quality of life [17, 106].

In parallel, there has been a growth of consumer-grade products for self-monitoring. Similarly to [mHealth](#) devices, these give their users the ability to get a picture of their health and to develop new habits, such as being more active or improving their sleep quality [107, 108]. Although these are small, portable, and non-intrusive, making them great mobile monitoring devices, there are some drawbacks to the implementation of

these devices, one being the need for constant charging. Since their primary function is not working as an ECG monitoring device, other functions such as displays or communication radios, take a toll on battery life, having an autonomy of around 1 to 5 days typically. With the need for regular charging, some users tend to either switch to devices with fewer features but more battery life, disable health tracking features, or simply stop wearing the device. Another obstacle is the novelty fade, where some features such as ECG recording are used once or twice when the device is new and abandoned after a (short) period, especially if such feature requires user interaction (e.g placing the finger from the opposite hand on the digital crown to record an ECG segment). Lastly, some users simply lose interest in these devices and stop using them. These obstacles led to questions on the long-term adoption of the technology, as 20% of consumers stop using their wearable devices after three months, with <50% continuing to use them after one and half years. Nevertheless, there is a silver lining, since there is a higher adoption rate of smartwatch technology among the elderly due to the more health-related features [105, 109].

To take advantage of the growing adoption of mHealth devices and dry electrodes for mobile off-the-person ECG acquisition systems, a novel system was developed. This system consists of a tablet capable of ECG monitoring based on naturalistic interaction, having the recording electrodes embedded in its back cover. An off-the-person ECG approach was selected since it is the most pervasive approach to record ECG traces. Therefore, the electrodes have to be embedded in the device instead of being attached to the end user's body. Moreover, by having the electrodes at the back of the tablet, the ECG rhythm strips can be recorded much more effortlessly just by holding the device.

As mentioned earlier, dry electrodes are a good candidate for long-term monitoring, and the materials from which they can be made also facilitate this task. One of the consortium partners, PIEP<sup>3</sup>, is an innovation center for polymer engineering. As such it was decided that a polymeric dry electrode was the best solution for this approach, which could be directly embedded during the manufacturing of a custom back cover for the tablet, lowering the manufacturing costs. Another factor in the choice of polymers to be used as electrodes was their good bio-compatibility, where prolonged direct contact with the material does not produce an adverse skin reaction [96, 100]. During the first stages of the project, a short list of five materials was selected by PIEP based on their theoretical properties, which will be discussed in the following subsections.

In summary, the Senior Inclusive project aimed to develop a tablet that can effortlessly acquire good quality ECG signals, which can be utilized by trained professionals for remote monitoring purposes. The primary objective was to ensure that the device enables user-friendly monitoring, and the quality of ECG recordings is comparable to those produced by clinical-grade ECG machines.

---

<sup>3</sup>Pólo de Inovação em Engenharia de Polímeros.

The device was specifically designed for elderly people to use at home or in assisted living homes, but it has the potential for other applications as well. The successful development of such a device could greatly enhance the diagnosis and management of cardiac conditions, especially among vulnerable populations who may face challenges accessing traditional medical care, or live isolated.

Thus, one of the critical aspects was selecting the appropriate materials that could meet the project's goals while remaining cost-effective and user-friendly. The goal was then to assess which of the materials enabled the project team to achieve the aforementioned goals, with a particular emphasis on identifying the material that could record a waveform similar to one recorded from a clinical-grade device. This was necessary to ensure that the resulting ECG signals were accurate and could be effectively used for diagnostic and monitoring purposes.

#### 4.2.2 Polymers Short List

There are already some devices on the market offering off-the-person ECG, focusing on embedding the electrodes on smartphone cases, building some wireless accessories, or telehealth systems, such as the Docobo's Careportal (Sub-Figure 4.4a), a tablet marketed for elderly people that can record 30s segments of ECG, or AliveCor's Kardia Mobile (Sub-Figure 4.4b), a small bar with two electrodes that can record and send to a smartphone 30s segments of ECG. However, these devices rely on Stainless Steel (SS) electrodes or are an add-on solution instead of being part of the device (e.g. AliveCor's Kardia Mobile).



(a) Docobo's Careportal.



(b) AliveCor's Kardia Mobile.

Figure 4.4: Examples of commercial available off-the-person ECG devices.

SS is a widely used material to construct dry electrodes [110–112]. Many studies used SS because of its availability, price, and good electrical performance [113], being the most common polarizable electrode in wireless biosensing applications [111]. However, electrodes made from metals are not ideal for recording applications since they are typically polarizable, which can lead to a high impedance mismatch on the interface between the

electrode and the skin and also higher susceptibility to motion artifacts [110]. Nevertheless, due to the high adoption of these electrodes by industry and researchers alike, they were also added to this study (Figure 4.5f) as a baseline electrode to compare with the polymeric electrode candidates.

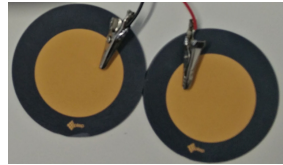
By being an add-on, these devices face the same problems facing smartwatches or ECG patches regarding their usage. For example, there are battery-life, practicality, or easy-of-use concerns, that can lead to poor user adoption and retentions. In the instance of devices similar to AliveCor's Kardia Mobile, the measurements have to be actively started by the user.

As mentioned before, the initial material selection was performed by PIEP and the following were selected due to their theoretical characteristics. Table 4.1 contains the values for some these characteristics:

- **PolyOne's OnForce LFT LF6600-5023 (PO)**, a polyamide with high elastic modulus and material strength (Figure 4.5a);
- **Vectra's 840i LCP (LDS)**, a liquid crystal polymer modified to be used in printed circuit boards (Figure 4.5b);
- **LUVOCOM's 1850-8023 PTB (LV)**, a polybutylene terephthalate polymer reinforced with carbon fiber designed to be electrically conductive (Figure 4.5c);
- **SAATI's CC202 ET445 (CF)**, a carbon fiber prepeg using an carbon fibers (Torayca T300 fibers) in an epoxy matrix (ET445) (Figure 4.5d);
- **RTP's 199 X 137556 E (RTPE)**, a polypropylene reinforced with carbon and stainless steel fibers designed for electrical conductive solutions (Figure 4.5e).



(a) FT LF6600-5023 (PO).



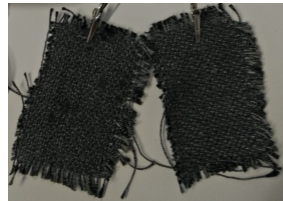
(b) 840i LCP (LDS).



(c) 1850-8023 PTB (LV).



(d) CC202 ET445 (CF).



(e) 199 X 137556 E (RTPE).



(f) Stainless Steel (SS).

Figure 4.5: Dry electrodes samples used to test their signal quality.

Table 4.1: Dry electrodes samples characteristics. For two of the materials, [PO](#) and [LDS](#), no value for the surface resistance was found, either on the provided datasheets or online. MPa - Megapascal

Material	Tensile Strength (MPa)	Flexural Strength (MPa)	Surface Resistance (Ohm)
PolyOne's OnForce FT LF6600-5023	165	260	-
Vectra's 840i LCP	102	109	2E16
LUVOCOM's 1850- 8023 PTB	105	155	$\leq 100$
SAATI's CC202 ET445	734	968	-
RTP's 199 X 137556 E	82	138	100

### 4.2.3 Preliminary Tests

Before the development of the data acquisition unit and subsequently choosing the polymer to be used in the prototypes of the final device, a preliminary test was devised. This test had the purpose of finding if any of the materials were good enough to record an [ECG](#) signal even in a non-ideal setting (i.e. electrodes connected to the acquisition system using alligator clips, with a setup similar to Figure 4.6).

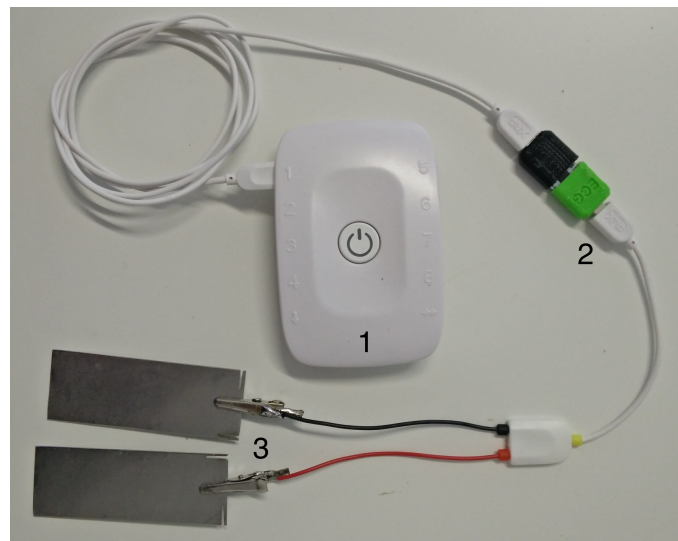


Figure 4.6: Preliminary test setup using alligator clips. In this figure is possible to see the biosignalsplux data acquisition hub (1), the BITalino (r)evolution [ECG](#) sensor (2), and the alligator clips interfacing with the electrode material in study (3), which in this figure is [SS](#).



Each material was tested using a placeholder data acquisition unit (PLUX's biosignalsplux<sup>4</sup>), employing a BITalino (r)evolution ECG sensor<sup>5</sup> as the electronic front-end between the acquisition unit and the polymer, and connecting each material using an alligator clip (Figure 4.5). The BITalino sensor was selected because it can record an ECG signal using only two electrodes (having a virtual ground) while recording signals that are very similar to clinical recording devices [101].

To gauge the performance of each polymer in these preliminary tests, a reference signal was recorded in parallel. These recordings used the same biosignalsplux hub, with pre-gelled Ag/AgCl wet electrodes placed on each wrist. The signals were recorded at 1000Hz and 16bits, using a biosignalsplux and a 1-lead differential ECG sensor<sup>6</sup>.

Sub-Figure 4.7a is an illustration of the preliminary test setup, and Sub-Figure 4.7b is an example of the overlap between a signal using the reference wet-electrodes placed at each wrist (red line) and signals recorded holding a PO disk (Sub-Figure 4.5a) in each hand (blue line).

The initial trials test results were promising, with PO and LDS having ECG waves very similar (e.g. Sub-Figure 4.7b), visually, to those recorded by the reference wet-electrodes. Furthermore, it is possible to identify the different morphological wave of an Einthoven's Triangle Lead-I signal (P-wave, QRS complex, and T-wave) in the signal from these materials using the aforementioned test setup (Figure 4.8).

These results were only visually assessed since the intent of these tests was to gauge the feasibility of recording signals with this polymer shortlist. In addition, the device and electronic front-end used were only a placeholder for the final acquisition system. Thus, the next step was to compare the intended novel ECG system (new device plus the polymeric electrodes) performance with a clinical grade system, using more objective metrics to this end.

#### 4.2.4 SiosLIFE Monitoring Device

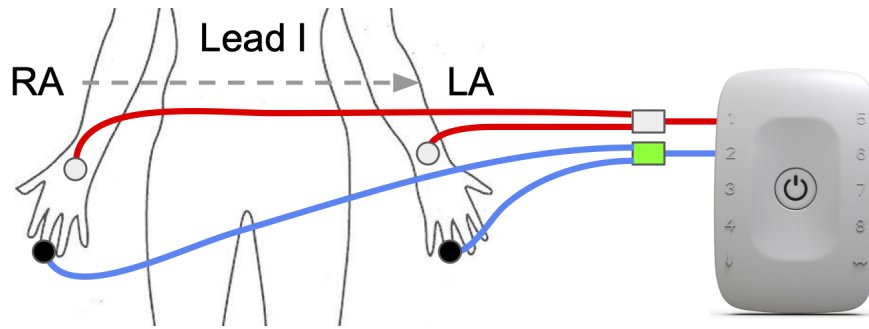
The device developed to serve as the data acquisition unit that will be embedded in the back of the tablet is a combination between the biosignalsplux hub and the BITalino ECG sensor front-end. This device boasts a system on a chip and Bluetooth transceiver from the biosignalsplux hub, which allows the device to stream 16-bit data at 1000Hz to the tablet. Since the only analog signal needed to be transmitted from this device is the ECG signal from the electrodes, the BITalino ECG sensor front-end was embedded into

---

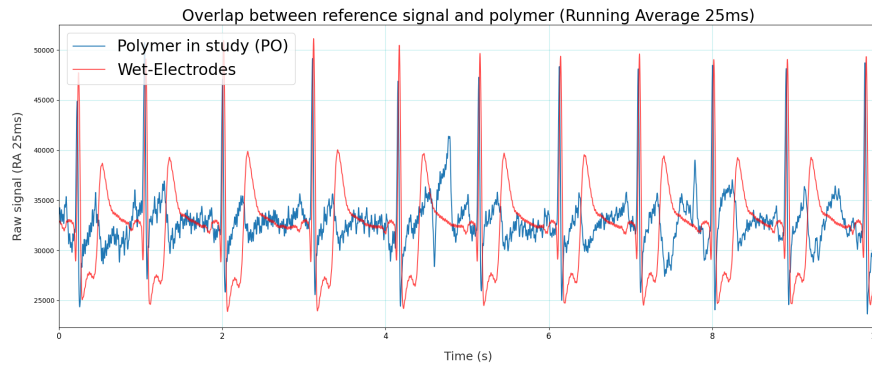
<sup>4</sup>The biosignalsplux hub datasheet can be found at <https://support.pluxbiosignals.com/wp-content/uploads/2021/10/biosignalsplux-8-Channel-Hub-Datasheet.pdf>.

<sup>5</sup>The BITalino (r)evolution ECG hub datasheet can be found at <https://support.pluxbiosignals.com/wp-content/uploads/2021/11/revolution-ecg-sensor-datasheet-revb-1.pdf>.

<sup>6</sup>The 1-lead differential ECG sensor datasheet can be found at <https://support.pluxbiosignals.com/wp-content/uploads/2021/10/biosignalsplux-Electrocardiography-ECG-Datasheet.pdf>.



(a) Electrode placement for the initial trials to gauge the possibility of acquiring ECG signals using the dry electrode samples. The red line is the connection to the reference wet-electrodes, while the blue line represents the connection to the polymer in study. The green box represents the BITalino (r)evolution ECG sensor. RA is the Right Arm; LA is the Left Arm; Signals recorded following the Einthoven's Triangle Lead-I configuration.



(b) Example of a signal using the PO dry electrodes (blue line), overlapping the signal recorded with the reference wet-electrodes (red line). A 25ms rolling average was used to smooth the signal. The raw overlap can be found at Annex C, Figure C.1.

Figure 4.7: Experimental setup and signal example obtained during preliminary testing of the polymer shortlist.

Example of a complete cardiac cycle (Running Average 25ms)

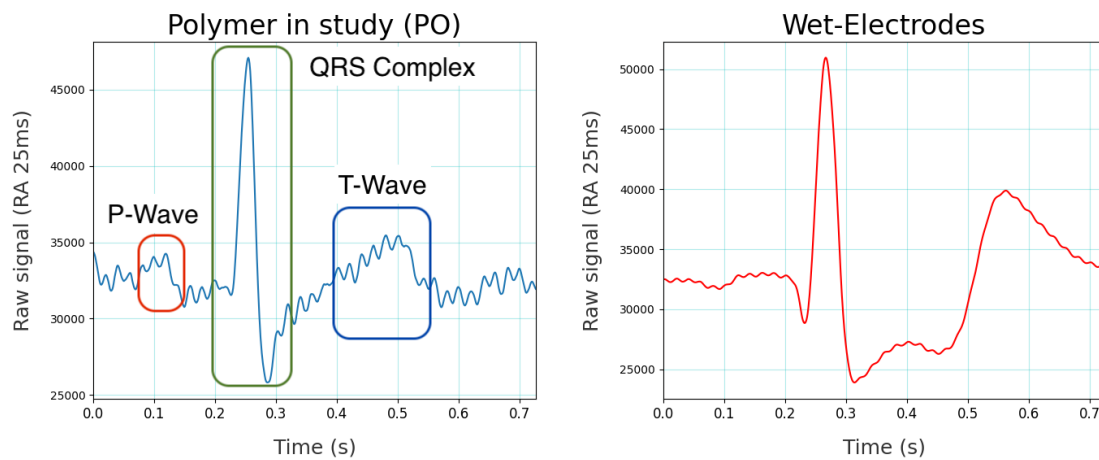


Figure 4.8: Example of a full cardiac cycle in the preliminary test. It is possible to identify the different morphological wave of a Einthoven's Triangle Lead-I signal, the P-wave, QRS complex, and T-wave.



the same PCB. The result is a very small, affordable, and easily embedded acquisition unit (Figure 4.9), having a footprint of 2.5 x 2.8 centimeters (cm) instead of the 8 x 5cm of a biosignalsplux hub (without the ECG front-end). In the prototype depicted in Figure 4.9, the device is powered via a USB cable and has a wire for each of the alligator clips in order to interface with the polymer samples. Using this approach, the same device can be used to easily test the different materials. For simplicity, this device will be called SiosLIFE throughout the rest of this section.



Figure 4.9: Prototype of the data acquisition unit to be embedded in the tablet. The green and yellow wires are alligator clips soldered to the ECG front-end and used to connect the dry electrode samples. The device's PCB footprint is a 2.5 x 2.8cm rectangle.

## 4.3 SiosLIFE Experimental Evaluation

### 4.3.1 Data Acquisition Protocol

After visually gauging if the different materials were suitable for recording an ECG rhythm strip, a more objective analysis followed. For that purpose, signals recorded with the various materials using the SiosLIFE data acquisition unit were compared to those recorded using a medical-grade ECG system.

By using a medical-grade system as the gold standard, the morphology of the recorded ECG strips using the SiosLIFE device can be compared to those used by clinicians, providing a reference for the quality of the signal acquired by this novel device. If signals recorded with the proposed device and material combination are similar to those recorded with the gold standard, then the combination can be considered a good candidate to be implemented in the tablet.

For this purpose, a GE© MAC 800 ECG machine, a certified medical-grade ECG, was used as a gold standard. This system is capable of recording a 12-lead ECG with a sampling rate of 500Hz. Crucially for this analysis, the recorded signals can be exported, with the machine outputting a 10-second segment in digital format (as XML files).

An experimental protocol was devised for acquiring and comparing data recorded using the previously described materials and methods. The first step consists of placing the electrodes of the reference ECG recorder on the test subject. To compare the signal from both sources, only Lead-I of the Einthoven triangle was used out of the 12 leads that are possible to be recorded with the GE MAC 800. This was accomplished by connecting

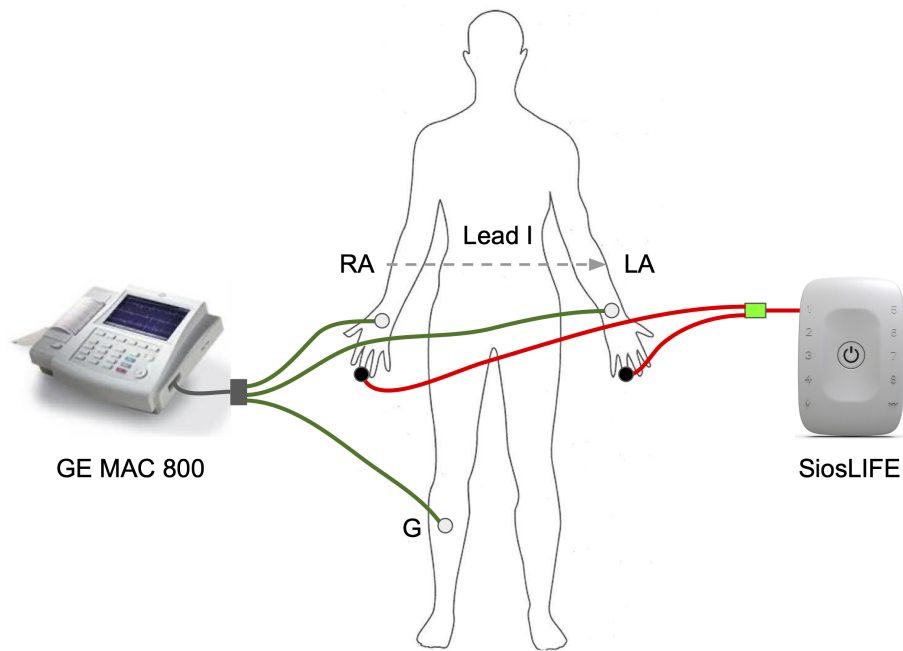


Figure 4.10: Experimental setup used for comparing the performance of the polymeric materials being studied, using a medical grade ECG recorder (green wires) and the dry electrode samples using the SiosLIFE data acquisition module (red wires, represented by a biosignalsplux). RA is the Right Arm; LA is the Left Arm; G is the Ground Electrode; Signals recorded following the Einthoven's Triangle Lead-I configuration.

the right arm electrode on the right wrist (RA in Figure 4.10), the left arm electrode on the left wrist (RF in Figure 4.10), and connecting the ground electrode in the right leg (G in Figure 4.10). Figure 4.10 provides a representation of the electrode placement.

After the electrodes were placed, a visual analysis of the signal was performed to confirm if there was a valid ECG signal present (i.e. a recognizable morphology similar to the one in Figure 4.8). Using this experimental setup, it was frequent for the alligator clips to loosen from the polymer, leading to a loss of signal. Moreover, contact with the sample sometimes was difficult, primarily due to the size of the disk samples, leading to motion artifacts being present in the signal (e.g. signal saturation or going from bottom to top of the scale)<sup>7</sup>.

The second step consisted of asking the volunteer to hold a mockup tablet that had the dry polymeric electrode in study glued to its back, thus simulating a more realistic test. The way in which the fingers were placed over the electrodes was also visually monitored, to ensure correct contact with each of them. With the user grabbing the tablet, the acquisition was started. This acquisition was made using OpenSignals<sup>8</sup>, an easy-to-use and versatile software suite for real-time biosignals visualization. If the signal of both data sources is stable (when possible), then a 10-second window is recorded from the GE MAC 800.

<sup>7</sup>The different noise sources present in an ECG are explored in Chapter 5.

<sup>8</sup>Available at <https://biosignalsplux.com/products/software/opensignals.html>.

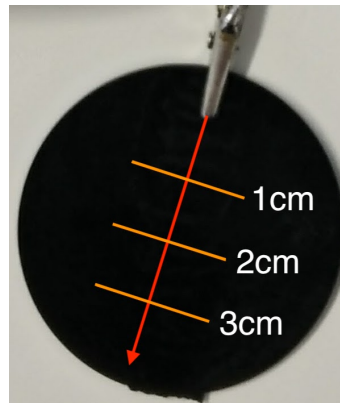


Figure 4.11: Distances used to assess their influence in signal quality, drawn over a sample disk of PO.

The preceding steps are performed at three different distances from the point of contact of the closest finger and the alligator clip, 1, 2, and 3cm (Figure 4.11). This was conducted to determine if there was a considerable difference between having the fingers close to the alligator. The distances were chosen due to the size of the disk samples, which have an approximate diameter of 5cm.

In summary:

- Place the reference electrodes on the user and check signal quality;
- Ask the user to hold the mockup tablet at 1cm from the alligator clips and start the signal acquisition;
- Wait for the signal stability (if possible) and record a 10-seconds window on the reference system;
- Repeat for the last two points for the remaining distances;
- Extract the data from the reference machine and change the material in study;

This protocol was used on 4 different test subjects, all of them males and with no reported cardiac pathology. Their mean age was 24.5 years with a 2.6 years standard deviation.

### 4.3.2 Data Synchronization and Analysis Methodology

The data recorded by the reference system can be digitally exported as a XML file, organized in a proprietary format (GE MUSE). To read this file, parse it, and extract the relevant data, a Python script was developed. This Python script, which can either be imported as a module or run as a command line tool, loads the file and returns two outputs, a JavaScript Object Notation (JSON) file with the header information, such as the

patient, device, and acquisition info, and the ECG signal in one of the following outputs: Comma Separated Value (CSV), Microsoft Excel workbook, JSON file, or a NumPy object. This library was published as an open-source tool and made publicly available [on a GitHub repository](#)<sup>9</sup>. For the signals recorded using the SiosLIFE device, the first step was to downsample them to match the sampling rate of the reference signal. Furthermore, both signals were filtered using a digital notch filter with a cutoff frequency of 50Hz to reduce the power-line interference.

Since the signals were recorded using different devices, these need to be synchronized. For this purpose, a method based on the inter-beat intervals was developed, since this interval will be the same in both devices. To ensure correct synchronization, the R-peak locations were manually annotated in both rhythm strips, and their inter-beat interval was calculated. The method developed to synchronize both signals is summarized in Algorithm 1, in pseudo-code format.

With the GE MAC 800 rhythm strips being smaller than those recorded with the SiosLIFE system, the number of extracted R-Peak intervals, and consequently inter-beat intervals, is lower. Thus, this shorter inter-beat sequence (Marker 2 in Algorithm 1) was sled across the one obtained using the SiosLIFE system (Marker 1 in Algorithm 1).

Starting at the first inter-beat interval from the SiosLIFE system (Marker 1 in Algorithm 1), the absolute difference between the inter-beat intervals of both sources was calculated and added to the iteration difference variable (Marker 3 in Algorithm 1). Each window has a width equal to the number of inter-beat intervals found in the GE MAC 800 rhythm strip (Marker 2 in Algorithm 1). When all the differences for a window are added, the resulting sum is saved in a differences array (Marker 4 in Algorithm 1), and the window is sled over one inter-beat to the right (i.e. in the second iteration, the window would start at the second inter-beat interval from the SiosLIFE).

The GE MAC 800 inter-beat interval sequence is then sled across all intervals from the SiosLIFE system until an upper bound (Marker 1 in Algorithm 1). This upper bound is the difference between the number of inter-beat intervals extracted in the SiosLIFE strip and those found in the GE MAC 800 strip. With all the differences saved in an array, the next step is finding the index of the minimum value for this array (Marker 5 in Algorithm 1).

At this stage the signals are almost synchronized, with the index of the first common R-Peak for both sources discovered. Since the first point in the GE MAC 800 rhythm strip may not be the R-Peak, the position of this peak is used to adjust the synchronization index. By subtracting the location of the first R-Peak from the GE MAC 800 system to the latter index (Marker 6 in Algorithm 1), a 10s window can be segmented from the SiosLIFE rhythm strip, synchronized with the one recorded by the GE MAC 800 system. Figure 4.12a is an visual representation of the synchronization process, while Figure 4.12b is an example of the result of this process, the two synced 10s ECG rhythm.

<sup>9</sup><https://github.com/DFNOrorio/GEMuseXMLReader>.

---

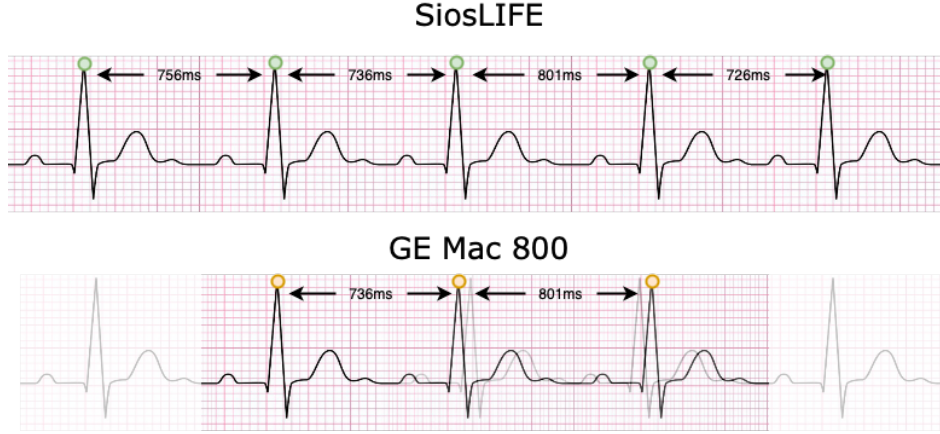
**Algorithm 1:** ECGs sources signal synchronization.

---

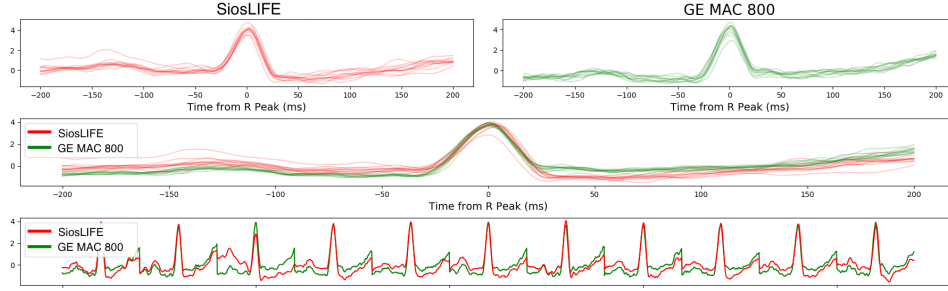
**Data:** SiosLife ECG rhythm strip (SiosECG)  
**Data:** SiosLIFE R-Peak location array RSios  
**Data:** GE MAC 800 first peak R-Peak (FirstRMac800)  
**Data:** SiosLife inter-beat interval array (RRSios)  
**Data:** GE MAC 800 inter-beat interval array (RRMac800)  
**Result:** A 10s (size of the GE MAC 800 rhythm strip) sub-array from SiosECG, synchronized with the reference system

```
begin
  /* Sliding window upper bound */
  UpperBound  $\leftarrow$  lenght(RRSios) – lenght(RRMac800)
  /* Array where the differences will be saved */
  Differences  $\leftarrow$  Emptyarray
  /* Sliding windows (size of RRMac800 array) over all the (bounded)
  SiosLife inter-beat intervals */
1  for i = 0 to UpperBound do
    /* Local variable to save the iteration's difference value */
    Difference  $\leftarrow$  0
    /* Compare each point of both inter-beat array */
2    for j = 0 to lenght(RRMac800) do
      /* Get the two inter-beat interval for each source and save the
      absolute value between their difference */
      RRMac800Value  $\leftarrow$  RRMac800[j]
      RRSiosValue  $\leftarrow$  RRSios[i + j]
3      Difference  $\leftarrow$  abs(RRMac800Value – RRSiosValue)
4    Append the local Difference value to the Differences array
5  MinSequenceInd  $\leftarrow$  Get the index of the minimum value of Differences
  SiosLIFESyncedIndex  $\leftarrow$  RSios[MinSequenceInd]
  /* Adjust the sync index by subtrating the location of the first GE
  MAC 800 R-Peak */
  SiosSyncedIndex  $\leftarrow$  SiosSyncedIndex – RMac800[0]
6  return A 10s sub-array of SiosECG starting at SiosSyncedIndex
```

---



(a) Illustration of the synchronization process using synthetic data. Syncing of the two signals starts by sliding the shorter MAC 800 signal until the interbeat intervals match with those of the longer recording using the SiosLIFE data acquisition unit. When the inter-beat interval between recordings of the two devices matches, then the signals are considered to be synchronized.



(b) Overlay of the standardized ECG signals recorded using the clinical system and one of the dry electrode samples (PO). From each source, the mean value is subtracted and then divided by the standard deviation, thus standardizing the source, and making it easier to compare different sources.

Figure 4.12: Illustration of the synchronization process between the data collected using the SiosLIFE device and one of experimental electrode materials (PO) and the reference system.

After the signals were extracted and synchronized, they are compared for their similarity. Three different metrics were chosen to perform this assessment, namely cosine similarity, **Root Mean Square Error (RMSE)**, and Spearman correlation coefficient.

The cosine similarity measures the cosine of the angle between two non-zero vectors of an inner product space. This similarity measurement is particularly concerned with orientation, rather than magnitude. In short, two vectors that are aligned in the same orientation will have a similarity measurement of 1, whereas two vectors aligned perpendicularly will have a similarity of 0. This value is calculated using Equation 4.1, with  $x$  and  $y$  being the two signals in study, and  $N$  their size.

$$D_{cos}(x, y) = \frac{\sum_{i=1}^N x_i y_i}{\sqrt{\sum_{i=1}^N x_i^2} \sqrt{\sum_{i=1}^N y_i^2}} \quad (4.1)$$



Unlike the cosine similarity, the **RMSE** is amplitude-dependent, reason for which the signals were normalized between 0 and 1 in order to assess their morphological similarity and not the difference in output scale (thus also minimizing any amplitude attenuation caused by higher impedance materials). This metric is the square root of the mean of all the errors, which in this case is the difference between the two normalized signals, the **Normalized Root Mean Square Error (NRMSE)**. In Equation 4.2,  $xnorm$  and  $ynorm$  are the two (normalized) signals in study, and  $N$  their size.

$$NRMSE(xnorm, ynorm) = \sqrt{\frac{\sum_{i=1}^N (xnorm_i - ynorm_i)^2}{N}} \quad (4.2)$$

$xnorm$  (and  $ynorm$ ) was obtained by concatenating each of the normalized cardiac cycles within the **ECG** rhythm strip. For example, in Figure 4.12b, the cardiac cycles for each of the systems are overlayed in the top two charts, while the bottom chart is the concatenated wave, which is constructed from all of the normalized cycles. The cycles were normalized using Equation 4.3, where  $x$  is the signal to be normalized,  $\mu$  the signal average, and  $\sigma$  its standard deviation.

$$Norm(x) = \frac{x - \mu}{\sigma} \quad (4.3)$$

Finally, the correlation was used to assess the linear relation between them in addition to their morphological similarity, with the range of values spanning from 1 (perfectly positive correlated), 0 (no correlation), to -1 (perfectly negative correlation). The rank function is built in the correlation function from the Python SciPy library (Equation 4.4, where  $xnorm$  and  $ynorm$  are the two (normalized) signals in study, and  $rank$  the observation rank).

$$r_s(xnorm, ynorm) = 1 - \frac{6 \sum_{i=1}^N (rank(xnorm_i) - rank(ynorm_i))^2}{N(N^2 - 1)} \quad (4.4)$$

### 4.3.3 Results and Discussion

For reference, **SS** refers to Stainless Steel, **PO** is PolyOne's OnForce FT LF6600-5023, **LV** is LUVOCOM 1850-8023 PTB, **LDS** is Vectra's 840i, **CF** is SAATI's CC202 ET445, and **RTPE** is RTP's 199 X 137556 E.

Regarding the cosine similarity, the results for each material can be seen in the boxplots of Figure 4.13a and Table 4.2a, while Figure C.2 is the boxplot per material and per distance. Going through the cosine similarity results, three materials have a good performance when using this metric, while the remaining three have worse to almost no similarity. **SS**, **PO**, and **LDS** have very high similarity values, with **PO** standing out for best performer. Poly-amides are regularly used in textile-based electrodes, as a dipping coating to some textile patches [114], while liquid crystal polymers usage can also be found [115]. Perhaps the most surprising is the **RTPE** and **CF** results, since carbon-based

Table 4.2: Average and standard deviation for the different metrics that were adopted. Results reported for each material by distance and global average. The best average result is in bold.

Distance	SS	PO	LDS	LV	CF	RTPE
Cosine Similarity						
1cm	0.88±0.06	0.89±0.02	0.84±0.07	0.66±0.30	0.31±0.34	0.16±0.18
2cm	0.89±0.02	0.89±0.03	0.87±0.02	0.65±0.17	0.38±0.26	0.13±0.10
3cm	0.80±0.08	0.88±0.03	0.67±0.39	0.79±0.12	0.36±0.27	0.10±0.06
Mean	0.86±0.07	<b>0.89±0.03</b>	0.79±0.24	0.70±0.22	0.35±0.29	0.13±0.13

(a) Cosine similarity, where values near 1 represent more similar signals.

NRMSE						
1cm	0.12±0.02	0.11±0.01	0.14±0.02	0.20±0.09	0.33±0.09	0.45±0.06
2cm	0.11±0.01	0.12±0.01	0.13±0.01	0.24±0.09	0.35±0.08	0.48±0.04
3cm	0.17±0.08	0.12±0.00	0.09±0.05	0.15±0.03	0.34±0.13	0.47±0.02
Mean	0.13±0.05	<b>0.12±0.01</b>	0.12±0.04	0.19±0.08	0.34±0.11	0.46±0.05

(b) NRMSE values, where values near 0 represent higher similarity between signals.

Spearman Correlation						
1cm	0.71±0.10	0.73±0.10	0.67±0.13	0.50±0.17	0.19±0.24	0.15±0.08
2cm	0.71±0.08	0.73±0.13	0.67±0.16	0.48±0.08	0.29±0.18	0.13±0.09
3cm	0.64±0.09	0.70±0.13	0.47±0.30	0.54±0.05	0.23±0.18	0.08±0.05
Mean	0.69±0.09	<b>0.72±0.12</b>	0.61±0.23	0.51±0.12	0.23±0.21	0.12±0.08

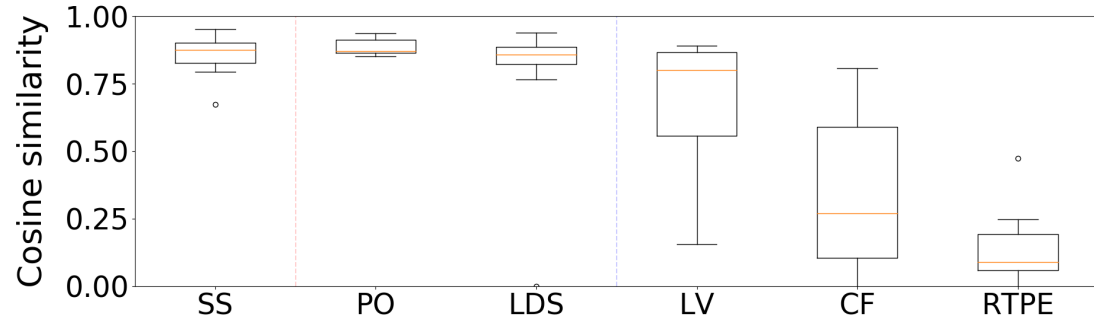
(c) Spearman correlation, where values near 1 represent more similar signals.

solutions are widely used in the manufacturing of dry electrodes [100]. Distance also seems to not play a big role in signal similarity for SS, PO, and LDS, while being more relevant in the remaining materials. This can be seen more evidently seen in Figure 4.13a, where the boxplots for LV, CF, and RTPE are substantially wider than the first three materials.

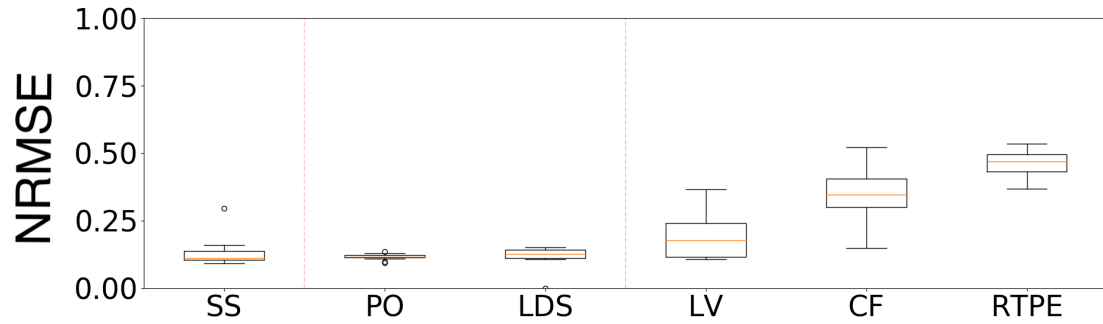
Tables 4.2b and 4.2c and Figures 4.13b and 4.13c (Figures C.3 and C.4 contain the boxplots for their metrics per material and per distance) confirm the results obtained using cosine similarity, where SS, PO, and LDS have a lower normalized root mean square error and better correlation coefficients. For CF and RTPE, the correlation coefficient is very close to zero, meaning there is almost no correlation between the signals recorded using the reference system and those using these two materials.

As a visual example of the performance of one of the materials that did not perform satisfactorily as an electrode to record ECG using the SiosLIFE data acquisition unit, Figure 4.14 is the comparison using a clinical system and one of the dry electrode samples, CF, recorded at 1 (Sub-Figure 4.14a) and 2cm (Sub-Figure 4.14b) from the alligator clips. None of the signals is morphologically similar to their reference, the rhythm strip recorded using the GE MAC 800, confirmed by the values for the computed metrics.

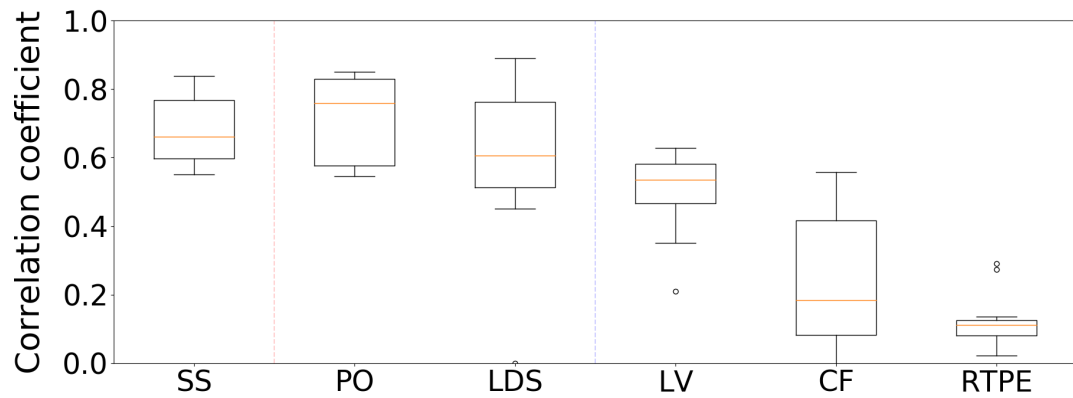




(a) Boxplot with the cosine similarity per material. This figure contains the aggregate results, while the per distance boxplot can be found in Annex C, Figure C.2.

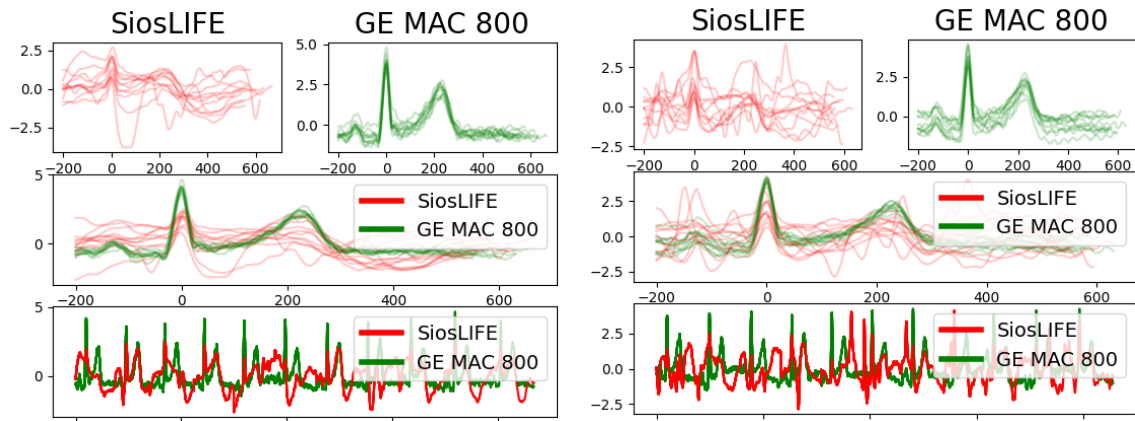


(b) Boxplot with the [NRMSE](#) per material, using normalized units. This figure contains the aggregate results, while the per distance boxplot can be found in Annex C, Figure C.3.



(c) Boxplot with the Spearman correlation per material. This figure contains the aggregate results, while the per distance boxplot can be found in Annex C, Figure C.4.

Figure 4.13: Boxplots of the aggregate results (all distances) for the different analytical metrics.



(a) Example recorded at the 1cm mark. The cosine similarity was  $\approx 0.45$ , the  $\text{NRMSE} \approx 0.38$ , and the Spearman correlation  $\approx 0.41$ .

(b) Example recorded at the 2cm mark. The cosine similarity was  $\approx 0.32$ , the  $\text{NRMSE} \approx 0.32$ , and the Spearman correlation  $\approx 0.15$ .

Figure 4.14: Overlay of the standardized ECG signals recorded using the clinical system and one of the dry electrode samples (CF), recorded at 1 (a) and 2cm (b).

Nevertheless, the strip recorded at 1cm has a more similar morphology to its reference compared to the strip recorded at 2cm, reflected by the better results of the analytical metrics, and also being more similar visually.

### Pressure Influence on Signal Quality

As a final test, a brief study using pressure sensors was performed to check if higher pressure exerted on the electrodes changes the results, which in these cases led to higher cosine similarity and lower  $\text{NRMSE}$ . For these tests, three membrane force-sensing resistor were placed behind each PO electrode<sup>10</sup>, at the top, middle, and bottom regions of the electrode. Afterward, three different grip pressures were exerted on the electrodes, low (the result of the sum of the force-sensing resistors lower than 30% of maximum recorded pressure), medium (30% to 70%), and high (>70%). The result of this test can be found in Table 4.3.

Table 4.3: Pressure influence tests using SS and PO electrodes. CS refers to cosine similarity.

	SS				PO			
	Run 1		Run 2		Run 1		Run 2	
	CS	RMSE	CS	RMSE	CS	RMSE	CS	RMSE
Low Force	0.65	0.88	0.71	0.91	0.32	0.88	0.61	0.92
Medium Force	0.48	0.88	0.68	0.92	0.63	0.89	0.68	0.92
High Force	0.70	0.89	0.68	0.91	0.59	0.90	0.75	0.92

<sup>10</sup>Force-sensing resistor's datasheet can be found in [https://support.pluxbiosignals.com/wp-content/uploads/2021/11/Pressure\\_FSR\\_Datasheet.pdf](https://support.pluxbiosignals.com/wp-content/uploads/2021/11/Pressure_FSR_Datasheet.pdf)

Although there is a slight improvement in the cosine similarity with higher pressure (which could be due to better contact in the skin-electrode interface and the reduction of the air pockets that could be present [96]), the **NRMSE** remained practically the same.

## 4.4 Summary

Electrodes are responsible for converting the signal propagation carried out by ions inside our body to electrons, which are responsible for signal conduction outside the body. There are two main types of electrodes, dry and wet. Wet electrodes use an electrolytic gel to help reduce the impedance, thus aiding the signal conversion. However, this gel has drawbacks when used for long periods of time, motivating the development of dry electrodes, suitable for longer periods of time, while also being able to be easily reused in multiple acquisitions. These can be penetrating, capacitive, or surface electrodes, with the latter being the most common and possible to be produced using metals, carbon materials, or polymers.

They can also be divided into three categories, considering their placement in relation to the person in which they will be used. An electrode can be placed in-, on-, or off-the-person, with decreasing levels of intrusiveness while increasing their potential outreach. Some commercially available wearable devices, such as smartwatches, fall into the on-the-person category, despite their electrodes being embedded in the device instead of attached to the body. This is due to their intrusiveness, with the user having to make a conscious action to record a rhythm strip. Therefore, the combination of an off-the-person solution and dry electrodes can be an effective solution for pervasive monitoring of **CVDs**, having a more naturalist method to record an **ECG** rhythm strip.

To this effect, a new solution based on a custom back cover for a tablet was presented. This cover will have dry electrodes embedded into it, which will be made out of a polymeric material that was selected due to its characteristics and signal similarity comparatively to a clinical device. Of all identified candidate materials, PolyOne's OnForce LFT LF6600-5023 (**PO**), a polyamide with high elastic modulus and material strength had the best results in all three metrics used, cosine similarity, **RMSE**, and Spearman correlation.

The present study was then able to identify a practical solution for one of the project's objectives, the pervasive and continuous monitoring of **ECG** signals, producing high-quality signals. Figure 4.15 shows a pre-production unit of the final product, although still without the electrodes embedded (a conceptual position for them is marked in the image).



Figure 4.15: Pre-production unit of the final design for the tablet. This unit featured a custom back cover without the electrodes embedded, serving as a visual aid. Thorough tests will be done for optimal electrode placement in the back cover to ensure long-term comfort while using the tablet and recording [ECG](#). In green, a conceptual position for the electrodes.

## OUTLIER DETECTION

One major problem with acquiring data using devices that have embedded electrodes, e.g. using a wearables device such as a smartwatch, or using an off-the-person device such as a tablet with electrodes embedded in the back cover, is the quality of the signals recorded, more specifically, the amount of noise that could be present in the recordings or even the lack of signal due to loss of contact with the electrodes. This problem is even more troublesome if the aim of the device is pervasive acquisitions, where there is a constant flux of data that needs to be either saved or transmitted. In the event of an outlier segment, there is no need to handle such a section, thus saving computational, cellular data, and/or device storage resources by discarding it.

This section focuses on [Electrocardiogram \(ECG\)](#) outlier detection, the typical sources, the state-of-art signal quality features and indices, and proposing a new approach to detecting and classifying outlier segments.

### 5.1 What are Outliers in an ECG?

There have been major advances from the 1960s to 2020s in automated electrocardiography analysis, with the first major work in this field by Dr. Hubert V. Pipberger in 1957 using three simultaneously recorded orthogonal leads [116, 117], in which those were digitized and automatically recognized by a computer. One such task that can be automated is outlier detection, i.e the discovery of segments that are not suitable for further analysis. There are different scales of suitability, but these can be aggregated into two major classes [22]:

- Basic quality, where the R-peaks are clearly identifiable. In this case, reliable [Heart Rate \(HR\)](#) and [Heart Rate Variability \(HRV\)](#) information can be extracted, as well as some types of arrhythmia;
- Diagnostic quality: P (if present), QRS, and T waveforms are clearly identifiable. In this case, the signal can also be used for the clinical diagnosis of more subtle conditions such as myocardial ischemia and coronary heart disease.

These classes are the result of not only ample knowledge of the ECG signal properties but also the ones from noise [118]. However, this is not a trivial task. Even in 1984, thirty years from the first steps in automated ECG analysis, Skordalakis in "Recognition of noisy peaks in ECG waveforms" wrote that "this goal is very hard to achieve because in general, it is difficult to distinguishing noisy from real peaks." [119]. Furthermore, even in a clean ECG, analyzing and identifying the different waves is challenging, since the morphology of the signal is unique to each individual, and influenced by differences introduced by electrode type or placement. Additionally, some disorders can also deform the ECG wave. As examples, atrial fibrillation<sup>1</sup> is typically diagnosed due to the absence of the P-wave, which is generated by the depolarization of the atria [120, 121], or myocardial ischemia<sup>2</sup>, which is associated with abnormalities of the T wave [122].

Pan and Tompkins [88], known for their R-peak detector, described the types of noise more commonly found in the ECG and which can influence the robustness of QRS detection. These are "muscle noise, artifacts due to electrode motion, power-line interference, baseline wander, and T-waves with high-frequency characteristics similar to QRS complexes". These sources not only affect the wave's morphology, but also influence the frequency domain. For diagnostic-quality ECG, signals typically require a bandwidth of 0.05–100Hz, whereas monitor-quality ECG may be limited to 0.5–40Hz [123]. As an example of spectrum interception, muscles have an electrical activity that has a frequency bandwidth of 20 to 400-500Hz [124], while power lines introduce a frequency component at 50/60Hz (depending on the region of the world) [123]. The following is a list of the principal noise sources that effects an ECG, described in greater detail throughout this subsection:

- Baseline wander;
- Respiratory Sinus Arrhythmia (RSA);
- Motion artifacts;
- Muscle activity;
- Power-line interference;
- Electrode misplacement;
- Electromagnetic Interference (EMI);
- Poor or inexistent contact (off-the-person).

---

<sup>1</sup>A form of heart arrhythmia, which is a rapid and irregular beating of the atria.

<sup>2</sup>Reduction or absence of blood flow to the heart muscles.

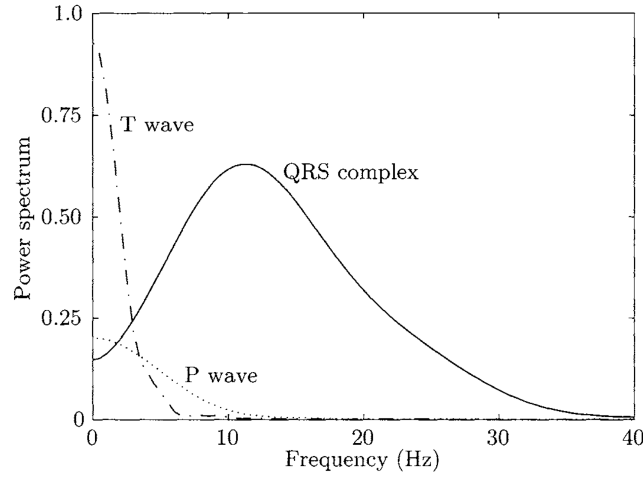


Figure 5.1: Normalized ECG power spectrum of the P wave, QRS complex, and T wave. The diagram serves primarily as a rough guide to where the spectral components are located; large variations exist between beats of different leads, origin, and subjects. Extracted from [118].

These different types of noises can be considered either non-physiologic or physiologic. A non-physiologic artifact is usually caused by poor electrode contact, electromagnetic interference, or defective ECG equipment. A physiologic artifact can be produced by muscle activity (electromyographic potentials) or the skin contact condition [125]. A typical (normalized) ECG Power Spectral Density (PSD) distribution of each wave (P, T, and QRS complex) can be seen in Figure 5.1.

A visual example of different ECG traces affected by noise can be found in Figure 5.2. The different types of noises can be also distinguished by the amount of distortion they introduce to the ECG morphology. Some, like high amplitude motion artifacts (Figure 5.2 a)) and muscle activity (Figure 5.2 c)) can make the recovering of those segments, either by filtering or other techniques, a very hard if not impossible task, thus making that segment non-analyzable. On the other hand, there are sources such as baseline wander (Figure 5.2 b)) or power-line interference (Figure 5.2 d)) that have a more subtle effect on the signal trace, preserving the underlying morphology or being easy to "remove", allowing for the extraction of basic features such as HR (basic quality) or even the complete reconstruction of a noise-free ECG [22].

### Baseline Wander

Baseline wander noise is considered to be a low-frequency modulation of the ECG signal, typically non-distorting, and is often exercise-induced (due to perspiration, respiration, body movements, and poor electrode contact). Its spectral content is usually within an interval below 1Hz and can be easily filtered out. This type of noise becomes a problem if the oscillations cause the signal to partially saturate, leading to irreversible losses [118].

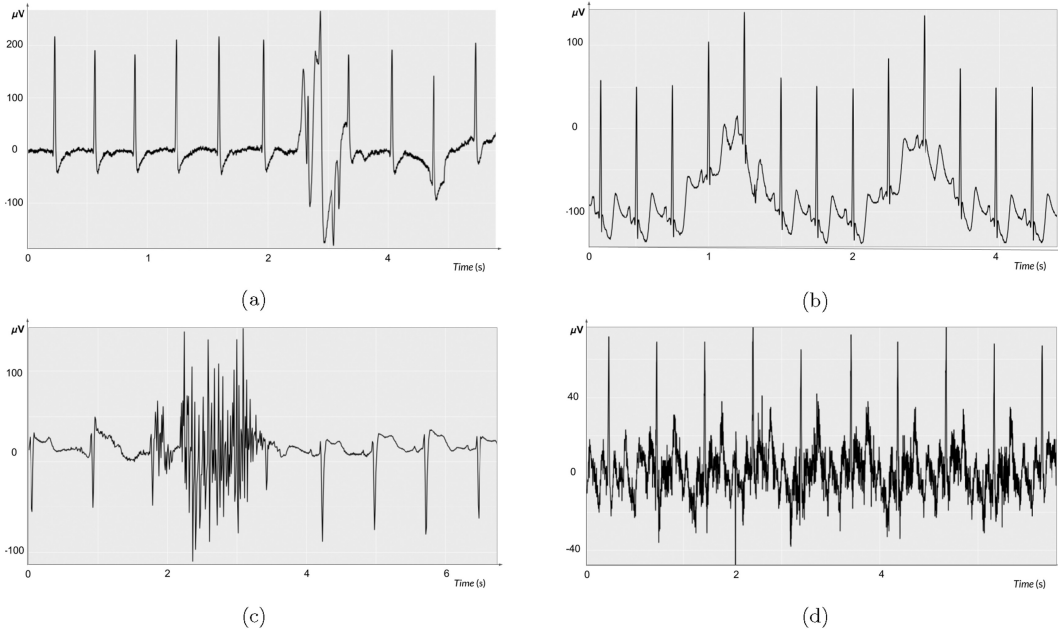


Figure 5.2: Example of most common noise sources and also different morphology depending on electrode placement. a) Motion artifact; b) Baseline wander; c) Muscle activity; d) Power-line interference. Extracted from [126].

## RSA

Respiratory activity influences ECG measurements not only through the variation of the HR but also beat morphology. The HR modulation is known as RSA, which manifests itself through the number of Heartbeat (HB)s in a breath changing according to the respiration cycle, increasing during inspiration and decreasing during expiration [127], as demonstrated in Figure 5.3 d). Such beat-to-beat variations in morphology are caused by chest movements, changes in the position of the heart, and changes in lung conductivity, which can lead to variations in QRS amplitude (Figure 5.3 c)) or a baseline wander like modulation (Figure 5.3 b)).

## Motion Artifacts

Electrode motion artifacts are mainly caused by skin stretching (especially when these are attached to the skin), which alters the impedance of the skin around the electrode [128]. This is also problematic when using dry, off-the-person electrodes, as there is no non-physiological electrolyte, skin preparation, or constant contact with the electrodes [118]. Friction between the electrode against the skin, which is mainly caused by motion, can also change the local electrical charges, inducing a triboelectric current, further corrupting the signal [129]. This type of noise is characterized by large amplitude swings, which can sometimes be mistaken for QRS complexes, leading to falsely detected heartbeats. Their frequency range also overlaps this complex, typically spanning from 1 to 10Hz [118].



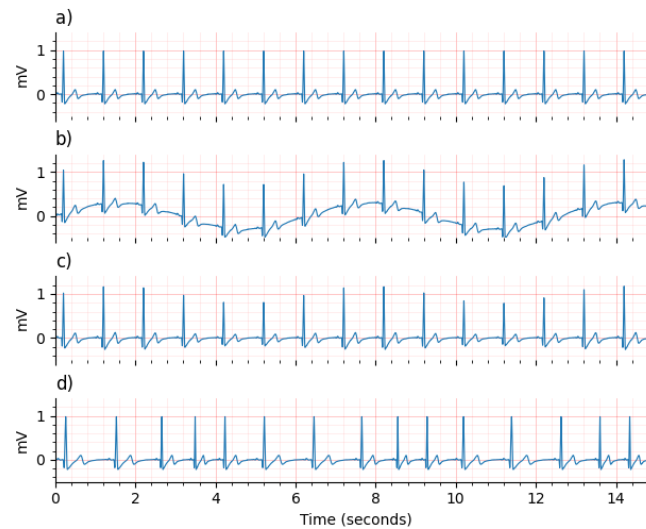


Figure 5.3: Respiratory modulation on ECG. a) Non modulated; b) Baseline wander modulation; c) Amplitude modulation; and d) HR modulation.

### Muscle Activity

Muscle activity (especially skeletal muscles) also causes distorting events on a ECG trace. The effect of this noise is more pronounced in body regions where there are a large number of superficial muscles contracting, for example, electrodes applied on the chest while exercising. As with motion artifacts, both the morphology and the spectral content of an ECG are corrupted by this type of noise, since it produces high magnitude in the rhythm strip and frequency amplitude swings, which also have an overlap between the ECG spectral content [118].

### Power-line Interference

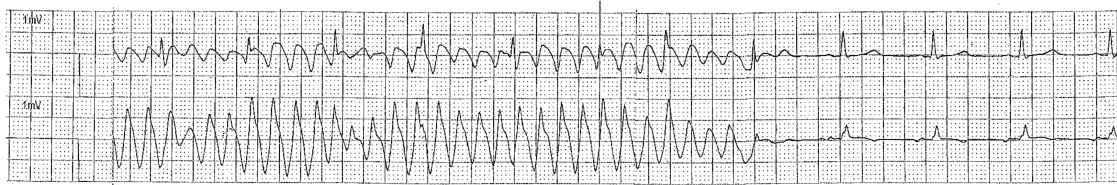
Power-line interference (50/60Hz) is commonly caused by the improper grounding of the ECG recording devices and/or interference from nearby equipment. Although this interference is characterized by morphological distortion and its frequency falling in the higher bound of the ECG spectrum, the constant frequency of this noise makes it very simple to filter out, usually by applying a notch filter [118].

### Electrode Misplacement

Limb electrode reversal is most commonly due to temporary confusion as to sidedness (confusion between left and right side), or reversal of the arm and leg electrodes by the technician. In certain leads, this causes predictable changes in the major QRS vectors or QRS complex morphology. For example, in Lead I if there is an electrode reversal, the QRS complex will be inverted, with a large depolarization followed by a large repolarization [130].

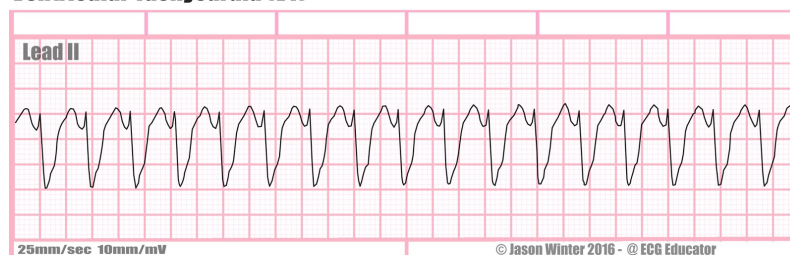
## EMI

EMI is not well recognized during ECG interpretation and is frequently misdiagnosed as other serious conditions, which can lead to preventable medical errors [131]. This interference typically originates from energy radiation by other electrical devices, and affects the ECG via broken or poorly shielded leads [132]. For example, in [133] the authors present a case study of an EMI artifact caused by an improperly isolated microdebrider<sup>3</sup> which resembled a Ventricular Tachycardia (VT). To confirm if the patient was under a VT, doctors checked the pulse and the pulse oximeter, only to find the readings obtained by those to be inconsistent with a VT, thus classifying it as an artifact. Figure 5.4a is the trace published in [133] while Figure 5.4b is a typical ECG during a VT.



(a) VT like EMI artifact on an ECG rhythm strip. Extracted from [133].

### Ventricular Tachycardia (VT)



(b) Typical ECG rhythm strip during a VT event. Extracted from [134].

Figure 5.4: Example of how an EMI artifact can be perceived as a life-threatening event, where the ECG recorded during the use of inadequately shielded electrical equipment mimicked a ventricular tachycardia.

## Poor or Inexistent Contact

Focusing more on off-the-person devices, not only there is the problem of lead inversion but also the problem of poor to inexistent contact at all with one of the leads. This can cause abnormal events, such as a saturation (Figure 5.5) or a flat line in the segment, with irreversible losses of parts of an ECG waveform. Furthermore, motion artifacts can be amplified since a constant and stable contact with the skin is not ensured when the electrodes are embedded in the device [100].

<sup>3</sup>A surgical tool that has a very small rotating blade with a hole in the middle allowing for removed material to be extracted by vacuum.

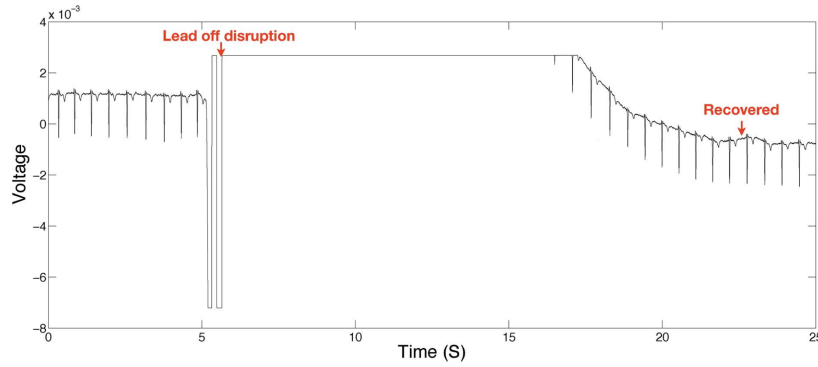


Figure 5.5: Lead off event on an ECG, where is possible to see the loss of signal caused by poor contact or even no contact with one of the leads. Adapted from [129].

In summary, distinguishing what is a clean ECG is not a task as trivial as saying this segment is indeed corrupted or clean, since a corrupted segment can be in fact a clinical event or, on the other hand, a clinical relevant segment can be confused with an artifact. Artifacts on the ECG may sometimes be obvious, but they may also be similar to clinical pathology [130], as seen in Figure 5.4. Although the potential for ECG artifacts is widely recognized, it is still difficult even for a specialist to distinguish artifacts from real clinical findings. In [125], the authors comment on a study (with 766 participants) where only 6% of internists, 42% of cardiologists, and 62% of cardiac electrophysiologists recognized the ECG abnormality present on the ECG in study. They further comment on how artifacts are such a common occurrence that formal training simply neglects its teaching, with the major textbooks offering no discussion on the topic.

## 5.2 How to Handle an ECG Outlier

There are many different approaches to try to answer the question "Is this a good/viable ECG segment?". These approaches rely typically on time and frequency domain features to try and find some connection between these and the noise seen in the signal. Time domain algorithms focus on the morphology of the ECG waveform and use it to devise heuristics or other statistical indices to assess the segment in study, e.g. detecting unusually large stationary segments or saturated regions. Frequency domain algorithms on the other hand use the spectral information of the signal, where different parts of the spectrum are usually compared to assess the quality of the signal, e.g. the relative power of the baseline wander power band (<1Hz) and the monitor quality power band (<40Hz) can be used to assess the influence of baseline wander in the signal [135].

Typically these features are combined and mixed in different rules, having also many stages in the decision-making process. These start simple, with some initial checks such as flat-line or saturation detectors, and increase in complexity and sophistication, regularly involving some sort of machine learning or complex rules [22].

Before taking a more in-depth look into different examples, a brief note is made concerning single and multi-lead features, and the area of focus of most algorithms. Starting with the latter, these are typically designed to be employed in situations where basic quality detection (i.e. segments with quality enough for HB detection) is good enough rather than full diagnostic quality. The last-mentioned are more arduous to classify, requiring a more knowledgeable database capable of distinguishing segments acceptable for diagnosis from those with just noise, and all the variations within these two extremes.

Furthermore, the new trend of wearable devices focuses more on HB detection rather than diagnosis-grade signals (although the introduction of US Food and Drug Administration (FDA)-approved Atrial Fibrillation detection algorithms in smartwatches can start shift the focus from basic to diagnosis quality) [22].

Regarding the number of leads used, the big difference between single and multi-lead channel approaches is the presence of multiple data sources to test the level of agreement between their features and estimations, while single-lead have to rely only on one ECG rhythm strips and some sort of heuristic [22].

### 5.2.1 Time-domain Techniques

For most time-domain techniques, the first step consists of applying a beat detector to the ECG. For that, robust beat detection algorithms are needed. Two of the most popular are the Pan-Tompkins algorithm [136] and the one proposed by Zong in [137], both available as open-source on PhysioNet [138]. The detected beats will then be used as part of feasibility checks, either by being the reference for the segmentation of the signal, used for example to create templates, or used to assess the physiological viability of the segment in respect of HB/HR [22].

These feasibility checks are simple rules, which are designed to quickly discard ECG segments without complex techniques, and are typically applied in succession [22]. Below is a summary of some of these simple feasibility checks.

**Flat line detection** As seen in Chapter 5, the ECG waveform has a distinctive morphology, with very few isoelectric regions within a cardiac cycle (e.g. the segment between the end of the P wave and the start of the QRS segment is one of such regions). A signal (or its derivative) where there is a constant value for long periods (0.2 to 1s) cannot be an ECG waveform [22, 139, 140].

**Amplitude limits and variations** Another common technique consists of checking the number of times a signal reaches the acquisition device maximum (saturation) or the minimum range limits. The peak-to-peak amplitude (maximum-minimum) or the amount of time a certain signal is above/below a threshold is also another technique used to quickly classify signals into noisy or usable [22, 139, 141].

**Noise-Power measurements** Using standard noise-power ratios by selecting certain features and baselines can create metrics, prone to quickly exclude certain segments. Some of these measurements are as follows [22, 142]:

- **Root Mean Square (RMS)** power in the isoelectric region, where the potential should be zero. These regions are, e.g., the segment between the end of the P-wave and the QRS complex;
- Ratio between the R-peak amplitude and the noise amplitude in the isoelectric region;
- Ratio between the peak value of a signal and its **RMS** value.

**Physiological viability** Using the output of the beat detector, some simple physiological viability tests can be performed, such as the average **HR** or the minimum/maximum R-R intervals. These values can then be compared to the normal ranges and used to evaluate the segments, such as the normal **HR** range of 40-180 **Beats Per Minute (BPM)** [143] or changes of R-R intervals within a time frame (although pathological cases may also be manifested as irregular R-R intervals) [22].

Using these simple checks it is already possible to classify the more blatant noise segments, but other techniques can be applied. More examples of algorithms using a combination of these simple metrics are as follows:

- In [144], the authors use the area under the **ECG** curve, more specifically the area of each QRS segment, and its difference between two successive beats to assess the quality of the segment. In a noise-free signal, the difference between areas should be small, and when a noisy segment is encountered the difference in areas increases (or becomes highly variable), thus indicating the presence of noise [135, 144];
- In [145], a multi-stage algorithm is proposed: (a) basic **ECG**, quality properties such as amplitude, spike features, and constant portions; (b) number of crossing points<sup>4</sup> between different leads; and (c) a comparison between QRS and non-QRS amplitude [135, 145, 146];
- In Moody [139], the author uses time-domain features to develop three criteria to assess if the segment contains any outlier. These features include the amount of time a segment has a low range amplitude, the correlation between different leads, or if a signal is stationary for a relatively long period of time [135, 139].

---

<sup>4</sup>When dealing with a 12 lead **ECG**, one common way of displaying the signals is plotting each lead underneath the previous. When one lead drifts, it can cross to the other lead plot, overlapping it.

### 5.2.2 Frequency-domain Techniques

Frequency-domain methods are based on the analysis of the spectral features of the ECG signal in order to identify its noise content [135]. The reasoning behind this is that noise manifests itself on the spectrum of the ECG as increased power in frequencies outside the physiologically known limits of the ECG, or as a change in the distribution of power [22]. Since most physiologically relevant information in the ECG is contained in frequencies below 40Hz (monitor quality top bandwidth limit, as shown in Figure 5.1)), unusually high spectral density outside this bandwidth will likely correspond to the presence of noise [22].

**Noise-Power measurements** As with time-domain techniques, noise-power ratios can be formed using spectral information [22]:

- Ratio between in-band (5–40Hz) and out-of-band spectral power;
- Power in the residual after a filtering process.

In the work of Allen et. al [147], the spectrum was divided into six different power bands from 0.05 to 100Hz, with two of the six power bands, ECG1 - [0.25–10Hz] and ECG2 - [10–20Hz], corresponding to the ECG components and the remaining four to noise. To these six features, a seventh was added, corresponding to the number of times the signal exceeds the  $\pm 4$  mV range (Out-of-Range Events - ORE) in order to account for high-intensity electrode movement [22, 135].

Another example of the usage of different spectral bands is the work of Zaunseder [148], where an algorithm based on an ensemble of decision trees was proposed. In this, the monitor quality spectrum (0.5-40Hz) is compared with the low-frequency noise band (<0.5 Hz) and high-frequency noise band (45–250Hz) in order to assess the quality of the signal. Some of these metrics include the median, maximum, and minimum values of these power bands, afterward used to build decision trees [135, 148].

Finally, and continuing the work by Allen, the study by Li et al. [149] uses the PSD of the 5–14Hz frequency band and the 5–50Hz frequency band to produce the so-called spectral distribution ratio (SDR) of the ECG, by comparing the value of these two ranges [22, 149].

**Spectral analysis of the HRV signal** Another candidate for a noise quality indicator is the spectral analysis of the HRV. The basis of HRV is the distance between two consecutive HBs, therefore relying on accurate beat detection, which in the presence of noise will be distorted. A warped HRV signal would also have a different spectral distribution, since there would be energy in the non-physiologically-relevant bands, e.g., in frequencies greater than 0.4Hz<sup>5</sup> [22, 143].

<sup>5</sup>In the HRV spectrum all physiological relevant data is contained bellow 0.4Hz, the upper limit of the high-frequency power band. For more information about HRV, refer to Chapter 2, Sub-Sections 2.4 and 2.5.

### 5.2.3 Trend-based Approaches

As mentioned abundantly, the [ECG](#) waveform, especially the QRS complex, is quasi-periodic and has a very stationary morphology, with the amplitudes and the distance between each component of a cardiac cycle being relatively constant [22]. These characteristics can be useful to find irregular patterns.

**High Order Statistics (HOS)** Some statistical features can be used to assess the morphology of the segments. Two examples are the skewness, which is a metric to evaluate the symmetry of the distribution, and kurtosis, which measures the distribution's peak sharpness. A normal [ECG](#) will have a high value for both the skewness and kurtosis since the values will be very symmetrical and have a sharp peak (if a histogram for the values was plotted, a normal [ECG](#) would resemble a normal distribution). As a result, skewness and kurtosis have been proposed as indices of the presence of outliers in an [ECG](#) segment (e.g. a 10-second waveform), since their existence will typically broaden the distribution, lowering the kurtosis, and can also cause asymmetries, decreasing the skewness [22].

**Template Matching** Last but not least, the morphology of the beat can be used to make a short-term template (e.g., using a 10-second window) and then compare each beat to a known quality template, e.g., using the Pearson's correlation coefficient. The template produced can then be used to assess if the segments have a good or bad correlation with it. If there is a good average correlation, then the signal is probably good. On the other hand, if the average correlation value is low, then the segment is probably a noisy one [22].

### 5.2.4 Decision Rules

All the previous metrics and examples presented can be combined to produce better results, with varying order and complexity of the metrics applied. Some approaches apply multiple rules at the same time, while others choose to use them in stages. In the latter, one of the approaches is the "black box" model, where the interconnection and relation between features are very complex to understand and therefore only the input and output are known to the user.

**Thresholds and Combinations of Rules** The various metrics used have some type of limit, enabling the definition of a threshold from which normal and abnormal values can be separated. In [22], the authors described two different techniques to set these, namely:

- Signal characteristics determined heuristically - Some thresholds are found by trial and error, based on the experience of what the signal should look like. These lead to most works proposing decision rules based on expected signal characteristics and do not contain detailed justifications of the thresholds set, often seeming arbitrary [22].



- Empirical based - Opposed to the last point, thresholds can also be "learned". For example, different thresholds can be used to classify the data and their performance tracked in the [Receiver Operating Characteristics \(ROC\)](#) curve plot in order to select the best out of them. The [ROC](#) curve plots the 1-specificity (horizontal axis) against the sensitivity (vertical axis), with the optimal point being (0, 1). Therefore, their performance can be assessed in order to select the best one programmatically [22].

A final note on combining different rules to assess the quality of a segment is the order they appear. Simpler rules, such as flat line detection or signal saturation, should be applied first in order to optimize computation resources if the algorithm is to run on a mobile device.

**Machine Learning Models** Opposed to rule-based algorithms, those using machine learning can be modeled without having to know beforehand what the features should appear like in order to classify the segments as acceptable or unacceptable. In other words, these algorithms need only to know the quality of the segment to map the features to it, learning how to replicate the labeling process without the need for understanding it [22].

More advanced types of this approach, such as [Artificial Neural Network \(ANN\)](#), operate in such a way that the relation between the input and the output result is very complex, and sometimes even not understandable. These types of models are called "black boxes" due to their obscure mapping, "showing" the user only their output. This complexity allows them to find multidimensional and non-linear relations for the labeling process, which for the task at hand (outlier detection) is an advantage rather than a drawback [22]. Some examples of usage of machine learning models in signal quality assessment are as follow:

- In [150], the authors compared the performance of three different machine learning algorithms using signals from a wearable device. One of those was a [Support Vector Machine \(SVM\)](#). From the waveform a set of non-morphological features were extracted, e.g. kurtosis, and used to train these classifiers [150];
- In [151], an [ANN](#) (see Sub-Section 5.3.3) was trained using seven morphological, spectral and statistical features from a multichannel [ECG](#), resulting in 84 feature inputs [151];
- In [152], a [Deep Neural Network \(DNN\)](#) (see Sub-Section 5.3.3) was trained using as input both a 10-second [ECG](#) segment and its spectral information directly to classify the segment in good or bad. In this example, no features are selected, using the time series and the frequency content directly as inputs in order to label the segments [152].



### 5.2.5 Discussion

Outlier detection is not a trivial task, since some of the anomalies are due to physiological sources, such as arrhythmias. This leads to increasingly complex algorithms, which tend to be computationally expensive tasks. [22, 135]

A drawback of these methods that is intrinsic to their development and performance, is the need for great amounts of data in order to generate models with good performances. This adds an extra step to the task of finding artifacts, i.e. the discovery of training datasets. As with finding the artifact, this is not an easy task. Most datasets are either focused on arrhythmia discovery or are highly unbalanced (many more examples of good segments compared to those that are noisy). An example of a dataset more focused on noise detection is the Physionet Challenge of 2011, entitled "The development of an algorithm for assessing the quality of 12-lead ECG recordings collected via a mobile phone in real-time" [153], where more than 40 different institutions submitted a proposed algorithm for the challenge [145].

## 5.3 Proposed Approach

As seen in the last section (Section 5.2), a large number of outlier detection algorithms rely on a good detection of the QRS complex. There are many techniques and research in this field, with the goal of developing accurate and fast algorithms [154]. One such technique, which was developed to be implemented in small microcontrollers, is the usage of phase portraits, a method derived from chaos physics [154].

Phase portraits is a technique to geometrically represent the trajectory of a dynamical system in the phase plane instead of the time plane. This portrait can be obtained by transforming the signal from a one-dimensional time series to a two-dimensional phase domain using lag-coordinate mapping. This is a widely used method to reconstruct and analyze non-linear systems' dynamics from a time series source, which in the case of the cardiac system, a two-dimension phase portrait of an ECG is good enough to reconstruct its dynamical behavior [154, 155].

In other words, by plotting the original ECG wave (x-axis) against a delayed version of itself (y-axis), that signal is mapped from the time domain to a two dimension phase domain, and a phase portrait is constructed. Figure 5.6 illustrates this transformation.

As it can be seen in Figures 5.6.b), .c), and .d), the phase portrait has a distinct morphology and a specific trajectory. These trajectories are delay specific, with different time delays producing a unique shape. While analyzing this technique, a new idea came to fruition, using these plots to detect outliers rather than finding the QRS complex.

Signal morphology is a common technique used to distinguish between clean and noisy sources, however, this is done almost exclusively in the time domain (e.g. template matching of QRS complex). However, time-domain methods also have the limitation of relying on a specific signal segmentation methods, such as beat detection to find the

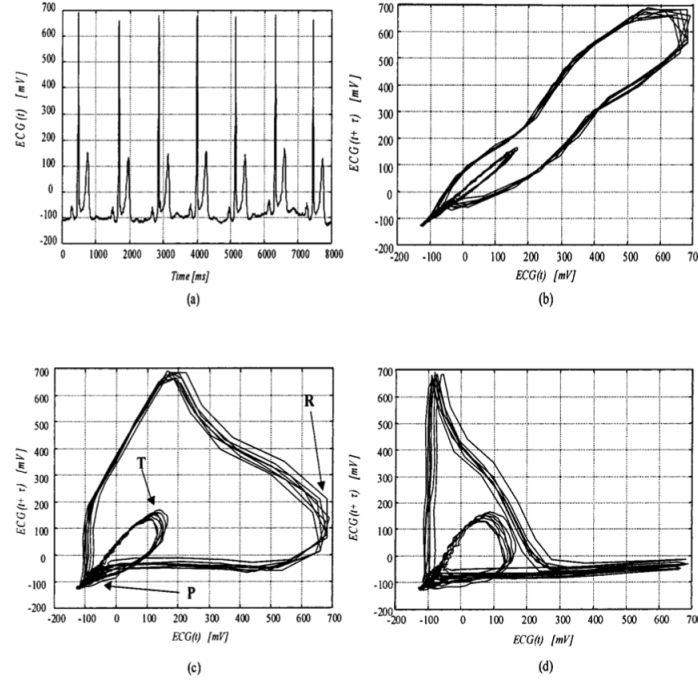


Figure 5.6: Phase portrait reconstruction using lag-coordinate mapping, transforming a one-dimension time domain wave (a) to a two-dimension phase domain representation of the wave using an 8ms (b), 20ms (c), and 40ms (d) time delay. Extracted from [154].

QRS complex, in order to create segments to compare. Therefore, these techniques are conditioned to the performance of such segmentation steps. By constructing the phase portrait, the need for a segmentation algorithm is eliminated.

To distinguish usable from outlier segments, three different methodologies were selected and will be described in the following sections:

- Area - Calculate the area of the shape and compare it to the overall area;
- Image descriptors - Use a common image descriptor to extract features from the shape;
- Image as input to a ANN - Use the image directly to build a classifier.

A brief overview of all these methodologies, as well as a description of the estimators used for each of them, will be presented in the following sub-section, but before diving into them, a short introduction to chaos analysis in ECG.

The three main properties of a chaotic system, namely aperiodicity, determinism, and confinement, in conjunction with sensitive dependence on initial conditions, play a crucial role in defining and understanding such systems [156]. Due to slight variations in anatomy and other properties, it cannot be universally claimed that every moment of every human heart's function conforms to a non-linear and deterministic system [157].

This assumption generally holds true, although some hearts, typically those with low heart rate variability, may exhibit linear and deterministic behavior. Furthermore, the human heart displays a chaotic pattern, with the time between beats varying depending on factors such as physical activity. By extension, it can be inferred that ECGs are most regular when the heart is static, as evidenced by the completely flat ECG record observed in the heart after death [156, 157].

An attractor of the phase trajectory of the system, the set of boundary points in the phase space, can be constructed as one of the visual methods to assess the chaotic behavior of a system, which has been applied to observe ECG dynamical rhythms due to its being a good choice for analyzing such non-linear and non-deterministic/deterministic signals [158, 159].

To visualize the attractor and its characteristics, the most frequently embedding method is the time delay embedding. It uses delayed values of the time series and embedding dimension to obtain the reconstructed vectors, which are then plotted on the phase space and used to characterize the dynamics of system state trajectories on the phase space attractor [159, 160]. Therefore, embedding dimension and time delay play an important role during the reconstruction of the phase space of a dynamical system [161].

The embedding dimension is usually determined using either the method of false nearest neighbours, while the time delay is usually determined using either the first minimum of the average mutual information function (AMIF) [161].

With the attractor defined, different features can then be extracted to study the systems, such as correlation dimension, spatial filling index, central tendency measure, fractal dimension, approximate entropy and sample entropy, or Lyapunov exponent [156, 159].

This work aimed to investigate the potential of using image-based features instead of conventional ones, and to this end, only one embedded dimension was utilized with multiple time delays.

### 5.3.1 Area

The first method used to label a segment, is based on the calculation of the area inside the polygon versus the total area, using the ratio between these two features to assess the signal quality. Since the output is an image, the outline of the shape produced has to be determined, which can be done using for example an edge detector or the convex hull algorithm.

One very popular edge detector is the Canny algorithm, which works by applying a Gaussian filter to reduce noise, then computing the intensity gradient in four directions by tracking the pixel-to-pixel changes, and afterward applying thresholds. This creates a point cloud, the most relevant of which are then connected to form an edge [162].

The convex hull algorithm works by finding the smallest polygon that can encapsulate all the data points [163]. Figure 5.7 is a representation of a convex hull.

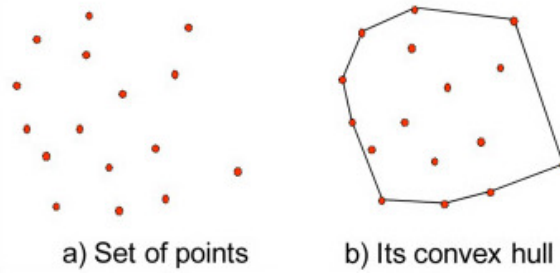


Figure 5.7: Convex hull representation. (a) The point cloud; (b) The resulting convex hull. Adapted from [163].

After the edges are detected, the next step is to calculate the area. Since not all the different heartbeats are aligned (i.e. in Figure 5.6 phase portraits it is possible to see this misalignment) and the shape itself is complex, this tends to cause the edge detection to produce many different small areas. The easier method to calculate the area of such shapes is to use the Jordan Curve Theorem.

To assess if a point is inside a polygon, the Jordan Curve Theorem states that a point is said to be inside it if any ray emerging from that point crosses the polygon's edges an odd number of times [164]. Figure 5.8 illustrates the principle.

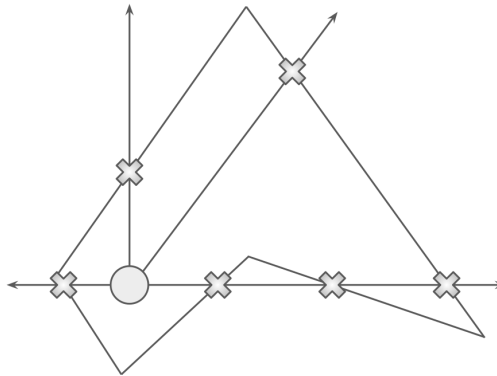


Figure 5.8: Example of the Jordan Curve Theorem, where a point is considered inside the polygon if a ray traced from it crosses its edges an odd number. As an example, multiple rays are cast from a point inside the polygon to show that independently of its direction, a ray from this point crosses the polygon's edges (gray crosses) an odd number of times. Based from [164].

With these two steps, it is then possible to calculate the ratio between the number of points inside and outside the shape produced, and then train a classifier to label the segments.

### 5.3.2 Image Descriptors

Another method to extract features from an image is to use descriptors, capable of (as the name implies) describing what is represented by the image using different features. For example, some edge detection algorithms use image gradients, i.e. direction changes in image intensity obtained by comparing the intensity of neighboring pixels, thus describing how the intensity of a picture changes using a feature.

Other popular image descriptors are image moments, typically used in shape recognition. These can be calculated using weighted averages of pixel intensity; and in theory, two very similar shapes will have approximately the same image moment [165]. Figure 5.9 is an example of how an image moment can be used to distinguish between different shapes.





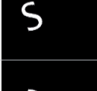

id	Image	H[0]	H[1]	H[2]	H[3]	H[4]	H[5]	H[6]
K0		2.78871	6.50638	9.44249	9.84018	-19.593	-13.1205	19.6797
S0		2.67431	5.77446	9.90311	11.0016	-21.4722	-14.1102	22.0012
S1		2.67431	5.77446	9.90311	11.0016	-21.4722	-14.1102	22.0012
S2		2.65884	5.7358	9.66822	10.7427	-20.9914	-13.8694	21.3202
S3		2.66083	5.745	9.80616	10.8859	-21.2468	-13.9653	21.8214
S4		2.66083	5.745	9.80616	10.8859	-21.2468	-13.9653	-21.8214

Figure 5.9: Example of Hu image moments for different shapes and transformations. There is a difference between the letter K and the letter S. However, when different transformations are applied, i.e. rotation, translation, scaling, etc., the moment's values stay very similar. Extracted from [166].

There are many different image moments, however, one popularized for pattern recognition is the Hu image moments [167], a set of seven different features that together allow for matching shapes that are invariant to translation, scaling, and rotation. Using these seven moments (included in Appendix D), an image classifier can be built to distinguish between a normal and an outlier segment.

These classifiers can range from methods based on simple distance metrics to advanced algorithms such as SVM. The following is a list with the classifiers used:

- **k-Nearest Neighbors (k-NN)** - algorithm uses the proximity between neighbor points to classify a new one, using the principle that similar data will be grouped together [168];
- **Random Forests** - classifier composed of an N amount of decision trees (hierarchical structures) [169];
- **K-Means** - algorithm that groups the data into different clusters without the need for a classification label [170];
- **SVM** - builds a classifier by finding a hyperplane that is able to separate the different classes [171];

### 5.3.3 Images as Input to an Artificial Neural Network

As opposed to the previous section (Sub-Section 5.3.2), where seven different features are extracted from the phase plot, in this approach, the resulting shape is used directly to train an ANN, more specifically a DNN. The use of DNN as the classifier results from it becoming the state-of-the-art for image classification, especially when compared to more traditional methods using the shape and color to extract features [172].

An ANN is a machine learning technique that is inspired by and resembles the human nervous system and the structure of the brain. It consists of processing units organized in input, hidden, and output layers. There are many different types of neural networks, but the common element is the perceptron, the computational analog to the human neuron. This unit takes the different inputs, attributes weights to them, sums, and then finally takes the result and applies an activation function, much like the physiological working of a neuron [173]. Figure 5.10 is a comparison between a human neuron and a perceptron.

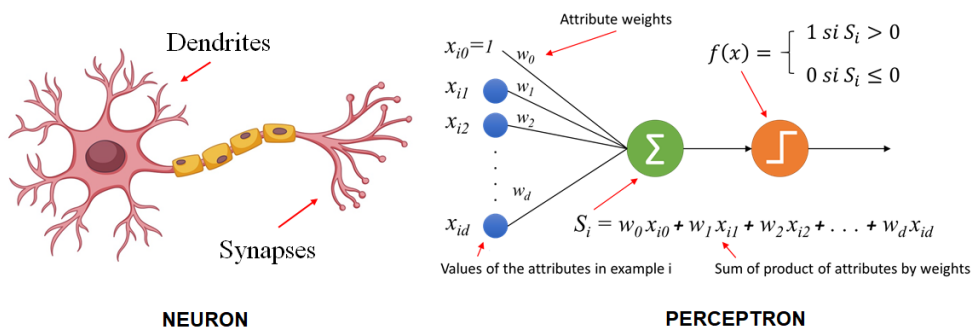


Figure 5.10: Comparison between the basic unit in the human nervous system and that of an ANN, a neuron versus a perceptron. A signal enters a neuron via the dendrites, or inputs in an ANN, which are weighted by the number of synapses that occur in a dendrite, or input weights in an ANN. Afterward, the input signal is processed in the nucleus of the neuron, or by the combination of a linear function and an activation function in a ANN, and finally, the stimulus is outputted. Extracted from [174].

DNNs are a family of networks that, as the name implies, have a higher (deeper) number of perceptron layers, which in turn allow for more complex and non-linear relations to be established between the input features and the output, without any manual design [173].

There are two major challenges when training a ANN. The first one is premature convergence, where the network can become "stuck" in a local minimum during its training, finding a good solution but not the best. The other is overfitting, where the network becomes a replicator of the input data, reporting very good results but has a low generalization ability, essentially learning the mapping between the input and output data and not the relation between them [173].

For image processing, one type of network that is frequently used is **Convolutional Neural Network (CNN)**, especially in computer vision and image recognition. These networks take cues from the human visual cortex, by employing different layers for different tasks, similar to the different regions of the visual cortex. A series of convolutions, subsampling, and normalizations are employed to simulate the image processing performed by the human cortex. For example, edge detection can be performed by using a Sobel Kernel and performing a convolution with it [173]. Figure 5.11 is an example of a CNN for image classification, in this case character recognition.

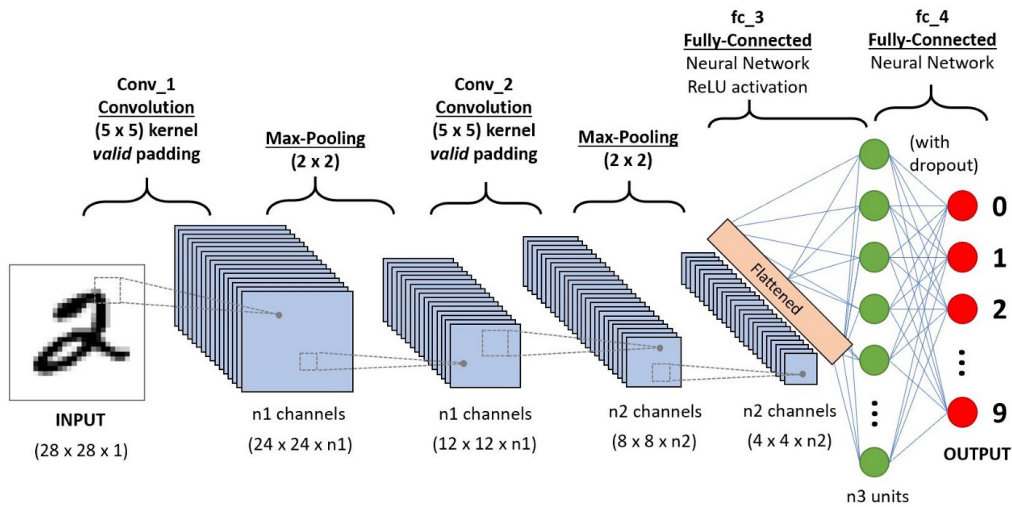


Figure 5.11: Example of a CNN for character recognition. It is possible to observe the different basic build blocks of a CNN in action, with multiple convolution layers to detect features, pooling layers to reduce the image size, and the output stage. Extracted from [175].

Although there is no standard network for noise detection using a phase portrait in ECG, this can be seen as a challenge similar to a character recognition task. Therefore, a simple architecture based on networks used in the MNIST (and also similar to Figure 5.11)<sup>6</sup> problem was deployed.

<sup>6</sup>Widely used database for handwritten number recognition



The model starts with two convolution layers, then applies a max pooling layer, before dropping out 25% of the nodes. Finally, it passes through a fully connected layer, before dropping out 50% of the nodes and outputting the probability of the two classes using a softmax activation function.

The convolution layers are the basis of a [CNN](#), acting as a filter to highlight and automatically extract/create features. The max pooling layer helps in reducing the overall size of the images resulting from the convolutions since it takes (in this case) the maximum value of a 2x2 grid. Finally, the dropout layer help avoids overfitting, by randomly selecting nodes to be turned off before the next training passage. Figure 5.12 is the graph representation of such network, taking a 320x320 pixel phase plot as the input and outputting if the plot corresponds to a clean signal or a noisy one.

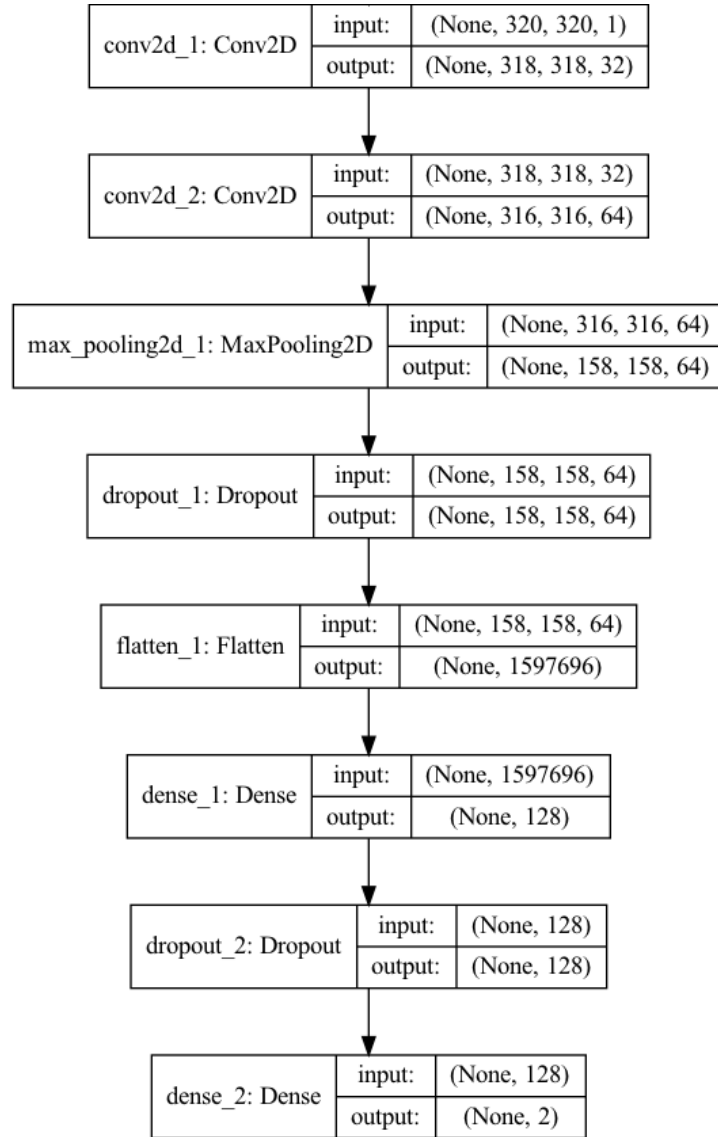


Figure 5.12: [CNN](#) model graph. At the input the network takes a 320x320 plot, and applies the two convolution layers before passing the features to a fully connected [ANN](#).



## 5.4 Results of each technique

This section is divided into 4 subsections, starting with the database used to train the different machine algorithms, then the results for each of the techniques used. A general discussion about the results obtained using the different methods is presented in the next section.

### 5.4.1 Database

The database selected to train and test the performance of each technique was the one provided for the 2017 PhysioNet Challenge "AF Classification from a Short Single Lead ECG Recording: The PhysioNet/Computing in Cardiology Challenge 2017" [176]. This database contains 8528 recordings of single lead ECG, sampled at 300Hz, with their length ranging from 9 to 60 seconds.

From all the recordings, only the ones classified as Normal and Noisy were used, in order to assess the performance in the best possible conditions. Therefore, 5076 records classified as good and 279 as noise can be used<sup>7</sup>. Since this database was not intended primarily for noise vs. normal distinction, there is a significant class unbalance. However, it is very difficult to find a publicly and widely used database for that purpose.

Of the 5355 records, the majority of them have a duration of approximately 30 seconds (Figure 5.13), a long period when assessing the signal's quality of the whole segment, i.e. mapping the complete segment to a phase portrait. For example, Sub-Figure 5.14a is a 30-second ECG rhythm strip labeled as Normal in the database. However, there is a big noise event at the beginning of the ECG rhythm strip (first 5 seconds of the recording), which in turn completely distorts the phase portrait. By comparison, the 12-second strip presented in Sub-Figure 5.14b is labeled as Noisy. Visually comparing both phase portraits, they appear to be very similar, which may affect the suggested approach performance. Sub-Figure 5.14c is a 30-second rhythm strip labeled as Normal, with a similar (albeit inverted) phase portrait to those reported in Figure 5.6.(c).

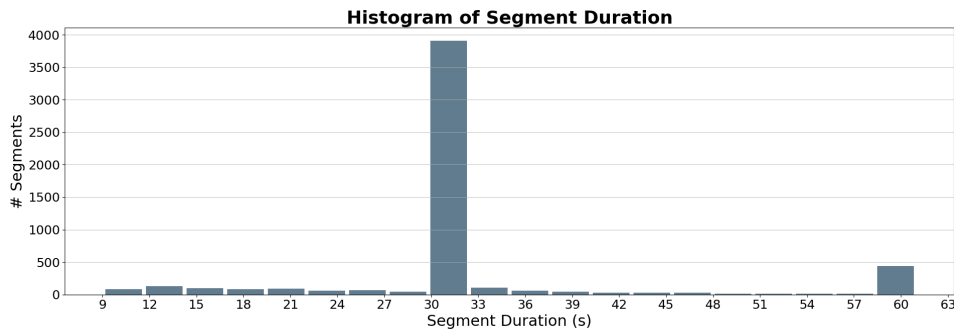
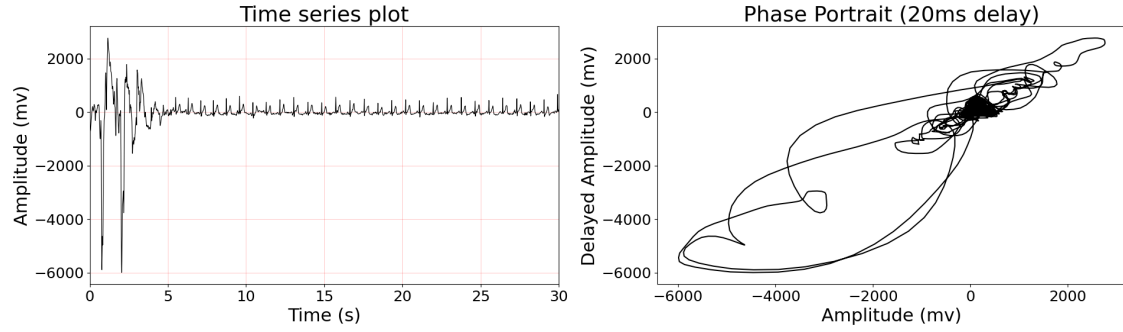
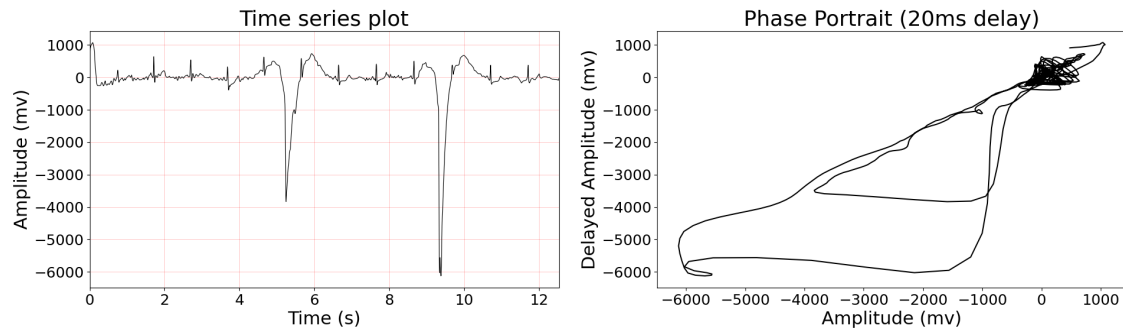


Figure 5.13: Histogram of segments' duration, with the majority of segments having approximately 30 seconds.

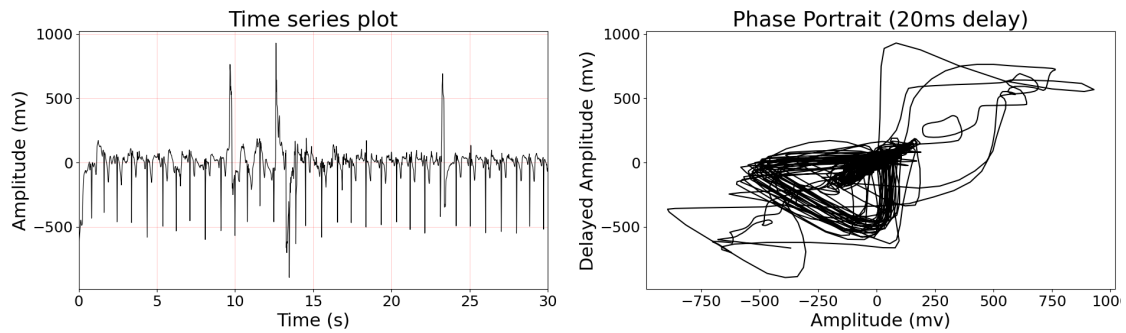
<sup>7</sup>Using the REFERENCE-v3.csv file present in the challenge web page [176].

**Incorrect Label (Normal) - File A03922.mat**

(a) Incorrectly labeled Noise ECG rhythm strip. In the first seconds of the recording, there is a noisy segment that completely distorts the phase portrait. However, since it is a large time window, the creators of this database labeled this segment as Normal.

**Noisy Example (Noisy) - File A00139.mat**

(b) ECG rhythm strip labeled as Noisy in the database.

**Inverted Lead (Normal) - File A04567.mat**

(c) ECG rhythm strip labeled as Normal in the database. Notice the inverted QRS complex, which indicates lead reversal (or bad lead placement) but no indication is given regarding this situation.

Figure 5.14: Example of different signals from the database and the effect of segment duration and noise in ECG strip classification.

To avoid some of the problems associated with having longer period rhythm strips, only segments with a duration of 15 seconds or less were chosen, resulting in 247 ECG strips. Of those, 173 are labeled as Normal, while the remaining 74 are labeled as Noise. Another benefit of using segments with a shorter period is lowering the class unbalance, going from 5% to 30% of the data being labeled as Noise.

Another database that could have been used was the 2011 Physionet Challenge "Improving the Quality of ECGs Collected using Mobile Phones" [153], however, this is a multi-lead database with a single reference, in other words, the labeling process reflects the signal quality as a whole, without discriminating the per channel classification, falling outside of the scope for this thesis.

### 5.4.2 Area

The usage of the area as a feature for detecting the presence of outlier passed through three different stages, namely finding the best method for calculating the area, followed by an initial test of classifier performance, and finally abandonment. Although no real results were obtained, i.e. no public available dataset was tested using this approach, the approaches and challenges encountered when implementing this method are worth discussing.

Regarding outline detection, two different techniques were used: the convex hull and the Canny edge detection algorithm. Figure 5.15 shows the delay plot using a test ECG signal, and thus the polygon these algorithms will try to outline.

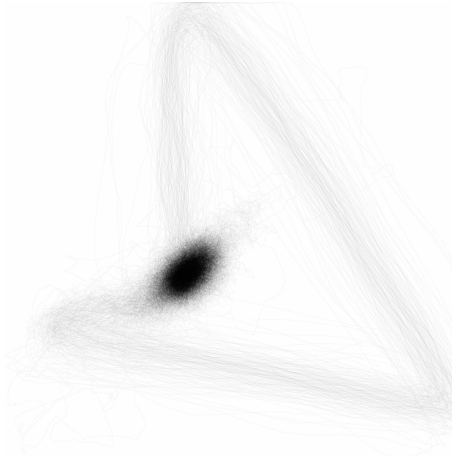


Figure 5.15: Example of a phase portrait using a 20 milliseconds delay.

Starting with the convex hull approach, this was the simplest of the two since the resulting polygon has a more simple shape (e.g when comparing the convex hull shape in Figure 5.16 with the shape resulting from edge detection, represented in Figure 5.18), being easier to calculate the number of internal points. Furthermore, at this stage, the idea was to develop a template of what a normal signal should look like in order to count the number of points that fall within the said template (presented in 5.16).

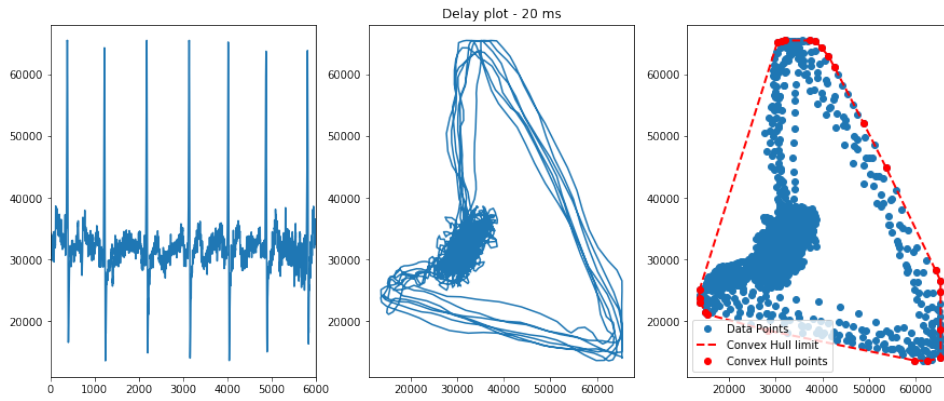


Figure 5.16: Convex hull template using a 20 milliseconds delay.

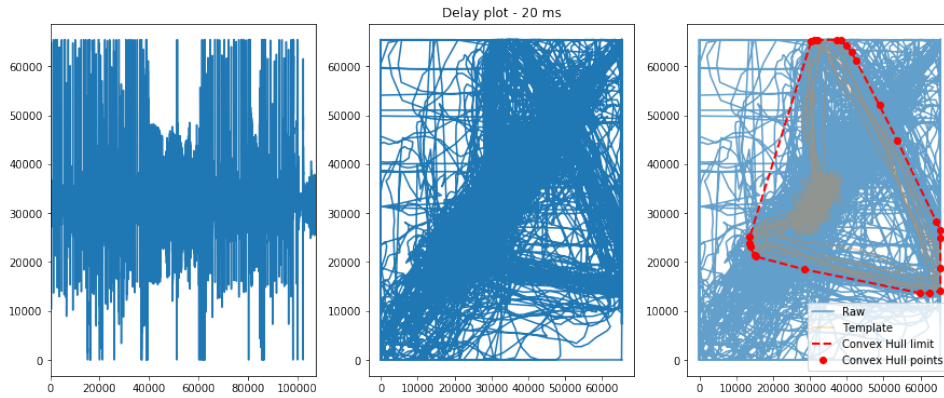


Figure 5.17: Example of a noisy segment using the convex hull template.

The idea was then to use this template to count the number of points that were inside the convex hull and assess if the number was higher than a threshold, e.g. 70% for medium quality signals and 90% for good quality signals<sup>8</sup>. Figure 5.17 depicts a signal segment classified as noisy when using a 70% threshold for the minimum number of points within the convex hull.

One major drawback with using the convex hull in this approach is that the shape of the polygon formed by this algorithm is too broad, encompassing many different areas of the phase plot where the signal should not be expected in normal conditions. To try and solve this problem, an edge detection algorithm was thus employed to better outline the polygon drawn by the delayed phase plot.

To detect the edges, the Canny algorithm was used<sup>9</sup> with a sigma of 25. This edge detector is one of the most used, and the threshold value was selected by empirical experimentation, being chosen the value that resulted in a better outline detection.

<sup>8</sup>These thresholds were defined by empirical experimentation during the initial tests.

<sup>9</sup>The algorithm was not implemented. A Python library with the implementation was used by calling the *canny* function from the *skimage* library.

Afterward, the ratio between the points inside and outside the shape can be done by performing a Monte-Carlo simulation, placing random points on the plot, and checking if the point is within the polygon using the Jordan Curve Theorem. Figure 5.18 illustrates such simulation.

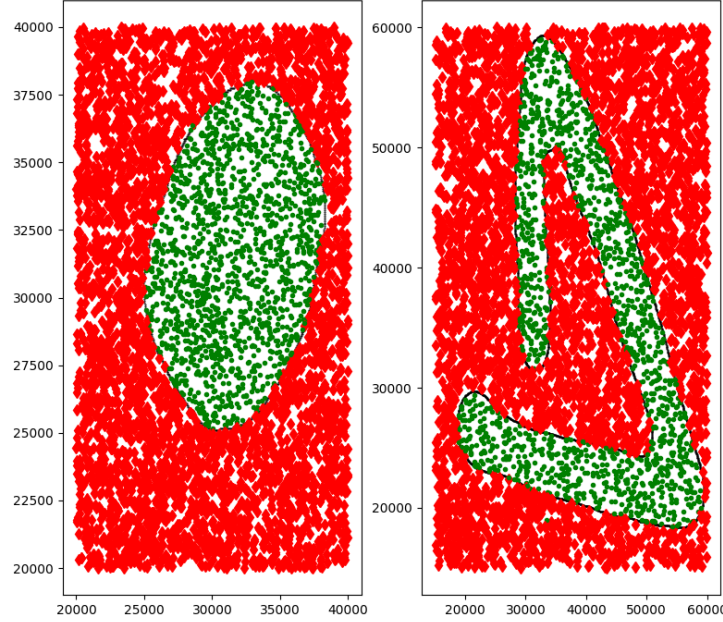


Figure 5.18: Result of edge detection and Monte-Carlo simulation, where points are placed randomly in the image and their position is assessed to be inside or outside the polygon. The two different shapes correspond to all waveforms except the QRS complex (left), and the QRS complex (right).

There are two major drawbacks to this approach, the difficulty in consistently finding the edges of the image, and also calculating the area within the polygon. The task of calculating the area within was also very computationally demanding, since the polygon formed by this approach is not a simple shape, requiring many edge crossing detections, which in turn leads to an increase in complexity.

Another major problem of this approach is scale, since the shape is very dependent on the amplitude of the input signal, more specifically the ratio between the device range of measurement and the amplitude of the QRS signal. Smaller amplitudes will produce a smaller polygon, which in turn will have a smaller area. This makes the change of area dependent not only on the noise and its effect on the final shape, but also on the original amplitude of the QRS signal compared to the device measuring range or the type of electrodes used. To tackle this problem, normalization of the segment could help, however, spurious spikes could interfere with said process, thus resulting in small polygons nevertheless.

Although no tangible results were presented in this section, some major challenges were identified, such as signal scale, which influenced the choices of the next techniques used to solve the problem at hand, the search for outlier segments in the ECG waveform.

### 5.4.3 Hu Image Moments

This subsection will first provide a summary of how the data was prepared and afterwards used by each of the classifiers, with their results presented. In the end, a brief comparison between different delays closes this subsection.

#### Data Preparation and Estimator Parameter Tuning

For each file, a delayed phase portrait was created by plotting on the x-axis all the value except the last  $n$  samples (0 to  $length - delay$ ), with  $delay$  being the delay, and in the y-axis all the values starting at the index  $delay$  ( $delay$  to  $length$ ). With the data plotted, the grayscale image was obtained and saved. Afterward, for each of the delayed phase plots, their Hu moments were obtained<sup>10</sup> and saved in order to build the different classifiers.

Algorithm 2 presents a more visual interpretation, where *ECG* is the waveform in study,  $n$  is the last sample, and the *delay* is the millisecond delay converted to an index. The square brackets represent a subset of the data.

---

**Algorithm 2:** Building a delayed phase portrait.

---

**Input:** ECG rhythm strip

**Result:** The delayed phase portrait

**begin**

$n \leftarrow ECG\ length$

$delay \leftarrow$  Delay converted to an array index

/\* E.g. for a signal sampled at 250Hz and a delay of 20ms, delay will  
be 5 samples \*/

$x\ axis \leftarrow ECG[0 : n - delay]$

$y\ axis \leftarrow ECG[delay : n]$

Draw image and save it

---

The Normal and Noise segments were then all joined in one array to be divided into a train (60%), test (20%), and validation (20%) subsets<sup>11</sup>, in order to ensure that each of the classifiers uses did not suffer from overfitting. This splits were done with a fixed random state in order to replicate the results between techniques.

Also, when possible, the parameters used for each of the estimators were optimized using an automatic function that runs through all these different parameters<sup>12</sup>. For example, in the *k-NN* classifier, the number of neighbors, the distance metric, and the weights used in the prediction can be optimized using this technique.

---

<sup>10</sup>Using the Open CV HuMoments function.

<sup>11</sup>Using the *train\_test\_split* function from the Python package sklearn, with the stratify option set as true. This option ensures that both classes appear in all three data splits, by maintaining the same ratio between classes in each of the splits.

<sup>12</sup>Using the *GridSearchCV* function from the Python package sklearn.

Table 5.1: Example of the output of a grid-search optimization using a [k-NN](#) classifier and the following parameter to be optimized: the number of neighbors, the distance metric, and the weights. The mean test score is the average from the 10-fold cross validation accuracy (based on a scoring metric, such as F1-score) used to find the best combination of parameters.

Rank	Distance Metric	Number of Neighbors	Weights	Mean Test Score (Standard Deviation)
1	Cosine	13	Uniform	0.69 (0.09)
2	Cosine	15	Uniform	0.69 (0.10)
3	Cosine	9	Uniform	0.68 (0.10)
.....				
142	Euclidean	7	Distance	0.50 (0.15)
143	Minkowski	7	Distance	0.50 (0.15)

All of these combinations will be used to make a table similar to Table 5.1, where a total of 143 combinations were analyzed.

For each combination of parameters, the models are evaluated using cross-validation (in this case, using 10 folds), and their performance is calculated using one of the following scoring metrics: accuracy, F1-score, or the F1-score macro average. The F1-score is typically used for binary classifications, combining the precision and recall of a classifier into a single metric, being a good method for comparing classifiers. The macro average is similar to the latter but does not take into account any class unbalances, being an unweighted average of the scores.

Finally, for the Random Forest<sup>13</sup> and SVM<sup>14</sup> classifiers, the functions used to build these estimators had the option to set a weight for each class in the dataset. This option, class weight, was set to "balanced", which will automatically adjust each class's weights inversely proportional to their frequencies, helping to counter the unbalance of the dataset used.

## Results

Table 5.2 contains the results for the test and validation sets using the different estimators trained employing the Hu image moments, using a 30-millisecond delay to construct the phase portraits. These represent the best models found using the automatic parameter optimizer<sup>15</sup>, producing three sets of results<sup>16</sup>, one for each scoring metric used in assessing the model performance by the optimizer. Table E.31 contains the results using two other delays (20 and 40 milliseconds).

<sup>13</sup>Using the *RandomForestClassifier* function from the Python package sklearn.

<sup>14</sup>Using the *SVC* function from the Python package sklearn.

<sup>15</sup>Trained on 60% of the data and using 10-fold cross-validation to discover the best model.

<sup>16</sup>Except for the K-Means.



Table 5.2: Hu image moment’s estimators results, using a 30 millisecond delay. For each dataset (Test and Validation), the best model’s (found using the parameter optimizer) F1-score average and macro average (averaging the unweighted mean per label) are reported.

Optimizer Scoring Metric	Test set		Validation set	
	F1 Accuracy	F1 Macro Average	F1 Accuracy	F1 Macro Average
<b>k-NN</b>				
Accuracy	0.74	0.70	0.84	0.82
F1	0.74	0.70	0.84	0.82
F1 Macro Average	0.74	0.70	0.84	0.82
<b>Random Forest</b>				
Accuracy	0.72	0.65	0.88	0.84
F1	0.72	0.65	0.86	0.81
F1 Macro Average	0.72	0.65	0.84	0.79
<b>SVM</b>				
Accuracy	0.70	0.64	0.72	0.62
F1	0.70	0.64	0.72	0.62
F1 Macro Average	0.70	0.64	0.72	0.62
<b>K-Means</b>				
	0.62	0.46	0.66	0.52

Starting with the **k-NN**, this was one of the best estimators, getting the highest F1-score accuracies and macro averages for the Test set (20% of the data that was not used in training), with a score of 0.74 and 0.70 respectively. From the F1-score of each class<sup>17</sup> (0.81 for the Normal class and 0.58 for the Noise, in Table E.4b) and the confusion matrix (Table E.4a), there is a high percentage of Noise labeled segments that are considered Normal. At the same time, there is also a substantial number of Normal labeled segments that are misclassified. Though, when tested with the Validation set (the remaining 20%), these results improve, increasing the F1-score accuracy and macro average to 0.84 and 0.82. This is due to higher class F1-score (0.88 and 0.75, Table E.4b), with more segments correctly classified in both classes, an effect also visible in the confusion matrix (Table E.4a).

The best results out of all the estimators come from the Random Forest classifier, achieving 0.88 and 0.84 for the F1-score accuracy and macro average (respectively, and using accuracy as the optimizer scoring metric) using the Validation set. These results<sup>18</sup> are due to a very high F1-score in the Normal class (0.92, Table E.13b) and a relatively good one for the Noise class (0.77, Table E.13b). For the Test set, the results are similar to those obtained with the **k-NN** estimator, with the F1-score accuracy and macro averages being lower (0.72 and 0.65) using the Random Forest classifier.

<sup>17</sup>When using a 30 millisecond delay and *accuracy* for the optimizer’s scoring metric.

<sup>18</sup>When using a 30 millisecond delay and *accuracy* for the optimizer’s scoring metric.



The SVM classifier had the most consistent results between the Test and the Validation set, being almost identical. However, their performance was mediocre compared to the other two techniques, achieving a maximum F1-score accuracy and macro averages of 0.72 (Validation set) and 0.64 (Test set), lower than those obtained with the other two techniques. Analyzing one of the confusion matrices<sup>19</sup>, it is possible to observe a very high rate of misclassified noise segments in both sets (Table E.22a), leading to a low F1-score for this class (lower than 0.5, table Table E.22a).

Out of all 4 estimators, K-Means had the worst results, with a F1-score accuracy and macro averages of 0.62 and 0.46 for the Test set, and 0.66 and 0.52 for the Validation set. Looking at the Confusion Matrices<sup>20</sup> (Table E.29a), it becomes apparent the reason for such low scores, with almost no Noise segments being labeled as such, with 2 out of 15 for the Test set and 3 out of 15 for the Validation (Table E.29a), leading to Noise class F1-scores of 0.17 and 0.26 (Table E.29b). On the other hand, the F1-scores for the Normal class (0.75 and 0.78) are on par with those obtained using the other estimators.

The amount of time used as the delay tends to have some effect on the results (Table E.31). For the k-NN classifier, the best results for the Test set are obtained when using a 20 ms delay, while 30 ms is the best for the Validation set. Nevertheless, the results are very similar, with the metrics differing by 6% at most. Using the random forest classifier, the 20ms delay has the worst Test set F1-scores macro averages, being around 10-15% lower for some optimizers. On the other hand, using a 40ms delay leads to lower performance in the Validation set.

The results from the SVM classifier are very similar for all the different delays, with the results using the 40ms delay being slightly better than those using a 30ms. Finally, there is the K-Means clustering, the best results are obtained when using a 40ms delay. Nevertheless, these better results still place this method as the worst.

From all three delays, 30ms is a tradeoff between having either better results in the Test set (40ms) or the Validation set (20 ms). Table 5.3 are the different F1-scores for the Noise class in the two best classifiers, the k-NN and Random Forest, using the three different parameter optimizer's scoring metrics (Accuracy, F1-score, and F1 Macro Score).

Table 5.3: F1-Scores for the Noise Class using k-NN and Random Forests classifiers. This results include the different delays and using the three different parameter optimizer's scoring metrics (Accuracy, F1-score, and F1 Macro Score).

	Delay	Test (20 %) optimizer scoring metrics				Validation (20 %) optimizer scoring metrics			
		Accuracy	F1-score	F1 Macro Score	Mean	Accuracy	F1-score	F1 Macro Score	Mean
k-NN	20ms	0.38	0.62	0.62	0.54 ± 0.11	0.50	0.75	0.75	0.67 ± 0.12
	30ms	0.58	0.58	0.58	0.58 ± 0.00	0.75	0.75	0.75	0.75 ± 0.00
	40ms	0.53	0.57	0.57	0.56 ± 0.02	0.62	0.65	0.65	0.64 ± 0.01
Random Forest	20ms	0.36	0.30	0.37	0.34 ± 0.03	0.71	0.69	0.69	0.70 ± 0.01
	30ms	0.50	0.50	0.50	0.50 ± 0.00	0.77	0.72	0.69	0.73 ± 0.03
	40ms	0.58	0.53	0.53	0.55 ± 0.02	0.62	0.62	0.60	0.61 ± 0.01

<sup>19</sup>Using a 30 millisecond delay and *accuracy* for the optimizer's scoring metric.

<sup>20</sup>When using a 30 millisecond delay

#### 5.4.4 Image as Input to an Artificial Neural Network

##### Data Preparation

As previously mentioned, there is a class unbalance between the two labels of the dataset. To even the number of elements in each label, the least represented class, Noise, was oversampled. This technique was chosen instead of undersampling for two reasons: the number of Noise labeled samples, and the difference in the number of elements between the two (a difference of 100 elements in a total of 247, almost a 2:1 ratio). Thus, this class was resampled to have the same amount of samples as the Normal class. Another step in preparing the data before being used to train the CNN models was reshaping the saved phase portraits from a single row image (1 x 102400 pixels) to a squared one (320 x 320 pixels).

Due to the amount of data, the network was trained in batches of 32 images. To train the models, the network previously shown in Figure 5.12 (and based in character recognition CNNs) was implemented using the Python library Keras. and fitted with the following parameters:

- Loss function - Cross-entropy<sup>21</sup>;
- Optimizer - Adadelata<sup>22</sup>, with the following parameters:  $learning\_rate = 0.001$ ,  $\rho = 0.95$ ,  $\epsilon = 1e-7$ ;

##### Results

Table 5.4 contains the results for the test and validation sets using three different delays for the model depicted in Figure 5.12.

Table 5.4: CNN estimators results for different delay. For each dataset (Test and Validation), the best model's F1-score average and macro average (averaging the unweighted mean per label) are reported.

Delay Used	Test set		Validation set	
	F1 Accuracy	F1 Macro Average	F1 Accuracy	F1 Macro Average
<b>CNN</b>				
20ms	0.68	0.60	0.74	0.67
30ms	0.72	0.65	0.72	0.64
40ms	0.70	0.68	0.84	0.82

<sup>21</sup>Using the *CategoricalCrossentropy* function from the Python package Keras.

<sup>22</sup>Using the *Adadelata* function from the Python package Keras.

The results obtained by this network are similar to those obtained using the Hu image moment estimators, with an F1-score accuracy of around 0.70 and an F1-Score Macro Average of 0.65. Furthermore, the effect delay has on these results seems to be the same as with the Hu image moment estimators, having small variations between them (around 2-5%), with the 30-millisecond delay being a tradeoff between both the results of the Test set and the Validation set.

However, upon a closer inspection of the confusion matrices and classification reports (Tables E.32, E.33, and E.34), the results using the 40-millisecond delay appear to produce better results. The F1-score for the Noise class is higher using this delay compared to the others (Table E.34b), which is mainly due to higher precision and recall scores when using this delay. The results for the F1-scores of the Noise class are summarized in Table 5.5.

Table 5.5: F1-Scores for the Noise Class using CNN model.

	Delay	Test (20 %)	Validation (20 %)
CNN	20ms	0.43	0.47
	30ms	0.50	0.46
	40ms	0.59	0.75

## 5.5 Discussion

The results obtained using delay phase plots to detect outliers, namely noise, are positive and promising, although some work still needs to be done to improve its performance. Between the two approaches that were explored in more detail, the Hu image moments and an image as input to a CNN, the results show that using the Hu image moments coupled with a k-NN produces the best results.

Regarding the models' Normal class labeling performance, all the estimators (regardless of using the Hu image moments or the CNN model, and for all the delays used) got reasonable F1-Scores, of around 0.80. For the Noise class labeling performance, the best F1-Scores when using the Hu image moments were obtained when using a 30-millisecond delay (Table 5.3), while the CNN model produces better results using a 40-millisecond delay (Table 5.5). The CNN model got very poor results when using the other two delays (<0.50). However, when using a 40-millisecond delay, the results become very similar to those when using a k-NN or a Random Forests classifier with the Hu image moments. These results were around 0.60 for the CNN and the k-NN classifiers in the Test set, and 0.70-0.75 in the Validation set.

The F1-scores of each label led to reasonable F1-score and F1 Macro Averages for the trained models. The Random Forest classifier achieved the highest score of 0.72 and 0.86 in the Test and Validation sets, respectively, using a 30-millisecond delay (Table 5.2). For the k-NN classifier, it scored a 0.74 and 0.84 in the Test and Validation sets, respectively, using a 30ms delay (Table 5.2). Finally, the CNN model scored a 0.70 and 0.84 using 40ms delay, Table 5.4.

Table 5.6: Example of models trained using the same (complete) database.

Authors	Features	Classifier	F1-Score Normal label	F1-Score Noise label
Goodwin et al. [177]	Morphology, templates and HRV features	Ensemble classifier	0.91	0.66
Xiong et al. [178]	ECG waveform	CNN	0.90	0.60
Yazdani et. al [179]	Morphology, statistical, and HRV features	Ensemble classifier	0.82	0.57
Zabihi et. al [180]	491 features, reduced to 150	Random forest	0.90	0.61
Behar et. al [181]	Morphology, HRV, and others	SVM	0.90	0.65

These results are acceptable when compared to other models which used the same database (Table 5.6). The target of those works was not exclusively to distinguish between Normal and Noise labeled segments, but rather to train models capable of classifying segments showing signs of Atrial Fibrillation. Furthermore, these models were trained using the entire database, while the models and results presented in this work were only trained using segments shorter than 15 seconds that were labeled as either Normal or Noise. Therefore, the results should not be used as a direct comparison, but rather serve as an indication of the future potential of this methodology.

The results presented in these examples are very similar between themselves and to the results obtained by the proposed methodology, where the Normal segments have a slightly better performance than the proposed models, with a Normal class F1-score of around 0.90 vs the 0.80 of the proposed models. In the Noise class scores, the results obtained by the proposed model are very similar, with the examples presented in Table 5.6 having an F1-score of 0.60 and the ones from the proposed methodology scoring similar results.

In [177] and [179], the authors use a multitude of morphological references, templates, and HRV features to train an ensemble classifier and make their predictions. A similar approach was used by Behar et. al [181], where these features were used to develop a 3-stage classifier (using a SVM for each of the stages), to first distinguish between Normal segments and the rest of the labels (Atrial Fibrillation, Other, and Noise), followed by Atrial Fibrillation vs the remaining two, and in the end, Other vs Noise. In [180], the authors hand-crafted 491 features, with the best 150 selected to train a random forest classifier. All of these previous works use a much higher number of features to classify the segments than the proposed approaches, while the F1-score of the Noise label for each of these works is similar to the results obtained. However, these works used the whole database in training their models and also had to distinguish between the other 2 classes, so the comparison has to be done with this in mind. The only approach in the examples that is similar to one of the proposed approaches, is the work done by Xiong et al. [178], where the ECG rhythm strip is fed directly in a CNN model to be classified. Nevertheless, the results obtained by this approach had similar results to those previously discussed.

One of the reasons that might help to explain the mediocre results obtained when trying to distinguish the Noise label from the other might be the dataset itself. One of the authors of the examples in Table 5.6 stated that the highly unbalanced (even with label modification) and the imperfect labeling might explain why the Noise label F1-score was not included in the final scoring system of the challenge [179], indicating some problems with the dataset itself. Even when using only segments that were shorter than 15 seconds, the Noise class represented only 30% of the subset of data, which even after the balancing methodologies applied in the different classifiers, might not be enough percentage to thoroughly distinguish between the two classes.

Furthermore, the incorrect labeling also influences the results. This was also one of the reasons to adopt 15 seconds threshold for each segment, previously mentioned in Sub-Section 5.4.1. As an example of own an incorrect label influences the performance of the proposed methodology, Figure 5.19 contains a raw ECG example that is a true positive (TP), a fake positive (FP), a fake negative (FN), and a true negative (TN), using a  $k$ -NN classifier with a 30-millisecond delay. Figure 5.20 are their phase portraits.

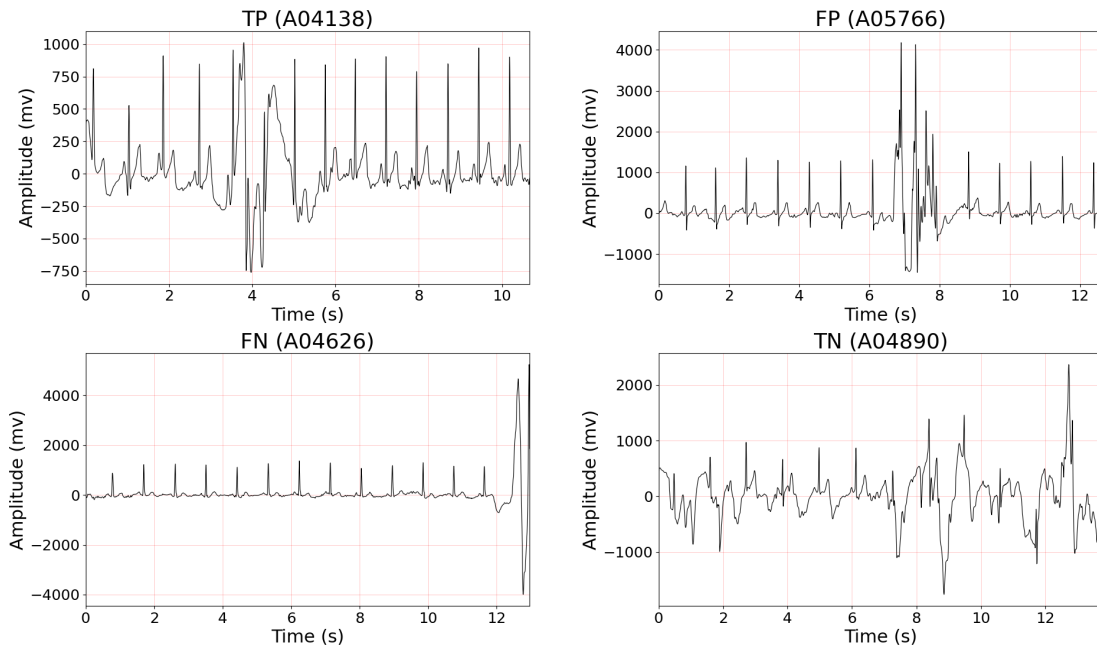


Figure 5.19: Example of correct and incorrectly classified rhythm strips, using an  $k$ -NN classifier and a 30 millisecond delay. TP: True positive; FP: fake positive; FN: fake negative; TN: true negative.

Starting with the fake negative, the artifact present in the last second of the segment leads to the phase portrait being completely altered. This rhythm strip was labeled as Normal in the dataset, however, due to the distortion of the phase plot, it was classified by the model as a noisy signal. Without the last 2s of data, this signal would be labeled as Normal.

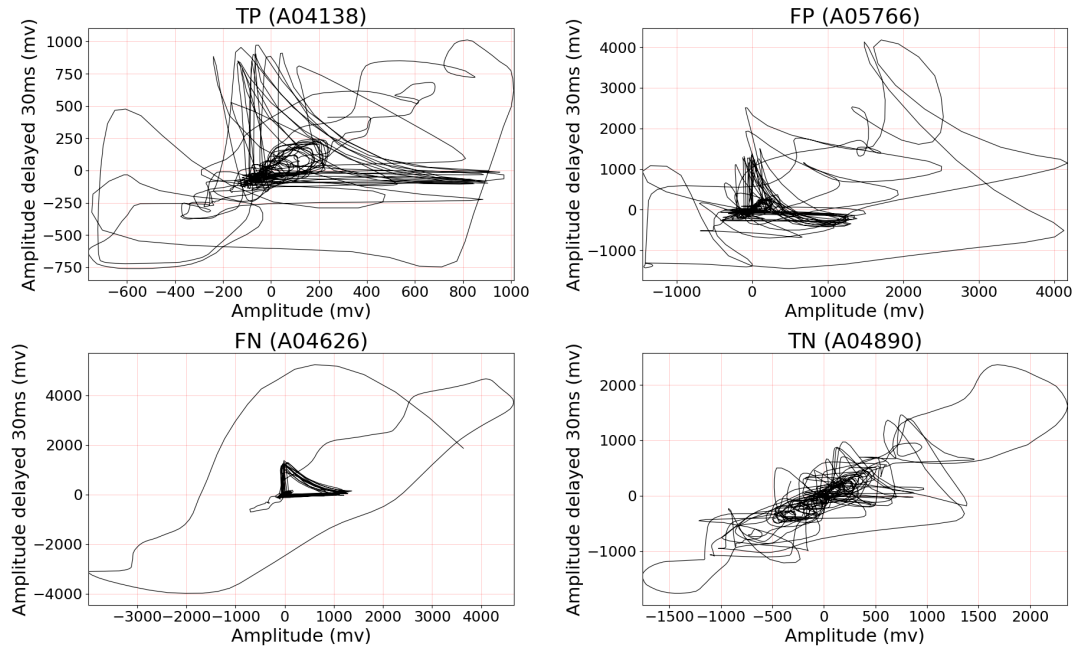


Figure 5.20: Phase portraits of the rhythm strips in Figure 5.19. TP: True positive; FP: fake positive; FN: fake negative; TN: true negative.

On the other hand, the distortion present in the fake positive example was not enough to completely distort the phase plot, which led it to be classified as a Normal signal. However, except for a 2-second window in the middle of the signal, the ECG rhythm strip is indeed a clean one, leading to inconsistent labeling of the signals. This is further confirmed when looking at the true positive signals, exhibiting a similar artifact with the same approximate duration (albeit with a less pronounced amplitude swing), but unlike the fake positive trace, this was labeled as Normal.

Nevertheless, the results obtained show that this approach might be useful in artifact detection for small duration segments (<15 seconds), requiring either only 7 features to describe the segment when using the Hu image moments, or using the segment itself as an input to a CNN model. However, a major drawback of this approach is when it is used in larger segments, being very sensitive to large amplitude swings, labeling the entire segment as Noise.

## 5.6 Summary

Throughout this chapter, the problem that is noise and how to identify it in an ECG trace was explored. This is a non-trivial problem, since some forms of noise are similar to the signal itself, especially in the case of physiological events, while others can mimic valid signals.

There are four major noise sources in an [ECG](#), namely: motion artifact, baseline wander, muscle activity, and power-line interference. To assess the quality of the signal, the first step is typically based on a QRS complex detector, from which other metrics can then be constructed. These techniques can be divided into four major groups, time-domain, frequency-domain, trend-based, and decision rules, with the latter normally being a combination of the first three.

A new approach was presented in this chapter based on the phase portrait of the [ECG](#), which can be obtained by using delay mapping, plotting the signal against a delayed version of itself. To develop this technique, a publicly available database was used, however, the number of Noise samples was highly unbalanced compared to those labeled as Normal, while also having different duration (between 9 and 60s). To this effect, only segments shorter than 15 seconds were used in the development of this technique.

Furthermore, the different sizes of the samples lead to some being labeled as Normal even though there was a clear noise event within the sample.

Different approaches were tried using the phase portrait, with one of them being abandoned fairly early in the development, based on the total area of the point contained by the polygon drawn by the phase portrait.

The second approach was based on the Hu image moments, a widely used image descriptor in shape recognition. With this approach, different estimators were tried, with varying degrees of success, with their performance being promising, in line with some of the state-of-art models (albeit in dissimilar experimental conditions). These estimators were able to classify the Normal segments with a high F1-score (approximately 0.90) but had lower results for the Noise class F1-score (approximately 0.60-0.70).

The final approach was using the phase portrait as an image input of a [CNN](#), leveraging the power of this type of networks in computer vision problems to label the segments. Since no standard network exists for this problem, inspiration was drawn from networks used in character recognition. The approach had results very similar to those obtained by the Hu image moments.

To assess if the delay value was a major influence on the results obtained by these estimators, this approach was tried using 20, 30, and 40 milliseconds delays. The delay had an effect in Noise class F1-Score, with the Hu image moment estimators performing best when using a 30 millisecond delay, and the [CNN](#) models with a 40-millisecond one.

A better database needs to be found to properly assess the performance of this approach since the results obtained do not allow for a clear decision if this technique does or does not yield any potential as a robust noise estimator. Nevertheless, the results obtained were similar to those obtained by the others using the same database (although with some differences in experimental conditions).



## CONCLUSION

Being the last chapter in this thesis, there is a reflection on the work developed throughout, starting with an overview of each chapter, then an outline of the main contributions in the different fields, future work, and a summary of work done in other fields.

### 6.1 Overview

In Chapter 1, the main motivation for this thesis was laid-out. Mortality caused by [Cardiovascular Disease \(CVD\)](#)s, the major leading cause of death worldwide, can be reduced by investing in better prevention and diagnosis techniques and devices. An exam widely used to this effect is [Electrocardiogram \(ECG\)](#), and its incorporation in mobile devices allows its use more pervasively. With more pervasive devices, the opportunities for early detection of potentially life-changing or even life-treating disorders are increased and thus could have a positive effect on the mortality numbers of these types of diseases. On the other hand, the [ECG](#) can be used not only to study the heart but also the inner working of other systems in the body through their effects on the [Autonomic Nervous System \(ANS\)](#) and subsequently on the inter-beat intervals. These solutions, pervasive and focused on continuous monitoring, can reach a broader audience if designed using electrodes embedded in a daily use device rather than being attached directly to the body. However, off-the-person solutions have a major drawback, the increased sensitivity to noise, mainly due to the difficulty in maintaining constant contact with the electrodes.

In Chapter 2, an overview of the rich story of the [ECG](#) is presented. The [ECG](#) is a technique that started with a machine that occupied an entire room, needing five people to operate it, and used buckets full of electrolytic solution as electrodes. It has evolved throughout the last century to devices worn on the patient's wrists or small patches attached to the chest, capable of recording an [ECG](#) trace with very high quality and reliability. This technique is very useful for clinicians to either analyze and make a decision in the present, or study what happened in the past, based on the characteristic morphology of a normal [ECG](#). Nowadays, the [ECG](#) is one of the key tools in emergency rooms for fast triage, or in clinicians' offices to detect cardiac disorders.

Another tool that can be used by clinicians is [Heart Rate Variability \(HRV\)](#), especially in analyzing long-term changes in the cardiac function. This technique focuses on changes in the inter-beats intervals, establishing a relation between those and the [ANS](#) that regulates them. With this relation, clinicians are able to predict the evolution of some disorders, or at least have a more probable outcome, with risk stratification grouping as an example of a practical application of this technique, by using metrics extracted from the study of these variations. The ability to correlate changes in the [Heart Rate \(HR\)](#) and the [ANS](#) activity also opens new doors for researchers wanting to study it, allowing them to use a relatively cheap, easy-to-use, and reliable technique. At the end of Chapter 2, there is a brief overview of the history of this technique, the [HRV](#), its relation with the [ANS](#), and how some metrics can be correlated with the two branches that make up the [ANS](#).

In Chapter 3 this relation is leveraged, using the [ECG](#) and [HRV](#) to study changes in the [ANS](#) due to an experimental medical procedure. This procedure, designated as [Remote Ischemic Conditioning \(RIC\)](#), comprises alternating cycles of ischemia and non-ischemia to a limb, in order to trigger a proceeding effect in a vital organ, such as reducing infarct size after a [MI](#). All the mechanisms that regulate this protection are still not fully established, which can be either humoral, neural, immune system-mediated, and/or a mixture of all the latter. In order to advance the knowledge in this field, a pilot trial was designed and applied, recording an [ECG](#) signal at the same time the [RIC](#) was performed, with the objective of finding if there are some differences in [ANS](#) activity as expressed by the [HRV](#) and therefore provide more evidence of the neural pathways influences in mediating the protection offered by the procedure.

To record an [ECG](#), an interface is needed to convert the potentials transmitted through the body to potentials that can be recorded by electronic devices. In the human body, these are transmitted due to changes in ions concentration, while outside the body, electrons are used. These interfaces are called electrodes, and throughout time these too suffered an evolution. Electrodes can be classified by the usage of electrolyte gel or by their position in relation to the body. Concerning the first topic, electrodes can be wet if they use an electrolytic gel to aid in the recording of the signal, or dry if no extra gel is used, only the body's natural excreted electrolytes. Regarding the positioning of electrodes relatively to the body, these can be positioned inside the subject's body (in-the-person), attached onto the skin (on-the-person), and finally embedded in day-to-day devices (off-the-person). All these concepts were discussed in Chapter 4.

One of the materials from which dry electrodes can be constructed is a polymer. These have generally good biocompatibility, a favorable cost-to-signal-quality ratio, and are a good solution for being embedded into mass-produced solutions. Dry electrodes, in general, are more suitable for long acquisition sessions or when there is a frequent hands-on/hands-off cycle, making them the better solution for the development of pervasive [ECG](#) recording solutions, one of the main objectives of this thesis. Building an easy-to-use solution, where the user does not have to consciously close the [ECG](#) circuit (as with

smartwatches, for example), capable of monitoring the user while using the device, could bring an increased value to both the prevention and diagnostic field. The development of such a novel device for this purpose was the focus in Chapter 4.

Nevertheless, these approaches have some drawbacks, out of which noise is perhaps the more concerning in a mobile context. Long recordings of ECG signals can generate a large amount of data in devices that are storage constraint, have to transmit this data to central repositories or process the data locally, and have a limited supply of power before they need to be charged again. Therefore there is the need to identify noisy portions of the signal and remove them to save resources and discard erroneous results. When using an off-the-person approach for recording ECG, the principal sources of noise are motion artifacts and poor or non-existent contact, leading to ECG distortion and loss of its morphological features.

Although at first glance this problem could be seen as a trivial task, it is far from it, with the morphology of the waveform sometimes being mistaken for noise and vice versa. There are three main approaches for classifying a segment as outlier (or not), namely, the usage of time-domain metrics and rules, frequency domain ones, and combination of both. Furthermore, in the last decades, the usage of machine learning has also increased in this field, which was typically dominated by the combination of different rules. Chapter 5 proposes a new method for outlier detection based on machine learning techniques.

## 6.2 Contributions

A pilot study was designed and implemented to observe if any changes occurred in the most used metrics extracted from HRV to identify the contributions of the neural pathways, more specifically those from the ANS, in modulating the protection provided by the RIC procedure. It was possible to observe a statistically significant change in the before and after periods of applying the procedure, with the non-linear metric SD2 increase. This metric is typically associated with an increase of long-term changes in the HRV, with an increase in activity of both ANS branches.

These results offer a different outlook on the role of the ANS system in the mediation of the protection, since most of the state-of-the-art studies infer its mediation due to the lack of cardioprotection when these systems are suppressed, while by using HRV it was possible to observe a more direct contribution of the neural pathways.

In Chapter 4 the development of a tablet for monitoring health and aiding elderly people while also giving their caregivers peace of mind was described. This work was done in partnership with other laboratories and industry partners, with the goal of bringing to market a suite of solutions with a handheld tablet at its core. Among other features, it has the ability to monitor heart activity using a pervasive ECG recording solution, developed using an off-the-person approach, with dry polymeric electrodes embedded in a custom-designed back cover.

The final polymeric material was selected from a short list of five possible candidates, pre-selected due to their properties. To assess which material would be the best, the signal similarity between recordings using a clinical-grade ECG machine with Ag/AgCl electrodes glued to the wrists and those using a PLUX biosignalsplux acquisition unit connected to the materials in study were compared. Of all materials, PolyOne's OnForce LFT LF6600-5023 (PO), a polyamide with high elastic modulus and material strength had the best results in all three metrics used: cosine similarity, root mean square error, and Spearman correlation.

By using a polymer as a dry electrode, it made it simpler for the acquisition of the ECG signal to be extracted more seamless, with the electrodes embedded directly in the back of the tablet, making contact with both hands when the user holds the tablet in portrait mode. This approach enables more periodic monitoring by the tablet, since the user does not have to place their hand consciously on the electrodes or can be taught very easily the best way to interact with the tablet.

The combination of all these characteristics allows this novel device to be a more pervasive method for recording and monitoring heart activity. The proposed device differs from what is commercially available by implementing an acquisition system that enables a more naturalistic recording of ECG rhythm strips, as opposed to the current approach of embedding the electrodes on wearable devices that require a conscious action by its user. Another distinguishable point of this device is the material from which the electrodes are made off, using a polymer instead of a metal, enabling a more customizable integration with the device's chassis/back cover.

Finally, there was the work done in the field of ECG signal quality assessment, through the development of a new approach to detect outlier segments. To accomplish this goal, a technique used to detect the QRS complex in microcontrollers was repurposed to the task of detecting outliers using two different methodologies. Phase portraits, a method derived from chaos physics, were used to geometrically represent the trajectory of a dynamical system in the phase plane instead of the time plane, creating a distinct shape. This shape is then used to distinguish between a good segment or an outlier one.

The two approaches used to detect outliers in the ECG were either based on image descriptors or the image itself. The first approach applied a commonly used image descriptor in image recognition, the Hu image moments. By using these, a set of seven features describes the image, which are scale, rotation, and translation invariant. The other approach uses the image as an input to a deep neural network, trained to distinguish between good and outlier segments.

The results obtained when using these two approaches are in line with the state-of-art of works that used the database used to train and verify these approaches, albeit with some differences in the segments used<sup>1</sup>. Although both techniques are able to

---

<sup>1</sup>The target of these works was to train models capable of classifying segments where Atrial Fibrillation occurred. Furthermore, these used the whole database. This comparison is more of an indication that this technique could be used for the task at hand.

correctly classify the normal segments as such, when classifying outliers it has slightly worse performance. In general, the trained models were able to correctly classify the Noise labeled segments with an F1-score of 0.6-0.7 (depending if it is on the Test or Validation set). With such a distinctive shape, it should have been possible to have a better distinction between the two types of segments. In Chapter 5, there is a more in-depth explanation of why there was a lack of performance, with the overall conclusion being that the database used played a major role in this.

The main difference between the proposed approach and the state-of-art, especially the works that used this database, is the type and number of the features used to train the models. These typically use a very large number of morphological, [HRV](#), time-domain, frequency-domain, and templates to train complex models. In the proposed approaches, a segment can be either described by seven features or be fed directly into a [Convolutional Neural Network \(CNN\)](#) model, simplifying the classification process.

### 6.3 Future work

There are some limitations to the pilot designed for assessing the influences of neural pathways in the protection offered by the [RIC](#) procedure using [HRV](#). These include the small sample size, having only a one-time window to compare the effects of the [RIC](#) (for example, recording a 5-minute segment after 2 or 24 hours of the procedure), and only performing one full [RIC](#) cycle. Future studies should address these limitations to confirm the results obtained in this pilot trial.

For the development of the tablet, the first major task to accomplish is performing real-world testing (e.g. in an assisted living facility). These trials will be very helpful in finding any shortfalls with the current design, providing insights for future revisions of the electrode positioning and interaction with them. For the tablet to be accepted and used by the target populations, which sometimes can be resistant to changes, taking their feedback and examining their interactions with the product is essential. At the same time, these tests will also provide feedback if any changes are required to the acquisition frontend, to be more performant with the target population (e.g. age-related changes in skin impedance [182]), or if any unaccounted [EMI](#) exists between the acquisition unit and the tablet. In addition to the recording and comparison of [ECG](#) signals, it would also be beneficial to perform a clinical assessment of the signals to determine if a trained expert can accurately identify the specific landmarks in the [ECG](#) waveform. Another interesting study that should be performed is to record [ECG](#) strips of patients with known [CVDs](#), to find if those recordings can be used by a clinician or trained expert to find the markers used in the diagnosis and monitoring of such disorders.

Another important aspect that needs to be evaluated is the durability of the polymer chosen for the electrodes. With time, some materials start to break down and lose some qualities, either by mechanical or chemical wear down. Long-term monitoring of the electrode surfaces should then be performed, to evaluate if/how the quality of the signal

being recorded does not suffer any significant loss. Other materials could also be tested and compared to the performance of the chosen polymer. For example, graphene is increasingly used as a material to produce electrodes, and it could be interesting to compare its performance, or the usage of bendable electrodes, studying their application in the back of the tablet to improve the contact with the fingers.

Finally, there is the signal quality index. To better assess the performance of the algorithm at least two major improvements should be made. The first one is to find better annotated datasets to replicate the results obtained and build better estimators. It is crucial to validate and create a better outlier labeling model, especially since the techniques used scale with the amount of data that is used to train them. Furthermore, the dataset should be more balanced, with a more equal number of normal and outlier labeled data.

Another major improvement is the architecture of the developed [Artificial Neural Network \(ANN\)](#). Works in other computer vision fields can be applied to this problem, from more optimized layer architecture, with different activation functions or different types of layers, to completely different networks. One of these different architectures that could be used for this problem is Long Short Term Memory networks [183], a type of network that can leverage past knowledge to assess current information, thus introducing a time element to the classification. The [CNNs](#) employed in this work were based on existing character recognition focus networks, leaving space to improve on this complex field that is [ANN](#).

Another potential application for the phase plots is the diagnosis/classification of [CVDs](#), which could generate different patterns in the delay map. By using these maps to classify the rhythm strips, their usefulness in mobile [ECG](#) devices can further be increased, even flagging the segment for review by an expert. These patterns could also be used, in theory, to track the evolution of a patient's [CVD](#).

## 6.4 Other Contributions

During the development of this thesis, there were research, work, and knowledge gathering in other fields.

Starting with the support to master students during their work, where four master students were supported. Two of the thesis focused on posturography studies ("[Development of a normative base in pathologies of the rheumatologic forum based on posturography and electromyography](#)"<sup>2</sup> and "[Development of a normative base for neurological pathologies based on posturography and electromyography](#)"<sup>3</sup>), using a force platform and four pairs of muscles to build normative databases. Working on another electrophysiological field of study, electromyography, allowed for the development of a better understanding of signal processing, how noise affects other signals, and in particular how the [ECG](#)

---

<sup>2</sup><http://hdl.handle.net/10362/61560>.

<sup>3</sup><http://hdl.handle.net/10362/61560>.



and the [Electromyography \(EMG\)](#) interact. Furthermore, these works also involved the recruitment of test subjects and the management of large amounts of data, offering an opportunity to develop skills in these fields. From these works, a conference paper was published as part of the conference proceedings as a book chapter (winning the best paper award) [184].

A third thesis focused on the study of the [ANS](#) using [HRV](#) and electrodermal activity (measure in changes of electrical current due to sweat). Using a wearable device, these two techniques recorded the subject's response to a mental arithmetic stress test and used to create a classifier to predict the subject's response ("[Autonomous Nervous System biosignal processing via EDA and HRV from a wearable device](#)"<sup>4</sup>). This work was another example where [HRV](#) can be used to study the [ANS](#), this time to correlate changes in another electrophysiological technique with changes in the [ANS](#), applying the knowledge learned in Chapter 2 and 3 to aid in this thesis. These results were also presented at a conference and published in its proceedings as a book chapter [185].

The last thesis focused on the use of off-the-shelf radars in vital signs monitoring, with the development of an equivalent processing pipeline for two different radar technologies. With this pipeline, breathing rate was easily detected, while in some cases it was possible to extract the [Heartbeat \(HB\)](#) ("[Bio-Radar applications for remote vital signs monitoring](#)"<sup>5</sup>). Here a more extreme off-the-person monitoring tool was explored, the use of radar to achieve near-continuous extraction of the respiration rate and in some conditions the heart rate, comparatively to using more traditional methods (microphone and an [ECG](#) sensor) to validate these results. These results were published in a paper [186].

Another contribution was the work done for a data collection tool in the context of web navigation, the Latent project, where the aim was to study human behavior while using the internet. To this effect, the skeleton of a web extension and a data collection server were developed. This framework can also be embedded directly on a website, which, for example, could be used as a further monitoring tool for elderly patients. A special website could be developed to analyze their behavior and cognitive functions while at the same time recording their [ECG](#), and in the end, combining both data sources to get a better understanding of the subject's health. There were further developments in the tool, with the final product published in a paper [187]. As a final published research contribution, there was the opportunity to help in the development of a genetic algorithm used for job rotation scheduling, by contributing with ideas on how genetic algorithms could be helpful in this field [188, 189].

In parallel with all these activities, there were some direct contributions to the work developed by this thesis co-sponsor, PLUX. As mentioned in Chapter 4, PLUX was one of the partners in the consortium responsible for the development of the tablet, with project management tasks performed in addition to research work.

---

<sup>4</sup><http://hdl.handle.net/10362/59608>.

<sup>5</sup><http://hdl.handle.net/10362/118695>.



## 6.5 Published Scientific Contributions

The following is a list of the published scientific contributions, divided into core publications (first author and part of a chapter in this thesis) and support publications (not the first author or not part of a chapter in this thesis).

- Core publications
  - D. N. Osório et al. “Comparison of different polymeric materials for mobile off-the-person ECG”. In: 5th EAI International Conference on IoT Technologies for HealthCare. Springer International Publishing, 2019-12, pp. 15–22. doi: 10.1007/978-3-030-30335-8\_2;
  - D. N. Osório et al. “Autonomic nervous system response to remote ischemic conditioning: Heart rate variability assessment”. In: BMC Cardiovascular Disorders 19.1 (2019-09). doi: 10.1186/s12872-019-1181-5.
- Support publications
  - R. Lima, D. Osório, and H. Gamboa. “Heart rate variability and electrodermal activity biosignal processing: Predicting the autonomous nervous system response in mental stress”. In: Biomedical Engineering Systems and Technologies. Springer International Publishing, 2020, pp. 328–351. doi: 10.1007/978-3-030-46970-2\_16;
  - C. Cepeda et al. “Latent: A flexible data collection tool to research human behavior in the context of web navigation”. In: IEEE Access 7 (2019), pp. 77659–77673. doi: 10.1109/access.2019.2916996;
  - D. N. Osório et al. “Development and validation of an experimental protocol to evaluate posture control”. In: IFIP Advances in Information and Communication Technology. Springer International Publishing, 2020, pp. 387–394. doi: 10.1007/978-3-030-45124-0\_37 (Won best paper award);
  - J. Rodrigues et al. “A genetic algorithm to design job rotation schedules with low risk exposure”. In: IFIP Advances in Information and Communication Technology. Springer International Publishing, 2020, pp. 395–402. doi: 10.1007/978-3-030-45124-0\_38;
  - A. Lopes et al. “Equivalent pipeline processing for IR-UWB and FMCW radar comparison in vital signs monitoring applications”. In: IEEE Sensors Journal 22.12 (2022-06), pp. 12028–12035. doi: 10.1109/jsen.2022.3173218;
  - A. Assunção et al. “A genetic algorithm approach to design job rotation schedules ensuring homogeneity and diversity of exposure in the automotive industry”. In: Heliyon 8.5 (2022-05), e09396. doi: 10.1016/j.heliyon.2022.e09396.

## BIBLIOGRAPHY

- [1] J. M. Lourenço. *The NOVAthesis L<sup>A</sup>T<sub>E</sub>X Template User's Manual*. NOVA University Lisbon. 2021. URL: <https://github.com/joaomlourenco/novathesis/raw/master/template.pdf> (cit. on p. ii).
- [2] E. Wilkins et al. "European cardiovascular disease statistics 2017". In: (2017) (cit. on p. 1).
- [3] M. F. Piepoli et al. "Guidelines: Editor's choice: 2016 European Guidelines on cardiovascular disease prevention in clinical practice: The Sixth Joint Task Force of the European Society of Cardiology and Other Societies on Cardiovascular Disease Prevention in Clinical Practice (constituted by representatives of 10 societies and by invited experts) Developed with the special contribution of the European Association for Cardiovascular Prevention & Rehabilitation (EACPR)". In: *European Heart Journal* 37.29 (2016), p. 2315 (cit. on p. 1).
- [4] G. A. Roth et al. "Global and regional patterns in cardiovascular mortality from 1990 to 2013". In: *Circulation* 132.17 (2015-10), pp. 1667–1678. DOI: [10.1161/circulationaha.114.008720](https://doi.org/10.1161/circulationaha.114.008720) (cit. on p. 2).
- [5] A. Bansal and R. Joshi. "Portable out-of-hospital electrocardiography: A review of current technologies". In: *Journal of Arrhythmia* 34.2 (2018-02), pp. 129–138. DOI: [10.1002/joa3.12035](https://doi.org/10.1002/joa3.12035) (cit. on pp. 2, 3, 24, 25).
- [6] M. Aitken, J. Lyle, et al. *Patient adoption of mHealth: Use, evidence and remaining barriers to mainstream acceptance*. Research rep. Parsippany, NJ: IMS Institute for Healthcare Informatics, 2015. URL: <https://www.iqvia.com/-/media/iqvia/pdfs/institute-reports/patient-adoption-of-mhealth.pdf> (visited on 2022-07-26) (cit. on pp. 2, 5, 57).
- [7] H. Saner. "Digital health implementation: How to overcome the barriers?" In: *European Journal of Preventive Cardiology* 26.11 (2019-05), pp. 1164–1165. DOI: [10.1177/2047487319848222](https://doi.org/10.1177/2047487319848222) (cit. on p. 2).

- [8] R. J. Moss, A. Süle, and S. Kohl. “eHealth and mHealth”. In: *European Journal of Hospital Pharmacy* 26.1 (2018-12), pp. 57–58. DOI: [10.1136/ejhpharm-2018-001819](https://doi.org/10.1136/ejhpharm-2018-001819) (cit. on p. 2).
- [9] J. Li et al. “Health care provider adoption of eHealth: Systematic literature review”. In: *Interactive Journal of Medical Research* 2.1 (2013-04), e7. DOI: [10.2196/ijmr.2468](https://doi.org/10.2196/ijmr.2468) (cit. on p. 2).
- [10] M. R. Cowie and C. S. P. Lam. “Remote monitoring and digital health tools in CVD management”. In: *Nature Reviews Cardiology* 18.7 (2021-04), pp. 457–458. DOI: [10.1038/s41569-021-00548-x](https://doi.org/10.1038/s41569-021-00548-x) (cit. on p. 2).
- [11] P. Kamga, R. Mostafa, and S. Zafar. “The use of wearable ECG devices in the clinical setting: A review”. In: *Current Emergency and Hospital Medicine Reports* (2022-06). DOI: [10.1007/s40138-022-00248-x](https://doi.org/10.1007/s40138-022-00248-x) (cit. on pp. 3, 4).
- [12] R. Trobec et al. “Commercial ECG systems”. In: *Body Sensors and Electrocardiography*. Springer International Publishing, 2017-07, pp. 101–114. DOI: [10.1007/978-3-319-59340-1\\_6](https://doi.org/10.1007/978-3-319-59340-1_6) (cit. on pp. 3–5).
- [13] G. Cosoli et al. “Wireless ECG and cardiac monitoring systems: State of the art, available commercial devices and useful electronic components”. In: *Measurement* 177 (2021-06), p. 109243. DOI: [10.1016/j.measurement.2021.109243](https://doi.org/10.1016/j.measurement.2021.109243) (cit. on p. 3).
- [14] A. Bravi, A. Longtin, and A. J. Seely. “Review and classification of variability analysis techniques with clinical applications”. In: *BioMedical Engineering OnLine* 10.1 (2011), p. 90. DOI: [10.1186/1475-925x-10-90](https://doi.org/10.1186/1475-925x-10-90) (cit. on pp. 4, 32).
- [15] U. R. Acharya et al. “Heart rate variability: A review”. In: *Medical and Biological Engineering and Computing* 44.12 (2006-11), pp. 1031–1051. DOI: [10.1007/s11517-006-0119-0](https://doi.org/10.1007/s11517-006-0119-0) (cit. on pp. 4, 31, 32).
- [16] T. F. of the European Society of Cardiology the North A Electrophysiology. “Heart rate variability”. In: *Circulation* 93.5 (1996-03), pp. 1043–1065. DOI: [10.1161/01.cir.93.5.1043](https://doi.org/10.1161/01.cir.93.5.1043) (cit. on pp. 4, 31–34, 48, 136, 137).
- [17] Z. Xie and C. K. Or. “Acceptance of mHealth by elderly adults: A path analysis”. In: *Proceedings of the Human Factors and Ergonomics Society Annual Meeting* 64.1 (2020-12), pp. 755–759. DOI: [10.1177/1071181320641174](https://doi.org/10.1177/1071181320641174) (cit. on pp. 5, 57).
- [18] H. M. School, ed. *The danger of “silent” heart attacks*. [Online; Accessed July 27, 2022]. URL: <https://www.health.harvard.edu/heart-health/the-danger-of-silent-heart-attacks> (cit. on pp. 5, 25).
- [19] A. S. Silva, M. V. Correia, and H. P. Silva. “Invisible ECG for high throughput screening in eSports”. In: *Sensors* 21.22 (2021-11), p. 7601. DOI: [10.3390/s21227601](https://doi.org/10.3390/s21227601) (cit. on p. 6).

- [20] H. Silva, A. Lourenço, and A. Fred. “In-vehicle driver recognition based on hand ECG signals”. In: *Proceedings of the 2012 ACM international conference on Intelligent User Interfaces - IUI '12*. ACM Press, 2012. DOI: [10.1145/2166966.2166971](https://doi.org/10.1145/2166966.2166971) (cit. on p. 6).
- [21] D. C. Bauer. “Association of major and minor ECG abnormalities with coronary heart disease events”. In: *JAMA* 307.14 (2012-04), p. 1497. DOI: [10.1001/jama.2012.434](https://doi.org/10.1001/jama.2012.434) (cit. on pp. 6, 25).
- [22] C. Orphanidou. “Quality assessment for the electrocardiogram (ECG)”. In: *Springer-Briefs in Bioengineering*. Springer International Publishing, 2017-10, pp. 15–40. DOI: [10.1007/978-3-319-68415-4\\_2](https://doi.org/10.1007/978-3-319-68415-4_2) (cit. on pp. 6, 76, 78, 82–88).
- [23] B. Ziskind. “L’examen cardiovasculaire à la lumière des papyrus médicaux de l’Egypte ancienne”. In: *Histoire des Sciences Médicales* 40.1 (2006), p. 61 (cit. on p. 9).
- [24] M. M. Saba et al. “Ancient egyptian medicine and the concept of heart failure”. In: *Journal of Cardiac Failure* 12.6 (2006-08), pp. 416–421. DOI: [10.1016/j.cardfail.2006.03.001](https://doi.org/10.1016/j.cardfail.2006.03.001) (cit. on p. 9).
- [25] S. G. Schultz. “William Harvey and the circulation of the blood: The birth of a scientific revolution and modern physiology”. In: *Physiology* 17.5 (2002-10), pp. 175–180. DOI: [10.1152/nips.01391.2002](https://doi.org/10.1152/nips.01391.2002) (cit. on pp. 9, 10).
- [26] M. Piccolino and M. Bresadola. “Drawing a spark from darkness: John Walsh and electric fish”. In: *Trends in Neurosciences* 25.1 (2002-01), pp. 51–57. DOI: [10.1016/S0166-2236\(00\)02003-8](https://doi.org/10.1016/S0166-2236(00)02003-8) (cit. on p. 10).
- [27] M. Rivera-Ruiz, C. Cajavilca, and J. Varon. “Einthoven’s string galvanometer: The first electrocardiograph.” In: *Texas Heart Institute journal* 35 (2 2008), pp. 174–178. ISSN: 0730-2347 (cit. on pp. 10, 11, 16–18).
- [28] W. Fye. “A history of the origin, evolution, and impact of electrocardiography”. In: *The American Journal of Cardiology* 73.13 (1994-05), pp. 937–949. DOI: [10.1016/0002-9149\(94\)90135-x](https://doi.org/10.1016/0002-9149(94)90135-x) (cit. on pp. 10, 11, 18, 19, 22).
- [29] A. D. Waller. “A demonstration on man of electromotive changes accompanying the heart’s beat”. In: *The Journal of Physiology* 8.5 (1887-10), pp. 229–234. DOI: [10.1113/jphysiol.1887.sp000257](https://doi.org/10.1113/jphysiol.1887.sp000257) (cit. on p. 11).
- [30] S. S. Barold. “Willem Einthoven and the birth of clinical electrocardiography a hundred years ago.” In: *Cardiac Electrophysiology Review* 7 (1 2003-01), pp. 99–104. ISSN: 1385-2264. DOI: [10.1023/a:1023667812925](https://doi.org/10.1023/a:1023667812925) (cit. on pp. 11, 16–18).
- [31] M. AlGhatrif and J. Lindsay. “A brief review: History to understand fundamentals of electrocardiography”. In: *Journal of Community Hospital Internal Medicine Perspectives* 2.1 (2012-01), p. 14383. DOI: [10.3402/jchimp.v2i1.14383](https://doi.org/10.3402/jchimp.v2i1.14383) (cit. on pp. 11, 12, 17–21).

- [32] W. Einthoven. “Ueber die form des menschlichen electrocardiogramms”. In: *Pflüger, Archiv für die Gesamte Physiologie des Menschen und der Thiere* 60.3-4 (1895-03), pp. 101–123. DOI: [10.1007/bf01662582](https://doi.org/10.1007/bf01662582) (cit. on pp. 11, 12).
- [33] J. E. Hall and M. E. Hall. *Guyton and Hall textbook of medical physiology e-book*. Elsevier Health Sciences, 2020-06. ISBN: 9780323640039 (cit. on pp. 12, 13, 15).
- [34] N. G. Science, ed. *Section 2: The muscular system*. [Online; Accessed July 27, 2022]. URL: <https://nittygrittyscience.com/textbooks/human-body-part-1/section-2-the-muscular-system/> (cit. on p. 13).
- [35] J. Gordon Betts, OpenStax College, and Rice University. *Anatomy & physiology*. 2017. Chap. 19.2 Cardiac Muscle and Electrical Activity. ISBN: 1-947172-04-2 (cit. on pp. 14, 15).
- [36] J. Gordon Betts, OpenStax College, and Rice University. *Anatomy & physiology*. 2017. Chap. 19.3 Cardiac Cycle. ISBN: 1-947172-04-2 (cit. on p. 16).
- [37] W. Einthoven. “The different forms of the human electrocardiogram and their signification”. In: *The Lancet* 179 (1912), pp. 853–861. ISSN: 0140-6736. DOI: [10.1016/s0140-6736\(00\)50560-1](https://doi.org/10.1016/s0140-6736(00)50560-1) (cit. on pp. 17, 18).
- [38] C. R. Conti. “Triage of chest pain patients in the emergency department”. In: *Clinical Cardiology* 33.8 (2010-08), pp. 458–459. DOI: [10.1002/clc.20829](https://doi.org/10.1002/clc.20829) (cit. on p. 18).
- [39] ECG and E. Learning, eds. *Section 1, Chapter 3 - The ECG leads: From electrodes to limb leads, chest leads and 12-lead ECG*. [Online; Accessed July 27, 2022]. URL: <https://ecgwaves.com/topic/ekg-ecg-leads-electrodes-systems-limb-chest-precordial/> (cit. on p. 19).
- [40] F. Kusumoto. “Physics of electrocardiography”. In: *ECG Interpretation*. Springer International Publishing, 2020, pp. 13–22. DOI: [10.1007/978-3-030-40341-6\\_2](https://doi.org/10.1007/978-3-030-40341-6_2) (cit. on p. 20).
- [41] J. L. Salinet and O. L. Silva. “ECG signal acquisition systems”. In: *Developments and Applications for ECG Signal Processing*. Elsevier, 2019, pp. 29–51. DOI: [10.1016/b978-0-12-814035-2.00008-6](https://doi.org/10.1016/b978-0-12-814035-2.00008-6) (cit. on pp. 21, 52).
- [42] C. W. R. University, ed. *Cambridge Electrocardiograph, 1920*. [Online; Accessed July 27, 2022]. URL: <https://artsci.case.edu/dittrick/online-exhibits/explore-the-artifacts/cambridge-electrocardiograph-1920/> (cit. on p. 22).
- [43] S. M. Group, ed. *Sanborn Viso 100 portable electrocardiograph machine in wooden case*. [Online; Accessed July 27, 2022]. URL: <https://collection.sciencemuseumgroup.org.uk/objects/co93980/sanborn-viso-100-portable-electrocardiograph-machi-electrocardiograph-machines> (cit. on p. 22).

- 
- [44] E. Besterman. “The beginnings and development of the electrocardiograph”. In: *West Indian Medical Journal* 54.3 (2005-06). DOI: [10.1590/s0043-31442005000300012](https://doi.org/10.1590/s0043-31442005000300012) (cit. on p. 22).
  - [45] F. C. Inc., ed. *Fifty years of physiologic monitors*. [Online; Accessed July 27, 2022]. URL: <http://www.femtoclinical.com/History%20of%20Physiologic%20Monitors.htm> (cit. on p. 23).
  - [46] H. L. Kennedy. “The evolution of ambulatory ECG monitoring”. In: *Progress in Cardiovascular Diseases* 56.2 (2013-09), pp. 127–132. DOI: [10.1016/j.pcad.2013.08.005](https://doi.org/10.1016/j.pcad.2013.08.005) (cit. on p. 23).
  - [47] X.-L. Yang et al. “The history, hotspots, and trends of electrocardiogram.” In: *Journal of Geriatric Cardiology : JGC* 12 (4 2015-07), pp. 448–456. ISSN: 1671-5411. DOI: [10.11909/j.issn.1671-5411.2015.04.018](https://doi.org/10.11909/j.issn.1671-5411.2015.04.018) (cit. on p. 24).
  - [48] J. Allen. “Photoplethysmography and its application in clinical physiological measurement”. In: *Physiological Measurement* 28.3 (2007-02), R1–R39. DOI: [10.1088/0967-3334/28/3/r01](https://doi.org/10.1088/0967-3334/28/3/r01) (cit. on p. 24).
  - [49] S. Bagha and L. Shaw. “A real time analysis of PPG signal for measurement of SpO2 and pulse rate”. In: *International Journal of Computer Applications* 36.11 (2011), pp. 45–50. ISSN: 0975 – 8887 (cit. on p. 24).
  - [50] D. D. Bacquer et al. “Prognostic value of ECG findings for total, cardiovascular disease, and coronary heart disease death in men and women”. In: *Heart* 80.6 (1998-12), pp. 570–577. DOI: [10.1136/hrt.80.6.570](https://doi.org/10.1136/hrt.80.6.570) (cit. on p. 25).
  - [51] A. Goldman et al. “Incidental abnormal ECG findings and long-term cardiovascular morbidity and all-cause mortality: A population based prospective study”. In: *International Journal of Cardiology* 295 (2019-11), pp. 36–41. DOI: [10.1016/j.ijcard.2019.08.015](https://doi.org/10.1016/j.ijcard.2019.08.015) (cit. on p. 25).
  - [52] B. Vogel et al. “ST-segment elevation myocardial infarction”. In: *Nature Reviews Disease Primers* 5.1 (2019-06). DOI: [10.1038/s41572-019-0090-3](https://doi.org/10.1038/s41572-019-0090-3) (cit. on pp. 25, 26).
  - [53] P. K. Jain and A. K. Tiwari. “Heart monitoring systems—A review”. In: *Computers in Biology and Medicine* 54 (2014-11), pp. 1–13. DOI: [10.1016/j.combiomed.2014.08.014](https://doi.org/10.1016/j.combiomed.2014.08.014) (cit. on p. 26).
  - [54] T. H.-N. Le et al. “Feature extraction techniques for automatic detection of some specific cardiovascular diseases using ECG: A review and evaluation study”. In: *IFMBE Proceedings*. Springer Singapore, 2019-06, pp. 543–549. DOI: [10.1007/978-981-13-5859-3\\_94](https://doi.org/10.1007/978-981-13-5859-3_94) (cit. on p. 26).

- [55] F.-Y. Su et al. “A comparison of Cornell and Sokolow-Lyon electrocardiographic criteria for left ventricular hypertrophy in a military male population in Taiwan: the Cardiorespiratory fitness and Hospitalization Events in armed Forces study”. In: *Cardiovascular Diagnosis and Therapy* 7.3 (2017-06), pp. 244–251. DOI: [10.21037/cdt.2017.01.16](https://doi.org/10.21037/cdt.2017.01.16) (cit. on p. 26).
- [56] N. Darouian et al. “The Romhilt-Estes electrocardiographic score predicts sudden cardiac arrest independent of left ventricular mass and ejection fraction”. In: *Annals of Noninvasive Electrocardiology* 22.4 (2017-01), e12424. DOI: [10.1111/anec.12424](https://doi.org/10.1111/anec.12424) (cit. on p. 26).
- [57] S. Benjamens, P. Dhunoo, and B. Meskó. “The state of artificial intelligence-based FDA-approved medical devices and algorithms: An online database”. In: *NPJ Digital Medicine* 3.1 (2020-09). DOI: [10.1038/s41746-020-00324-0](https://doi.org/10.1038/s41746-020-00324-0) (cit. on p. 26).
- [58] L. Xie et al. “Computational diagnostic techniques for electrocardiogram signal analysis”. In: *Sensors* 20.21 (2020-11), p. 6318. DOI: [10.3390/s20216318](https://doi.org/10.3390/s20216318) (cit. on p. 26).
- [59] G. E. Billman. “Heart Rate Variability: A historical perspective”. In: *Frontiers in Physiology* 2 (2011). DOI: [10.3389/fphys.2011.00086](https://doi.org/10.3389/fphys.2011.00086) (cit. on pp. 27–30, 33, 34, 36).
- [60] F. Shaffer, R. McCraty, and C. L. Zerr. “A healthy heart is not a metronome: An integrative review of the heart’s anatomy and heart rate variability”. In: *Frontiers in Psychology* 5 (2014-09). DOI: [10.3389/fpsyg.2014.01040](https://doi.org/10.3389/fpsyg.2014.01040) (cit. on pp. 27, 34–36).
- [61] B. Xhyheri et al. “Heart rate variability today”. In: *Progress in Cardiovascular Diseases* 55.3 (2012-11), pp. 321–331. DOI: [10.1016/j.pcad.2012.09.001](https://doi.org/10.1016/j.pcad.2012.09.001) (cit. on p. 27).
- [62] L. K. McCorry. “Physiology of the autonomic nervous system.” In: *American Journal of Pharmaceutical Education* 71 (4 2007-08), p. 78. ISSN: 1553-6467. DOI: [10.5688/aj710478](https://doi.org/10.5688/aj710478) (cit. on p. 27).
- [63] J. M. Karemaker. “An introduction into autonomic nervous function”. In: *Physiological Measurement* 38.5 (2017-04), R89–R118. DOI: [10.1088/1361-6579/aa6782](https://doi.org/10.1088/1361-6579/aa6782) (cit. on p. 28).
- [64] G. Ernst. “Hidden signals—The history and methods of heart rate variability”. In: *Frontiers in Public Health* 5 (2017-10). DOI: [10.3389/fpubh.2017.00265](https://doi.org/10.3389/fpubh.2017.00265) (cit. on pp. 28–37, 48, 50, 137).
- [65] A. N. Bosmia et al. “Karl Ewald Konstantin Hering (1834–1918), Heinrich Ewald Hering (1866–1948), and the namesake for the Hering-Breuer reflex”. In: *Child’s Nervous System* 32.9 (2015-08), pp. 1561–1565. DOI: [10.1007/s00381-015-2854-8](https://doi.org/10.1007/s00381-015-2854-8) (cit. on p. 29).



- [66] H. D. Modanlou. “Edward H. Hon, MD (1917–2006): A scientist, inventor, academician and the pioneer for the development of electronic fetal heart rate monitoring”. In: *Journal of Obstetrics and Gynaecology Research* 45.12 (2019-09), pp. 2364–2368. DOI: [10.1111/jog.14123](https://doi.org/10.1111/jog.14123) (cit. on p. 29).
- [67] P. G. Katona and F. Jih. “Respiratory sinus arrhythmia: Noninvasive measure of parasympathetic cardiac control”. In: *Journal of Applied Physiology* 39.5 (1975-11), pp. 801–805. DOI: [10.1152/jappl.1975.39.5.801](https://doi.org/10.1152/jappl.1975.39.5.801) (cit. on p. 30).
- [68] S. Akselrod et al. “Power spectrum analysis of heart rate fluctuation: A quantitative probe of beat-to-beat cardiovascular control”. In: *Science* 213.4504 (1981-07), pp. 220–222. DOI: [10.1126/science.6166045](https://doi.org/10.1126/science.6166045) (cit. on pp. 30, 31).
- [69] T. Pham et al. “Heart rate variability in psychology: A review of HRV indices and an analysis tutorial”. In: *Sensors* 21.12 (2021-06), p. 3998. DOI: [10.3390/s21123998](https://doi.org/10.3390/s21123998) (cit. on pp. 31–37, 48).
- [70] M. E. Renna et al. “Distress disorder histories predict HRV trajectories during and after stress”. In: *Psychoneuroendocrinology* 135 (2022-01), p. 105575. DOI: [10.1016/j.psyneuen.2021.105575](https://doi.org/10.1016/j.psyneuen.2021.105575) (cit. on p. 32).
- [71] M. Vollmer. “HRVTool - an open-source Matlab toolbox for analyzing Heart Rate Variability”. In: *2019 Computing in Cardiology Conference (CinC)*. Computing in Cardiology, 2019-12. DOI: [10.22489/cinc.2019.032](https://doi.org/10.22489/cinc.2019.032) (cit. on p. 32).
- [72] G. Surrel et al. “Design of ultra-low-power smart wearable systems”. In: *2015 16th Latin-American Test Symposium (LATS)*. IEEE, 2015-03. DOI: [10.1109/latw.2015.7102527](https://doi.org/10.1109/latw.2015.7102527) (cit. on p. 32).
- [73] G. Clifford and L. Tarassenko. “Quantifying errors in spectral estimates of HRV due to beat replacement and resampling”. In: *IEEE Transactions on Biomedical Engineering* 52.4 (2005-04), pp. 630–638. DOI: [10.1109/tbme.2005.844028](https://doi.org/10.1109/tbme.2005.844028) (cit. on p. 32).
- [74] F. Shaffer and J. P. Ginsberg. “An overview of heart rate variability metrics and norms”. In: *Frontiers in Public Health* 5 (2017-09). DOI: [10.3389/fpubh.2017.00258](https://doi.org/10.3389/fpubh.2017.00258) (cit. on pp. 33–37, 48, 137).
- [75] J. E. Mietus. “The pNNx files: Re-examining a widely used heart rate variability measure”. In: *Heart* 88.4 (2002-10), pp. 378–380. DOI: [10.1136/heart.88.4.378](https://doi.org/10.1136/heart.88.4.378) (cit. on p. 33).
- [76] D. N. Osório et al. “Autonomic nervous system response to remote ischemic conditioning: Heart rate variability assessment”. In: *BMC Cardiovascular Disorders* 19.1 (2019-09). DOI: [10.1186/s12872-019-1181-5](https://doi.org/10.1186/s12872-019-1181-5) (cit. on pp. 39, 45, 49).
- [77] D. C. Hess et al. “Remote ischaemic conditioning—a new paradigm of self-protection in the brain”. In: *Nature Reviews Neurology* 11.12 (2015-11), pp. 698–710. DOI: [10.1038/nrneurol.2015.223](https://doi.org/10.1038/nrneurol.2015.223) (cit. on pp. 39, 40, 42).

- [78] S. Baig et al. “Remote ischaemic conditioning for stroke: Unanswered questions and future directions”. In: *Stroke and Vascular Neurology* 6.2 (2021-04), pp. 298–309. DOI: [10.1136/svn-2020-000722](https://doi.org/10.1136/svn-2020-000722) (cit. on p. 39).
- [79] M. Cour and S. Lecour. “Remote ischaemic conditioning: In search of a suitable match”. In: *Nature Reviews Cardiology* 16.12 (2019-10), pp. 704–705. DOI: [10.1038/s41569-019-0296-9](https://doi.org/10.1038/s41569-019-0296-9) (cit. on pp. 39, 41).
- [80] M. V. Basalay et al. “Neural mechanisms in remote ischaemic conditioning in the heart and brain: Mechanistic and translational aspects”. In: *Basic Research in Cardiology* 113.4 (2018-06). DOI: [10.1007/s00395-018-0684-z](https://doi.org/10.1007/s00395-018-0684-z) (cit. on pp. 40, 42–44).
- [81] V. Sivaraman, J. M. J. Pickard, and D. J. Hausenloy. “Remote ischaemic conditioning: Cardiac protection from afar”. In: *Anaesthesia* 70.6 (2015-02), pp. 732–748. DOI: [10.1111/anae.12973](https://doi.org/10.1111/anae.12973) (cit. on pp. 40, 42–44).
- [82] J. P. Gillebert and H. Bulluck. “Cardioprotection for acute MI in light of the CONDI2/ERIC-PPCI trial: New targets needed”. In: *Interventional Cardiology Review* 15 (2020-08). DOI: [10.15420/icr.2020.01](https://doi.org/10.15420/icr.2020.01) (cit. on p. 40).
- [83] L. Pearce, S. M. Davidson, and D. M. Yellon. “Does remote ischaemic conditioning reduce inflammation? A focus on innate immunity and cytokine response”. In: *Basic Research in Cardiology* 116.1 (2021-02). DOI: [10.1007/s00395-021-00852-0](https://doi.org/10.1007/s00395-021-00852-0) (cit. on pp. 41, 43).
- [84] D. J. Hausenloy, M. Ntsekhe, and D. M. Yellon. “A future for remote ischaemic conditioning in high-risk patients”. In: *Basic Research in Cardiology* 115.3 (2020-04). DOI: [10.1007/s00395-020-0794-2](https://doi.org/10.1007/s00395-020-0794-2) (cit. on p. 41).
- [85] S. L. Page and F. Prunier. “Remote ischemic conditioning: Current clinical perspectives”. In: *Journal of Cardiology* 66.2 (2015-08), pp. 91–96. DOI: [10.1016/j.jjcc.2015.01.009](https://doi.org/10.1016/j.jjcc.2015.01.009) (cit. on p. 44).
- [86] New York Heart Association. *Nomenclature and criteria for diagnosis of diseases of the heart and great vessels*. en. 9th ed. Philadelphia, PA: Lippincott Williams and Wilkins, 1994-03 (cit. on p. 45).
- [87] I. Antelmi et al. “Influence of age, gender, body mass index, and functional capacity on heart rate variability in a cohort of subjects without heart disease”. In: *The American Journal of Cardiology* 93.3 (2004-02), pp. 381–385. DOI: [10.1016/j.amjcard.2003.09.065](https://doi.org/10.1016/j.amjcard.2003.09.065) (cit. on pp. 45, 50).
- [88] J. Pan and W. J. Tompkins. “A real-time QRS detection algorithm”. In: *IEEE Transactions on Biomedical Engineering* BME-32.3 (1985-03), pp. 230–236. DOI: [10.1109/tbme.1985.325532](https://doi.org/10.1109/tbme.1985.325532) (cit. on pp. 46, 77).

- [89] M. Brennan, M. Palaniswami, and P. Kamen. “Do existing measures of Poincare plot geometry reflect nonlinear features of heart rate variability?” In: *IEEE Transactions on Biomedical Engineering* 48.11 (2001), pp. 1342–1347. DOI: [10.1109/10.959330](https://doi.org/10.1109/10.959330) (cit. on p. 49).
- [90] M. J. Marino. “Statistical analysis in preclinical biomedical research”. In: *Research in the Biomedical Sciences*. Elsevier, 2018. Chap. Chapter 3, p. 133. DOI: [10.1016/b978-0-12-804725-5.00003-3](https://doi.org/10.1016/b978-0-12-804725-5.00003-3) (cit. on p. 49).
- [91] M. T. L. Rovere et al. “Baroreflex sensitivity and heart-rate variability in prediction of total cardiac mortality after myocardial infarction”. In: *The Lancet* 351.9101 (1998-02), pp. 478–484. DOI: [10.1016/s0140-6736\(97\)11144-8](https://doi.org/10.1016/s0140-6736(97)11144-8) (cit. on p. 50).
- [92] D. N. Osório et al. “Comparison of different polymeric materials for mobile off-the-person ECG”. In: *5th EAI International Conference on IoT Technologies for HealthCare*. Springer International Publishing, 2019-12, pp. 15–22. DOI: [10.1007/978-3-030-30335-8\\_2](https://doi.org/10.1007/978-3-030-30335-8_2) (cit. on p. 52).
- [93] M. R. Neuman et al. “Biopotential electrodes”. In: *Medical Instrumentation: Application and Design*. Ed. by J. Webster and A. Nimunkar. 4th. Wiley, 2020. Chap. 5, pp. 189–240. ISBN: 9781119457329 (cit. on pp. 52, 53).
- [94] E. McAdams. *Bioelectrodes*. 2006-04. DOI: [10.1002/0471732877.emd013](https://doi.org/10.1002/0471732877.emd013) (cit. on pp. 53, 54).
- [95] Y. Fu et al. “Dry electrodes for human bioelectrical signal monitoring”. In: *Sensors* 20.13 (2020-06), p. 3651. DOI: [10.3390/s20133651](https://doi.org/10.3390/s20133651) (cit. on pp. 53–55).
- [96] S. Yao and Y. Zhu. “Nanomaterial-enabled dry electrodes for electrophysiological sensing: A review”. In: *JOM* 68.4 (2016-02), pp. 1145–1155. DOI: [10.1007/s11837-016-1818-0](https://doi.org/10.1007/s11837-016-1818-0) (cit. on pp. 53–55, 58, 74).
- [97] J. Heikenfeld et al. “Wearable sensors: Modalities, challenges, and prospects”. In: *Lab on a Chip* 18.2 (2018), pp. 217–248. DOI: [10.1039/c7lc00914c](https://doi.org/10.1039/c7lc00914c) (cit. on pp. 53, 54).
- [98] E. Huigen, A. Peper, and C. A. Grimbergen. “Investigation into the origin of the noise of surface electrodes”. In: *Medical and Biological Engineering and Computing* 40.3 (2002-05), pp. 332–338. DOI: [10.1007/bf02344216](https://doi.org/10.1007/bf02344216) (cit. on p. 54).
- [99] E. K. Lee et al. “Recent advances in electrode development for biomedical applications”. In: *Biomedical Engineering Letters* 11.2 (2021-04), pp. 107–115. DOI: [10.1007/s13534-021-00189-6](https://doi.org/10.1007/s13534-021-00189-6) (cit. on p. 55).
- [100] X. Niu et al. “Surface bioelectric dry Electrodes: A review”. In: *Measurement* 183 (2021-10), p. 109774. DOI: [10.1016/j.measurement.2021.109774](https://doi.org/10.1016/j.measurement.2021.109774) (cit. on pp. 55, 58, 71, 81).

- [101] H. P. da Silva et al. "Off-the-person electrocardiography: Performance assessment and clinical correlation". In: *Health and Technology* 4.4 (2015-02), pp. 309–318. DOI: [10.1007/s12553-015-0098-y](https://doi.org/10.1007/s12553-015-0098-y) (cit. on pp. 56, 57, 62).
- [102] Y.-J. Choi, J.-Y. Lee, and S.-H. Kong. "Driver ECG measuring system with a conductive fabric-based dry electrode". In: *IEEE Access* 6 (2018), pp. 415–427. DOI: [10.1109/access.2017.2766098](https://doi.org/10.1109/access.2017.2766098) (cit. on p. 56).
- [103] Y. K. Lim, K. K. Kim, and K. S. Park. "The ECG measurement in the bathtub using the insulated electrodes". In: *The 26th Annual International Conference of the IEEE Engineering in Medicine and Biology Society*. IEEE, 2004. DOI: [10.1109/iembs.2004.1403690](https://doi.org/10.1109/iembs.2004.1403690) (cit. on p. 56).
- [104] T.-H. Kang. "Textile-embedded sensors for wearable physiological monitoring systems". PhD thesis. North Carolina State University, 2007 (cit. on p. 56).
- [105] N. Isakadze and S. S. Martin. "How useful is the smartwatch ECG?" In: *Trends in Cardiovascular Medicine* 30.7 (2020-10), pp. 442–448. DOI: [10.1016/j.tcm.2019.10.010](https://doi.org/10.1016/j.tcm.2019.10.010) (cit. on pp. 56, 58).
- [106] H. C. Ossebaard and L. V. Gemert-Pijnen. "eHealth and quality in health care: Implementation time". In: *International Journal for Quality in Health Care* 28.3 (2016-03), pp. 415–419. DOI: [10.1093/intqhc/mzw032](https://doi.org/10.1093/intqhc/mzw032) (cit. on p. 57).
- [107] S. Berryhill et al. "Effect of wearables on sleep in healthy individuals: A randomized crossover trial and validation study". In: *Journal of Clinical Sleep Medicine* 16.5 (2020-05), pp. 775–783. DOI: [10.5664/jcsm.8356](https://doi.org/10.5664/jcsm.8356) (cit. on p. 57).
- [108] L. Piwek et al. "The rise of consumer health wearables: Promises and barriers". In: *PLOS Medicine* 13.2 (2016-02), e1001953. DOI: [10.1371/journal.pmed.1001953](https://doi.org/10.1371/journal.pmed.1001953) (cit. on p. 57).
- [109] M. Realist, ed. *The US smartwatch adoption rate continues to increase*. [Online; Accessed July 27, 2022]. URL: <https://marketrealist.com/2019/02/the-us-smartwatch-adoption-rate-continues-to-increase/> (cit. on p. 58).
- [110] J. Kim and G. Yoon. "Study on reusable electrodes for personal electrocardiography". In: *Journal of Sensor Science and Technology* 27.5 (2018), pp. 340–344. DOI: [10.5369/JSST.2018.27.5.340](https://doi.org/10.5369/JSST.2018.27.5.340) (cit. on pp. 59, 60).
- [111] A. Albulbul. "Evaluating major electrode types for idle biological signal measurements for modern medical technology". In: *Bioengineering* 3.3 (2016-08), p. 20. DOI: [10.3390/bioengineering3030020](https://doi.org/10.3390/bioengineering3030020) (cit. on p. 59).
- [112] M. Burke, C. Molloy, and H. Fossan. "Contact monitoring of un-gelled stainless-steel ECG electrodes". In: *International Journal Of Biology and Biomedical Engineering* 10 (2016), pp. 30–39. ISSN: 1998-4510 (cit. on p. 59).

- [113] N. Meziane et al. “Dry electrodes for electrocardiography”. In: *Physiological Measurement* 34.9 (2013-08), R47–R69. DOI: [10.1088/0967-3334/34/9/r47](https://doi.org/10.1088/0967-3334/34/9/r47) (cit. on p. 59).
- [114] D. Pani, A. Achilli, and A. Bonfiglio. “Survey on textile electrode technologies for electrocardiographic (ECG) monitoring, from metal wires to polymers”. In: *Advanced Materials Technologies* 3.10 (2018-06), p. 1800008. DOI: [10.1002/admt.201800008](https://doi.org/10.1002/admt.201800008) (cit. on p. 70).
- [115] C. J. Lee et al. “Neural signal recording using microelectrode arrays fabricated on liquid crystal polymer material”. In: *Materials Science and Engineering: C* 24.1-2 (2004-01), pp. 265–268. DOI: [10.1016/j.msec.2003.09.143](https://doi.org/10.1016/j.msec.2003.09.143) (cit. on p. 70).
- [116] P. W. Macfarlane and J. Kennedy. “Automated ECG interpretation—A brief history from high expectations to deepest networks”. In: *Hearts* 2.4 (2021-09), pp. 433–448. DOI: [10.3390/hearts2040034](https://doi.org/10.3390/hearts2040034) (cit. on p. 76).
- [117] H. V. Pipberger et al. “Preparation of electrocardiographic data for analysis by digital electronic computer”. In: *Circulation* 21.3 (1960-03), pp. 413–418. DOI: [10.1161/01.cir.21.3.413](https://doi.org/10.1161/01.cir.21.3.413) (cit. on p. 76).
- [118] L. Sörnmo and P. Laguna. “The electrocardiogram—a brief background”. In: *Bioelectrical Signal Processing in Cardiac and Neurological Applications*. Elsevier, 2005, pp. 411–452. DOI: [10.1016/b978-012437552-9/50006-4](https://doi.org/10.1016/b978-012437552-9/50006-4) (cit. on pp. 77–80).
- [119] E. Skordalakis. “Recognition of noisy peaks in ECG waveforms”. In: *Computers and Biomedical Research* 17.3 (1984-06), pp. 208–221. DOI: [10.1016/s0010-4809\(84\)80012-9](https://doi.org/10.1016/s0010-4809(84)80012-9) (cit. on p. 77).
- [120] I. Romero, J. Penders, and C. Kriatselis. “P-wave analysis for atrial fibrillation detection in ambulatory recordings”. In: *Journal of Electrocardiology* 43.6 (2010-11), p. 647. DOI: [10.1016/j.jelectrocard.2010.10.022](https://doi.org/10.1016/j.jelectrocard.2010.10.022) (cit. on p. 77).
- [121] J. W. Hurst. “Naming of the waves in the ECG, with a brief account of their genesis”. In: *Circulation* 98.18 (1998-11), pp. 1937–1942. DOI: [10.1161/01.cir.98.18.1937](https://doi.org/10.1161/01.cir.98.18.1937) (cit. on p. 77).
- [122] K. Channer. “ABC of clinical electrocardiography: Myocardial ischaemia”. In: *BMJ* 324.7344 (2002-04), pp. 1023–1026. DOI: [10.1136/bmj.324.7344.1023](https://doi.org/10.1136/bmj.324.7344.1023) (cit. on p. 77).
- [123] K. Venkatachalam, J. E. Herbrandson, and S. J. Asirvatham. “Signals and signal processing for the electrophysiologist”. In: *Circulation: Arrhythmia and Electrophysiology* 4.6 (2011-12), pp. 965–973. DOI: [10.1161/circep.111.964304](https://doi.org/10.1161/circep.111.964304) (cit. on p. 77).
- [124] H. Hermens and Commission des Communautés européennes. *SENIAM: European recommendations for surface electromyography: Results of the SENIAM project*. 2nd ed. [Pays-Bas]: Roessingh Research and Development, 1999 (cit. on p. 77).

- [125] W. G. Stevenson and W. H. Maisel. “Electrocardiography artifact: What you do not know, you do not recognize”. In: *The American Journal of Medicine* 110.5 (2001-04), pp. 402–403. DOI: [10.1016/s0002-9343\(01\)00637-4](https://doi.org/10.1016/s0002-9343(01)00637-4) (cit. on pp. 78, 82).
- [126] J. Rodrigues, D. Belo, and H. Gamboa. “Noise detection on ECG based on agglomerative clustering of morphological features”. In: *Computers in Biology and Medicine* 87 (2017-08), pp. 322–334. DOI: [10.1016/j.combiomed.2017.06.009](https://doi.org/10.1016/j.combiomed.2017.06.009) (cit. on p. 79).
- [127] D. G. Farmer et al. “Brainstem sources of cardiac vagal tone and respiratory sinus arrhythmia”. In: *The Journal of Physiology* 594.24 (2016-12), pp. 7249–7265. DOI: [10.1113/jp273164](https://doi.org/10.1113/jp273164) (cit. on p. 79).
- [128] H. de Talhouet and J. G. Webster. “The origin of skin-stretch-caused motion artifacts under electrodes”. In: *Physiological Measurement* 17.2 (1996-05), pp. 81–93. DOI: [10.1088/0967-3334/17/2/003](https://doi.org/10.1088/0967-3334/17/2/003) (cit. on p. 79).
- [129] Y. M. Chi, T.-P. Jung, and G. Cauwenberghs. “Dry-contact and noncontact biopotential electrodes: Methodological review”. In: *IEEE Reviews in Biomedical Engineering* 3 (2010), pp. 106–119. DOI: [10.1109/rbme.2010.2084078](https://doi.org/10.1109/rbme.2010.2084078) (cit. on pp. 79, 82).
- [130] R. A. Harrigan, T. C. Chan, and W. J. Brady. “Electrocardiographic electrode misplacement, misconnection, and artifact”. In: *The Journal of Emergency Medicine* 43.6 (2012-12), pp. 1038–1044. DOI: [10.1016/j.jemermed.2012.02.024](https://doi.org/10.1016/j.jemermed.2012.02.024) (cit. on pp. 80, 82).
- [131] A. Baranchuk et al. “Electromagnetic interference of communication devices on ECG machines”. In: *Clinical Cardiology* 32.10 (2009-10), pp. 588–592. DOI: [10.1002/clc.20459](https://doi.org/10.1002/clc.20459) (cit. on p. 81).
- [132] S. I. Patel et al. “Equipment-related electrocardiographic artifacts”. In: *Anesthesiology* 108.1 (2008-01), pp. 138–148. DOI: [10.1097/01.anes.0000296537.62905.25](https://doi.org/10.1097/01.anes.0000296537.62905.25) (cit. on p. 81).
- [133] R. R. Gaiser, D. J. Demetry, and R. Schlosser. “Ventricular tachycardia as an electrocardiography artifact during functional endoscopic sinus surgery”. In: *American Journal of Rhinology* 17.2 (2003-03), pp. 83–85. DOI: [10.1177/194589240301700203](https://doi.org/10.1177/194589240301700203) (cit. on p. 81).
- [134] J. Winter, ed. *Ventricular tachycardia (VT)*. [Online; Accessed July 27, 2022]. URL: <https://ecg-educator.blogspot.com/2016/11/ventricular-tachycardia-vt.html> (cit. on p. 81).
- [135] N. Gambarotta et al. “A review of methods for the signal quality assessment to improve reliability of heart rate and blood pressures derived parameters”. In: *Medical and Biological Engineering and Computing* 54.7 (2016-02), pp. 1025–1035. DOI: [10.1007/s11517-016-1453-5](https://doi.org/10.1007/s11517-016-1453-5) (cit. on pp. 82, 84, 85, 88).



- 
- [136] P. S. Hamilton and W. J. Tompkins. “Quantitative investigation of QRS detection rules using the MIT/BIH arrhythmia database”. In: *IEEE Transactions on Biomedical Engineering* BME-33.12 (1986-12), pp. 1157–1165. DOI: [10.1109/tbme.1986.325695](https://doi.org/10.1109/tbme.1986.325695) (cit. on p. 83).
- [137] W. Zong, G. Moody, and D. Jiang. “A robust open-source algorithm to detect onset and duration of QRS complexes”. In: *Computers in Cardiology, 2003*. IEEE, 2003. DOI: [10.1109/cic.2003.1291261](https://doi.org/10.1109/cic.2003.1291261) (cit. on p. 83).
- [138] A. L. Goldberger et al. “PhysioBank, PhysioToolkit, and PhysioNet”. In: *Circulation* 101.23 (2000-06). DOI: [10.1161/01.cir.101.23.e215](https://doi.org/10.1161/01.cir.101.23.e215) (cit. on p. 83).
- [139] B. E. Moody. “Rule-based methods for ECG quality control”. In: *2011 Computing in Cardiology*. IEEE. 2011, pp. 361–363 (cit. on pp. 83, 84).
- [140] L. Johannesen. “Assessment of ECG quality on an Android platform”. In: *2011 Computing in Cardiology*. IEEE. 2011, pp. 433–436 (cit. on p. 83).
- [141] P. Langley et al. “An algorithm for assessment of quality of ECGs acquired via mobile telephones”. In: *2011 Computing in Cardiology*. IEEE. 2011, pp. 281–284 (cit. on p. 83).
- [142] G. D. Clifford, F. Azuaje, P. McSharry, et al. “ECG statistics, noise, artifacts, and missing data”. In: *Advanced methods and tools for ECG data analysis*. Artech House, 2006. Chap. 3, pp. 55–93. ISBN: 9781580539678 (cit. on p. 84).
- [143] C. Orphanidou and I. Drobnjak. “Quality assessment of ambulatory ECG using wavelet entropy of the HRV signal”. In: *IEEE Journal of Biomedical and Health Informatics* 21.5 (2017-09), pp. 1216–1223. DOI: [10.1109/jbhi.2016.2615316](https://doi.org/10.1109/jbhi.2016.2615316) (cit. on pp. 84, 85).
- [144] J. Wang. “A new method for evaluating ECG signal quality for multi-lead arrhythmia analysis”. In: *Computers in Cardiology*. IEEE, 2002, pp. 85–88. DOI: [10.1109/cic.2002.1166713](https://doi.org/10.1109/cic.2002.1166713) (cit. on p. 84).
- [145] D. Hayn, B. Jammerbund, and G. Schreier. “QRS detection based ECG quality assessment”. In: *Physiological Measurement* 33.9 (2012-08), pp. 1449–1461. DOI: [10.1088/0967-3334/33/9/1449](https://doi.org/10.1088/0967-3334/33/9/1449) (cit. on pp. 84, 88).
- [146] D. Hayn, B. Jammerbund, and G. Schreier. “ECG quality assessment for patient empowerment in mHealth applications”. In: *2011 Computing in Cardiology*. IEEE. 2011, pp. 353–356 (cit. on p. 84).
- [147] J. Allen and A. Murray. “Assessing ECG signal quality on a coronary care unit”. In: *Physiological Measurement* 17.4 (1996-11), pp. 249–258. DOI: [10.1088/0967-3334/17/4/002](https://doi.org/10.1088/0967-3334/17/4/002) (cit. on p. 85).
- [148] S. Zaunseder, R. Huhle, and H. Malberg. “CinC challenge—Assessing the usability of ECG by ensemble decision trees”. In: *2011 Computing in Cardiology*. IEEE. 2011, pp. 277–280 (cit. on p. 85).



- [149] Q. Li, R. G. Mark, and G. D. Clifford. “Robust heart rate estimation from multiple asynchronous noisy sources using signal quality indices and a Kalman filter”. In: *Physiological Measurement* 29.1 (2007-12), pp. 15–32. DOI: [10.1088/0967-3334/29/1/002](https://doi.org/10.1088/0967-3334/29/1/002) (cit. on p. 85).
- [150] F. Fu et al. “Comparison of machine learning algorithms for the quality assessment of wearable ECG signals via Lenovo H3 devices”. In: *Journal of Medical and Biological Engineering* 41.2 (2021-04), pp. 231–240. DOI: [10.1007/s40846-020-00588-7](https://doi.org/10.1007/s40846-020-00588-7) (cit. on p. 87).
- [151] G. D. Clifford et al. “Signal quality indices and data fusion for determining clinical acceptability of electrocardiograms”. In: *Physiological Measurement* 33.9 (2012-08), pp. 1419–1433. DOI: [10.1088/0967-3334/33/9/1419](https://doi.org/10.1088/0967-3334/33/9/1419) (cit. on p. 87).
- [152] D. Yoon et al. “Deep learning-based electrocardiogram signal noise detection and screening model”. In: *Healthcare Informatics Research* 25.3 (2019), p. 201. DOI: [10.4258/hir.2019.25.3.201](https://doi.org/10.4258/hir.2019.25.3.201) (cit. on p. 87).
- [153] I. Silva, G. B. Moody, and L. Celi. “Improving the quality of ECGs collected using mobile phones: The Physionet/Computing in Cardiology Challenge 2011”. In: *2011 Computing in Cardiology*. IEEE, 2011, pp. 273–276 (cit. on pp. 88, 98).
- [154] J.-W. Lee et al. “A real time QRS detection using delay-coordinate mapping for the microcontroller implementation”. In: *Annals of Biomedical Engineering* 30.9 (2002-10), pp. 1140–1151. DOI: [10.1114/1.1523030](https://doi.org/10.1114/1.1523030) (cit. on pp. 88, 89).
- [155] A. Eftekhari et al. “Stabilizing embedology: Geometry-preserving delay-coordinate maps”. In: *Physical Review E* 97.2 (2018-02), p. 022222. DOI: [10.1103/physreve.97.022222](https://doi.org/10.1103/physreve.97.022222) (cit. on p. 88).
- [156] A. Jovic and N. Bogunovic. “Feature extraction for ECG time-series mining based on chaos theory”. In: *2007 29th International Conference on Information Technology Interfaces*. IEEE, 2007-06. DOI: [10.1109/iti.2007.4283745](https://doi.org/10.1109/iti.2007.4283745) (cit. on pp. 89, 90).
- [157] A. Kumar. “Chaos theory: Impact on and applications in medicine”. In: *Journal of Health and Allied Sciences NU* 02.04 (2012-12), pp. 93–99. DOI: [10.1055/s-0040-1703623](https://doi.org/10.1055/s-0040-1703623) (cit. on pp. 89, 90).
- [158] E. Gospodinova, M. Gospodinov, and M. Negreva. “Nonlinear dynamics methods for analysis of ECG signals”. In: *Proceedings of the 21st International Conference on Computer Systems and Technologies*. ACM, 2020-06. DOI: [10.1145/3407982.3408000](https://doi.org/10.1145/3407982.3408000) (cit. on p. 90).
- [159] V. Gupta, M. Mittal, and V. Mittal. “Chaos theory and ARTFA: Emerging tools for interpreting ECG signals to diagnose cardiac arrhythmias”. In: *Wireless Personal Communications* 118.4 (2021-04), pp. 3615–3646. DOI: [10.1007/s11277-021-08411-5](https://doi.org/10.1007/s11277-021-08411-5) (cit. on p. 90).

- 
- [160] K. M. Ishtiaq and A. H. M. Z. Karim. "Classification of ECG using chaotic models". In: *International Journal of Modern Education and Computer Science* 4.9 (2012-09), pp. 30–38. DOI: [10.5815/ijmecs.2012.09.04](https://doi.org/10.5815/ijmecs.2012.09.04) (cit. on p. 90).
  - [161] S. K. Nayak et al. "A review on the nonlinear dynamical system analysis of electrocardiogram signal". In: *Journal of Healthcare Engineering* 2018 (2018), pp. 1–19. DOI: [10.1155/2018/6920420](https://doi.org/10.1155/2018/6920420) (cit. on p. 90).
  - [162] J. Canny. "A computational approach to edge detection". In: *IEEE Transactions on Pattern Analysis and Machine Intelligence* PAMI-8.6 (1986-11), pp. 679–698. DOI: [10.1109/tpami.1986.4767851](https://doi.org/10.1109/tpami.1986.4767851) (cit. on p. 90).
  - [163] R. Laurini. "Geographic relations". In: *Geographic Knowledge Infrastructure*. Elsevier, 2017, pp. 83–109. DOI: [10.1016/b978-1-78548-243-4.50005-0](https://doi.org/10.1016/b978-1-78548-243-4.50005-0) (cit. on p. 91).
  - [164] E. Haines. "Point in polygon strategies". In: ed. by P. S. Heckbert. Academic Press, 1994. Chap. I.4, pp. 24–46. ISBN: 0-12-336155-9 (cit. on p. 91).
  - [165] Z. Huang and J. Leng. "Analysis of Hu's moment invariants on image scaling and rotation". In: *2010 2nd International Conference on Computer Engineering and Technology*. IEEE, 2010. DOI: [10.1109/iccet.2010.5485542](https://doi.org/10.1109/iccet.2010.5485542) (cit. on p. 92).
  - [166] LearnOpenCV, ed. *Shape matching using Hu moments (C++/Python)*. [Online; Accessed July 27, 2022]. URL: <https://learnopencv.com/shape-matching-using-hu-moments-c-python> (cit. on p. 92).
  - [167] M.-K. Hu. "Visual pattern recognition by moment invariants". In: *IEEE Transactions on Information Theory* 8.2 (1962-02), pp. 179–187. DOI: [10.1109/tit.1962.1057692](https://doi.org/10.1109/tit.1962.1057692) (cit. on p. 92).
  - [168] S. Raschka. *STAT 479: Machine learning lecture notes*. [Online; Accessed July 27, 2022]. Department of Statistics University of Wisconsin–Madison. 2018-09. URL: [https://sebastianraschka.com/pdf/lecture-notes/stat479fs18/02\\_knn\\_notes.pdf](https://sebastianraschka.com/pdf/lecture-notes/stat479fs18/02_knn_notes.pdf) (cit. on p. 93).
  - [169] S. Suthaharan. "A cognitive random forest". In: *Handbook of Statistics*. Elsevier, 2016, pp. 207–227. DOI: [10.1016/bs.host.2016.07.006](https://doi.org/10.1016/bs.host.2016.07.006) (cit. on p. 93).
  - [170] H.-H. Bock. "Clustering methods: A history of k-Means algorithms". In: *Selected Contributions in Data Analysis and Classification*. Springer Berlin Heidelberg, 2007, pp. 161–172. DOI: [10.1007/978-3-540-73560-1\\_15](https://doi.org/10.1007/978-3-540-73560-1_15) (cit. on p. 93).
  - [171] J. Bell. "Machine learning". In: 2nd ed. Nashville, TN: John Wiley & Sons, 2020-04. Chap. 8 - Support Vector Machines, pp. 143–151. ISBN: 978-1-119-64214-5 (cit. on p. 93).
  - [172] X. Feng et al. "Computer vision algorithms and hardware implementations: A survey". In: *Integration* 69 (2019-11), pp. 309–320. DOI: [10.1016/j.vlsi.2019.07.005](https://doi.org/10.1016/j.vlsi.2019.07.005) (cit. on p. 93).

- [173] A. Shrestha and A. Mahmood. “Review of deep learning algorithms and architectures”. In: *IEEE Access* 7 (2019), pp. 53040–53065. DOI: [10.1109/access.2019.2912200](https://doi.org/10.1109/access.2019.2912200) (cit. on pp. 93, 94).
- [174] R. Pramoditha, ed. *The concept of artificial neurons (perceptrons) in neural networks*. [Online; Accessed July 27, 2022]. URL: [https://miro.medium.com/max/700/1\\*hkY1T0DpjJgo32DoCOWN5w.png](https://miro.medium.com/max/700/1*hkY1T0DpjJgo32DoCOWN5w.png) (cit. on p. 93).
- [175] S. Saha, ed. *A comprehensive guide to convolutional neural networks — The ELI5 way*. [Online; Accessed July 27, 2022]. URL: [https://miro.medium.com/max/1400/1\\*uAeANQIQPqWZnnuH-VEyw.jpeg](https://miro.medium.com/max/1400/1*uAeANQIQPqWZnnuH-VEyw.jpeg) (cit. on p. 94).
- [176] G. Clifford et al. “AF classification from a short single lead ECG recording: the Physionet computing in cardiology challenge 2017”. In: *Computing in Cardiology Conference (CinC)*. Computing in Cardiology, 2017-09. DOI: [10.22489/cinc.2017.065-469](https://doi.org/10.22489/cinc.2017.065-469) (cit. on p. 96).
- [177] A. Goodwin et al. “Classification of atrial fibrillation using multidisciplinary features and gradient boosting”. In: *Computing in Cardiology Conference (CinC)*. Computing in Cardiology, 2017-09. DOI: [10.22489/cinc.2017.361-352](https://doi.org/10.22489/cinc.2017.361-352) (cit. on p. 107).
- [178] Z. Xiong, M. Stiles, and J. Zhao. “Robust ECG signal classification for the detection of atrial fibrillation using novel neural networks”. In: *Computing in Cardiology Conference (CinC)*. Computing in Cardiology, 2017-09. DOI: [10.22489/cinc.2017.066-138](https://doi.org/10.22489/cinc.2017.066-138) (cit. on p. 107).
- [179] S. Yazdani et al. “Heart rhythm classification using short-term ECG atrial and ventricular activity analysis”. In: *Computing in Cardiology Conference (CinC)*. Computing in Cardiology, 2017-09. DOI: [10.22489/cinc.2017.067-120](https://doi.org/10.22489/cinc.2017.067-120) (cit. on pp. 107, 108).
- [180] M. Zabihi et al. “Detection of atrial fibrillation in ECG hand-held devices using a random forest classifier”. In: *Computing in Cardiology Conference (CinC)*. Computing in Cardiology, 2017-09. DOI: [10.22489/cinc.2017.069-336](https://doi.org/10.22489/cinc.2017.069-336) (cit. on p. 107).
- [181] J. A. Behar et al. “Rhythm and quality classification from short ECGs recorded using a mobile device”. In: *Computing in Cardiology Conference (CinC)*. Computing in Cardiology, 2017-09. DOI: [10.22489/cinc.2017.165-056](https://doi.org/10.22489/cinc.2017.165-056) (cit. on p. 107).
- [182] I. Nicander et al. “Baseline electrical impedance measurements at various skin sites - related to age and sex”. In: *Skin Research and Technology* 3.4 (1997-11), pp. 252–258. DOI: [10.1111/j.1600-0846.1997.tb00194.x](https://doi.org/10.1111/j.1600-0846.1997.tb00194.x) (cit. on p. 115).
- [183] S. Hochreiter and J. Schmidhuber. “Long short-term memory”. In: *Neural Computation* 9.8 (1997-11), pp. 1735–1780. DOI: [10.1162/neco.1997.9.8.1735](https://doi.org/10.1162/neco.1997.9.8.1735) (cit. on p. 116).

- 
- [184] D. N. Osório et al. “Development and validation of an experimental protocol to evaluate posture control”. In: *IFIP Advances in Information and Communication Technology*. Springer International Publishing, 2020, pp. 387–394. DOI: [10.1007/978-3-030-45124-0\\_37](https://doi.org/10.1007/978-3-030-45124-0_37) (cit. on p. 117).
- [185] R. Lima, D. Osório, and H. Gamboa. “Heart rate variability and electrodermal activity biosignal processing: Predicting the autonomous nervous system response in mental stress”. In: *Biomedical Engineering Systems and Technologies*. Springer International Publishing, 2020, pp. 328–351. DOI: [10.1007/978-3-030-46970-2\\_16](https://doi.org/10.1007/978-3-030-46970-2_16) (cit. on p. 117).
- [186] A. Lopes et al. “Equivalent pipeline processing for IR-UWB and FMCW radar comparison in vital signs monitoring applications”. In: *IEEE Sensors Journal* 22.12 (2022-06), pp. 12028–12035. DOI: [10.1109/jsen.2022.3173218](https://doi.org/10.1109/jsen.2022.3173218) (cit. on p. 117).
- [187] C. Cepeda et al. “Latent: A flexible data collection tool to research human behavior in the context of web navigation”. In: *IEEE Access* 7 (2019), pp. 77659–77673. DOI: [10.1109/access.2019.2916996](https://doi.org/10.1109/access.2019.2916996) (cit. on p. 117).
- [188] J. Rodrigues et al. “A genetic algorithm to design job rotation schedules with low risk exposure”. In: *IFIP Advances in Information and Communication Technology*. Springer International Publishing, 2020, pp. 395–402. DOI: [10.1007/978-3-030-45124-0\\_38](https://doi.org/10.1007/978-3-030-45124-0_38) (cit. on p. 117).
- [189] A. Assunção et al. “A genetic algorithm approach to design job rotation schedules ensuring homogeneity and diversity of exposure in the automotive industry”. In: *Heliyon* 8.5 (2022-05), e09396. DOI: [10.1016/j.heliyon.2022.e09396](https://doi.org/10.1016/j.heliyon.2022.e09396) (cit. on p. 117).
- [190] F. Chouchou et al. “Dominance in cardiac parasympathetic activity during real recreational SCUBA diving”. In: *European Journal of Applied Physiology* 106.3 (2009-03), pp. 345–352. DOI: [10.1007/s00421-009-1010-0](https://doi.org/10.1007/s00421-009-1010-0) (cit. on p. 136).

## TYPICAL HRV FEATURES

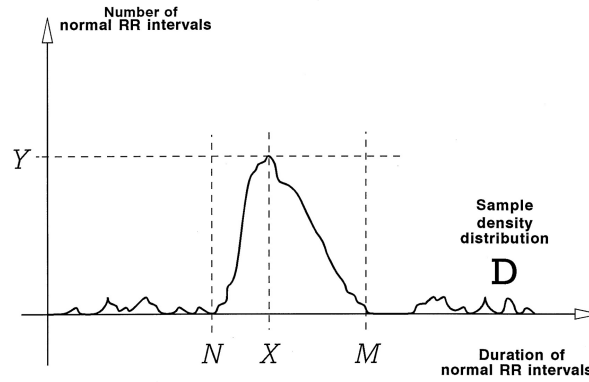


Figure A.1: Sample density distribution of the RR intervals. The letter Y is the maximum of this distribution, having a normal RR interval bin X. N and M are used to get the TINN, the width of the triangle. Extracted from [16].

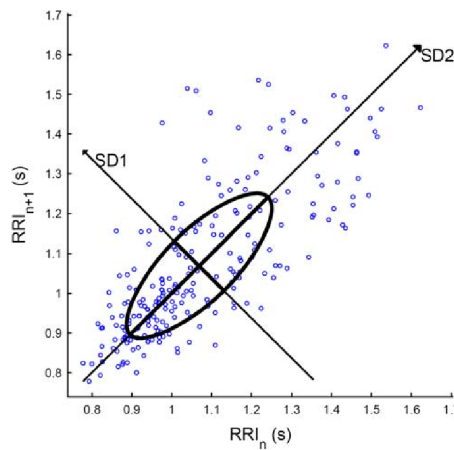


Figure A.2: Example of a Poincaré plot. It is possible to see the two main axes of the ellipsis, SD1 corresponding to its width, and SD2 corresponding to its height. Extracted from [190].

Table A.1: Principal metrics used in HRV [16, 64, 74].

#### Time domain features

SDNN	Standard deviation of normal beat intervals (ms)
RMSSD	Root mean square of successive difference (ms)
SDSD	Standard deviation of the successive difference (ms)
NNxx	Number successive NNs pairs larger than a given threshold
pNNxx	Percentage of number successive NNs pairs larger than a given threshold (%)
HTI	HRV triangular index
TINN	Triangular interpolation of NN histogram (ms)

#### Frequency domain features

ULF ( $<0.003\text{Hz}$ )	Ultra low frequencies ( $\text{ms}^2$ )
VLF ( $0.003 - 0.04\text{Hz}$ )	Very low frequencies ( $\text{ms}^2$ )
LF ( $0.04 - 0.15\text{Hz}$ )	Low frequencies ( $\text{ms}^2$ )
HF ( $0.15 - 0.40\text{Hz}$ )	High frequencies ( $\text{ms}^2$ )
TP ( $0.04 - 0.40\text{Hz}$ )	Total Power ( $\text{ms}^2$ )
nuLF ( $0.04 - 0.15\text{Hz}$ )	Normalized units low frequencies (LF/TP)
nuHF ( $0.15 - 0.40\text{Hz}$ )	Normalized units high frequencies (LF/TP)
LF/HF ratio	Low to high frequency ratio

#### Non-linear domain features

S	Total area of the Poincaré plot ellipsis
SD1	Width of the Poincaré plot ellipsis
SD2	Length of the Poincaré plot ellipsis
SD1/SD2	Ratio between the width and the length
ApEn	Aproximate entropy
SampEn	Sample entropy
MSE	Multiscale entropy
DFA	Detrended fluctuation analysis
CD	Correlation dimension

## REMOTE ISCHEMIC CONDITIONING

Table B.1: Overview of pre pilot subjects condition. This table is divided into demographics and current medication for the all the individuals and the two sub sets, senior and young. Two senior individuals were fully excluded from the data analysis due to missing data.

	Included subjects (n=18)	Senior subjects (n=8)	Young subjects (n=10)
<b>Demographics</b>			
Age, years	47.0 $\pm$ 21.9	69.6 $\pm$ 7.6	28.9 $\pm$ 6.3
Female sex	11 (61.1%)	6 (75.0%)	5 (50%)
<b>Cardiovascular risk factors</b>			
Arterial Hypertension	5 (27.8%)	5 (62.5%)	0 (0.0%)
Diabetes	2 (11.1%)	2 (25.0%)	0 (0.0%)
Dyslipidemia	6 (33.3%)	6 (75.0%)	0 (0.0%)
Smoking	3 (16.7%)	2 (25.0%)	1 (10.0%)
Obesity	1 (5.6%)	1 (12.5%)	0 (0.0%)
Coronary artery disease	0 (0.0%)	0 (0.0%)	0 (0.0%)
Atrial fibrillation	0 (0.0%)	0 (0.0%)	0 (0.0%)
<b>Current medication</b>			
Beta-blocker	1 (5.6%)	1 (12.5%)	0 (0.0%)
Alfa-blocker	1 (5.6%)	1 (12.5%)	0 (0.0%)
Calcium channel blockers	1 (5.6%)	1 (12.5%)	0 (0.0%)



Table B.2: Global population analysis for the first and last 10 minutes and occlusion and non-occlusion intervals. Statistically significant values are in bold.

Global population		First 10 minutes mean	Last 10 minutes mean	First vs Last	Wilcoxon signed-rank test p-value: Before - After pairs
<b>Time Features</b>	Mean R-R Interval (ms)	819.069	834.266	Last higher	0.076
	Median R-R Interval (ms)	821.868	837.588	Last higher	0.107
	pNN50 (%)	11.351	11.670	Last higher	0.619
	RMSSD (ms)	32.430	34.152	Last higher	0.435
<b>Frequency Features</b>	nuLF PSD (%)	40.971	44.029	Last higher	0.193
	nuHF PSD (%)	36.176	32.912	First higher	0.107
	nuLF/nuHF ratio	1.424	1.644	Last higher	0.149
<b>Non linear Features</b>	SD1 axis (ms)	22.931	24.148	Last higher	0.435
	SD2 axis (ms)	69.039	78.627	Last higher	<b>0.044</b>
	SD1/SD2 ratio	0.352	0.316	First higher	0.149

Global population (continuation)		Non-occlusion	Occlusion	Non-Occlusion	Wilcoxon signed-rank test
		intervals mean	intervals mean	vs Occlusion	p-value: non-occlusion - occlusion
Time Features	Mean R-R Interval (ms)	827.052	823.577	Non-occlusion higher	0.210
	Median R-R Interval (ms)	829.437	825.779	Non-occlusion higher	0.177
	pNN50 (%)	11.541	11.112	Non-occlusion higher	0.084
	RMSSD (ms)	33.639	32.572	Non-occlusion higher	<b>0.044</b>
Frequency Features	nuLF <b>PSD</b> (%)	42.690	43.588	Occlusion higher	0.586
	nuHF <b>PSD</b> (%)	33.872	33.824	Non-occlusion higher	0.868
	nuLF/nuHF ratio	1.583	1.706	Occlusion higher	0.723
Non linear Features	SD1 axis (ms)	23.785	23.031	Non-occlusion higher	<b>0.044</b>
	SD2 axis (ms)	74.078	71.451	Non-occlusion higher	0.084
	SD1/SD2 ratio	0.335	0.327	Non-occlusion higher	0.332

Table B.3: Senior population analysis for the first and last 10 minutes and occlusion and non-occlusion intervals. Statistically significant values are in bold.

Senior population		First 10 minutes	Last 10 minutes	First vs Last	Wilcoxon signed-rank test p-value: Before - After pairs
		Mean	Mean		
<b>Time Features</b>	Mean R-R Interval (ms)	834.475	854.718	Last higher	0.128
	Median R-R Interval (ms)	836.929	859.607	Last higher	0.176
	pNN50 (%)	4.655	4.298	First higher	0.866
	RMSSD (ms)	24.387	26.096	Last higher	0.866
<b>Frequency Features</b>	nuLF PSD (%)	32.571	38.143	Last higher	0.310
	nuHF PSD (%)	45.429	40.714	First higher	0.310
	nuLF/nuHF ratio	0.900	1.158	Last higher	0.398
<b>Non linear Features</b>	SD1 axis (ms)	17.244	18.452	Last higher	0.866
	SD2 axis (ms)	44.309	59.366	Last higher	<b>0.018</b>
	SD1/SD2 ratio	0.416	0.329	First higher	0.128

Senior population (continuation)		Non-occlusion	Occlusion	Non-Occlusion	Wilcoxon signed-rank test
		intervals mean	intervals mean	vs Occlusion	p-value: non-occlusion - occlusion
Time Features	Mean R-R Interval (ms)	842.691	833.762	Non-occlusion higher	0.176
	Median R-R Interval (ms)	845.401	835.339	Non-occlusion higher	0.176
	pNN50 (%)	4.310	4.069	Non-occlusion higher	0.237
	RMSSD (ms)	25.637	24.216	Non-occlusion higher	0.310
Frequency Features	nuLF PSD (%)	35.629	36.143	Occlusion higher	0.612
	nuHF PSD (%)	42.058	41.000	Non-occlusion higher	0.612
	nuLF/nuHF ratio	1.096	1.191	Occlusion higher	0.866
Non linear Features	SD1 axis (ms)	18.128	17.123	Non-occlusion higher	0.310
	SD2 axis (ms)	51.500	48.099	Non-occlusion higher	0.176
	SD1/SD2 ratio	0.371	0.353	Non-occlusion higher	0.237

Table B.4: Young population analysis for the first and last 10 minutes and occlusion and non-occlusion intervals. Statistically significant values are in bold.

Young population		First 10 minutes Mean	Last 10 minutes Mean	First vs Last	Wilcoxon signed-rank test p-value: Before - After pairs
<b>Time Features</b>	Mean R-R Interval (ms)	808.285	819.949	Last higher	0.285
	Median R-R Interval (ms)	811.325	822.175	Last higher	0.359
	pNN50 (%)	16.039	16.830	Last higher	0.508
	RMSSD (ms)	38.061	39.792	Last higher	0.445
<b>Frequency Features</b>	nuLF <b>PSD</b> (%)	46.850	48.150	Last higher	0.444
	nuHF <b>PSD</b> (%)	29.700	27.450	First higher	0.102
	nuLF/nuHF ratio	1.791	1.985	Last higher	0.241
<b>Non linear Features</b>	SD1 axis (ms)	26.912	28.136	Last higher	0.445
	SD2 axis (ms)	86.350	92.111	Last higher	0.508
	SD1/SD2 ratio	0.308	0.307	First higher	0.878

Young population (continuation)		Non-occlusion	Occlusion	Non-Occlusion	Wilcoxon signed-rank test
		intervals mean	intervals mean	vs Occlusion	p-value: non-occlusion - occlusion
Time Features	Mean R-R Interval (ms)	816.104	816.448	Occlusion higher	0.959
	Median R-R Interval (ms)	818.261	819.087	Occlusion higher	0.878
	pNN50 (%)	16.602	16.042	Non-occlusion higher	0.241
	RMSSD (ms)	39.240	38.422	Non-occlusion higher	0.093
Frequency Features	nuLF PSD (%)	47.632	48.800	Occlusion higher	0.575
	nuHF PSD (%)	28.142	28.800	Occlusion higher	0.878
	nuLF/nuHF ratio	1.924	2.066	Occlusion higher	0.799
Non linear Features	SD1 axis (ms)	27.746	27.168	Non-occlusion higher	0.093
	SD2 axis (ms)	89.882	87.798	Non-occlusion higher	0.333
	SD1/SD2 ratio	0.310	0.308	Non-occlusion higher	0.721

## PROPOSED MOBILE ECG ACQUISITION SYSTEM

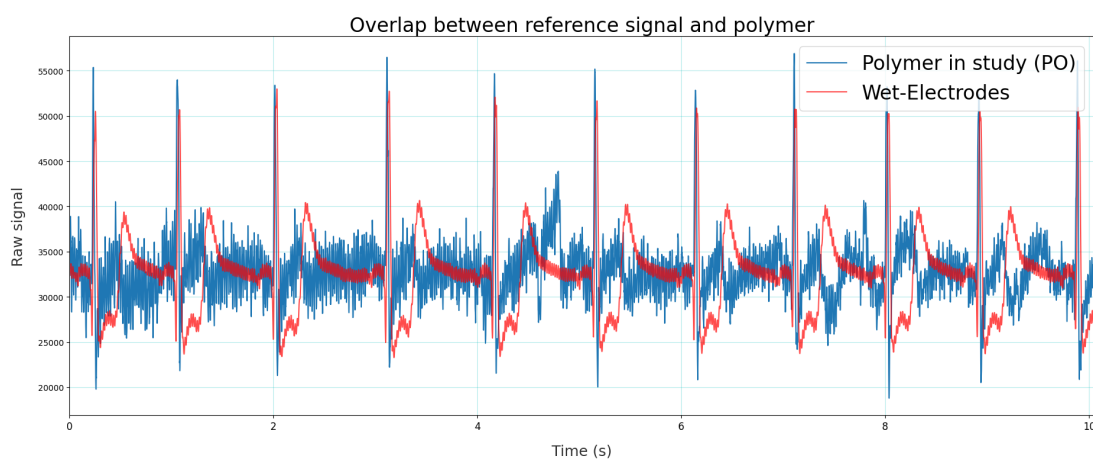


Figure C.1: Example of the raw signal using the PolyOne's OnForce LFT LF6600-5023 dry electrodes (blue line), overlapping the signal recorded with the reference wet-electrodes (red line).



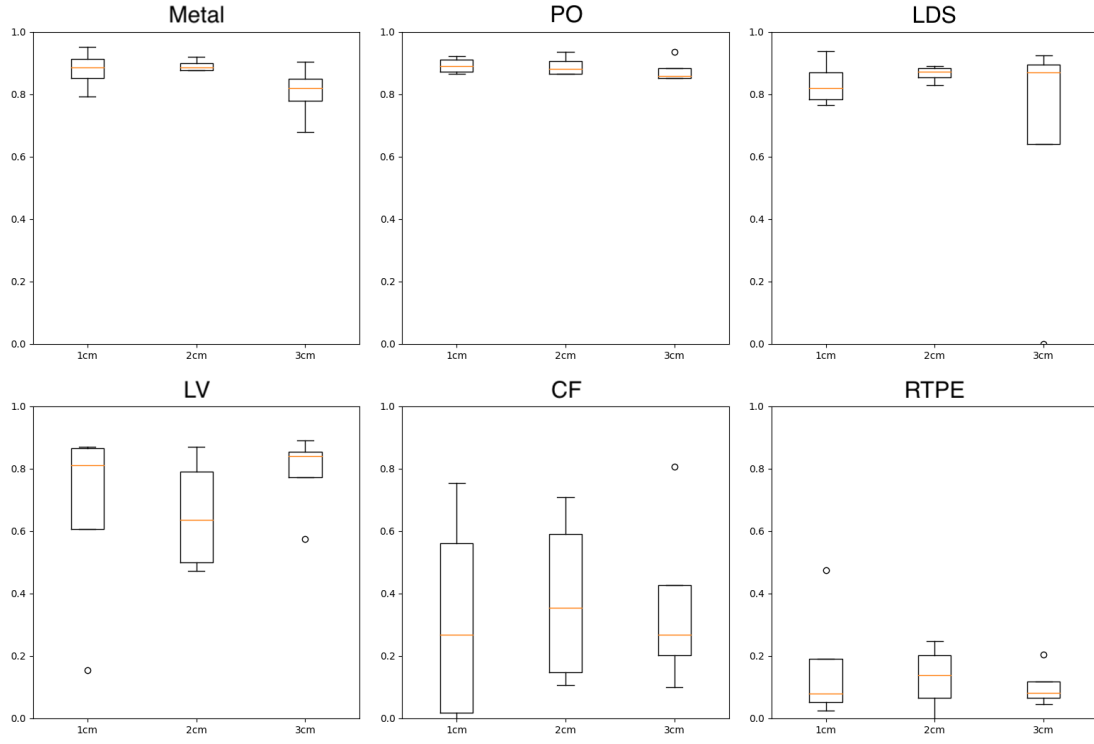


Figure C.2: Boxplot with the cosine similarity per material and per distance.

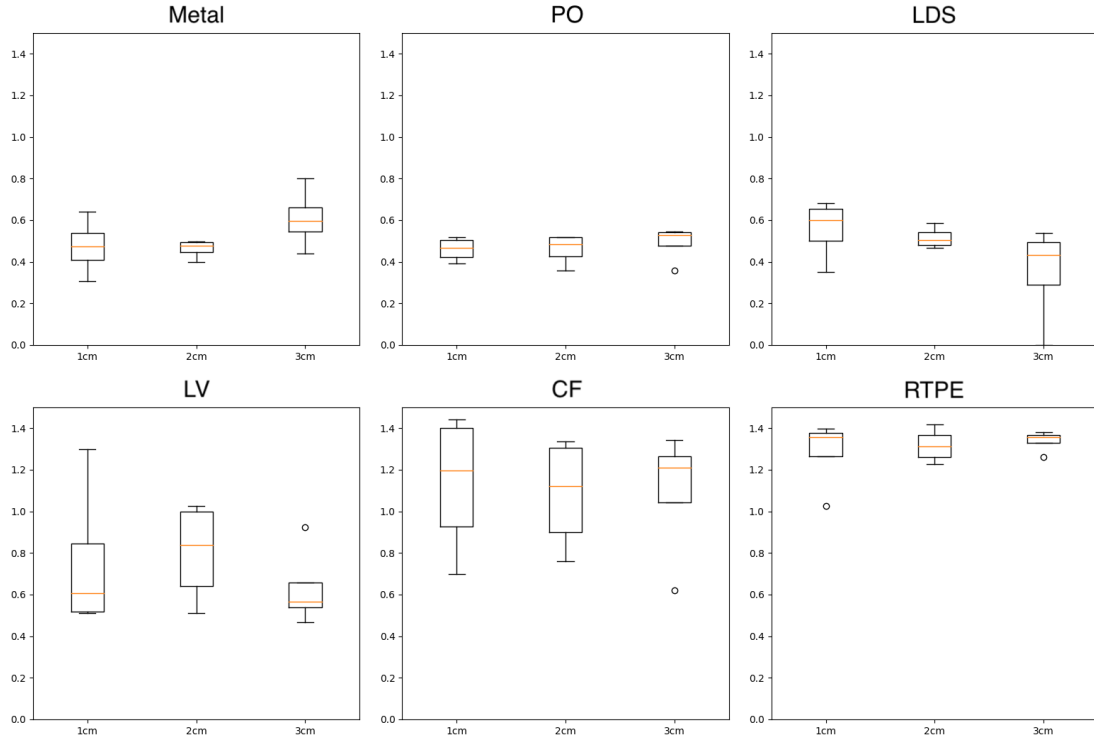


Figure C.3: Boxplot with the NRMSE per material and per distance.

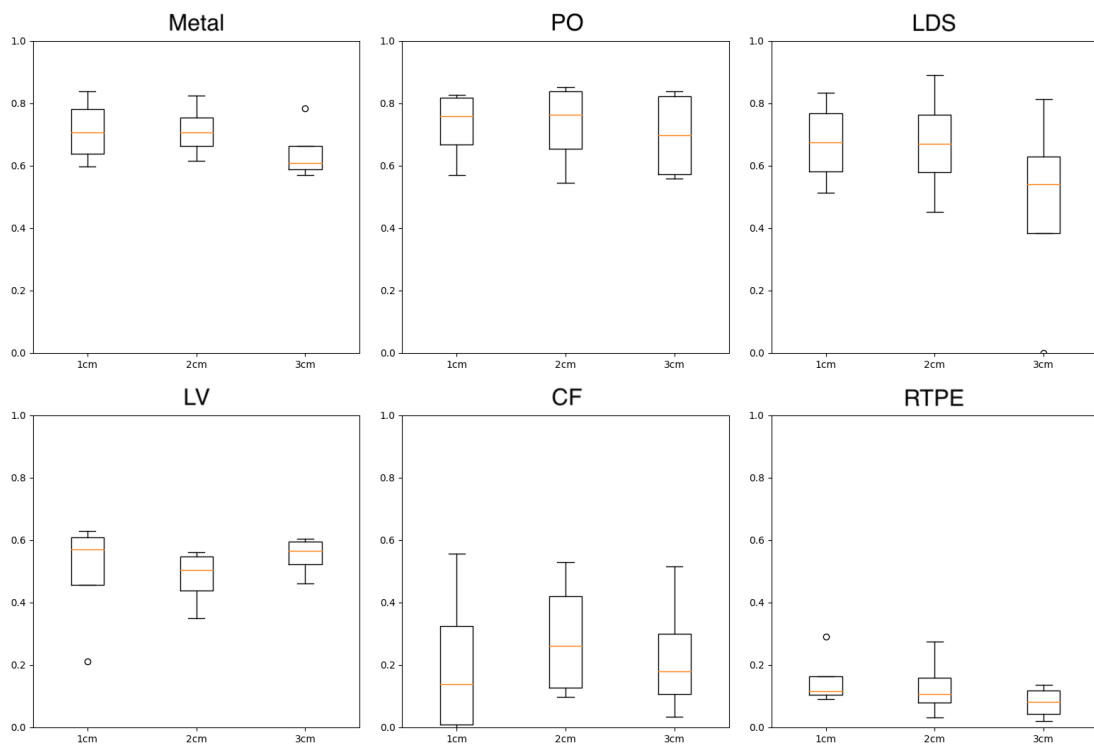


Figure C.4: Boxplot with the Spearman correlation per material and per distance.

## HU IMAGE MOMENTS

The regular moment of a shape (for a binary image) can be obtained using the following equation (Equation D.1):

$$M_{ij} = \sum_x \sum_y x^i y^j I(x, y) \quad (\text{D.1})$$

, where  $I(x, y)$  is the pixel intensity at the  $x$  and  $y$  coordinates, while  $i$  and  $j$  are integers denoting the moment order. This calculation is based on the intensity of all the pixels, and not their position. The image centroid can then be used to obtain translation invariance. The centroid can be calculated using the following equations (Equations D.2 and D.3):

$$\bar{x} = \frac{M_{10}}{M_{00}} \quad (\text{D.2})$$

$$\bar{y} = \frac{M_{01}}{M_{00}} \quad (\text{D.3})$$

, where  $\bar{x}$  and  $\bar{y}$  are the coordinates of the image centroid. With these coordinates, the central moments can be calculated, which are obtained by subtracting the centroids from the  $x$  and  $y$  coordinate, and thus becoming invariant to translation, nullifying the effect of the location of the shape (Equation D.4).

$$\mu_{ij} = \sum_x \sum_y (x - \bar{x})^i (y - \bar{y})^j I(x, y) \quad (\text{D.4})$$

To convert the already translation invariant moments to also scale invariant, these can be normalized using the following equation (Equation D.5):

$$\eta_{ij} = \frac{\mu_{ij}}{\mu_{00}^{\frac{(i+j)}{2} + 1}} \quad (\text{D.5})$$

---

Using these normalized moments, the Hu image moments can be constructed. The 7 moments are invariant to translation, scale, rotation, and reflection. The moments are as follow:

$$\begin{aligned}
h_0 &= \eta_{20} + \eta_{02} \\
h_1 &= (\eta_{20} - \eta_{02})^2 + 4\eta_{11}^2 \\
h_2 &= (\eta_{30} - 3\eta_{12})^2 + (3\eta_{21} - \eta_{03})^2 \\
h_3 &= (\eta_{30} + \eta_{12})^2 + (\eta_{21} + \eta_{03})^2 \\
h_4 &= (\eta_{30} - 3\eta_{12})(\eta_{30} + \eta_{12})[(\eta_{30} + \eta_{12})^2 - 3(\eta_{21} + \eta_{03})^2] \\
&\quad + (3\eta_{21} - \eta_{03})[3(\eta_{30} + \eta_{12})^2 - (\eta_{21} + \eta_{03})^2] \\
h_5 &= (\eta_{20} - \eta_{02})[(\eta_{30} + \eta_{12})^2 - (\eta_{21} + \eta_{03})^2 + 4\eta_{11}(\eta_{30} + \eta_{12})(\eta_{21} + \eta_{03})] \\
h_6 &= (3\eta_{21} - \eta_{03})(\eta_{30} + \eta_{12})[(\eta_{30} + \eta_{12})^2 - 3(\eta_{21} + \eta_{03})^2] \\
&\quad + (\eta_{30} - 3\eta_{12})(\eta_{21} + \eta_{03})[3(\eta_{30} + \eta_{12})^2 - (\eta_{21} + \eta_{03})^2]
\end{aligned} \tag{D.6}$$

## SIGNAL QUALITY INDEX TABLE APPENDIX

### E.1 Hu Image Moments

#### E.1.1 **k-NN**

For this classifier, the *KNeighborsClassifier* function from the Python package *sklearn* was used. For each of the estimators (3 in total, each using a different metric to assess the performance of the grid search optimizer), the following parameters were evaluated:

- Number of neighbors: between 1 and 25;
- Weight: uniform or by distance (closer points have more weight);
- Distance metric: Euclidean, Cosine, or Minkowski;

Table E.1: **k-NN** classifier results for a 20ms delay and using the *accuracy* score metric for the optimizer. Parameters after optimization: Number of neighbors - 6; Distance metric - euclidean; Weights - uniform.

Test set		20ms Delay	Validation set	
Normal	Noise		Normal	Noise
29	6	Normal	32	3
10	5	Noise	9	6

(a) **k-NN** classifier confusion matrices.

Test set					Validation set			
Precision	Recall	F1-score	Support		Precision	Recall	F1-score	Support
0.74	0.83	0.78	35	Normal	0.78	0.91	0.84	35
0.45	0.33	0.38	15	Noisy	0.67	0.40	0.50	15
		0.68	50	Accuracy			0.76	50
0.60	0.58	0.58	50	Macro avg	0.72	0.66	0.67	50
0.66	0.68	0.66	50	Weighted avg	0.75	0.76	0.74	50

(b) **k-NN** classification reports.

Table E.2: **k-NN** classifier results for a 20ms delay and using the *F1-Score* score metric for the optimizer. Parameters after optimization: Number of neighbors - 11; Distance metric - cosine; Weights - uniform.

Test set		20ms Delay	Validation set	
Normal	Noise		Normal	Noise
30	5	Normal	30	5
6	9	Noise	3	12

(a) **k-NN** classifier confusion matrices.

Test set					Validation set			
Precision	Recall	F1-score	Support		Precision	Recall	F1-score	Support
0.83	0.86	0.85	35	Normal	0.91	0.86	0.88	35
0.64	0.60	0.62	15	Noisy	0.71	0.80	0.75	15
		0.78	50	Accuracy			0.84	50
0.74	0.73	0.73	50	Macro avg	0.81	0.83	0.82	50
0.78	0.78	0.78	50	Weighted avg	0.85	0.84	0.84	50

(b) **k-NN** classification reports.

Table E.3: **k-NN** classifier results for a 20ms delay and using the *F1 Macro Average* score metric for the optimizer. Parameters after optimization: Number of neighbors - 11; Distance metric - cosine; Weights - uniform.

Test set		20ms Delay	Validation set	
Normal	Noise		Normal	Noise
30	5	Normal	30	5
6	9	Noise	3	12

(a) **k-NN** classifier confusion matrices.

Test set					Validation set			
Precision	Recall	F1-score	Support		Precision	Recall	F1-score	Support
0.83	0.86	0.85	35	Normal	0.91	0.86	0.88	35
0.64	0.60	0.62	15	Noisy	0.71	0.80	0.75	15
		0.78	50	Accuracy			0.84	50
0.74	0.73	0.73	50	Macro avg	0.81	0.83	0.82	50
0.78	0.78	0.78	50	Weighted avg	0.85	0.84	0.84	50

(b) **k-NN** classification reports.

Table E.4: **k-NN** classifier results for a 30ms delay and using the *accuracy* score metric for the optimizer. Parameters after optimization: Number of neighbors - 6; Distance metric - euclidean; Weights - uniform.

Test set		30ms Delay	Validation set	
Normal	Noise		Normal	Noise
28	7	Normal	30	5
6	9	Noise	3	12

(a) **k-NN** classifier confusion matrices.

Test set					Validation set			
Precision	Recall	F1-score	Support		Precision	Recall	F1-score	Support
0.82	0.80	0.81	35	Normal	0.91	0.86	0.88	35
0.56	0.60	0.58	15	Noisy	0.71	0.80	0.75	15
		0.74	50	Accuracy			0.84	50
0.69	0.70	0.70	50	Macro avg	0.81	0.83	0.82	50
0.75	0.74	0.74	50	Weighted avg	0.85	0.84	0.84	50

(b) **k-NN** classification reports.

Table E.5: **k-NN** classifier results for a 30ms delay and using the *F1-Score* score metric for the optimizer. Parameters after optimization: Number of neighbors - 13; Distance metric - cosine; Weights - uniform.

Test set		30ms Delay	Validation set	
Normal	Noise		Normal	Noise
28	7	Normal	30	5
6	9	Noise	3	12

(a) **k-NN** classifier confusion matrices.

Test set					Validation set			
Precision	Recall	F1-score	Support		Precision	Recall	F1-score	Support
0.82	0.80	0.81	35	Normal	0.91	0.86	0.88	35
0.56	0.60	0.58	15	Noisy	0.71	0.80	0.75	15
		0.74	50	Accuracy			0.84	50
0.69	0.70	0.70	50	Macro avg	0.81	0.83	0.82	50
0.75	0.74	0.74	50	Weighted avg	0.85	0.84	0.84	50

(b) **k-NN** classification reports.

Table E.6:  $k$ -NN classifier results for a 30ms delay and using the *F1 Macro Average* score metric for the optimizer. Parameters after optimization: Number of neighbors - 13; Distance metric - cosine; Weights - uniform.

Test set		30ms Delay	Validation set	
Normal	Noise		Normal	Noise
28	7	Normal	30	5
6	9	Noise	3	12

(a)  $k$ -NN classifier confusion matrices.

Test set					Validation set			
Precision	Recall	F1-score	Support		Precision	Recall	F1-score	Support
0.82	0.80	0.81	35	Normal	0.91	0.86	0.88	35
0.56	0.60	0.58	15	Noisy	0.71	0.80	0.75	15
		0.74	50	Accuracy			0.84	50
0.69	0.70	0.70	50	Macro avg	0.81	0.83	0.82	50
0.75	0.74	0.74	50	Weighted avg	0.85	0.84	0.84	50

(b)  $k$ -NN classification reports.

Table E.7:  $k$ -NN classifier results for a 40ms delay and using the *accuracy* score metric for the optimizer. Parameters after optimization: Number of neighbors - 19; Distance metric - cosine; Weights - uniform.

Test set		40ms Delay	Validation set	
Normal	Noise		Normal	Noise
28	7	Normal	28	7
7	8	Noise	5	10

(a)  $k$ -NN classifier confusion matrices.

Test set					Validation set			
Precision	Recall	F1-score	Support		Precision	Recall	F1-score	Support
0.80	0.80	0.80	35	Normal	0.85	0.80	0.82	35
0.53	0.53	0.53	15	Noisy	0.59	0.67	0.62	15
		0.72	50	Accuracy			0.76	50
0.67	0.67	0.67	50	Macro avg	0.72	0.73	0.72	50
0.72	0.72	0.72	50	Weighted avg	0.77	0.76	0.76	50

(b)  $k$ -NN classification reports.



Table E.8: **k-NN** classifier results for a 40ms delay and using the *F1-Score* score metric for the optimizer. Parameters after optimization: Number of neighbors - 17; Distance metric - cosine; Weights - uniform.

Test set		40ms Delay	Validation set	
Normal	Noise		Normal	Noise
30	5		29	6
7	8		5	10

(a) **k-NN** classifier confusion matrices.

Test set					Validation set			
Precision	Recall	F1-score	Support		Precision	Recall	F1-score	Support
0.81	0.86	0.83	35		0.85	0.83	0.84	35
0.62	0.53	0.57	15		0.62	0.67	0.65	15
		0.76	50	Accuracy			0.78	50
0.71	0.70	0.70	50	Macro avg	0.74	0.75	0.74	50
0.75	0.76	0.75	50	Weighted avg	0.78	0.78	0.78	50

(b) **k-NN** classification reports.

Table E.9: **k-NN** classifier results for a 40ms delay and using the *F1 Macro Average* score metric for the optimizer. Parameters after optimization: Number of neighbors - 17; Distance metric - cosine; Weights - uniform.

Test set		40ms Delay	Validation set	
Normal	Noise		Normal	Noise
30	5		29	6
7	8		5	10

(a) **k-NN** classifier confusion matrices.

Test set					Validation set			
Precision	Recall	F1-score	Support		Precision	Recall	F1-score	Support
0.81	0.86	0.83	35		0.85	0.83	0.84	35
0.62	0.53	0.57	15		0.62	0.67	0.65	15
		0.76	50	Accuracy			0.78	50
0.71	0.70	0.70	50	Macro avg	0.74	0.75	0.74	50
0.75	0.76	0.75	50	Weighted avg	0.78	0.78	0.78	50

(b) **k-NN** classification reports.

## E.1.2 Random Forest

For this classifier, the *RandomForestClassifier* function from the Python package *sklearn* was used. For each of the estimators, the following parameters were tried to be optimized:

- Number of estimators (size of the forest): between 70 and 100;
- Max depth: between 5 and 25;
- Split quality metric: Gini, Entropy, or Log loss;

Furthermore, the class weight was set as *balanced* due to the large class unbalance of the data set.

Table E.10: Random forest classifier results for a 20ms delay and using the *accuracy* score metric for the optimizer. Parameters after optimization: Number of estimators - 72; Max Depth - 19; Split quality metric - Log Loss.

Test set				20ms Delay	Validation set	
Normal	Noise				Normal	Noise
27	8			Normal	32	3
10	5			Noise	5	10

(a) Random forest classifier confusion matrices.

Test set					Validation set			
Precision	Recall	F1-score	Support		Precision	Recall	F1-score	Support
0.73	0.77	0.75	35	Normal	0.86	0.91	0.89	35
0.38	0.33	0.36	15	Noisy	0.77	0.67	0.71	15
		0.64	50	Accuracy			0.84	50
0.56	0.55	0.55	50	Macro avg	0.82	0.79	0.80	50
0.63	0.64	0.63	50	Weighted avg	0.84	0.84	0.84	50

(b) Random forest classifier classification reports.

Table E.11: Random forest classifier results for a 20ms delay and using the *F1-Score* score metric for the optimizer. Parameters after optimization: Number of estimators - 84; Max Depth - 21; Split quality metric - Log Loss.

Test set				20ms Delay	Validation set	
Normal	Noise				Normal	Noise
27	8			Normal	33	2
11	4			Noise	6	9

(a) Random forest classifier confusion matrices.

Test set					Validation set			
Precision	Recall	F1-score	Support		Precision	Recall	F1-score	Support
0.71	0.77	0.74	35	Normal	0.85	0.94	0.89	35
0.33	0.27	0.30	15	Noisy	0.82	0.60	0.69	15
		0.62	50	Accuracy			0.84	50
0.52	0.52	0.52	50	Macro avg	0.83	0.77	0.79	50
0.60	0.62	0.61	50	Weighted avg	0.84	0.84	0.83	50

(b) Random forest classifier classification reports.

Table E.12: Random forest classifier results for a 20ms delay and using the *F1 Macro Average* score metric for the optimizer. Parameters after optimization: Number of estimators - 70; Max Depth - 20; Split quality metric - Entropy.

Test set				20ms Delay	Validation set	
Normal	Noise				Normal	Noise
28	7			Normal	33	2
10	5			Noise	6	9

(a) Random forest classifier confusion matrices.

Test set					Validation set			
Precision	Recall	F1-score	Support		Precision	Recall	F1-score	Support
0.74	0.80	0.77	35	Normal	0.85	0.94	0.89	35
0.42	0.33	0.37	15	Noisy	0.82	0.60	0.69	15
		0.66	50	Accuracy			0.84	50
0.58	0.57	0.57	50	Macro avg	0.83	0.77	0.79	50
0.64	0.66	0.65	50	Weighted avg	0.84	0.84	0.83	50

(b) Random forest classifier classification reports.

Table E.13: Random forest results for a 30ms delay and using the *accuracy* score metric for the optimizer. Parameters after optimization: Number of estimators - 92; Max Depth - 20; Split quality metric - Gini.

Test set				30ms Delay	Validation set	
Normal	Noise				Normal	Noise
29	6			Normal	34	1
8	7			Noise	5	10

(a) Random forest classifier confusion matrices.

Test set					Validation set			
Precision	Recall	F1-score	Support		Precision	Recall	F1-score	Support
0.78	0.83	0.81	35	Normal	0.87	0.97	0.92	35
0.54	0.47	0.50	15	Noisy	0.91	0.67	0.77	15
		0.72	50	Accuracy			0.88	50
0.66	0.65	0.65	50	Macro avg	0.89	0.82	0.84	50
0.71	0.72	0.71	50	Weighted avg	0.88	0.88	0.87	50

(b) Random forest classifier classification reports.

Table E.14: Random forest classifier results for a 30ms delay and using the *F1-Score* score metric for the optimizer. Parameters after optimization: Number of estimators - 93; Max Depth - 17; Split quality metric - Gini.

Test set				30ms Delay	Validation set	
Normal	Noise				Normal	Noise
29	6			Normal	34	1
8	7			Noise	6	9

(a) Random forest classifier confusion matrices.

Test set					Validation set			
Precision	Recall	F1-score	Support		Precision	Recall	F1-score	Support
0.78	0.83	0.81	35	Normal	0.85	0.97	0.91	35
0.54	0.47	0.50	15	Noisy	0.90	0.60	0.72	15
		0.72	50	Accuracy			0.86	50
0.66	0.65	0.65	50	Macro avg	0.88	0.79	0.81	50
0.71	0.72	0.71	50	Weighted avg	0.88	0.86	0.85	50

(b) Random forest classifier classification reports.

Table E.15: Random forest classifier results for a 30ms delay and using the *F1 Macro Average* score metric for the optimizer. Parameters after optimization: Number of estimators - 71; Max Depth - 21; Split quality metric - Gini.

Test set				30ms Delay	Validation set	
Normal	Noise				Normal	Noise
29	6			Normal	33	2
8	7			Noise	6	9

(a) Random forest classifier confusion matrices.

Test set					Validation set			
Precision	Recall	F1-score	Support		Precision	Recall	F1-score	Support
0.78	0.83	0.81	35	Normal	0.85	0.94	0.89	35
0.54	0.47	0.50	15	Noisy	0.82	0.60	0.69	15
		0.72	50	Accuracy			0.84	50
0.66	0.65	0.65	50	Macro avg	0.83	0.77	0.79	50
0.71	0.72	0.71	50	Weighted avg	0.84	0.84	0.83	50

(b) Random forest classifier classification reports.

Table E.16: Random forest classifier results for a 40ms delay and using the *accuracy* score metric for the optimizer. Parameters after optimization: Number of estimators - 75; Max Depth - 22; Split quality metric - Gini.

Test set				40ms Delay	Validation set			
Normal	Noise				Normal	Noise		
28	7			Normal	30	5		
6	9			Noise	6	9		

(a) Random forest classifier confusion matrices.

Test set					Validation set			
Precision	Recall	F1-score	Support		Precision	Recall	F1-score	Support
0.82	0.80	0.81	35	Normal	0.83	0.86	0.85	35
0.56	0.60	0.58	15	Noisy	0.64	0.60	0.62	15
		0.74	50	Accuracy			0.78	50
0.69	0.70	0.70	50	Macro avg	0.74	0.73	0.73	50
0.75	0.74	0.74	50	Weighted avg	0.78	0.78	0.78	50

(b) Random forest classifier classification reports.

Table E.17: Random forest classifier results for a 40ms delay and using the *F1-Score* score metric for the optimizer. Parameters after optimization: Number of estimators - 76; Max Depth - 16; Split quality metric - Log Loss.

Test set				40ms Delay	Validation set			
Normal	Noise				Normal	Noise		
28	7			Normal	30	5		
7	8			Noise	6	9		

(a) Random forest classifier confusion matrices.

Test set					Validation set			
Precision	Recall	F1-score	Support		Precision	Recall	F1-score	Support
0.80	0.80	0.80	35	Normal	0.83	0.86	0.85	35
0.53	0.53	0.53	15	Noisy	0.64	0.60	0.62	15
		0.72	50	Accuracy			0.84	50
0.67	0.67	0.67	50	Macro avg	0.74	0.73	0.73	50
0.72	0.72	0.72	50	Weighted avg	0.78	0.78	0.78	50

(b) Random forest classifier classification reports.

Table E.18: Random forest classifier results for a 40ms delay and using the *F1 Macro Average* score metric for the optimizer. Parameters after optimization: Number of estimators - 94; Max Depth - 24; Split quality metric - Gini.

Test set				40ms Delay	Validation set	
Normal	Noise				Normal	Noise
26	9			Normal	29	6
6	9			Noise	6	9

(a) Random forest classifier confusion matrices.

Test set					Validation set			
Precision	Recall	F1-score	Support		Precision	Recall	F1-score	Support
0.81	0.74	0.78	35	Normal	0.83	0.83	0.83	35
0.50	0.60	0.55	15	Noisy	0.60	0.60	0.60	15
		0.70	50	Accuracy			0.76	50
0.66	0.67	0.66	50	Macro avg	0.71	0.71	0.71	50
0.72	0.70	0.71	50	Weighted avg	0.76	0.76	0.76	50

(b) Random forest classifier classification reports.

### E.1.3 SVM

For this classifier, the SVC function from the Python package sklearn was used. For each of the estimators, the following parameters were tried to be optimized:

- Kernel: [Radial Basis Function \(RBF\)](#), liner, [Polynomial \(poly\)](#);

Furthermore, the class weight was set as *balanced* due to the large class unbalance of the data set.

Table E.19: [SVM](#) classifier results for a 20ms delay and using the *accuracy* score metric for the optimizer. Parameters after optimization: Kernel - [RBF](#)

Test set				20ms Delay	Validation set	
Normal	Noise				Normal	Noise
28	7			Normal	31	4
8	7			Noise	11	4

(a) [SVM](#) classifier confusion matrices.

Test set					Validation set			
Precision	Recall	F1-score	Support		Precision	Recall	F1-score	Support
0.78	0.80	0.79	35	Normal	0.74	0.89	0.81	35
0.50	0.47	0.48	15	Noisy	0.50	0.27	0.35	15
		0.70	50	Accuracy			0.70	50
0.64	0.63	0.64	50	Macro avg	0.62	0.58	0.58	50
0.69	0.70	0.70	50	Weighted avg	0.67	0.70	0.67	50

(b) [SVM](#) classifier classification reports.

Table E.20: SVM classifier results for a 20ms delay and using the *F1-Score* score metric for the optimizer. Parameters after optimization: Kernel - RBF

Test set		20ms Delay	Validation set	
Normal	Noise		Normal	Noise
27	8	Normal	25	10
6	9	Noise	10	5

(a) SVM classifier confusion matrices.

Test set					Validation set			
Precision	Recall	F1-score	Support		Precision	Recall	F1-score	Support
0.82	0.77	0.79	35	Normal	0.71	0.71	0.71	35
0.53	0.60	0.56	15	Noisy	0.33	0.33	0.33	15
		0.72	50	Accuracy			0.60	50
0.67	0.69	0.68	50	Macro avg	0.52	0.52	0.52	50
0.73	0.72	0.72	50	Weighted avg	0.60	0.60	0.60	50

(b) SVM classifier classification reports.

Table E.21: SVM classifier results for a 20ms delay and using the *F1 Macro Average* score metric for the optimizer. Parameters after optimization: Kernel - RBF

Test set		20ms Delay	Validation set	
Normal	Noise		Normal	Noise
28	7	Normal	31	4
8	7	Noise	11	4

(a) SVM classifier confusion matrices.

Test set					Validation set			
Precision	Recall	F1-score	Support		Precision	Recall	F1-score	Support
0.78	0.80	0.79	35	Normal	0.74	0.89	0.81	35
0.50	0.47	0.48	15	Noisy	0.50	0.27	0.35	15
		0.70	50	Accuracy			0.70	50
0.64	0.63	0.64	50	Macro avg	0.62	0.58	0.58	50
0.69	0.70	0.70	50	Weighted avg	0.67	0.70	0.67	50

(b) SVM classifier classification reports.

Table E.22: **SVM** classifier results for a 30ms delay and using the *accuracy* score metric for the optimizer. Parameters after optimization: Kernel - **RBF**

Test set				30ms Delay	Validation set	
Normal	Noise				Normal	Noise
28	7			Normal	31	4
8	7			Noise	10	5

(a) **SVM** classifier confusion matrices.

Test set					Validation set			
Precision	Recall	F1-score	Support		Precision	Recall	F1-score	Support
0.78	0.80	0.79	35	Normal	0.76	0.89	0.82	35
0.50	0.47	0.48	15	Noisy	0.56	0.33	0.42	15
		0.70	50	Accuracy			0.72	50
0.64	0.63	0.64	50	Macro avg	0.66	0.61	0.62	50
0.69	0.70	0.70	50	Weighted avg	0.70	0.72	0.70	50

(b) **SVM** classifier classification reports.

Table E.23: **SVM** classifier results for a 30ms delay and using the *F1-Score* score metric for the optimizer. Parameters after optimization: Kernel - **RBF**

Test set				30ms Delay	Validation set	
Normal	Noise				Normal	Noise
28	7			Normal	31	4
8	7			Noise	10	5

(a) **SVM** classifier confusion matrices.

Test set					Validation set			
Precision	Recall	F1-score	Support		Precision	Recall	F1-score	Support
0.78	0.80	0.79	35	Normal	0.76	0.89	0.82	35
0.50	0.47	0.48	15	Noisy	0.56	0.33	0.42	15
		0.70	50	Accuracy			0.72	50
0.64	0.63	0.64	50	Macro avg	0.66	0.61	0.62	50
0.69	0.70	0.70	50	Weighted avg	0.70	0.72	0.70	50

(b) **SVM** classifier classification reports.



Table E.24: **SVM** classifier results for a 30ms delay and using the *F1 Macro Average* score metric for the optimizer. Parameters after optimization: Kernel - **RBF**

Test set				30ms Delay	Validation set	
Normal	Noise				Normal	Noise
28	7			Normal	31	4
8	7			Noise	10	5

(a) **SVM** classifier confusion matrices.

Test set					Validation set			
Precision	Recall	F1-score	Support		Precision	Recall	F1-score	Support
0.78	0.80	0.79	35	Normal	0.76	0.89	0.82	35
0.50	0.47	0.48	15	Noisy	0.56	0.33	0.42	15
		0.70	50	Accuracy			0.72	50
0.64	0.63	0.64	50	Macro avg	0.66	0.61	0.62	50
0.69	0.70	0.70	50	Weighted avg	0.70	0.72	0.70	50

(b) **SVM** classifier classification reports.

Table E.25: **SVM** classifier results for a 40ms delay and using the *accuracy* score metric for the optimizer. Parameters after optimization: Kernel - **RBF**

Test set				40ms Delay	Validation set	
Normal	Noise				Normal	Noise
28	7			Normal	32	3
8	7			Noise	10	5

(a) **SVM** classifier confusion matrices.

Test set					Validation set			
Precision	Recall	F1-score	Support		Precision	Recall	F1-score	Support
0.78	0.80	0.79	35	Normal	0.76	0.91	0.83	35
0.50	0.47	0.48	15	Noisy	0.62	0.33	0.43	15
		0.70	50	Accuracy			0.74	50
0.64	0.63	0.64	50	Macro avg	0.69	0.62	0.63	50
0.69	0.70	0.70	50	Weighted avg	0.72	0.74	0.71	50

(b) **SVM** classifier classification reports.

Table E.26: **SVM** classifier results for a 40ms delay and using the *F1-Score* score metric for the optimizer. Parameters after optimization: Kernel - **RBF**

Test set		40ms Delay	Validation set	
Normal	Noise		Normal	Noise
28	7	Normal	32	3
8	7	Noise	10	5

(a) **SVM** classifier confusion matrices.

Test set					Validation set			
Precision	Recall	F1-score	Support		Precision	Recall	F1-score	Support
0.82	0.77	0.79	35	Normal	0.76	0.91	0.83	35
0.53	0.60	0.56	15	Noisy	0.62	0.33	0.43	15
		0.72	50	Accuracy			0.74	50
0.67	0.69	0.68	50	Macro avg	0.69	0.62	0.63	50
0.73	0.72	0.72	50	Weighted avg	0.72	0.74	0.71	50

(b) **SVM** classifier classification reports.

Table E.27: **SVM** classifier results for a 40ms delay and using the *F1 Macro Average* score metric for the optimizer. Parameters after optimization: Kernel - **RBF**

Test set		40ms Delay	Validation set	
Normal	Noise		Normal	Noise
28	7	Normal	32	3
8	7	Noise	10	5

(a) **SVM** classifier confusion matrices.

Test set					Validation set			
Precision	Recall	F1-score	Support		Precision	Recall	F1-score	Support
0.82	0.77	0.79	35	Normal	0.76	0.91	0.83	35
0.53	0.60	0.56	15	Noisy	0.62	0.33	0.43	15
		0.72	50	Accuracy			0.74	50
0.67	0.69	0.68	50	Macro avg	0.69	0.62	0.63	50
0.73	0.72	0.72	50	Weighted avg	0.72	0.74	0.71	50

(b) **SVM** classifier classification reports.

### E.1.4 K-Means

For this estimator, the *KMeans* function from the Python package *sklearn* was used to build two clusters and afterwards place each sample into one of them. Since there is a big class unbalance, the cluster with a larger number of members is assumed to be the one for Normal segments.

Table E.28: K-Means clustering results for a 20ms delay.

Test set				20ms Delay	Validation set			
Normal	Noise				Normal	Noise		
34	1			Normal	34	1		
14	1			Noise	14	1		

(a) K-Means clustering confusion matrices.

Test set					Validation set			
Precision	Recall	F1-score	Support		Precision	Recall	F1-score	Support
0.71	0.97	0.82	35	Normal	0.71	0.97	0.82	35
0.50	0.07	0.12	15	Noisy	0.50	0.07	0.12	15
		0.70	50	Accuracy			0.70	50
0.60	0.52	0.47	50	Macro avg	0.60	0.52	0.47	50
0.65	0.70	0.61	50	Weighted avg	0.65	0.70	0.61	50

(b) K-Means clustering classification reports.

Table E.29: K-Means clustering results for a 30ms delay.

Test set				30ms Delay	Validation set			
Normal	Noise				Normal	Noise		
29	6			Normal	30	5		
13	2			Noise	12	3		

(a) K-Means clustering confusion matrices.

Test set					Validation set			
Precision	Recall	F1-score	Support		Precision	Recall	F1-score	Support
0.69	0.83	0.75	35	Normal	0.71	0.86	0.78	35
0.25	0.13	0.17	15	Noisy	0.38	0.20	0.26	15
		0.62	50	Accuracy			0.66	50
0.47	0.48	0.46	50	Macro avg	0.54	0.53	0.52	50
0.56	0.62	0.58	50	Weighted avg	0.61	0.66	0.62	50

(b) K-Means clustering classification reports.

Table E.30: K-Means clustering results for a 40ms delay.

Test set		40ms Delay	Validation set	
Normal	Noise		Normal	Noise
30	5	Normal	31	4
10	5	Noise	11	4

(a) K-Means clustering confusion matrices.

Test set					Validation set			
Precision	Recall	F1-score	Support		Precision	Recall	F1-score	Support
0.75	0.86	0.80	35	Normal	0.74	0.89	0.81	35
0.50	0.33	0.40	15	Noisy	0.50	0.27	0.35	15
		0.70	50	Accuracy			0.70	50
0.62	0.60	0.60	50	Macro avg	0.62	0.58	0.58	50
0.68	0.70	0.68	50	Weighted avg	0.67	0.70	0.67	50

(b) K-Means clustering classification reports.

## E.1.5 Comparison

Table E.31: Hu image moment's estimators results, for each delay (20, 30, and 40 millisecond (ms)). For each dataset (Test and Validation), the best model's (found using the parameter optimizer) F1-score average and macro average (averaging the unweighted mean per label) are reported.

Optimizer Scoring Metric		Test set		Validation set	
		F1 Accuracy	F1 Macro Average	F1 Accuracy	F1 Macro Average
<b>k-NN</b>					
20ms	Accuracy	0.68	0.58	0.76	0.67
	F1	0.78	0.73	0.84	0.82
	F1 Macro Average	0.78	0.73	0.84	0.82
		.....		.....	
30ms	Accuracy	0.74	0.70	0.84	0.82
	F1	0.74	0.70	0.84	0.82
	F1 Macro Average	0.74	0.70	0.84	0.82
		.....		.....	
40ms	Accuracy	0.72	0.67	0.76	0.72
	F1	0.76	0.70	0.78	0.74
	F1 Macro Average	0.76	0.70	0.78	0.74
<b>Random Forest</b>					
20ms	Accuracy	0.64	0.55	0.84	0.80
	F1	0.62	0.52	0.84	0.79
	F1 Macro Average	0.66	0.57	0.84	0.79
		.....		.....	
30ms	Accuracy	0.72	0.65	0.88	0.84
	F1	0.72	0.65	0.86	0.81
	F1 Macro Average	0.72	0.65	0.84	0.79
		.....		.....	
40ms	Accuracy	0.74	0.70	0.78	0.73
	F1	0.72	0.67	0.78	0.73
	F1 Macro Average	0.70	0.66	0.76	0.71
<b>SVM</b>					
20ms	Accuracy	0.70	0.64	0.70	0.58
	F1	0.72	0.68	0.60	0.52
	F1 Macro Average	0.70	0.64	0.70	0.58
		.....		.....	
30ms	Accuracy	0.70	0.64	0.72	0.62
	F1	0.70	0.64	0.72	0.62
	F1 Macro Average	0.70	0.64	0.72	0.62
		.....		.....	
40ms	Accuracy	0.70	0.64	0.74	0.63
	F1	0.70	0.64	0.74	0.63
	F1 Macro Average	0.70	0.64	0.74	0.63
<b>K-Means</b>					
20ms		0.70	0.47	0.70	0.47
30ms		0.62	0.46	0.66	0.52
40ms		0.70	0.60	0.70	0.58

## E.2 Image as Input to an Artificial Neural Network

Table E.32: CNN model results for a 20ms delay.

Test set		20ms Delay	Validation set	
Normal	Noise		Normal	Noise
28	7	Normal	30	5
9	6	Noise	8	7

(a) CNN model confusion matrices.

Test set					Validation set			
Precision	Recall	F1-score	Support		Precision	Recall	F1-score	Support
0.76	0.80	0.78	35	Normal	0.79	0.86	0.82	35
0.46	0.40	0.43	15	Noisy	0.58	0.47	0.52	15
		0.68	50	Accuracy			0.74	50
0.61	0.60	0.60	50	Macro avg	0.69	0.66	0.67	50
0.67	0.68	0.67	50	Weighted avg	0.73	0.74	0.73	50

(b) CNN model classification reports.

Table E.33: CNN model results for a 30ms delay.

Test set		30ms Delay	Validation set	
Normal	Noise		Normal	Noise
29	6	Normal	30	5
8	7	Noise	9	6

(a) CNN model confusion matrices.

Test set					Validation set			
Precision	Recall	F1-score	Support		Precision	Recall	F1-score	Support
0.78	0.83	0.81	35	Normal	0.77	0.86	0.81	35
0.54	0.47	0.50	15	Noisy	0.55	0.40	0.46	15
		0.72	50	Accuracy			0.72	50
0.66	0.65	0.65	50	Macro avg	0.66	0.63	0.64	50
0.71	0.72	0.71	50	Weighted avg	0.70	0.72	0.71	50

(b) CNN model classification reports.

Table E.34: CNN model results for a 40ms delay.

Test set		40ms Delay	Validation set	
Normal	Noise		Normal	Noise
24	11	Normal	30	5
4	11	Noise	3	12

(a) CNN model confusion matrices.

Test set					Validation set			
Precision	Recall	F1-score	Support		Precision	Recall	F1-score	Support
0.86	0.69	0.76	35	Normal	0.91	0.86	0.88	35
0.50	0.73	0.59	15	Noisy	0.71	0.80	0.75	15
		0.70	50	Accuracy			0.84	50
0.68	0.71	0.68	50	Macro avg	0.81	0.83	0.82	50
0.75	0.70	0.71	50	Weighted avg	0.85	0.84	0.84	50

(b) CNN model classification reports.

# FITBIT ECG REPORT EXAMPLE

## Heart Rhythm Assessment

Recorded on Jul 2, 2022 5:31 PM

Daniel Osório

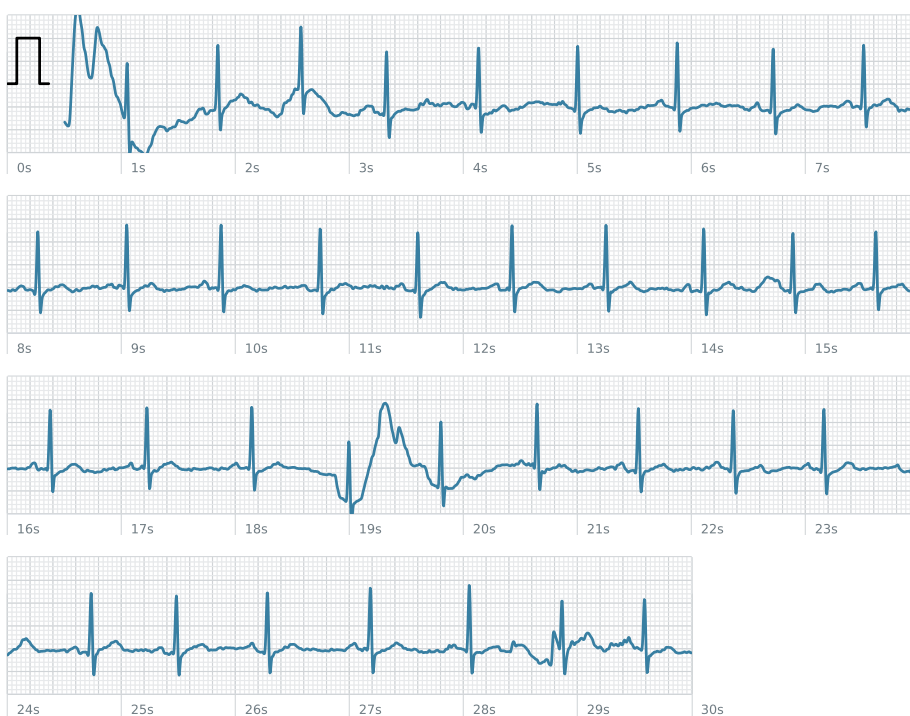
30 yr (May 18, 1992) • Male

### Normal Sinus Rhythm

Your heart rhythm appears normal.



Average  
73 bpm



[ 25mm/s, 10mm/mV, 250 Hz ] : [ Qualitatively similar to a Lead I ECG ]

## About Fitbit's Heart Rhythm Assessment

### How it works

We analyze data collected by the electrical sensors on your Fitbit device to determine if you have a normal sinus rhythm, an irregular heart rhythm suggestive of atrial fibrillation (AFib) or an inconclusive result.

### Purpose & Performance

A convenient way to detect AFib. (This is not a diagnosis.)  
Our proprietary algorithm has been tested in a clinical study. (98.7% sensitivity, 100% specificity)



Feature Version: [2.5.0-2.9-2.10] Hardware: [Sense] Firmware Version: [128.5.49]





# Novel Approach to Sensing Cardiac Disease

Assessing the

Impact of

Cardiac Disease

on the

Heart's

Electrical

Activity

and

Heart's

Structure

and

Function

and

Heart's

Electrical

Activity

and

Heart's

Structure

and

Function

and

Heart's

Electrical

Activity

